

Micro Droplet Evaporation and Modeling

by

Nguyen Trung Dung

Laboratory for Turbulence Research in Aerospace and Combustion
Department of Mechanical Engineering
Monash University, Australia

*A thesis submitted for the degree of
PhD of Engineering Science*

Sep 2012

© Nguyen Trung Dung 2012

Declaration

I hereby declare that the work presented in this thesis is solely my own work and to the best of my knowledge is original except where indicated by reference to other authors. No part of this work has been submitted for any other degree or diploma.

Nguyen Trung Dung

< September 2012 >

Notice 1

Under the Copyright Act 1968, this thesis must be used only under the normal conditions of scholarly fair dealing. In particular no results or conclusions should be extracted from it, nor should it be copied or closely paraphrased in whole or in part without the written consent of the author. Proper written acknowledgment should be made for any assistance obtained from this thesis.

Notice 2

I certify that I have made all reasonable efforts to secure copyright permissions for third-party content included in this thesis and have not knowingly added copyright content to my work without the owner's permission.

Abstract

The study of fuel droplets undergoing evaporation in convective environments has been made. Droplets studied have sizes less than 100 μm which are close to the range found in modern high pressure fuel spray systems. To enable this study, a co-flow reactor and a piezo-electric nozzle were used. The evaporation environments with varying degrees of convection were produced by use of an inverse flat-flame burner operating on a combination of CH_4 , H_2 , O_2 and N_2 . Temperatures studied are up to 676 K which closely resembles that at the end of the compression stroke of a diesel engine. To measure the evaporation rate in these circumstances, digital inline holography was selected and developed to a magnified version which was combined with particle image velocimetry for measurement.

This thesis presents the development of the measurement technique and a full analysis of potential sources that contribute to the measurement uncertainty. The development was based on use of a coherent collimated laser beam with a wavelength of 635 μm for illumination and a high speed camera with CCD array resolution of 12 $\mu\text{m}/\text{px}$ for recording. To find the focus position of the droplet in the optical path at which the image is used to calculate the droplet size, a criterion of maximum area with a threshold value was chosen. Magnification factor used in this study was 3.996 which enables the measurement of droplets with sizes down to about 10 μm . Droplet sizes measured were found to have acceptable uncertainty with the largest error to be about ± 4 μm resulting from optics imperfections. Although the cross-correlation of reconstructed images was found to be affected by the reconstruction quality, the uncertainty in velocity measurement was found negligible. The evaporation rate was estimated to have a typical error of 9%.

Experiment was done for petroleum distillates n-nonane, n-decane and n-dodecane; and standard light diesel as a multicomponent fuel in two varying heating conditions. It was found that the evaporation process is not only dependant on the surrounding temperature but also largely influenced by the preheating effect. For current conditions, all fuels initially experience thermal expansion except for nonane. This expansion level as well as the preheating time was found to be affected by the droplet size which, in turn, was found to play no noticeable role on the evaporation rate for the low convections used. Amongst alkane fuels the evaporation rate was found to be higher for the lighter fuel but when the gas temperature is close to the peak used, their rates become virtually the same to be about $0.22 \text{ mm}^2/\text{s}$. For all temperatures, diesel has the lowest evaporation rate which initially shows preferential vaporisation but then resembles the diffusion limit behaviour. For the peak temperature used, its rate is about $0.19 \text{ mm}^2/\text{s}$.

A simple infinite conductivity Lump model accounting for convection as well as the transient droplet preheating was formulated which was found to be efficient in describing the single component droplet behavior in this work in terms of the evaporation rate but slightly underpredicts the initial expansion and slightly overpredicts the droplet lifetime. If a proper set of properties is used, diesel may also be approximated by this model for certain conditions. This model indicated that the evaporation rate is controlled by the droplet temperature which tightly follows the gas temperature and that the droplet temperature is always well below the boiling point. Extension of the model to account for the Stefan flow effect and internal liquid temperature variation by using an effective conductivity concept revealed that for current conditions, the Stefan flow has very little effect in slowing down the process and that the initial strongly unsteady evaporation is due to the difference between the droplet surface and center temperatures. This difference is however not large for all cases even though the liquid thermal transport was found to be mostly by conduction. The Lump model was favored by the findings in this work that it could be used to approximate micro droplets undergoing evaporation in high temperature, strongly convective environments at least for single component fuels such as those used here.

Acknowledgements

I am heartily thankful to my supervisors, A/Prof. Damon Honnery and Prof. Julio Soria for their great support both in my work and in my life. They spent much of their time to discuss and give me invaluable advice every now and then. They provide encouragement whenever I face a difficulty and help to complete this work. I strongly believe that not only me but also all of their other students have gained so much of benefit from their enthusiastic supervision. Beside this, what can be seen from them is that they are real hard science researchers and spend so much of their time for work. They set a very good example for all of us.

I would also like to express my deepest acknowledgement to Monash engineering faculty and mechanical and aerospace engineering department for providing financial support through out my course. Without their support, this thesis would have been definitely impossible.

For building up the experimental system, I have gained considerable support from Mr. Ivor Little, Mr. Ken Sheridan, Mr. Heinrich Nowak, Mr. Hugh Venables, Mr. Nat deRose and other workers in the workshop of mechanical and aerospace engineering department. They were also willing to provide assistance whenever a problem occurred to equipment. I am so much indebted to them.

I would also like to show my gratitude to Mrs. Helen Frost, Mrs. Yvonne Arnold, Mrs. Christine Goodwin and Mr. Alex Bain for their continuous support and care. It has always been a pleasure to talk to them.

To all the students in my research group LTRAC, I am grateful to them for being friendly and helpful sometimes. We have fun and share our viewpoints whenever we have time to sit together. As students in our group are from many countries, we also explore and learn things from different cultures.

Last but not least, I owe my deepest gratitude to my parents, my wife and my son. I know my mother is always watching every step that I make even now she is so very far away. I would like to send her my love and warmest wishes. My farther, my wife and my son are here with me and they make their support available in many ways. My father always encourages me in my research work. He helps himself which is also a way to help me concentrate on my work. With my wife and my son I have had much more chance to go out and enjoy life. My wife has spent a lot of time and effort to cover much of the house work as well as to look after my son from whom I also earn many happy minutes each day when playing around with him, a very lovely but also naughty boy. Their smiles have brought so much delight to me. I love you all.

Publications from thesis

Conference proceedings

Nguyen, D. T., Honnery, D. R. and Soria, J., Magnified Digital Inline Holographic Measurement of Micro Droplets. *Proceedings of 5th Australian Conference on Laser Diagnostics in Fluid Mechanics and Combustion*. 3-4 December 2008, University of Western Australia, UWA, Crawley, WA. p. 107-110.

Nguyen, D. T., Honnery, D. R. and Soria, J., Velocity Measurement of Fuel Micro-Droplets Undergoing Evaporation using MDIH-PIV. *Proceedings of the 8th International Symposium on Particle Image Velocimetry*. 25-28 August 2009, Monash University, Melbourne. p. 658-661.

Nguyen, D. T., Honnery, D. R. and Soria, J., Use of MDIH for the Measurement of Diesel Droplet Evaporation Rates. *Proceedings of the Australian Combustion Symposium*. 2-4 December 2009, School of Mechanical and Mining Engineering, University of Queensland, Brisbane. p. 131-134.

Nguyen, D. T., Honnery, D. R. and Soria, J., Micro Droplet Evaporation and Modelling: Measurements and Validation. *9th Australian Heat and Mass Transfer Conference (9AHMTC)*. 2-4 November 2011, Monash University, Melbourne.

Journal Articles

Nguyen, D., Honnery, D. and Soria, J., Measuring Evaporation of Micro-fuel Droplets using Magnified DIH and DPIV. *Experiments in Fluids*, 2011. 50: p. 949-959.

Honnery, D., Nguyen, D. and Soria, J., Microdroplet evaporation under increasing temperature conditions: Experiments and modeling. *Fuel*, 2012. Accepted on 4th April 2012 and available online on 26th April 2012.

Nomenclature

2D, 3D	Two or three-dimensional
B_u	Velocity uncertainty limit (m/s)
B_x, B_t	Displacement uncertainty limit (μm) and timing uncertainty limit (μs)
B_Y, B_H	Mass and heat transfer (Spalding) numbers
C, C_{ref}	Density correlation factor and that at reference condition
C_{pl}, C_{pg}	Liquid and gas specific heat capacities (J/K)
C_D, C_F	Droplet drag coefficient and skin friction coefficient
d, d_o	Distance after and before effective lens (m)
d_f	Distance of focus (m)
dI	Elemental (pixel) intensity
D, D_o	Droplet diameter and its initial diameter (μm)
D_f	Flame diameter (μm)
D_{fg}	Mass binary diffusivity (m^2/s)
$\Delta x, \Delta t$	Distance (px) and time interval (ms) between two consecutive images
E	Recording exposure (mJ/cm^2)
f	Lens focal length (m)
f_x, f_y	Variables in frequency domain (cycles/mm)
F_D, F_B	Drag force and buoyancy (N)
F_Y, F_H	Correction factors for Stefan flow effect on mass and heat boundaries
g	Gravitational acceleration (m/s^2)
H	Liquid heat of vaporisation (kJ/kg)
I_0	Incident intensity (cd/m^2)
k	Wave number (m^{-1})

k_B	Boltzmann constant (J/K)
k_g, k_l	Thermal conductivities of gas and liquid (W/m.K)
K_v	Evaporation rate constant (mm ² /s)
Le	Lewis number in the gas phase
L	Lens
L_{eff}	Effective lens
m, n	2D indices of CCD array
m_d, \dot{m}_d	Droplet mass (kg) and droplet mass evaporation rate (kg/s)
m_r	Reference specific mass
m_s	Fuel vapor specific mass at the droplet surface
m_∞	Specific mass of surrounding gas at infinity
\mathcal{M}	Magnification factor
M	Number of terms in expansion series
M_t	Transverse magnification
MW_f, MW_g	Molecular weight of fuel vapor and surrounding gas (kg/kmol)
M, N	Linear size of the CCD array (μm)
n_c	Carbon number of fuel
N_t	Number of repeated test
Nu, Nu^*	Nusselt number and corrected Nusselt number
p	Pressure (Pa)
p_{cr}	Critical pressure (psia)
p_r	Reduced pressure
p_{ref}	Reference pressure (1atm)
p_v	Partial pressure of vapor at the droplet surface (psia)
P_{D^2}	Uncertainty limit in squared diameter (mm ²)
Pe_l	Peclet number in the liquid phase
Pr, Pr_l	Prandtl numbers in the gas and liquid phases
q	Total heat flux transfered to the droplet from the environment (W/m ²)
Q, Q_l	Total and sensible heat transfer rates to the droplet from the environment (W)
r_s, r_o, \bar{r}_s	Droplet radius (μm), initial radius (μm) and non-dimensional radius

Re, Re_l	Droplet and liquid phase Reynolds numbers
R^2	Correlation coefficient of functional fit
R_c	2D droplet centroid
Sc	Schmidt number in the gas phase
Sh, Sh^*	Sherwood number and corrected Sherwood number
SE_H, SE_L	Start of evaporation at high and low temperature settings
t, t_d	Droplet residence time and droplet lifetime (ms)
t_E	Exposure time (s)
T_*	Dimensionless temperature
T_B	Droplet boiling point (K)
T_{cr}	Critical temperature (K)
T_{dmax}	Maximum droplet temperature (K)
T_g, T_∞	Reactor gas temperature and temperature at infinity (K)
T_l	Droplet temperature (K)
T_o, \bar{T}	Droplet initial temperature (K) and non-dimensional temperature
T_r	Reduced temperature
T_{ref}	Reference temperature for estimating gas properties (K)
T_s	Droplet surface temperature (K)
T_{low}	Low gas temperature setting
T_{high}	High gas temperature setting
u, v	Co-ordinate system in Fourier domain
u_{rel}	Droplet relative velocity (m/s)
u_s	Maximum velocity at the droplet surface (m/s)
u, v	Droplet velocity data in x and y directions (m/s)
U_{Kv}	Uncertainty in K_v (mm ² /s)
V_o	Droplet initial velocity (m/s)
V_x	Droplet velocity function in x direction (m/s)
x, y, z	Co-ordinate system
x_o	Droplet planar centroid in x direction
X	Pixel size (μm)

Y_s	Vapor mass concentration at the droplet surface
z_o, z_i, z_r, z_c	Distances from the hologram recording plane of the object, virtual image, reference and reconstruction wave point sources, respectively (mm)

Functions

$a(x,y)$	Object wave function
$a^*(x,y)$	Conjugate object wave function
$A(x,y)$	Reference wave function
$A^*(x,y)$	Conjugate reference wave function
$h(x,y)$	Impulse response
$I(x,y)$	Intensity field
$\text{Im}\{\}$	Imaginary part of a function
$\text{Re}\{\}$	Real part of a function
$S(\Delta x, \Delta y)$	Cross-correlation function
$U(x,y)$	Hologram field
$\Phi(x,y)$	Phase of object wave
$\Psi(x,y)$	Phase of reference wave

Abbreviations

CCD	Charge coupled device
DFT	Discrete Fourier Transform
IDFT	Inverse Discrete Fourier Transform
DHM	Digital holography microscopy
DIH	Digital inline holography
DPIV	Digital particle image velocimetry
FFT	Fast Fourier Transform
IW	Interrogation window
MDIH	Magnified digital inline holography
RMS	Root mean square
ROI	Region of interest
TC	Teleconverter

Greek symbols

α	Normalization factor
α_L	Liquid thermal diffusivity (mm^2/s)
β	Slope of t_a - E curve (mW/cm^2)
ρ_g, ρ_l	Gas (air) and liquid mass densities (kg/m^3)
ρ_{ref}	Liquid density at reference condition (kg/m^3)
$\rho(\Delta x, \Delta y)$	Normalised cross-correlation function
δ_M, δ_H	Thicknesses of the gas films for mass and heat transfers
σ_L	Standard deviation of distribution function
σ_I	Standard deviation of droplet intensity field
σ_{fg}	Characteristic length between molecules of fuel vapor and gas (\AA)
σ_f, σ_g	Collision diameters of fuel vapor and gas molecules (\AA)
$\varepsilon_f, \varepsilon_g$	Characteristic Lennard-Jones energies of fuel vapor and gas molecules
λ	Wavelength (nm)
θ_L	Mean of distribution function of multicomponent fuel
θ_V	Mean of distribution function of multicomponent fuel vapor
ω	Acentric factor
ν_g	Kinematic viscosity of gas (m^2/s)
μ_g, μ_l	Dynamic viscosities of gas and liquid (Ns/m^2)
ξ, η	Co-ordinate system
ζ	Correction factor for liquid reference temperature
η	Non-dimensional radial coordinate within the droplet
χ	Liquid phase effective heat transport factor
Ψ_L	Second moment of distribution function
Ω_D	Dimensionless collision integral
T	Non-dimensional time
T_A	Amplitude transmittance
T_B	Bias transmittance
Γ	Gama distribution function

Contents

Declaration	ii
Abstract	iii
Acknowledgment	v
Nomenclature	viii
1 Introduction	1
2 Background	5
2.1 Introduction.....	5
2.2 Experimental Study	6
2.3 Theoretical Study.....	11
2.4 Proposed Research.....	19
2.5 Methods for Study	20
2.5.1 Choice of Facility	20
2.5.2 Choice of Measurement Technique.....	22
3 Methodology	25
3.1 Introduction.....	25
3.2 System Description.....	25
3.3 Heating Conditions	28

3.4	MDIH Technique.....	30
3.4.1	Basic Theory	30
3.4.2	Development of MDIH Technique.....	33
3.4.3	Reconstruction and Twin Image Elimination	35
3.4.4	Calibration of Imaging System.....	39
3.4.5	Image Processing and Size Estimation	40
3.5	Evaporation Rate Measurement.....	43
3.5.1	Residence Time Estimation	43
3.5.2	Basic DPIV Mathematics	45
3.5.3	DPIV Application	48
4	Uncertainty Analysis	52
4.1	Introduction.....	52
4.2	MDIH Measurement Uncertainty	52
4.2.1	Uncertainty from Droplet Generator and Random Noise.....	52
4.2.2	Uncertainty from Optics Imperfections	53
4.2.3	Uncertainty from Refractive Index Difference between Gases	54
4.2.4	Uncertainty from Criterion Used to Determine the Focal Plane	55
4.2.5	Uncertainty in Droplet Size Calculation.....	56
4.2.6	Uncertainty in Reference Source	57
4.2.7	Uncertainty due to the Selection of M	58
4.3	DPIV Measurement Uncertainty	59
4.3.1	Uncertainty from Displacement and Camera Timing.....	59
4.3.2	Uncertainty from MDIH Reconstruction Position.....	60
4.3.3	Uncertainty from Image Noise	60
4.4	Uncertainty in Calculating the Evaporation Rate	61
4.4.1	Uncertainty in Average Measurement	62
4.4.2	Uncertainty in Instantaneous Measurement.....	64
5	Experimental Results	65
5.1	Introduction.....	65

5.2	Experimental Conditions and Fuels.....	65
5.3	Droplet Dynamics Overview	69
5.4	Evaporation Rates of Fuels.....	70
5.4.1	Measurement of the Average Evaporation Rate	70
5.4.2	Instantaneous measurement of the evaporation rate	87
5.5	Summary of main findings	92
6	Droplet Evaporation Modeling	93
6.1	Introduction.....	93
6.2	Model Formulation	94
6.2.1	Justification of Assumptions.....	94
6.2.2	Mathematical Development.....	96
6.3	Application to Investigated Alkanes.....	99
6.4	Extension to Effective Conductivity Model	112
6.4.1	Integration of Stefan Flow Effect on the Gas Side	112
6.4.2	Liquid Phase Model.....	114
6.5	Comparison of Extended Models and Data	117
6.6	Predicted Behavior in a Variety of Conditions.....	123
6.6.1	Effect of Gas Temperature.....	123
6.6.2	Effect of Droplet Initial Velocity.....	129
6.6.3	Effect of Droplet Size	134
6.6.4	Effect of Fuel Chemistry	140
6.6.5	Multicomponent Effect.....	144
7	Conclusions	148
	Bibliography	154
	Appendix A	170
	Appendix B	175

List of Tables

5.1: Summary of experiments.....	67
5.2: Basic properties of liquid dodecane, decane, nonane and light diesel	68
5.3: Thermophysical properties of liquid dodecane, decane, nonane and light diesel	68
5.4: Summary of fuels' evaporation rates	87
6.1: Collision diameters and Lennard-Jones energies of fuel vapor taken from [94].....	100
B.1: Coefficients for calculating the heat of vaporisation of fuels	175
B.2: Reference correlation factor and density of fuels	176
B.3: Thermal conductivity at the boiling and freezing points of fuels	177
B.4: Correlation coefficients for estimating viscosity of fuels	178

List of Figures

3.1: System arrangement	26
3.2: System principle sketch	27
3.3: Inversed flat flame burner fitted on top of the reactor.....	28
3.4: Temperature profiles used for this work. Also shown are the boiling points of diesel, dodecane, decane and nonane. Position is relative to the injector tube exit. Two repeats of the temperatures are shown to indicate repeatability. Temperatures shown represent the difference between T_L and T_H	30
3.5: Recording and reconstruction of an object image in a classical holographic technique. The recording plane used to be made of a film which, after recording, becomes a hologram	31
3.6: a) Optical setup plan view; b) Principle dimensions	35
3.7: Reconstruction filter, after [91]	38
3.8: Digital reconstruction filter in Fourier transform domain, after [91]	39
3.9: a) Grids hologram; b) Reconstruction image	40
3.10: Largest area vs standard deviation criteria. Different symbols in each criterion represent different droplets	42
3.11: a) Hologram (raw data); b) Subtracted hologram; c) Reconstructed; d) Normalized and e) Filtered images of a 68 μm diesel droplet	43
3.12: An example of intensity profiles of a droplet a) along the lines passing through the droplet image mid body in x and y -directions; b) on the 2D image	45
3.13: Cross-correlation between two consecutive reconstructed droplet images: a) Droplet image at t_1 ; b) Droplet image at t_2 ; and c) DPIV cross-correlation analysis.....	49

3.14: Instantaneous time series of a single droplet passing through a measurement zone near the end of its lifetime. Every 4 th image is shown.....	50
3.15: Measurement of the u and v-velocity components of a series of evaporating droplets. The measurement domain is made up of 10 overlapped measurement zones. Each point corresponds to an individual droplet measurement	51
4.1: Droplet size distributions for droplets of approximately 62 μm with burner off	53
4.2: Effect of Gaussian noise with different sigma on MDIH results	54
4.3: PDF distributions of droplet diameters with.....	55
4.4: A typical variation in the z-direction of droplet diameter which falls below a set intensity threshold value	56
4.5: Calculated size and standard deviation as functions of individual threshold values which span the gradient field surrounding the droplet	57
4.6: Reconstruction of 85 μm diesel droplet at different M values of the filter.....	59
4.7: Variation of droplet diameter with respect to M . Different symbols represent different droplets.	59
4.8: Effect of Gaussian noise with different sigma on cross-correlation results	61
4.9: Example of average evaporation rate found for the steady evaporation period of dodecane droplet.....	63
4.10: Average evaporation rates of 5 consecutive data blocks with error bars. Each block is equivalent to a measurement zone.....	63
5.1: Dodecane droplet diameter variation against centre line position for two temperature settings. Initial diameters are about 75 μm and 76.5 μm for T_H and T_L , respectively. Two temperature profiles and dodecane boiling point are also shown.	71
5.2: Functional fits to velocity profiles and residence time calculation for dodecane droplets for high and low temperature settings	72
5.3: Dodecane droplet diameter and squared diameter against residence time for both temperature settings.....	73
5.4: Linear fits for dodecane evaporation data for two temperature settings for the whole evaporation process. Average and rolling evaporation rates are also shown for two	

settings which are found by rolling linear line fits with pivot point being the end point starting from about a measurement zone away from this point until the SE point.....	75
5.5: Average rates of dodecane of consecutive data blocks for both temperature settings ...	76
5.6: Diameter and velocity of decane droplets against position. Initial diameters are 74 μm and 45.5 μm for T_H and T_L , respectively. Gas temperature profiles are also included .	77
5.7: Linear fits for decane data for two temperature settings for the whole evaporation process. Average and rolling evaporation rates are also shown which are found by rolling linear line fits with pivot point being the end point starting from a measurement zone away until the SE	79
5.8: Average evaporation rates of decane droplets in consecutive data blocks for two temperature settings	79
5.9: Comparison of diesel droplets of 76 μm , dodecane droplets of 75 μm and decane droplets of 74 μm at high temperature setting. Gas temperature and boiling points of these fuels are also shown.....	81
5.10: Average and rolling evaporation rates of 76 μm diesel droplets for T_H	82
5.11: Average evaporation rates of diesel, dodecane and decane in 5 consecutive data blocks for T_H	83
5.12: Dodecane and nonane droplet diameters, initial values of 65 and 63.5 μm , against position for T_H . Gas temperature and boiling points are also shown	84
5.13: Square diameter against residence time for dodecane and nonane droplets in Figure 5.12. Gas temperature is also shown.	85
5.14: Diesel and nonane droplet diameters, initial values of 85 and 84 μm , against the position for T_H . Gas temperature and boiling points are also shown.	86
5.15: Instantaneous measurement setup: a) measurement zones; b) temperature profile along the reactor centerline measured at positions relative to the injector tube exit plane. The red diamond symbols correspond to the centre of each measurement zone.....	88
5.16: Droplet size histories at two different measurement locations and for different initial droplet diameters: a) $x = 10 \text{ mm}$ ($T = 530 \text{ K}$), $D_o = 64 \mu\text{m}$ and $50 \mu\text{m}$; b) $x = 20 \text{ mm}$ ($T = 600 \text{ K}$), $D_o = 58 \mu\text{m}$ and $46 \mu\text{m}$. Equations shown are lines of best fit for three individual measurements each of which has a separate symbol.....	90

5.17: Normal probability distribution of instantaneous rate a) in the measurement zone at $x = 10$ mm and b) in the measurement zone at $x = 20$ mm	91
5.18: “Instantaneous” K_v of diesel droplets plotted against the gas temperature for six measurement locations in Figure 5.15	92
6.1: Comparison between model predictions and dodecane experimental data in Figure 5.1 for both temperature settings. Shown are variations of diameter against position	100
6.2: Measured absolute velocity, predicted relative velocity and Reynolds number of dodecane droplets against position in both temperature settings	101
6.3: Comparison of predictions for dodecane droplets at two temperature settings. Shown are droplet squared diameters, droplet temperatures, gas temperature profiles and dodecane boiling point	102
6.4: Evaporation rate and temperature of dodecane droplets against gas temperature for two temperature settings	103
6.5: Predicted evaporation rates of dodecane droplets versus the droplet diameter for two temperature settings. Gas temperature profiles are also included.	105
6.6: Comparison of model predictions with experimental data of decane in Figure 5.6 for two temperature settings. Shown are variations of diameter against position	106
6.7: Evaporation rate and temperature of decane droplets against gas temperature for 74 μm droplet in high temperature setting and 45.5 μm droplet in low temperature setting..	107
6.8: Model prediction for dodecane and decane for T_H . Shown are the variations of squared diameters against residence time. Boiling points and droplet temperatures are also included.....	108
6.9: Evaporation rate and droplet temperature variations against gas temperature for dodecane and decane droplets in Figure 6.8 (at the high temperature setting).....	109
6.10: Comparison of model predictions with experimental data for the 65 μm dodecane droplet and 63.5 μm nonane droplet in Figure 5.12 for the high temperature setting. Shown are variations of diameter against position.	110
6.11: Predicted evaporation rate and droplet temperature variations against gas temperature for dodecane and nonane droplets in Figure 6.10.....	111

6.12: Comparison of model predictions with experimental data of 52 μm decane droplet and 84 μm nonane droplet for the high temperature setting. Shown are variations of diameter against position.	112
6.13: Comparison of results of three models (D vs t) with experimental data of 75 μm and 76.5 μm dodecane droplets in high and low temperature settings respectively	118
6.14: Comparison of results of three models (D vs t) with experimental data of 74 μm and 45.5 μm decane droplets in high and low temperature settings respectively	118
6.15: Comparison of results of three models (D vs t) with experimental data of 84 μm and 63 μm nonane droplets both in the high temperature setting.....	119
6.16: Liquid Prandtl, Reynolds and Peclet numbers of the 75 μm dodecane droplet evaporating at the high temperature setting.....	120
6.17: Droplet center and surface temperatures simulated by the effective conductivity model for the 75 μm dodecane droplet evaporating at the high temperature setting. Shown are also the gas temperature and droplet squared diameter.	121
6.18: Gas Lewis and mass and heat transfer numbers for the 75 μm dodecane droplet evaporating at the high temperature setting.....	122
6.19: Predicted variations of droplet diameters (x_2), temperatures and evaporation rates by the Eff Cond and the Lump model for 100 μm dodecane droplet at 500 K	124
6.20: Predicted variations of droplet diameters (x_2), temperatures and evaporation rates by the Eff Cond and the Lump model for 100 μm dodecane droplet at 1000 K	124
6.21: Predicted variations of droplet diameters (x_2), temperatures and evaporation rates by the Eff Cond and the Lump model for 100 μm dodecane droplet at 1500 K	125
6.22: Predicted variations of droplet diameters (x_2), temperatures and evaporation rates by the Eff Cond and the Lump model for 100 μm dodecane droplet at 2000 K	125
6.23: Gas temperature effect on the temperature distribution of a 100 μm dodecane droplet evaporating in still air at a) 500 K, b) 1000 K, c) 1500 K and d) 2000 K.....	127
6.24: Gas temperature effect on the preheating time, droplet lifetime and evaporation rate of a 100 μm dodecane droplet evaporating in still air.....	128
6.25: Stefan flow effect on the lifetime and evaporation rate of a 100 μm dodecane droplet with $V_o = 90$ m/s undergoing evaporation in still air at 1500 K. Shown is also the droplet velocity.	130

6.26: Stefan flow effect on the Sherwood, Nusselt numbers and the temperature of a 100 μm dodecane droplet with $V_o = 90$ m/s undergoing evaporation in still air at 1500 K.....	130
6.27: Predicted variations of droplet diameters (x2), temperatures and evaporation rates by the Eff Cond and the Lump models for a 100 μm dodecane droplet with $V_o = 90$ m/s undergoing evaporation in still air at 1500 K.	132
6.28: Effect of V_o on the variations of diameter and evaporation rate of a 100 μm dodecane droplet undergoing evaporation in still air at 1500 K. 0, 10, 30, 60 and 90, in turn, means $V_o = 0, 10, 30, 60$ and 90 m/s. Shown is also the droplet Reynolds number....	133
6.29: Effect of V_o on the liquid Reynolds and Peclet numbers of a 100 μm dodecane droplet undergoing evaporation in still air at 1500 K. 10, 30, 60 and 90, in turn, means $V_o = 10, 30, 60$ and 90 m/s.....	133
6.30: Effect of V_o on the temperatures of a 100 μm dodecane droplet undergoing evaporation in still air at 1500 K. 0, 10, 30, 60 and 90, in turn, means $V_o = 0, 10, 30, 60$ and 90 m/s.	134
6.31: Predictions by the Eff Cond model and the Lump model for a 300 μm dodecane droplet with $V_o = 0$ m/s undergoing evaporation in still air at 1500 K	135
6.32: Predictions by the Eff Cond model and the Lump model for a 300 μm dodecane droplet with $V_o = 90$ m/s undergoing evaporation in still air at 1500 K	135
6.33: Lump prediction of normalized squared diameter against the normalized time for the 100 and 300 μm droplets with $V_o = 0, 10$ and 90 m/s evaporating in still air at 1500 K	137
6.34: Lump predictions of evaporation rate and droplet Reynolds number for the 100 and 300 μm dodecane droplets with $V_o = 0, 10,$ and 90 m/s evaporating in still air at 1500 K	138
6.35: Eff Cond predictions of droplet temperatures and Peclet number for the 100 and 300 μm droplets with $V_o = 0$ and 90 m/s evaporating in still air at 1500 K.....	139
6.36: Variation of droplet preheating time and lifetime of the 100 and 300 μm droplets evaporating in still air at 1500 K against droplet initial velocity. Shown are also ratios of preheating time and lifetime of the 300 μm droplet to those of the 100 μm droplet.	139

6.37: Predictions of diameter (x2), evaporation rate and temperatures of a 100 μm nonane droplet with $V_o = 0$ m/s evaporating in still air at 1500 K by the Eff Cond and the Lump models.....	140
6.38: Predictions of diameter (x2), evaporation rate and temperatures of a 100 μm nonane droplet with $V_o = 90$ m/s evaporating in still air at 1500 K by the Eff Cond and the Lump models	141
6.39: Variations of diameter and evaporation rate of the 100 μm droplets of dodecane, decane and nonane with $V_o = 0$ m/s evaporating in still air at 500 K	142
6.40: Variations of diameter and evaporation rate of the 100 μm droplets of dodecane, decane and nonane with $V_o = 0$ m/s evaporating in still air at 1500 K	143
6.41: Variation of steady state K_v of the dodecane, decane and nonane droplets against gas temperature	143
6.42: Temperature variation of the 100 μm droplets of dodecane, decane and nonane with $V_o = 0$ m/s evaporating in still air at 1500 K	144
6.43: Comparison of the Lump prediction using the properties of tridecane with the experimental data of the 76 μm diesel droplet. Shown is also the gas temperature. ...	146
6.44: Comparison of the Lump prediction using the properties of tridecane with the experimental data of the 85 μm diesel droplet. Shown is also the gas temperature. ...	147
A.1: Variation of squared diameter against residence time of the 84 μm nonane droplet evaporating at high temperature setting.....	170
A.2: Variation of squared diameter against residence time of the 85 μm diesel droplet evaporating at high temperature setting.....	171
A.3: Droplet size histories at measurement location $x = 0$ mm ($T = 430$ K) for initial diameters $D_o = 68$ μm and 57 μm . Equations shown are lines of best fit for three individual measurements each of which has a separate symbol.....	171
A.4: Droplet size histories at measurement location $x = 5$ mm ($T = 480$ K) for initial diameters $D_o = 70$ μm and 62 μm . Equations shown are lines of best fit for three individual measurements each of which has a separate symbol.....	172

A.5: Droplet size histories at measurement location $x = 10$ mm ($T = 530$ K) for initial diameters $D_o = 64$ μm and 50 μm . Equations shown are lines of best fit for three individual measurements each of which has a separate symbol.....	172
A.6: Droplet size histories at measurement location $x = 15$ mm ($T = 570$ K) for initial diameters $D_o = 70$ μm and 56 μm . Equations shown are lines of best fit for three individual measurements each of which has a separate symbol.....	173
A.7: Droplet size histories at measurement location $x = 20$ mm ($T = 600$ K) for initial diameters $D_o = 58$ μm and 46 μm . Equations shown are lines of best fit for three individual measurements each of which has a separate symbol.....	173
A.8: Droplet size histories at measurement location $x = 25$ mm ($T = 630$ K) for initial diameters $D_o = 46$ μm and 35 μm . Equations shown are lines of best fit.	174
A.9: Model predictions for the 65 μm dodecane droplet and 63.5 μm nonane droplet for T_H . Shown are the variations of squared diameters against residence time. Boiling points and droplet temperatures are also indicated.....	174

Chapter 1

Introduction

For a wide range of heat engines, liquid fuel is introduced into the combustion chamber in the form of a spray consisting of a multitude of minute droplets. As such, the study of basic combustion characteristics of a fuel is normally done by investigating the behavior of these droplets when undergoing heating loads. The need to understand the evaporation processes which precede the combustion has over the last few years become more urgent. Increasingly stringent regulation of exhaust products has seen many manufacturers respond to this challenge by reducing the average size of the droplet in the fuel spray, typically by increasing the fuel injection pressure. In diesel engines for example, fuel injection pressures have now reached over 2000 Bar, with fuel typically atomized into droplets with diameters much less than 50 μm . Coupled to this is the increasing uptake of non-traditional fuels and the strong likelihood that future liquid fuels will be more complex in their makeup as new feedstocks are taken up. All of this supports the need to measure evaporation rates of fuels more typical of these new conditions.

There has over the years been much research focused on the experimental and theoretical aspects of both single and multi-component fuels undergoing evaporation. Experimental studies over the last fifty years have examined fuel droplets ranging in size from a few hundred to a few thousand microns in diameter such as those in [30, 31, 36, 53, 111, 142]; studies involving droplets less than 100 μm are less common and include among the more recent ones those in [22, 35]. The conditions used for these investigations are a variety

ranging from a spherically symmetric, quiescent configuration [36] to a turbulent one [143]. The study under high temperature, high pressure environment coupled with convection is more complicated than those typically studied but is however more desired as it closely resembles that in practical devices.

To measure the droplet size, a number of techniques have often been used and examples are video or photography based techniques [62, 72, 92], Backlit Stroboscopic Imaging [35, 104, 111, 122] and some laser based techniques such as light scattering [22]. From a measurement perspective, small droplet size brings a number of problems, especially if quantitative assessment is crucially required. For example, the fixed pixel size of digital imaging equipment limits the spatial resolution available for measurement. The use of high magnification to overcome this brings with it limited imaging volumes, and most importantly greatly reduced focal depth. Getting close to an evaporating droplet can often be difficult if a high temperature convective environment is being examined (e.g. Garcia-Perez et al [35]). Given these limitations, it is difficult or even impossible to use any of the existing techniques.

It is therefore necessary to develop a new experimental methodology which overcomes these problems. One such technique is based on the extension of digital in-line holography (DIH) as was used in [95] to include a lens mechanism, a technique referred to as magnified digital in-line holography (MDIH); this thesis builds upon this development work. In addition to enhanced image magnification, this technique provides significantly enhanced depth of field compared to traditional optics for a fixed magnification and, of equivalent importance, a much longer distance of focus compared to other studies using microscope objectives (e.g. [114]).

As applied to droplet studies in different implementations, an early example of the use of holography was that of Grabowski [39] in 1983, or a recent work of Palero et al [95] in 2007. By itself however MDIH is limited in what properties it can be used to measure, droplet evaporation rate for example requires the change in droplet area with time. Droplet residence time is needed for this, and this can be obtained from measurement of the velocity

of the evaporating droplet. To measure this velocity, a number of options are available such as the mentioned Backlit Stroboscope, Laser-Doppler Velocimetry [13, 81, 106] and Particle Image Velocimetry [11, 139]. This work combines MDIH with digital particle image velocimetry (DPIV) to measure the droplet evaporation rate. As important as it is, a full analysis of the measurement uncertainty is carried out with assessment of the limit of the technique being also provided.

Given such developments, it is the aim of this work to quantitatively analyse the behavior of droplets smaller than 100 μm undergoing evaporation in hot convective environments. To conduct such experiments, a purpose built quartz glass reactor which is capable of operating in a range of temperatures has been constructed. The hot gas flow is created by use of a flat flame burner. Being present in many petroleum products, a number of single Alkane liquids have been of much interest with studies focused very often on a range from n-pentane to n-hexadecane (e.g. [7, 31, 55, 69, 90, 107]). In this work, n-nonane, n-decane and n-dodecane are used together with automotive light diesel, as a standard multicomponent fuel, being also measured for comparison.

For this type of study, there are many parameters that can affect the droplet behavior such as droplet initial diameter, surrounding gas temperature and/or pressure, Reynolds number. The experimental task in this work is however limited to investigations of initial diameter and gas temperature effects. Measurements are done in two forms with one being to measure the average evaporation rate of the droplets over their trajectory through the reactor while the other being to measure the instantaneous rate of individual droplets over a limited trajectory. To enable a further understanding of the process, another task of this work is to formulate a mathematical model to simulate the experimental data.

In general, the mathematical formulation can be done via analytical, semi-analytical or numerical approaches and in this field a vast amount of droplet evaporation/combustion models have been built ranging from simple [36, 120] to very complex [28, 103]. For most of the cases the droplet modeling needs to consider the practical point of view, or to be more specific, to consider its integration into spray modeling. As such, the point is to seek for an

efficient model (simple and fast but accurate enough) without invoking more advanced models which usually involve a large amount of computing time. This implies that for a certain condition, the model adequately accounts for effects that are important and nonnegligible and this work aims at formulating such a model. Extension of this simple model is however still necessary to investigate more parameters and that the extended version also helps to explore the applicability of the simple model in extended conditions. With these models, more thorough investigations of important effects including droplet initial diameter, gas temperature, fuel chemistry and droplet Reynolds number are possible which have been impossible in current experimental setup.

The structure of this thesis is as followed. Previous work on fuel droplet both via experimental and theoretical approaches as well as measurement techniques are reviewed in Chapter 2. Descriptions of the experimental system, some mathematical background on the technique development and all related technical matters are presented in Chapter 3. Analysis of measurement uncertainty is followed in Chapter 4. Chapter 5 is devoted to experimental results while Chapter 6 accommodates droplet evaporation modeling, results and discussions. Major conclusions drawn from this research are given in Chapter 7.

Chapter 2

Background

2.1 Introduction

The study of fuel droplet evaporation and combustion has been the focus of a huge amount of research since it is a primary process occurring in so many practical applications that use liquid fuel in the form of a spray. Clearly, this is a problem with a long history [36, 120] and the work involved more recently has pointed to many advanced aspects such as spray effects, ignition/extinction (see [71, 116] with a lot of references therein). However this study is still currently of much interest with more work regularly published. In basic studies, it is to investigate the behavior of a single isolated cold droplet after being suddenly introduced into a hot environment. In the case of pure evaporation, the droplet receives the heat from the environment through conduction and/or radiation which is used to heat the droplet and to gasify it. Droplet combustion is the case where an ignition stimulus is used or the ambient temperature is high enough to introduce a flame from the gasified vapor. In this case, it is widely perceived as a spherical flame sheet surrounding the droplet (assuming no convection). The fuel vapor diffuses outward mixing with the inward stream of oxidizer at the flame sheet and reacts. Heat released from combustion is transferred outward to the environment and inward to heat the droplet and to gasify it.

Given the present status in the field, this chapter only reviews major investigations related to the study of fuel droplets both via experimental and theoretical methods. Some of the effects/factors reviewed are deemed relevant for further analysis and discussion of this work. In the past, experimental study has been done in a number of ways and examples of interested parameters are multi-component effects, droplet sizes, ambient temperature and/or pressure. While such an experimental approach is limited to certain conditions, a theoretical approach easily expands to those which are hard to setup for experiment, for example to simulate real environments in internal combustion engines [59] or gas turbines [55]. Also, quantities that can be investigated expand to others such as droplet internal temperature and composition, gas/vapor phase concentration profiles, etc. As droplet combustion in a turbulent forced convective flow is a problem involving many complex processes, detailed theoretical study provides insight on mechanisms governing complex heterogeneous combustion systems. Measurement techniques that are available for investigation are reviewed and some comparison is made.

To avoid confusion, there are terms often used in this field which need to be clarified. The terms “evaporation” and “vaporisation” usually means a pure evaporation case without the presence of a flame. While “combustion” means for the case with a flame surrounding the droplet, evaporation is still occurring on the droplet surface and this has led to the use of “gasification” or sometimes “vaporisation” to describe such a process while not intending any particular case. The term “gas” refers to the phase surrounding the liquid droplet even though the vapor is also present in this phase.

2.2 Experimental Study

In the field of fuel droplet study, a number of methods have often been used including droplet suspension [22, 36, 42, 72, 74], porous sphere [1, 6], droplet levitation [104, 140] and free fall techniques [22, 35, 111, 138, 142]. For the suspension techniques, a single droplet is suspended usually at the tip of a thin fibre. The second techniques make use of a porous sphere into which fuel is supplied and kept wet on the surface to simulate a droplet.

The levitation techniques use electrostatic force, acoustic wave or optical radiation pressure to suspend a droplet. The last techniques aim at studying free fall droplets. Amongst these techniques, only levitation and free fall techniques allow studying the droplet free of contact. Because of the simplicity in setup and experimentation the first two techniques are seen in many investigations. The last technique is the most desired but difficult in way to generate the single droplet or more often a continuous stream of droplets with uniform size in controllable spacing. It is also more involved with how to measure the moving droplets.

The behavior of fuel droplets in complex conditions such as that in combustors is affected by many parameters. To properly assess the effect of these parameters it is necessary to separate some or all of them and as such experiments are usually conducted in narrower and more specific conditions depending on the purpose. To understand the most fundamental features of droplet combustion, it is necessary to perform quiescent, spherically symmetric experiments. Experiments under the influence of gravity are always affected by buoyancy and even if there is no gas convection, the flame surrounding the droplet can still be distorted. Furthermore, this effect varies with droplet size and so it is a transient effect. Attempts to minimize this effect can be seen in previous work in two forms. The first and very complicated method is that used in a freely falling chamber by Kumagai [44, 45, 62, 92] in which the suspension fibre supporting the droplet is lifted up impulsively when the free fall starts so that the droplet released is supposed not affected by gravity. The second method is much simpler by studying suspended droplet in low pressure environment enriched with oxygen [72, 89].

In [62, 92] with the first method, a single droplet of heptane was used and a linear reduction of droplet squared diameter D^2 with respect to time t was observed after an initial short period. The slope of this $D^2(t)$ curve is known as the evaporation/combustion rate. Their data is however limited to a short period of droplet lifetime. Using the second method for octane, Law et al [72] also found the above linear relationship after an initial period of slow reduction rate. The flame front stand-off ratio, which is the ratio of flame diameter (D_f) to droplet diameter (D), was found to increase continuously for low oxygen concentration of the ambient gases while initially increasing but then leveling off for high oxygen

concentration; this shows an obvious effect of oxygen in droplet combustion. For all cases, the flame sheet expands initially and then shrinks toward the end of the droplet lifetime. With higher oxygen content, droplet life time is shorter which means higher burning rates. This expected behavior was also seen by other authors (e.g. [31]). These experiments were however limited to large droplets (minimum of about 700 μm) due to the size of the fibre tip. The initial transient period usually spans about 5-10% of the droplet lifetime and is due largely to the effect of droplet preheating. The D^2 - t linear relationship is known as the D^2 -law or steady state behavior which can be derived from very basic droplet theories.

To study the effect of convection, there have been investigations carried out in hot gas flows and examples are [23, 31, 143]. Wu et al [143] used a wind tunnel setup to investigate the effect of ambient turbulence with different intensities and length scales on heptane and decane droplets at room temperature. Studying a number of fuels Faeth and Lazar [31] used a suspension fibre but exposed the droplets to the hot combustion gas of a flat flame burner. Under these convective conditions, the above behavior was still observed. The study by Daïf et al [23] was done for binary heptane-decane droplets which were suspended on a sphere at the end of a glass capillary and exposed to electrically heated air with variable speed in a thermal wind tunnel. The vaporisation of these droplets was seen to proceed at different rates in sequence of volatilities which was characteristic of the batch distillation process.

The above behavior is known to be affected by circulation occurring inside the droplet. This internal motion generated by either natural or forced convection has been the focus of a considerable amount of studies. With the trend to use more and more complex fuels to help alleviate the problem of energy shortage, many of those studies used multicomponent liquids to investigate the role of internal circulation (e.g. heptane-decane [23], octanol-undecane [74], heavy-light diesels and kerosene-gasoline [30] or water-in-oil emulsion [75]). The evaporation behavior of these liquids depends on the intensity of circulation. For example, in their droplet combustion study El Wakil et al [29] measured similar temperatures at the droplet core and periphery even during the early heating period and the temperature history developed towards the batch distillation behaviour (components evaporate almost sequentially in the order of their volatility from high to low and droplet temperature follows

sequentially the wet-bulb temperature of the dominant vaporizing components with short transitions between them). Another example is the combustion of binary droplets by Wood et al [141] in hot air with circulation driven by buoyancy. In brief the faster the circulation is the closer to batch distillation the behavior is with preferential evaporation of the more volatile components. This is clearly different from steady state behavior. Without internal circulation the droplet concentration and surface temperature were shown to attain steady state very early [64, 74]. Except for the initial short period, the behavior is similar to D^2 -law and the droplet behaves like a single droplet with concentration weighted average properties. Viscous mixtures in quiescent environments should favor this behavior.

On mentioning droplet temperature measurement, it is noted from the literature that almost all theoretical formulations have been validated against the data of droplet sizes versus residence time which is obtained from measurements of droplet size and velocity. With many complex processes involved in this type of study, droplet temperature measurement can play a significant role in validation and is also useful as it gives further insight to what happens inside the droplet. There used to be limited work on this until more recently with some new investigations focused on this matter. A number of studies [13, 80, 81, 82, 136, 140, 148] have used techniques such as rainbow refractometry, two- or three-color laser induced fluorescence. One example is a recent study [13] belonging to a series done by the Lemoine group which measured the temperature distribution of moving droplets by use of a two-color laser induced fluorescence technique. They found that under their conditions the heat transfer is non-radial and the temperature distribution resembles a Hill vortex. Though useful, application of these techniques is limited to only single and binary droplets.

In practical devices, a multitude of droplets is present in an atomized spray. The evaporation and combustion of these droplets are therefore influenced by the effect of interactions which make the process different from that of an isolated droplet. Experiments in [30, 60, 89, 105] are some examples investigating this effect. Kristyadi [60] investigated the effect of interactions by use of a liquid jet device to produce a stream of closely spaced droplets. They found slower preheating and lower evaporation rates of a number of liquids

such as heptane, decane and dodecane. Miyasaka and Law [89] used suspension fibres arranged in different configurations and also included the effect of buoyancy by varying the ambient pressure and oxygen concentration. While similar effect of interaction was seen, the buoyancy significantly enhances the burning rate due to the enhanced convective transport between droplets [89]. It is generally concluded that the evaporation rate of arrayed droplets is slower with shorter inter-distances. More detailed study by Sangiovanni and Labowsky [105] for a range of fuels, ambient conditions, and droplet sizes (hundreds of micron) indicated that the increase in droplet lifetime depends solely on the inter-distance, not on the ambient condition, fuel type or droplet size. They estimated that combustion in practical devices needs to account for this effect as it is strong with inter-distances typically found in the spray. However the high Reynolds number in these situations should mitigate the interaction effect [30].

One of the effects which has attracted less research is the effect of initial diameter and, to the best of the author's knowledge, only few investigations have been done such as those of the Kumagai group [45, 62, 92] and other authors [49, 53] given also that the sizes studied were very large except for only one case by Hara and Kumagai [45]. Spherically symmetric combustion experiments by these authors for heptane droplets of two sizes, 400 μm under microgravity and 70 μm under normal gravity, have shown that whereas the typical behavior of transient heating followed by steady state was seen for large droplets, the steady burning stage of small droplets of the later case is followed by a final stage of pure evaporation (extinction occurred) with decreasing rate. For their size range 700-1800 μm , they claimed that evaporation rate tends to increase slightly with diameter. While a much clearer trend was seen in the study for kerosene by Khan et al [53] with sizes roughly from 700-1600 μm under a wider range of temperatures and pressures, the reverse trend was seen by Jackson et al [49] for some other fuels with sizes from 400-1100 μm . Regarding sooting tendency, the authors in [45] claimed that larger droplets tend to support formation of soot with no soot observed for small droplets. With the same observation the authors in [49] deduced that larger droplets burn slower due to more soot formed surrounding the droplet under their low convection condition which interferes with heat and mass transfer. Regarding the droplet preheating, it was found in [53] to take longer for a larger droplet which is as expected.

A phenomenon sometimes observed during multicomponent droplet gasification is microexplosion which has drawn quite a few investigations (e.g. [66, 67, 111, 138, 142]). This is an important phenomenon as it improves the atomization process by shredding the droplets into smaller sizes which is effective in reducing the burnout time. Wang et al [138] studied the combustion of freely falling binary droplets at low Reynolds number and found that its occurrence depends strongly on the mixture concentration and the stability of the droplet generation mode. Lasheras et al [67] observed isolated free droplets of binary n-paraffin mixtures. They stated that for disruption to occur the difference in boiling points must be higher than a certain limit and the initial concentration of the more volatile component must lie within a limited range. This phenomenon is more likely to happen with slow internal mixing as the more volatile, lower boiling point components are prevented to diffuse to the droplet surface (effect of diffusion limit). When the droplet temperature is high, its inner core with trapped low boiling point components becomes superheated. The superheat accumulates and nucleation bubbles, which usually start near the droplet center [138], are formed. As a result of extremely fast gasification with intense pressure build-up, disruption occurs [70]. For those experiments that used suspension technique, the combustion is affected (microexplosion promoted) due to the suspending filament [67]. This phenomenon is more intense for emulsions than miscible blends, Lasheras et al [66, 67].

More recently there has been a class of studies focused on extremely complex fuels such as biomass pyrolysis oil (e.g. [22, 35, 111, 142]). A typical complicated behavior can be seen from experiments by Wornat et al [142] for combustion of bio-oil droplets of 320 μm in a laminar flow reactor. While diesel showed one stage of quiescent sooty burning, bio-oil presented four stages. After burning, two forms of solid cenospheres have often been found as a result of polymerization [22, 35]. Microexplosion which frequently occurred was thought to be the result of wide range of volatilities and high viscosity of this fuel.

2.3 Theoretical Study

In the past few decades there have been numerous theoretical investigations of the gasification and oxidation of single isolated droplets. In basic classical (D^2 -law) theories,

mostly appeared in the 1950s [36, 120], a set of assumptions typically including spherical symmetry of the isolated droplet, constant and uniform droplet temperature, quiescent steady state, equilibrium evaporation, constant thermophysical properties, etc., is usually used to simplify the calculation while still yielding acceptable results such as approximate evaporation time and rate [72]. The square of droplet diameter was found to decrease linearly with time in the form of $D^2 = D_o^2 - K_v t$ where D_o is initial droplet diameter and K_v is the evaporation/burning rate constant. However there were differences compared to experiments and it was thus developed in later research to include other realistic effects. Examples are unsteadiness [48, 72], variable thermophysical properties [3, 4, 48], droplet internal circulation [4, 71], thermal radiation [3, 108], Stefan flow [4, 145], non-equilibrium [27, 43], kinetics effect [61]. The followings outline some important and common effects.

The unsteadiness in gasification (e.g. [48, 72, 151]) which can be strong during the early stage as seen in experiments was found to be controlled by a number of processes such as the droplet transient heating, vapor accumulation and unsteady heat and mass diffusion in the gas phase. To assess the droplet heat up period, a knowledge of temperature distribution within the droplet is needed which can be obtained by numerical solution of the liquid phase heat equation coupled with gas phase equations. Being dependent on liquid sensible heat, this process is affected by the driving force on the vapor side [48]. Initial preheat strongly affects the later process, especially at high pressure [71, 103, 151]. Regarding the heat and mass transport in the gas phase, the unsteadiness was found unimportant in pure evaporation [48] but important in combustion [72]. The steady state assumption assuming equality between gasification rate at the droplet surface and consumption rate at the flame sheet leads to an inaccurate estimate of the chemical heat release rate. The flame front stand-off ratio, found constant in D^2 -law theory, varies due to vapor accumulation or depletion between the droplet and the flame. At high ambient pressure and/or temperature gas phase unsteadiness becomes more profound [151] thus making the quasi-steady assumption more inappropriate and prediction for the initial period more erroneous.

Given the unsteadiness mostly in the initial period the later gasification in the main period is widely known to proceed quite steadily for single liquid droplets if gas temperature

is constant. It is meaningful to investigate how this gasification rate is affected by the surrounding temperature and pressure. This was done by Chin and Lefebvre [15] with a simple method applied to heptane, gasoline, jet fuel and diesel in a quiescent environment. Results indicated that at a constant pressure, the steady state gasification rate increases with temperature but the dependence on pressure is more complicated depending on temperature. At a low temperature of about 500 K the rate slightly decreases with pressure but at higher temperatures, especially higher than 800 K, it increases with pressure; similar trends were also observed by Kim and Sung [54] with a more detailed high pressure model. Chin and Lefebvre [15] also estimated the steady state droplet temperature which, under all their conditions of 500-2000 K and 100-2000 kPa, increases with ambient temperature but is always lower than the respective boiling point. Given a lack of data at high pressure (experimentation at high pressure is limited, e.g. [30, 53, 122]), their calculation at normal pressure was verified by the data of Godsave [36] at temperature of 2000 K. It is necessary to mention the finding by Manrique and Borman [79] that steady state behavior can never be attained once the pressures reach a sufficiently high value.

The variable nature of gas phase thermophysical properties such as specific heat capacity and transport coefficients which are dependant on temperature and concentration has been included in models developed in for e.g. [3, 4, 48, 68, 73]. This consideration is important in devices such as internal combustion engines because the turbulence in the late stage of the compression stroke can give rise to large variation in temperature and composition across the volume. In simple models, these properties assume average values and the gas phase Lewis number, a parameter that is directly derived from them, is assumed to be unity. During a typical evaporation process the Lewis number can however vary substantially from 1.0 to 4.0 [4]. According to [71], variable gas property effects are important for accurate estimation of the burning characteristics. The assumptions of constant properties can lead to over prediction of the flame size [73]. In the evaporation study of Hubbard et al [48], the variable properties solution was found to be best approximated by one using the simple 1/3 rule reference scheme of Sparrow and Gregg [121] in which properties are evaluated at $T_r = 2/3T_s + 1/3T_\infty$ and $m_r = 2/3m_s + 1/3m_\infty$. Besides variable gas phase thermophysical

properties, Abramzon and Sazhin [3] also accounted for variable thermophysical properties of the liquid phase and their formulation became more complicated.

In principle, a droplet can receive heat from the surrounding environment via conduction, convection and radiation. While a majority of modeling work accounts for conduction and convection there are lesser studies that include the effect of thermal radiation on droplet heating and evaporation (e.g. [3, 25, 26, 63, 108]). To include this effect, an average [26, 108] or distribution [3, 25, 63] of droplet thermal radiation absorption coefficient is taken into account which requires the knowledge of the spectral optical properties of the fuel like absorption and refractive indices. The higher the absorption coefficient is the more radiation heat is absorbed. Besides such dependence on liquid properties, this effect is also supposed to depend on the type of heat source used for investigation.

In many of the simplified models, a significant assumption used is that of spherical symmetry, which implies that only radial transport is possible and only the radial co-ordinate (1D) is therefore needed. The transport in the gas phase involves diffusion and radial convection while that in the droplet involves diffusion only. However, in situations involving external gas flow of either forced or natural convection, it is intrinsic to solve the problem in two dimensions (2D) as has been done by more advanced studies [87, 99, 129] due to the existence of a non-radial relative velocity between the droplet and the surrounding gas. This slip between the velocities exerts a shear stress on the droplet surface which induces the internal circulation mentioned earlier. Usually droplets with more than one component need to have a more detailed liquid phase description than the single component droplet [71].

Internal circulation enhances the heat and mass transfer, especially for a multicomponent droplet. Besides the dependence on liquid viscosity as expected, the vaporisation behavior also depends on the circulation intensity which in turns depends on the convection level represented by the droplet Reynolds number [65, 76, 87, 129]. In a mixture with widely differing component boiling points, transport processes within the droplet can play a significant role in controlling the surface composition which decides how the vaporisation

progresses. In theory these phenomena can have two opposite extremes: one is with an infinite circulation rate while the other is with no circulation. The first extreme has been modeled by Law [69] as a droplet of ideal-mixture in which the composition and temperature are assumed spatially uniform but temporally varying. Vaporisation is the process of batch distillation mentioned earlier. At high temperature, the vaporisation rate is insensitive to the fuel composition [69]. These phenomena were demonstrated for less viscous fuels of light alkane liquids and were supported by the mentioned experimentation. Based on those observations the author developed a simplified model treating the droplet as shells of individual components the radii of which increase with volatilities. With the assumption of quasi steady vaporisation for each shell, the bulk vaporisation time was found to agree very well with the ideal-mixture model.

The opposite extreme with a steady state gasification period has been modeled by Law and Law [74] based on their undecane-octanol droplet experiments at very low Reynolds number. Newbold and Amundson [90] also found this behavior for their model on binary and ternary droplets of heptane, octane and nonane. At these low Reynolds numbers, the burning rate depends on the composition [74]. The steady state behavior is characterized by an inner core with concentrations remaining almost constant and uniform at their initial values. A boundary layer at the droplet surface exists where concentrations of each component steeply adjust to its surface value which depends on the relative volatility while the fractional gasification rate of each component still equals to its initial mass fraction [74]. The above are characteristics of droplet diffusional resistance. In this low extreme with no circulation the transport is purely diffusion controlled and mass diffusion is the rate limiting factor. With a higher mass transport rate, more volatile compounds generally diffuse outward whereas less volatile compounds diffuse inward resulting in the mentioned preferential vaporisation. In the first extreme, volatility differentials are the rate limiting factors.

Given the proposed ideal-mixture model, it has however been stated that even with very fast circulation rate, both temperature and mass gradients are still significant as the transport in the direction normal to the circulating streamlines is still effected by the slow diffusion

process [65]. The above statement is supported by the experiments at high Reynolds number done by Lerner et al [78] who have shown that the vaporisation follows a mixed behavior between the distillation and diffusion limit. This has also been most recently shown in [147] in which the additional effect of high ambient pressure was found to reduce the diffusional resistance as the droplet temperature becomes higher which suggests the process tends toward the distillation limit.

The liquid phase models with internal circulation have been classified into two flow configurations. For intermediate Reynolds numbers, it is usually modeled as a Hill's vortex with boundary layers near the interface, while for high Reynolds numbers the flow separation occurs near the rear stagnation point and wake regions created (cf. [71]). In practical devices, strong internal circulation can also be attained during the violent atomization process. Being complicated when solving in 2D, this effect can nevertheless be simplified by effective diffusivity models represented by an effective coefficient as done for example in [4]. This is a good approximation as the net effect of internal circulation reduces the diffusion distance and hence shortens the diffusion time [71]. According to Kneer et al [55], the variation in liquid thermophysical properties helps to further reduce the diffusional resistance, these effective models should therefore also account for this fact as these properties depend on both temperature and concentration. In making the problem simpler, the convection on the gas side has been widely approximated by film theory [8, 131].

Theoretical studies mentioned so far on the multicomponent effects have been mostly for binary (e.g. [85, 87, 101, 138]) or a few for ternary (e.g. [90, 138]) mixtures and the formulation was based on a number of discrete components. For complex mixtures of hundreds or thousands of components as are some fuels (e.g. bio-oil mentioned earlier), the discrete concept is therefore not practical due to a huge numerical effort needed to solve a vastly growing number of equations. There have more recently arisen a few studies [2, 40, 41, 42, 125, 149] which used the concept of continuous thermodynamics to more appropriately describe the mixture composition, properties and vapor-liquid equilibrium to examine the vaporisation of such multicomponent droplets. The idea actually dates back at least 70 years (Katz and Brown [52]), but most of the development of the technique only

started since the late 1980s (e.g. Cotterman et al [20]) and initial applications were for petroleum mixtures as in [18, 21].

With this concept, complex mixtures can be described by continuous functions known as probability distribution functions (pdfs). In particular, the composition of a liquid is characterized by pdf parameters including distribution mean θ_L and second moment Ψ_L (or variance σ_L^2). Transport equations for these parameters are derived and numerically solved for the variation in liquid and vapor compositions with time as well as the variation of vapor composition in space. The differences between treatments of continuous thermodynamics in the literature lie mainly in the choice of distribution function such as Gamma or Gaussian distributions, in the selection of the distribution variable such as component molecular weight or boiling point, and the model for vapor-liquid equilibrium such as using Raoult's law combined with the Clausius-Clapeyron equation. This concept is realistic in representing the vaporisation behavior of complex liquid and is also simple by use of only two parameters to describe such mixtures.

Based on this concept, the study in [125] with a well-mixed assumption model for diesel and gasoline fuels found that during the evaporation the liquid droplet temperature increases with time while the mean θ_L and variance σ_L^2 of the molecular weight distribution increases and decreases respectively. This behavior is similar to that found in discrete models for simpler mixtures as it is indicative of the preferential vaporisation of light components leaving the heavy components near the end of the droplet lifetime. The droplet temperature, though increasing, is still well below the bubble point as compared to the single liquid case which is characteristic of the continued transient heating. In the vapor phase, the composition variation is mainly manifested by the dropping of the distribution mean θ_V with increasing radius which reflects the increase in θ_L with time.

Given the complexity of such mixtures, a simple quasi-steady evaporation model was developed by Hallett [40] using well-mixed and diffusion limited assumptions. The effect of convection was accounted for by use of film theory and the properties were assumed constant at a widely used 1/3 rule reference state. Interestingly, a D^2 -law behavior was found

and explicit expressions for vaporisation rate were derived. The droplet lifetimes were found nearly the same for both assumptions. The effective diffusivity concept [4, 101] was also used later to investigate the role of internal mixing in [2] in which continuous mixture formulations for the liquid phase transport equations and diffusivities were also developed. The results indicated that internal mixing has a smaller effect on the behavior of these mixtures than for binary mixtures. Most recently, they investigated the evaporation of bio-oil modeled by four main chemical fractions (typically found in these oils) each described by a separate Γ distribution function [42]. With assumptions of quasi-steady gas phase and well-mixed liquid phase, the similar preferential vaporisation of light components was found. The predicted time scales of the major events characteristic of this oil were in reasonable agreement with their experimental results.

Microexplosion mentioned in an earlier section has triggered a few theoretical investigations (e.g. [70, 74, 88, 115]). In classical investigations, knowledge of droplet temperature and concentration distributions is needed to check against the local superheat limit. Disruptive behavior was generally found to depend on internal circulation, volatility differentials and the ambient condition. On the liquid side, whereas volatility differentials support microexplosion [67, 74, 88], internal circulation tends to depress this phenomenon as it enhances the diffusion of more volatile components to the droplet surface and the vaporisation of these components keeps the droplet temperature lower [70]. On the gas side, as the heating rate was found to promote the droplet internal bubbling formation [35], microexplosion therefore depends on gas temperature as expected. The effect of pressure is more complicated [70, 91, 137, 146], high pressure generally promotes this phenomenon but too high a pressure will diminish it. As would also be expected, larger droplets favor microexplosion [88, 146]. According to Mikami et al [88] microexplosion is a stochastic process which is controlled by the ratio of liquid phase lifetime to nucleation time.

Generally a certain effect was found significant or not depending on the condition, on process (pure evaporation or combustion) or on the purpose of specific investigation. For example, the mentioned effect of gas phase mass and energy unsteadiness, while found negligible in pure evaporation processes, were found important in combustion cases.

Another example is the ambient pressure; effects such as real gas and solubility of gases into the droplet at high pressure were found important [12, 51, 54, 79, 145]. To simulate the conditions in practical devices, investigations in supercritical environments [149, 150, 151] and turbulent environments (see review in [9]) have also been done and for these conditions, formulations widely used for low pressure need to be replaced by new ones that account for other effects (e.g. the different phase change process at high pressure). For a particular problem, the more effects to be accounted for the more complicated the formulation will be. While some studies used fully numerical, time consuming computation to solve for many effects such as Dwyer [28] and Renksizbulut and Haywood [103], many others aimed at the convenience of integration into spray modeling but still kept acceptable accuracy such as [4, 12, 24, 102]. Depending on the purpose, it is essential that appropriate effects are accounted for so as to balance between accuracy and simplicity.

2.4 Proposed Research

While most previous work focused on droplets of sizes as large as few hundreds or even thousands of microns with very few exceptions such as [22, 35, 45], more stringent regulations on power efficiency and exhaust emission have pushed modern spray systems to produce droplets of sizes as small as tens of micron. The study of these small sizes is of most relevance these days. Whereas a great deal of experimentation was made in constant temperature environments with many of them being further restricted to stagnant atmosphere, the study of these droplets in convective environments (with variable temperatures) simulating those in practical combustion devices is even more desired.

The aim of this work is to investigate the quantitative behavior of droplets smaller than 100 μm undergoing evaporation in hot convective environments. To enable quantitative analysis of such small droplets, it is necessary to develop an appropriate technique which must also be capable of tracing and measuring droplets in such complex environments. A task of this work is therefore to develop such a technique. In the past with use of traditional techniques, the measurement uncertainty has however gained limited assessment. With

developments in technology, any new technique developed should be more accurate and a full analysis of the measurement uncertainty as well as assessment of the limitation of the technique needs to be undertaken; these are also an aim of this work.

Being widely present in petroleum products nonane, decane and dodecane are selected for this study. Besides these single alkanes, automotive diesel No.2 as a standard but complex fuel is also used for comparison to study multicomponent effects. To expand the knowledge gained from the study, another purpose of the current work is to formulate a simple mathematical model but accurate enough to closely simulate the evaporation process of the single component fuels used. This model is supposed to provide qualitative knowledge of quantities that cannot be obtained from the experiment. As the integration into spray modeling is very important, the suitability of this simple model for conditions close to those in real combustors needs to be assessed. As such, one of the factors that need to be considered is the ability of the simple model to simulate the droplets' behavior of the commonly used diesel in the present conditions. To explore the applicability of the simple model in a wider range of conditions, extension of this model is therefore necessary. With these developments, further investigation for the present conditions and other conditions is also made possible.

2.5 Methods for Study

2.5.1 Choice of Facility

To enable the evaporation study of a droplet, there are several choices of facility based on suspension, porous sphere, levitation, free fall techniques as outlined earlier and a less often used thermogravimetric technique. To gain a fundamental understanding of the phenomena at very low heating rates when the heat and mass transports do not control the evaporation, the thermogravimetric technique is used to investigate the effect of fuel thermodynamics [35]. With the suspension technique, advantages are that the temperature measurement can be coupled with high speed visualization to follow the changes in droplet size and shape and that the configuration also allows the study at high pressure. However, the disadvantages are

that the minimum droplet size is limited by the size of the suspending fibre and that the shape of the droplet is also modified. This fibre can also act as a nucleation site [142] to promote bubbling phenomena which further affects the droplet temperature and morphology. The limitation of the porous sphere method is that the droplet size studied is large and the initial transient processes generally seen in droplet behavior cannot be covered [71]. Levitation techniques share most advantages of the suspension techniques, however the design is also usually for stationary droplets and that the setup involved is not simple (cf. [33]).

Being the most sophisticated, free fall techniques however favor the most realistic study. For these techniques, the effect associated with the contact between the solid surface and the droplet is removed and thus droplets studied can be as small as desired. To produce a hot convective environment, methods often used have been a furnace/cylinder arrangement with electrical heaters plus a hot gas flow [22, 35] and a reactor with post combustion gases produced from a flat flame burner [111, 142]. The later is clearly more realistic of combustion environments. With those advantages, a free-fall droplet undergoing evaporation in an entrained flow reactor is the target of this work. To produce post combustion gases, a combination of oxidizer and fuel gases can be used as the input such as $\text{CO-H}_2\text{-O}_2\text{-N}_2$ [31] and $\text{CH}_4\text{-H}_2\text{-O}_2\text{-N}_2$ [111]. The later combination is chosen for this work.

Methods that have been used to generate a droplet stream with constant size and spacing are vibrating capillary [105], chopper technique [67], inkjet printing techniques [45, 78, 138], droplet-on-demand generators [14, 35, 140], Berglund-Liu atomizer [22] and other droplet devices as in [13, 111]. Given quite a few options, only some of them are capable of producing droplets with sizes as aimed for this work such as droplet-on-demand generators and the Berglund-Liu atomizer. A piezo-electric nozzle, a type of droplet-on-demand generator, is selected for this work which is also commercially available.

Droplet evaporation behavior is known to be affected a number of parameters such as droplet initial diameter [45, 49, 53], surrounding gas temperature and pressure [54, 122, 147, 151], Reynolds number [87, 129], oxygen concentration (for combustion case) [72, 92].

Having developed the experimental system, it is necessary to investigate some of the important effects. However, due to the difficult nature of this investigation which will be mentioned later, only the study of the effects of initial diameter and gas temperature is undertaken leaving extended investigations of these quantities and the droplet Reynolds number to the modeling work. With fuels chosen for study, knowledge of the fuel chemistry effect can also be obtained.

2.5.2 Choice of Measurement Technique

To measure the droplet size, a large number of methods have been used including the classical and frequently used techniques such as photography/video, Backlit Stroboscopic Imaging as mentioned earlier and newer techniques which often involve lasers such as Light Scattering methods [22, 57, 134], Phase Doppler technique [106], Laser 2-Focus (L2F) [132] or more recently digital holography techniques [94, 95]. There are also less often used techniques which can be found in text books, e.g. [33]. The need for quantitative assessment of small droplets poses a few problems. One of them is the fixed pixel size of digital imaging equipment which limits the spatial resolution available for measurement. High magnification used to overcome this problem will limit the imaging volume and greatly reduce the focal depth. Furthermore, getting close to evaporating droplets in a complex high temperature environment is challenging. With developments in technology, laser based techniques give far superior quality than classical illumination methods. Amongst those techniques, Light Scattering, Phase Doppler and L2F are potential but their setup often requires use of a number of optical equipment such as beam splitters, lens and/or even necessitate more than one sensor. Their application to this system is even more difficult as they are often designed for point (i.e. very small volume) and close-to-wall measurements [33].

A new technique to overcome these problems is developed in this work based on an extension of digital in-line holography [95]. The integration of a magnifying mechanism makes the original DIH most suitable for this work. In addition to enhanced image magnification, this technique provides significantly enhanced depth of field for a fixed

magnification. Furthermore, a capability to get close to the droplet from the far field is gained which is indispensable for this high temperature reactor facility. Compared to other techniques, the setup of MDIH is also much simpler with little equipment involved.

Wavefront reconstruction, the original name of holography, was invented by Gabor [34] when he proposed a novel two-step, lensless imaging process back in 1948. As applied to droplet studies, early examples of the use of holography in different forms were that of Grabowski [39] who used it to measure the size and position of aerosol droplets and Toker and Stricker [128] who measured the vapor properties of an evaporating droplet. Later developments have enabled the technique to be used in digital form which has now been implemented in many different configurations for different purposes. Examples are applications in two-phase flow study to measure particle size (e.g. [94, 95]) and in fluid diagnostics to measure 3D velocity fields (e.g. [114]). Most recently, there has been an attempt to measure the size and velocity of droplets in a cold spray through use of digital inline holography, Yang and Kang [144].

To calculate the droplet evaporation rate, not only droplet size but also residence time is needed which requires measurement of droplet velocity. To measure this velocity, a number of options are available including Backlit Stroboscope, Laser-Doppler Velocimetry, L2F Velocimetry and DPIV. While some of these techniques offer the ability to measure the size and velocity simultaneously, their application in this system is not favored. This work combines MDIH with DPIV to measure the droplet evaporation rate. Although not applied to droplets, examples of similar combination can be found in [16, 114].

To measure the evaporation rate, especially the average rate of the whole evaporation history of a droplet, there are many factors that need to be well under control which makes the task extremely complicated. For example, the most challenging requirement is repeatability. Because the average measurement requires connecting a series of spatially adjacent, instantaneous images from different droplets, these droplets need to travel the same trajectory to experience the same heating loads. To maintain this condition, experiment is limited to low droplet Reynolds number. Furthermore this ability is affected by the quality of

the burner and the nozzle. Controlling a piezo-electric nozzle is very difficult [140] given its operation is very sensitive to the liquid used as well as its cleanliness. Another example is that as the measurement space is limited due to use of high magnification, a slight fluctuation in the movement can easily bring the droplet out of the imaging area, which can be as small as $0.6 \times 3.8 \text{ mm}^2$.

Chapter 3

Methodology

3.1 Introduction

This chapter describes the experimental system, the reactor heating and the technique developed for droplet evaporation measurements. As a tool chosen for measuring the droplet size, the background mathematics of DIH and development to MDIH are described. This description is somewhat detailed as it helps with the uncertainty analysis in the next chapter. Evaporation rate measurement necessitates the use of another tool to measure the droplet residence time and DPIV is selected for this. Basic mathematical background of DPIV is briefly outlined and its coupling to MDIH will also be detailed.

3.2 System Description

Figure 3.1 shows the arrangement of the experimental system developed for this study. The central part of the system is the optically accessible square quartz reactor (sometimes called “vessel” in this work) measuring $120 \times 120 \times 300 \text{ mm}^3$ in which single droplets can be evaporated and burned in an oxidizing gas co-flow. This hot co-flow is created by fitting on top of the reactor an inverse flat flame burner operated on a combination of fuel and oxidizer gases. Fuel droplets are introduced into the reactor via a carrier gas which flows through a

500 mm long 9 mm diameter injector tube which passes through the centre of the burner. Droplet speed, hence residence time, is controlled initially by this gas and ultimately the burner gas. To help with the description, the principle sketch of the system is shown in Figure 3.2 while the burner, as a very technical part, is shown in Figure 3.3. As the burner operates up side down, it gets very hot during experiment and so it is designed to have a water cooling coil running inside the sinter plate to prevent thermal expansion and damage. This sinter plate also helps to prevent the migration of the flame front into the settling chamber in the burner. A thermocouple is fitted (Figure 3.3) to monitor the gas temperature inside the burner all the time during its operation. In addition, to prevent the injector tube from being warmed up, this tube has an outer jacket for water circulation thus insulating it from the burner. The droplets are therefore not evaporated in this tube giving a consistent size as desired before entering the reactor.

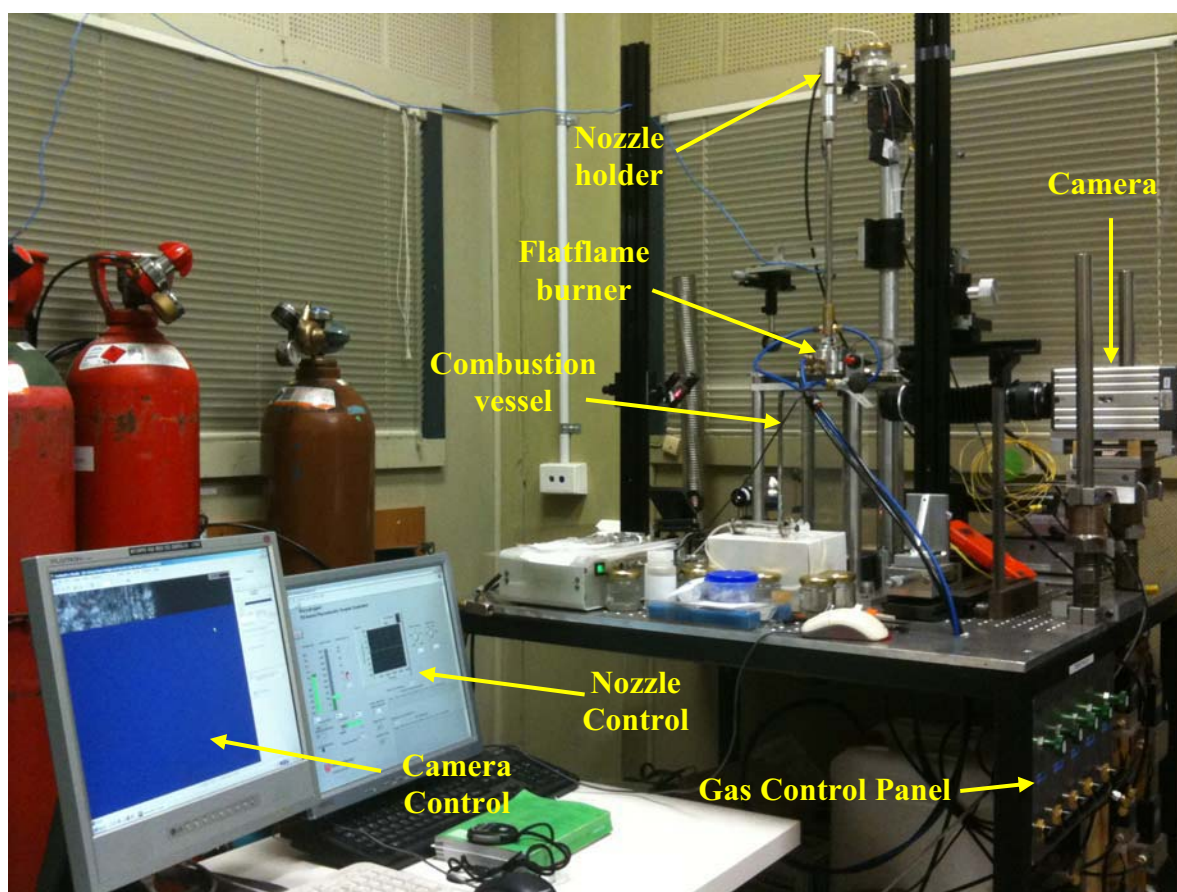


Figure 3.1: System arrangement

A piezo-electric droplet generator located at the top of the injector tube is used to produce droplets less than $90\text{ }\mu\text{m}$ in diameter. This generator (Model S0901, manufactured by IWT at Bremen University in Germany) consists of a piezoceramic tube in which sits a borosilicate glass capillary which acts as the fuel nozzle. High frequency oscillation of the glass capillary by the piezoceramic tube generates droplets from the fuel nozzle which in turn is connected to the fuel supply. A computer controlled high voltage signal generator (Model 010307) is used to drive the oscillation of the piezoceramic tube. In theory, parameters able to be varied are the droplet size and the injecting frequency. Fuel nozzle size can also be varied which sets the maximum droplet size attainable. Additional experimental parameters able to be varied are the post burner gas temperature and oxygen concentration, and droplet and reactor Reynolds numbers.

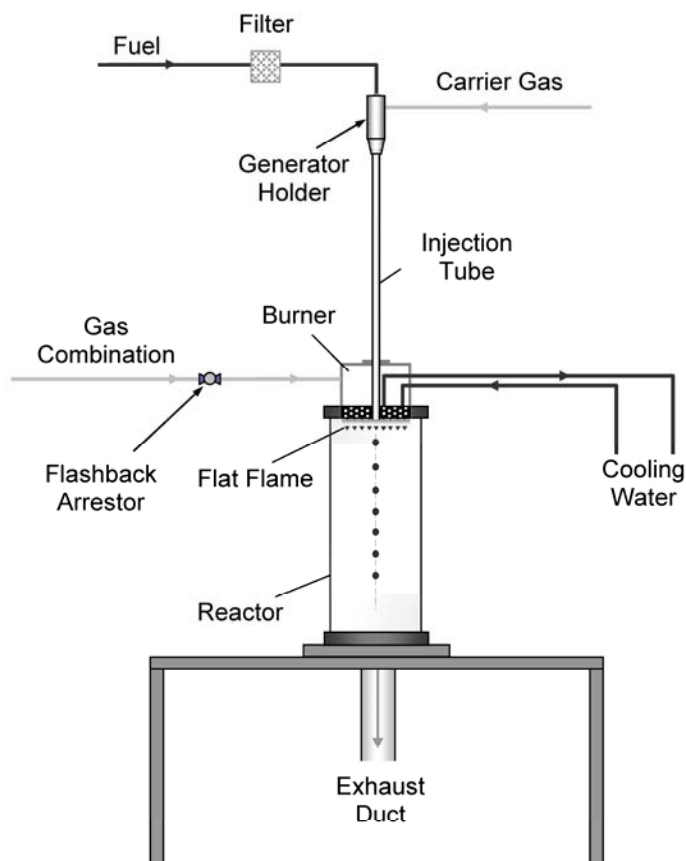


Figure 3.2: System principle sketch

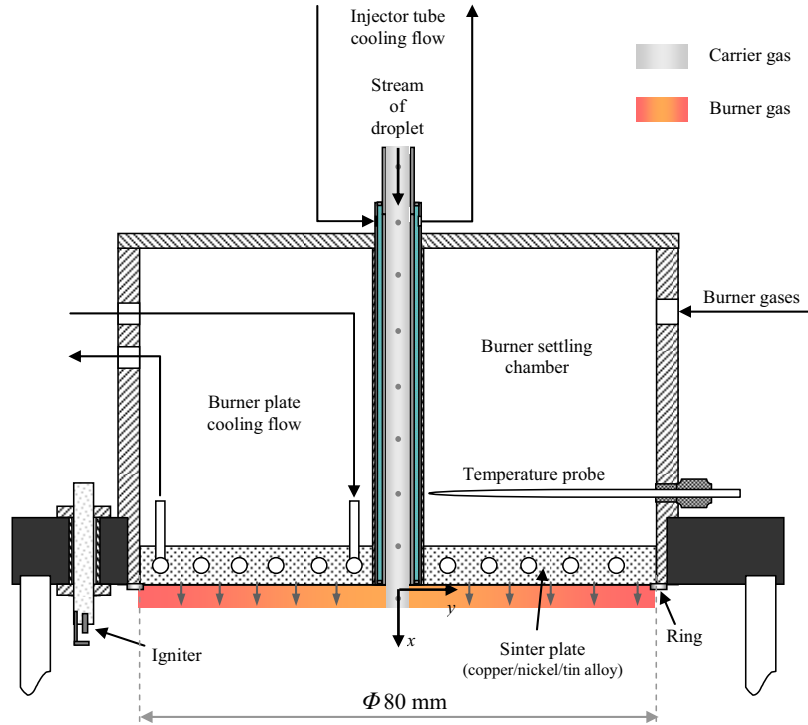


Figure 3.3: Inversed flat flame burner fitted on top of the reactor

3.3 Heating Conditions

As mentioned, to create a hot environment in the vessel, a combination of gases including CH_4 , H_2 , O_2 and N_2 is used. Together with the N_2 carrier gas, their composition will determine the heating condition inside the vessel. These gases are controlled via Alicat gas flow meters and their combustion is initialized with the help of an igniter placed underneath the burner. To have the vessel heated up to a desired temperature for experiment the burner component gases are calculated via an equilibrium calculation by use of the AEDsys software written by the authors in [84] based on the aircraft engine design tools. This provides an estimate of the adiabatic temperature accounting for chemical dissociation effect in high temperature reactions with pressure set to atmospheric in the vessel. The mixture fraction is calculated so that the post burner gas has 21% O_2 to approximate the air. The temperature along the vertical centerline of the vessel where the droplets fall through is

dependant on the burner gas flow rate, the carrier gas flow rate, the heat loss from the vessel to the air and from the burner to the cooling water. Once these thermal processes are balanced, stable vessel temperature is attained (about 10-12 minutes after ignition).

The temperature profiles along the vessel vertical centerline are measured by a K-type thermometer which is specifically designed for this system. The bead is about 2 mm in diameter giving the response time of about 1-2 s. A point raised with the use of this bead is that there should be a radiation correction term to get the true gas temperature, however this term is estimated to be negligible for conditions of low convection and temperature used in this work (c.f [47, 50]). To confirm the repeatability of the temperature profile (thermal state in the vessel stabilized) the measurement is repeated after 20 minutes with differences found to be small, typically about 6 K at a maximum. These profiles are used as the input for the droplet model presented in Chapter 6. Due to the limit of the current system, the temperature studied cannot be set too high as the burner gets too hot for higher temperature settings.

Figure 3.4 shows two temperature profiles used for this study with the lower temperature profile being denoted as T_L and the higher profile being denoted as T_H . Each profile has two repeats to indicate thermal stability as mentioned. The position is along the vertical centerline and is referenced from the injector tube exit. It can be seen that the temperatures attain maximum values of approximately 585 K and 675 K for T_L and T_H accordingly at roughly 25 mm downward from the burner surface. This is not unexpected as closer to the injector tube exit the cooling effect of the carrier gas is stronger. To have an idea how these conditions can affect the droplet, the boiling points of fuels used for this study including dodecane, decane and nonane are also shown as the horizontal lines. The middle of the diesel's boiling point range is also indicated. The differences between the maximum surrounding temperatures and the boiling temperature of dodecane are around 100 K and 200 K for low and high profiles respectively. This is clearly not high enough to combust the droplets but is enough to study the complete evaporation of droplets with sizes smaller than 100 μm . Given the time taken to thermally stabilize the system, the experiment is always carried out after the initial system warm up period.

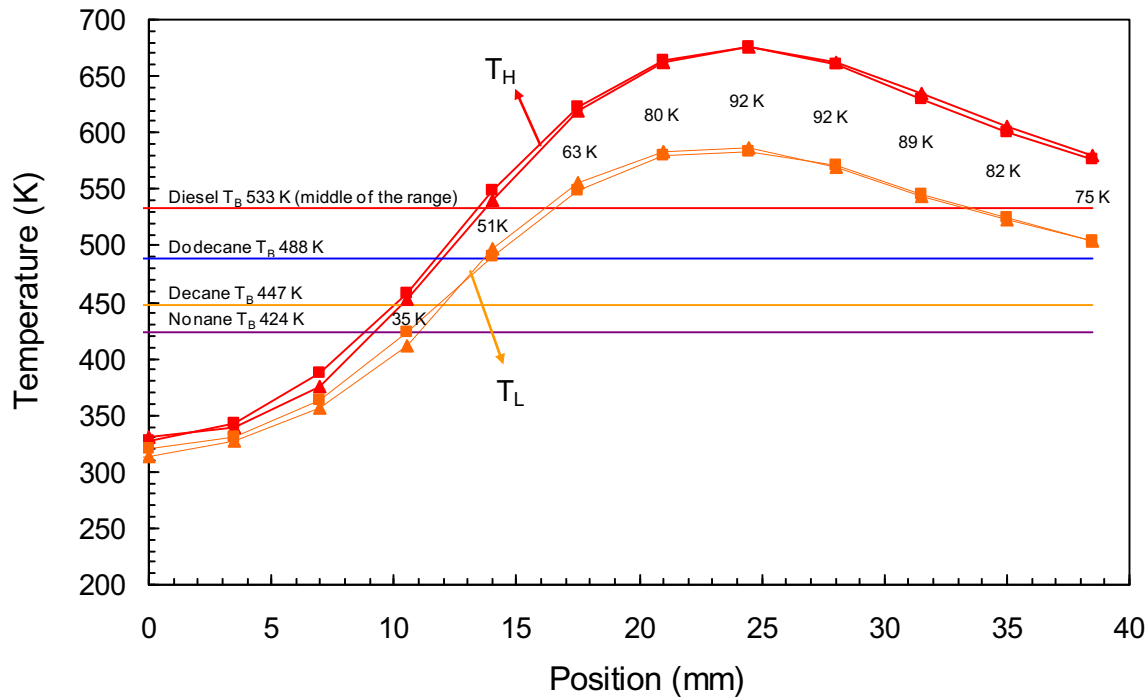


Figure 3.4: Temperature profiles used for this work. Also shown are the boiling points of diesel, dodecane, decane and nonane. Position is relative to the injector tube exit. Two repeats of the temperatures are shown to indicate repeatability. Temperatures shown represent the difference between T_L and T_H

3.4 MDIH Technique

3.4.1 Basic Theory

When we look at an object/image, it is actually the light (optical wavefront) from that object/image which reaches our eyes. The information contained in this wavefront includes the amplitude and phase of the light characteristic of the object/image. The problem addressed in holography is the reconstruction of the object/image from such information. By recording the information, reconstruction of the object can occur later without the presence of the object. When an object is to be imaged, it is illuminated by a coherent light source and the amplitude and phase of the wavefront which originated from the object can be recorded using digital cameras. As these devices only respond to light intensity, phase information needs to be encoded into the recorded intensity. Interferometry is an example of how this is

done and so, in a general sense, “Holography” is similar to this technique. A hologram is therefore a type of interference pattern. Figure 3.5 shows a typical example of the image recording Figure 3.5a and reconstruction Figure 3.5b in which a plane wave is used for both the illumination and reconstruction while the object is simply a sphere. The light source for illumination and reconstruction needs not necessarily be a plane wave.

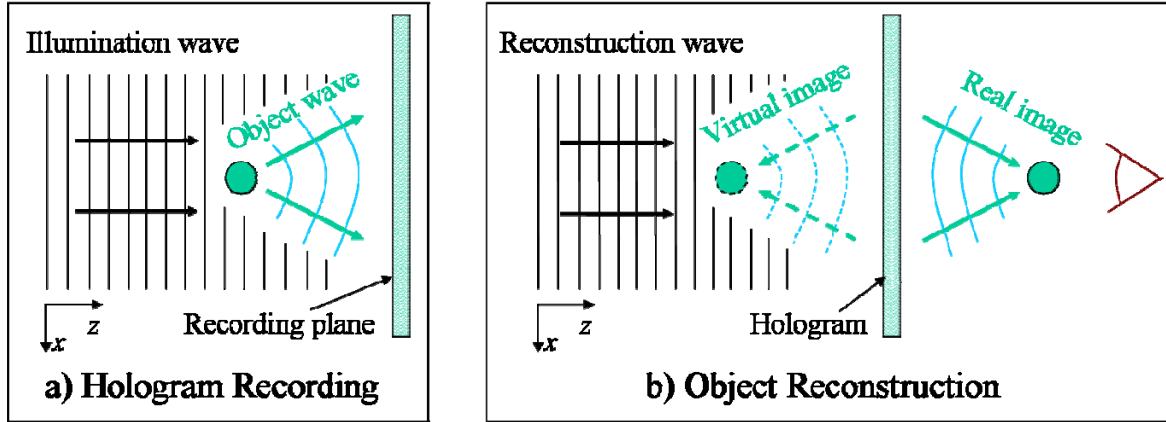


Figure 3.5: Recording and reconstruction of an object image in a classical holographic technique. The recording plane used to be made of a film which, after recording, becomes a hologram

A mutually coherent illumination wave, hereby called the reference wave, with known phase and amplitude is added to the light from the object and their interference is imaged on the hologram (recording medium). Suppose that an object wave, which needs to be recorded and reconstructed, arriving at the recording plane is represented by a complex function $a(x,y) = |a(x,y)|\exp[-j\Phi(x,y)]$ and a known reference wave represented by a complex function $A(x,y) = |A(x,y)|\exp[-j\Psi(x,y)]$ then the intensity of their sum will be:

$$I(x,y) = |A(x,y)|^2 + |a(x,y)|^2 + A^*(x,y)a(x,y) + A(x,y)a^*(x,y) \quad (3.1a)$$

in which $A^*(x,y)$ and $a^*(x,y)$ are the complex conjugate of $A(x,y)$ and $a(x,y)$, respectively. To be more detailed:

$$I(x,y) = |A(x,y)|^2 + |a(x,y)|^2 + 2|A(x,y)||a(x,y)|\cos[\psi(x,y) - \phi(x,y)]. \quad (3.1b)$$

From equations (3.1) which represent the interference pattern, it can be seen that both the amplitude and phase of the object wave are included.

Given the recorded image is in the form of a hologram, the second task of holography is to reconstruct the original wavefront from it. Under normal conditions, a majority of recording materials present a linear characteristic; that is the mapping from the intensity detected during recording into the amplitude transmitted during reconstruction is linear [38]. To be more detailed the exposure during recording lies in the linear portion of the T_A - E curve of the material where T_A is its amplitude transmittance and E is the exposure during detection which is the product of incident intensity I_0 and exposure time t_E . Assuming an even distribution of the reference wave $|A(x,y)|^2$ across the recording plane, the transmittance of this can be expressed by the following equation:

$$\tau_A(x,y) = \tau_B + \beta t_E (|a|^2 + A^* a + A a^*) \quad (3.2)$$

in which, T_B is the bias transmittance caused by the constant reference exposure (of $|A(x,y)|^2$ above) and β is the slope of the T_A - E curve at the bias point.

To reconstruct the object wave, it is popular to use the exact duplication of the reference wave. As applied to equation (3.2) when the hologram is illuminated by the reconstruction wave $A(x,y)$:

$$A \tau_A = A \tau_B + \beta t_E |a|^2 A + \beta t_E |A|^2 a + \beta t_E A A a^*. \quad (3.3)$$

the third term in the right hand side of equation (3.3) is then the exact duplication of the object wave $a(x,y)$ multiplied by a constant. This means that the reconstruction using a reference wave illumination yields this wavefront which appears (to the observer) to originate from a virtual image behind the hologram as if the object was still at the original position; see Figure 3.5b. The reconstruction can also be done by use of the conjugate of the reference wave, i.e. $A^*(x,y)$, and if so, its replacement in equation (3.3) above will make the last term become the real image wavefront which is represented by the conjugate $a^*(x,y)$. This image is on the opposite side of the hologram plane and of equal normal distance from the plane to that of the virtual image; also see Figure 3.5b as it is a special case in which the

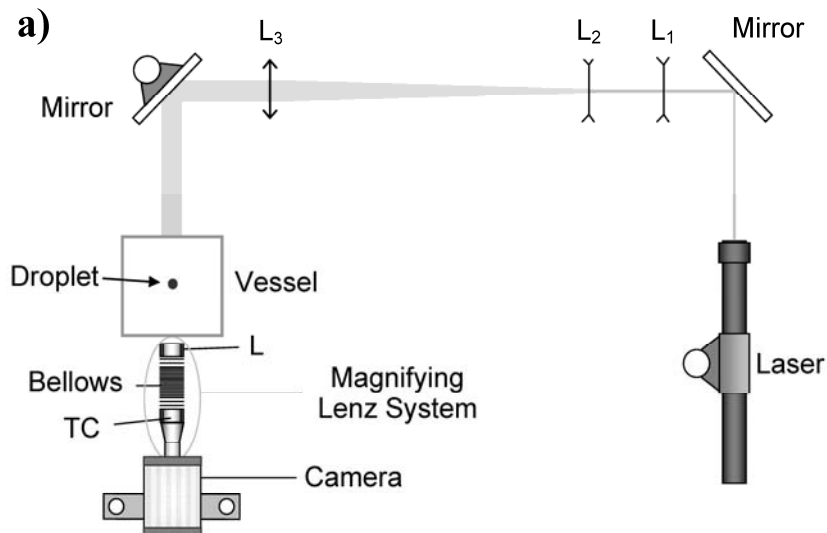
plane wave is also the conjugate of itself and therefore both virtual and real images are present. In either approach, the task of reconstruction is to eliminate all the remaining terms in the transmitted light function and generally, the former approach is used more often in practice. In this work a plane wave normal to the hologram plane is used both for reference and reconstruction as presented in Figure 3.5, the reasons for which will be mentioned later. When a plane wave $A(x,y)$ is normal to the plane, the first and second terms in the right hand side of equation (3.3) are constant across the plane and can be easily eliminated. When the third term in the transmitted light is brought to focus during reconstruction, i.e. to propagate it back to the original position of the object, it is affected by the out-of-focus real image (fourth term) and this is known to be the twin image problem.

3.4.2 Development of MDIH Technique

In this work, the recording process is done in a similar manner with the classical film based technique, Figure 3.5a. A coherent laser source is used to illuminate the object and the interference between the scattered light wave from the droplet (object) and the undefracted source as reference light is projected on to the CCD sensor of a digital camera. Both the amplitude and the phase of the diffracted wave from the droplet are recorded. The reconstruction together with twin image elimination is however numerically performed. The use of a collimated plane wave for both illumination and reconstruction renders this a so called digital inline holography (DIH) technique. Detail on numerical reconstruction will be presented in the next section.

There are a few well-known drawbacks of DIH and the most notable are the noise from defocused objects and the large depth of focus of the reconstructed hologram [95, 114]. In this system, the former is not present as the droplets are produced in a well paced single stream. The later as well as the pixel size resolution limit is improved by magnifying the interference pattern before recording. A magnification mechanism is specifically developed for this system and its variation from the original DIH is addressed briefly here as MDIH. Figure 3.6 shows the arrangement of this MDIH optical system.

The light source used to generate the hologram is a 10 mW, 632 nm He-Ne continuous coherent laser. After passing through a set of three spherical lenses ($L_1, f_1=-30$ mm, $L_2, f_2=-50$ mm and $L_3, f_3=200$ mm, Figure 3.6a) it is expanded to form a collimated beam of 20 mm in diameter which, after reflection by mirrors, illuminates the droplet. The interference pattern between the droplet wave and the laser beam is magnified by a mechanism which includes a Nikon lens 85 mm (L), a bellows and a 1:2 teleconverter (TC) as illustrated in Figure 3.6b (note that the teleconverter functions to magnify the object image). The magnified hologram is then recorded on the 1280×1024 px² CCD array of a Redlake MotionPro X3 high speed CCD camera with pixel size of 12×12 μm^2 . Compared to the similar DHM which stands for digital holographic microscopy using a microscope objective (e.g. in [114]), a significant improvement gained with this modification is the much longer distance of focus d_f (Figure 3.6b) which is the distance between the plane of focus of the imaging system and the lens' end. This plays a vital role in this facility because the image quality only becomes good when the object examined is close to the plane of focus. The centerline of the reactor where the droplets are located is 70 mm away from the outside wall of the reactor which, in principle, is the closest point where the lens can be positioned. By adjusting the bellows, the magnification factor \mathcal{M} can be changed which can be taken as the ratio of d/d_o as shown in Figure 3.6b when symbolizing the magnifying unit by an effective lens L_{eff} . For this work, a setup at $\mathcal{M} \approx 4$ was used which reduced the camera viewing area from 15.36×12.28 mm² to 3.8×3.1 mm² at a resolution of 3.003 $\mu\text{m}/\text{px}$.



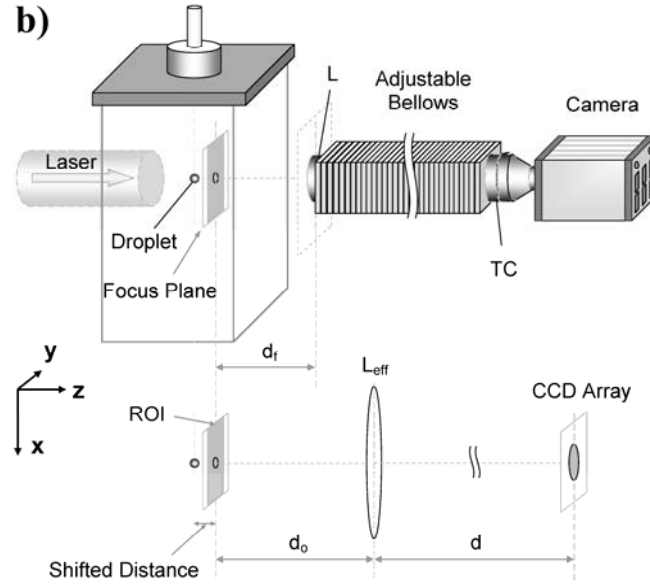


Figure 3.6: a) Optical setup plan view; b) Principle dimensions

3.4.3 Reconstruction and Twin Image Elimination

The method used for reconstruction and twin image elimination is that of [93]. This method is to regard the reconstruction process as an image processing problem. In particular, it is to extract the object wave numerically from the hologram and therefore can be understood to be a numerical decoding process.

When an object is illuminated by a monochromatic plane wave of wavelength λ , the field at the hologram plane can be approximated as the Fresnel-Kirchhoff integral:

$$U(x, y) = A \exp(-jkz) \iint_{-\infty-\infty}^{\infty \infty} [1 - a(\xi, \eta)] \left[\frac{\exp(jkz)}{j\lambda z} \exp\left\{j \frac{\pi}{\lambda z} [(x - \xi)^2 + (y - \eta)^2]\right\} \right] d\xi d\eta, \quad (3.4)$$

where A is the amplitude of the reference wave which can be assumed to be unity and k ($= 2\pi/\lambda$) is its wave number. For convenience in manipulation, the phase of the reference wave at the hologram plane has been assumed to be zero, $-kz$ in the above equation is therefore the phase of the reference wave at the object plane which is of distance z away from the hologram plane. The above equation can be regarded as the following convolution:

$$U(x, y) = [1 - a(x, y)] \otimes h_z(x, y), \quad (3.5)$$

where the symbol \otimes stands for the two-dimensional (2D) convolution operation and the impulse response $h_z(x, y) = \frac{1}{j\lambda z} \exp\left[j\frac{\pi}{\lambda z}(x^2 + y^2)\right]$. The intensity of the hologram is then the modulus square of the above field $U(x, y)$. With the identity $1 \otimes h_z(x, y) = 1$ the hologram intensity becomes:

$$I(x, y) = U(x, y)U^*(x, y) = 1 - a^*(x, y) \otimes h_z^*(x, y) - a(x, y) \otimes h_z^*(x, y) + |a(x, y) \otimes h_z^*(x, y)|^2. \quad (3.6)$$

We can see that this equation is equivalent to equation (3.1a) and in fact it is a specific form of the general equation (3.1a) with four similar components. With the assumption that $a(x, y)$ is real and much weaker than the original reference wave, the hologram intensity can then be simplified to:

$$I(x, y) = 1 - a(x, y) \otimes 2 \operatorname{Re}\{h_z(x, y)\}. \quad (3.7)$$

From equation (3.7), the recording process can be regarded as a 2D filtering operation (the system acts like an invariant linear filter) of the input $a(x, y)$ and $I(x, y)$ is the output which has been shifted. The main argument here is that to reconstruct the object wavefront, an inverse filter needs to be found so that with the input $I(x, y)$, the output of the filter will be $a(x, y)$. To find the inverse filter, the forward transfer function $g(x, y) = 2 \operatorname{Re}\{h_z(x, y)\}$ is transformed giving the transfer function in the Fourier domain $G(u, v) = 2 \cos\left[\frac{\lambda z}{4\pi}(u^2 + v^2)\right]$

where u and v are the Fourier transform domain variables. However, as this function has periodical zeros there is no direct inverse of this function, i.e. no valid $1/G(u, v)$. The inverse $R(u, v)$ is then found in the energy domain so that it satisfies the following equation:

$$\int_{-\infty}^{\infty} \int_{-\infty}^{\infty} |1 - R(u, v)G(u, v)|^2 du dv = 0. \quad (3.8)$$

A truncated series expansion function was found which approximates the above function $R(u, v)$ in the energy. This was discovered by the authors of [93] from their analysis on the

real and imaginary parts of the field $V(x,y)$ after the illuminated hologram. The illumination using the exact duplication of the reference wave allows the formulation for the reconstruction to be the same with that of recording which resulted in equation (3.7) above. Instead of using the amplitude transmittance of the object $[1-a(x,y)]$, that of the hologram is used and with the assumption of linear characteristics of the recording material the field after the illuminated hologram is then:

$$V(x,y) = [d + I(x,y)] \otimes h_z(x,y) \quad (3.9)$$

with d being a constant depending on the material. By replacing $I(x,y)$ in equation (3.6) into this equation and simplifying it using the properties of $h_z(x,y)$ (see the appendix of [93]), the field $V(x,y)$ can be represented as:

$$V(x,y) = d - a^*(x,y) + [1 - a(x,y) \otimes h_{2z}(x,y)], \quad (3.10)$$

with the last term being the hologram of the object at distance $2z$ away, another defocused twin image. The real and imaginary parts of this field are respectively:

$$\text{Re}\{V(x,y)\} = d + 1 - a(x,y) - a(x,y) \otimes \text{Re}\{h_{2z}(x,y)\} \quad (3.11)$$

and
$$\text{Im}\{V(x,y)\} = -a(x,y) \otimes \text{Im}\{h_{2z}(x,y)\}. \quad (3.12)$$

The third and last terms in equation (3.11) represent the desired object wave and the real part of the twin image while the only term in equation (3.12) is the imaginary part of the twin image. By denoting $q_{2^{n-1}z}(x,y) = -a(x,y) \otimes \text{Im}\{h_{2^n z}(x,y)\}$ and convoluting recursively:

$$p_{2^n z}(x,y) = q_{2^{n-1}z}(x,y) \otimes 2 \text{Im}\{h_{2^n z}(x,y)\} \quad (3.13)$$

and
$$q_{2^n z}(x,y) = q_{2^{n-1}z}(x,y) \otimes 2 \text{Re}\{h_{2^n z}(x,y)\} \quad (3.14)$$

with $n = 1, 2, 3 \dots$; each of functions $p_{2^n z}(x,y)$ will contain the object wavefront $a(x,y)$ and a twin image (hologram at distance $2^{n+1}z$ from the object). Taking the average of the last two terms in equation (3.11) (hereafter denoted as $b_z(x,y)$) and all functions $p_{2^n z}(x,y)$, the outcome will therefore contain the object wave term and a residual term:

$$S_M(x, y) = \frac{1}{M} \left[b_z(x, y) + \sum_{n=1}^{M-1} p_{2^n z}(x, y) \right] = -a(x, y) + a(x, y) \otimes \underbrace{\frac{1}{M} \left[-\text{Re}\{h_{2z}(x, y)\} + \sum_{n=1}^{M-1} \text{Re}\{h_{2^{n+1}z}(x, y)\} \right]}_{\text{residual term}}. \quad (3.15)$$

In the last term (residual term) of the above equation, the holograms at different distances actually cancel each other and it has been proved by the authors of [93] that when M approaches infinity, the convolution kernel of this term converges uniformly to zero leaving the outcome as a pure object wavefront. This procedure is equivalent to the truncated inverse filter mentioned earlier.

Figure 3.7 summarizes the above filtering operation by a block diagram with the input as the hologram intensity and the output is the object wave plus the residual term. The operation of this filter can be conveniently carried out in the Fourier transform domain as the recursive convolutions are just simple multiplications. Figure 3.8 shows the operation of the filter in the digital form which is exactly what the computational reconstruction does. The intensity recorded on the CCD array is discretely Fourier transformed and then after passing through the filter, it is inversely transformed to yield the desired output. These transformations are done using fast Fourier transform (FFT) routines.

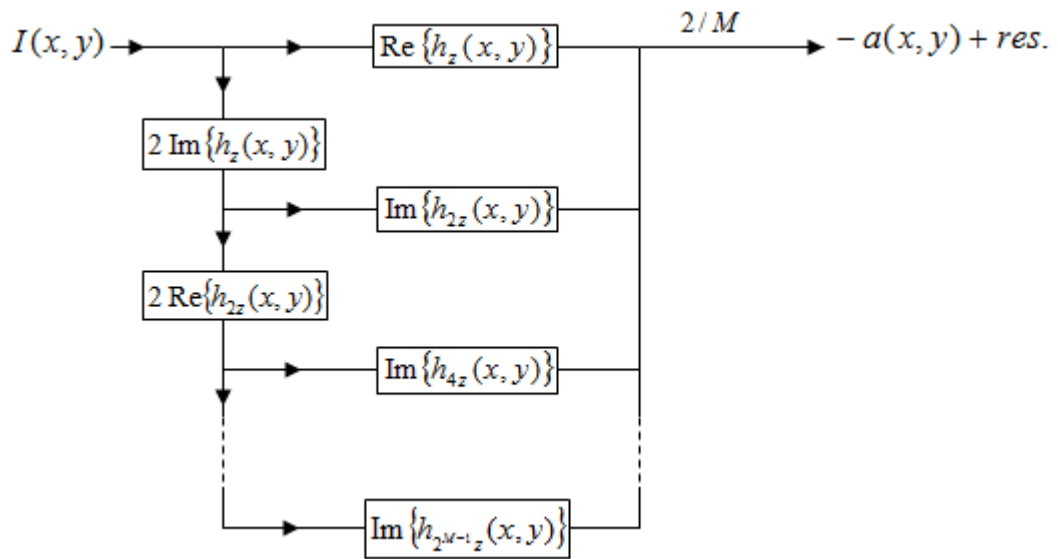


Figure 3.7: Reconstruction filter, after [93]

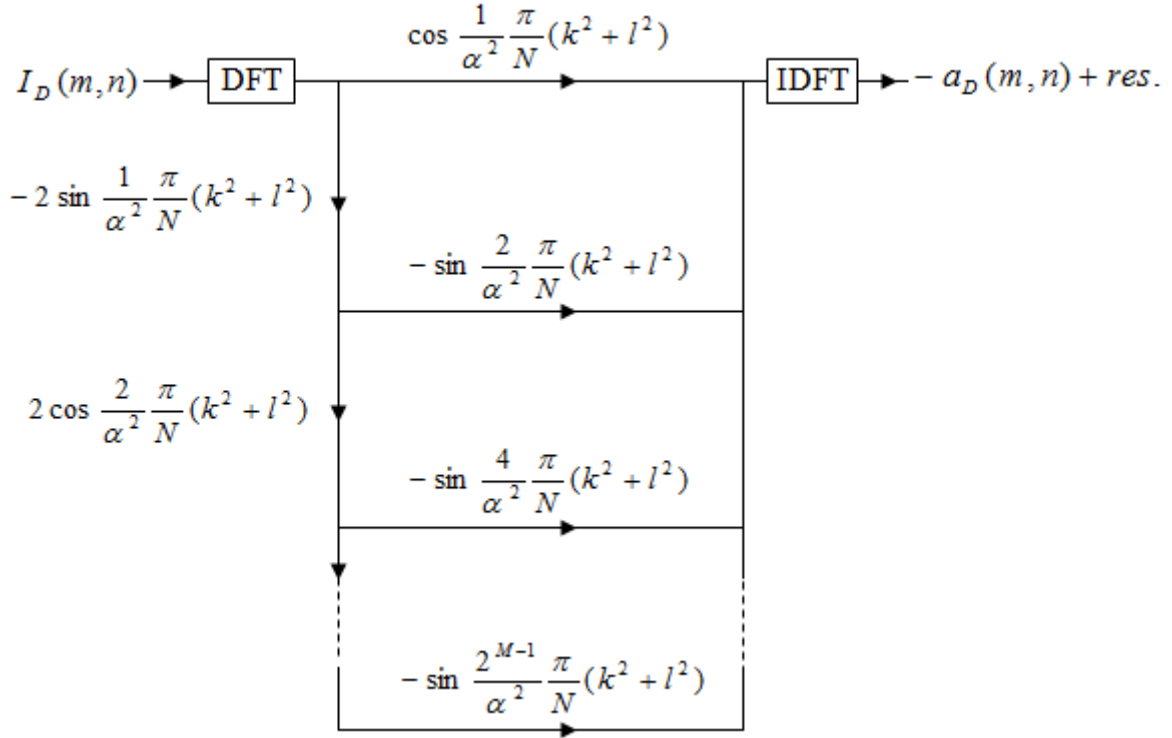


Figure 3.8: Digital reconstruction filter in Fourier transform domain, after [93]

In Figure 3.8, α is a normalization factor which is defined as $\alpha = N \frac{X^2}{\lambda z}$ with X being the pixel size, N being the linear size of the $N \times N$ px^2 array. These arise from the discrete version of the convolution kernel $h_z(m, n) = \frac{1}{j\lambda z} \exp \left[j \frac{\pi}{\lambda z} X^2 (m^2 + n^2) \right]$. With $M=1$, the reconstruction is similar to the conventional method. Usually M is chosen from 3 to 5 for particle field reconstruction [93]. For this work, $M = 3$ has been chosen. This fact also supports the use of this method for this work as the cancelation is very effective at even low M values. The effect of this value on the results will be assessed in Chapter 4.

3.4.4 Calibration of Imaging System

Image calibration was done by placing on the reactor centerline a glass slide etched with precise grids of 1 mm^2 . The whole imaging unit was adjusted to focus on the grids and the

focal distance d_f was checked to be 100 mm at $\mathcal{M} = 3.996$. The unit was then shifted 7 mm backward from the centerline (Figure 3.6b) to record the calibration image. The recorded hologram was reconstructed and these images are shown in Figure 3.9 (images are 1024×1024 px²). Image quality checks were performed over a range of ± 5 mm around the centerline in the direction normal to the image plane as this is the space that the droplets are present during experiment. The factor \mathcal{M} and the working distance were used as the input for the reconstruction program. The calibration error found from this process is around $\pm 0.15\%$ of the known grid dimensions. This will be further analysed in the next chapter.

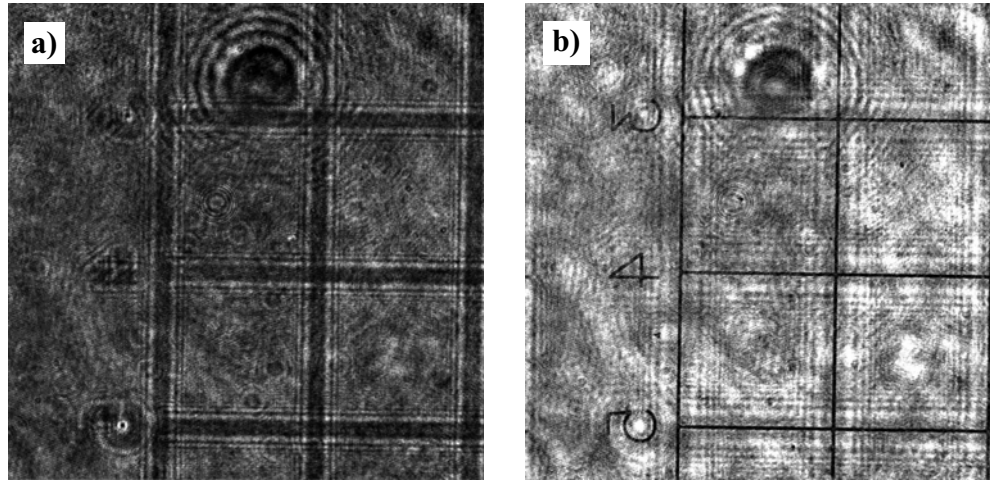


Figure 3.9: a) Grids hologram; b) Reconstruction image

3.4.5 Image Processing and Size Estimation

To improve image quality, a background image was recorded for each series of measurement and subtracted from the recorded holograms in that series before processing. This can be seen in Figure 3.11c to effectively eliminate the background noise, fixed speckles and nonuniformities from optical components in the droplet reconstructed image while still preserving the pattern for processing.

As the reconstructed droplet is characterized by an elongated shape in the depth direction z as illustrated in [114], to estimate the droplet size, it is necessary to find the best focus position in this direction of the droplet. There have been a number of studies which outline

various methods to locate the focal plane of a particle such as the work in [16, 17, 95, 114]. The work of Choo and Kang [17] for example, proposed three parameters which are the correlation coefficient, the sharpness index and the depth intensity to determine the focal plane of a particle along the optical axis, while the work of Choi and Lee [16] studied different autofocus functions quantifying the sharpness of reconstructed blood cell images. In this work, finding the droplet focal plane can be done by searching for the position with the lowest standard deviation of the droplet intensity field (σ_I) as done in Palero et al [95]. However with the use of a plane wave light source for record and reconstruction, and a collimated configuration, it has been found that at such a position the droplet pattern also has the largest area satisfying a threshold value as also found in [95]. Due to the low signal to noise ratio, the largest area criterion is used as the standard deviation criterion is not consistent in yielding a good result. These are illustrated in Figure 3.10 for some droplets over 60 μm in which there are greater fluctuations seen on some of the standard deviation curves in the elongated region of these droplets. The nature of this area criterion is similar to that of the last criterion used in [17].

Introduction of the variable density burner gases to the optical path introduces more noise typified by an increase in the background noise of the image. In addition to the subtraction from the hologram of a background image, other steps of improvement have been used. Following reconstruction, the image is normalized by the most popular intensity in the image. It is then further cleaned up by application of a digital median filter (with window size of $3 \times 3 \text{ px}^2$) to effectively eliminate speckle noise while still preserving the droplet edge. The area in the image corresponding to the droplet is then defined by use of another threshold value. Droplet diameter is then determined from this area assuming it corresponds to a droplet which is spherical in shape. The diameter therefore represents the average diameter of the imaged droplet area.

Figure 3.11 is an example showing the sequential steps taken during the processing for a 68 μm diesel droplet when the burner is in operation. Figure 3.11a is the droplet hologram before background subtraction (raw data obtained from the camera), while Figures 3.11b, c,

d and e are the subtracted hologram, the reconstructed, the normalized and the filtered images, respectively. These images are 200x200 px² which are cropped down versions.

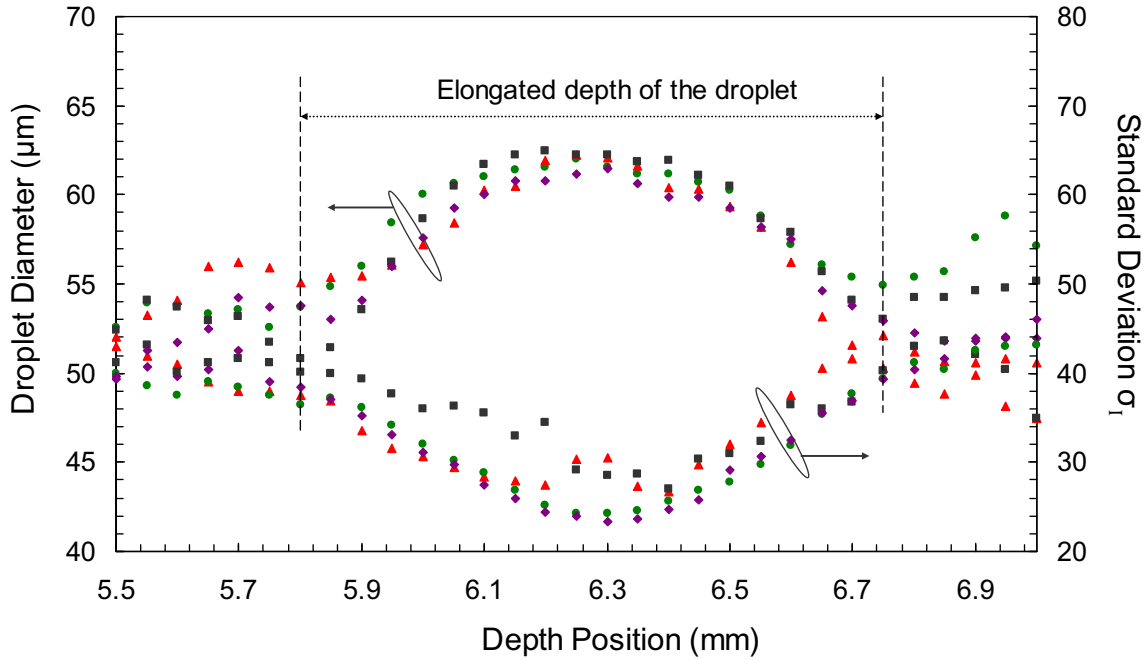


Figure 3.10: Largest area vs standard deviation criteria. Different symbols in each criterion represent different droplets

For the current magnification factor of $\mathcal{M} \approx 4$, the limit of droplet size at the lower end chosen for data cutting off is around 10 μm as the uncertainty becomes larger for smaller droplet. The error for this size limit will be given in the next chapter. This issue can certainly be improved if a higher magnification factor is used, particularly if combined with a camera with a larger CCD array than used here. However, in the current experiments one of the limiting factors is the ability to locate the droplet as it moves along its trajectory, particularly near the end when small upstream variations in the droplet trajectory have the potential to shift the droplet out of the measurement zone if the magnification is set too high. The additional requirement to image the droplet at high speed means for the camera used here a reduced number of pixels available for image collection. For the 5 kHz frame rate chosen, the 3.8x3.1 mm² viewing area (Figure 3.6b) is reduced in the y -direction from 1024 px to 200 px to give 3.8x0.6 mm², thus repeatability of the droplet trajectory over the typical 30 mm distance examined is of primary importance.

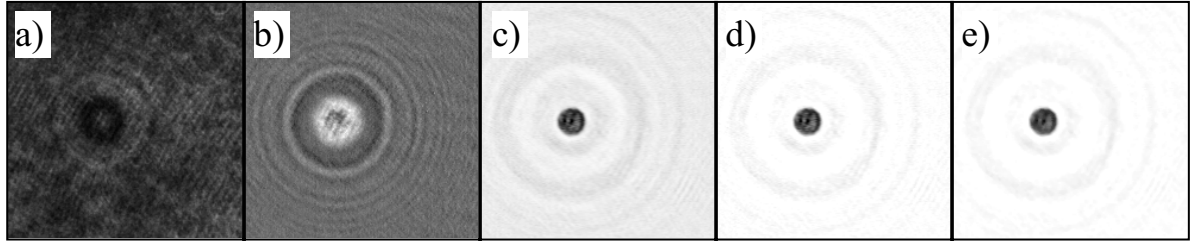


Figure 3.11: a) Hologram (raw data); b) Subtracted hologram; c) Reconstructed; d) Normalized and e) Filtered images of a 68 μm diesel droplet

3.5 Evaporation Rate Measurement

3.5.1 Residence Time Estimation

The aim of this work is to measure both the transient and average regression rates of fuel droplets undergoing evaporation. To calculate these rates, not only the droplet size needs to be measured but also its residence time. For transient measurements, the evaporation rate is measured only in a single viewing area hereafter called a measurement zone. The droplet residence time in this case is calculated relative to the time it first appears in the measurement zone. As mentioned, in order to obtain a sufficiently high temporal resolution a frame rate of 5 kHz was used which yields for this camera a reduced imaging region (ROI) on the CCD array of $1280 \times 200 \text{ px}^2$, equivalent to a measurement zone of $(x,y)=3.8 \times 0.6 \text{ mm}^2$ in the image plane. Droplet residence time can be obtained from this frame rate which will therefore be a multiple of 0.2 ms which is the time interval between consecutive realisations.

In the average evaporation rate measurement, droplet residence time at a particular position in the reactor is the time taken for the droplet to travel from the reactor entrance (injector tube exit) down to that position. In this system, droplets travel down almost vertically in the x -direction (Figure 3.6b) and the measurement is done by overlapping a number of measurement zones along the droplet trajectory. Assuming that the droplet velocity in the x -direction, V_x , as a function of vertical position is known, the residence time

can then be computed via $t = \int_0^x \frac{1}{V_x} dx$. If the instantaneous velocity between adjacent realisations can be measured for all these measurement zones then this velocity V_x can be found by least-square fitting a function on the velocity-position (u-x) data sequentially obtained from all zones which is a series of u-x matrices. Here, u is the instantaneous velocity in the x-direction which can be measured using DPIV while x is the droplet vertical position taking the injector tube exit as a fixed reference point. This absolute position x of a droplet that appears in a zone can be calculated by locating the 2D centroid (x_o) of its image first realized in that zone accounting for the zone height and shift between previous zones and then as a subsequent realisation, it follows the recursive formulation $x_n = x_{n-1} + u \Delta t$ in which Δt is the time interval between frames (realisations) of the camera which is 0.2 ms at 5 kHz frame rate.

Bear in mind that each droplet image or realisation mentioned is the image of the droplet reconstructed at a respective focused position in the z-direction and that data obtained from different zones along the trajectory is from different droplets. Strict requirements to validate this method are that the droplets move in almost the same trajectory during experiment and that the size of droplets before entering the vessel is repeatable. Due to the former requirement, the study of the effects of Reynolds number on the droplet evaporation is virtually impossible and that experiment is done at very low Reynolds number to ensure successful tracking of the droplet as the viewing area of the camera is very narrow (only 0.6 mm) due to high magnification used.

To locate the centroid x_o of a droplet, a 2D Gaussian function fit to the droplet image could be done and then the centroid (droplet position) would be the location of the function peak. However due to the low signal-to-noise ratio, this method cannot be used. An example of the intensity profiles of a droplet along the lines passing through the middle of the droplet image in the x and y-directions is shown in Figure 3.12a (top and bottom) while its 2D intensity map is shown in Figure 3.12b. As a result, a more general method is chosen which is derived from the 2D standard definition of the centroid in a discrete form

$R_c = (\sum_A R dI) / (\sum_A dI)$ in which A represents the area of the droplet, R is the distance of the element from the origin and dI the intensity of that element (pixel).

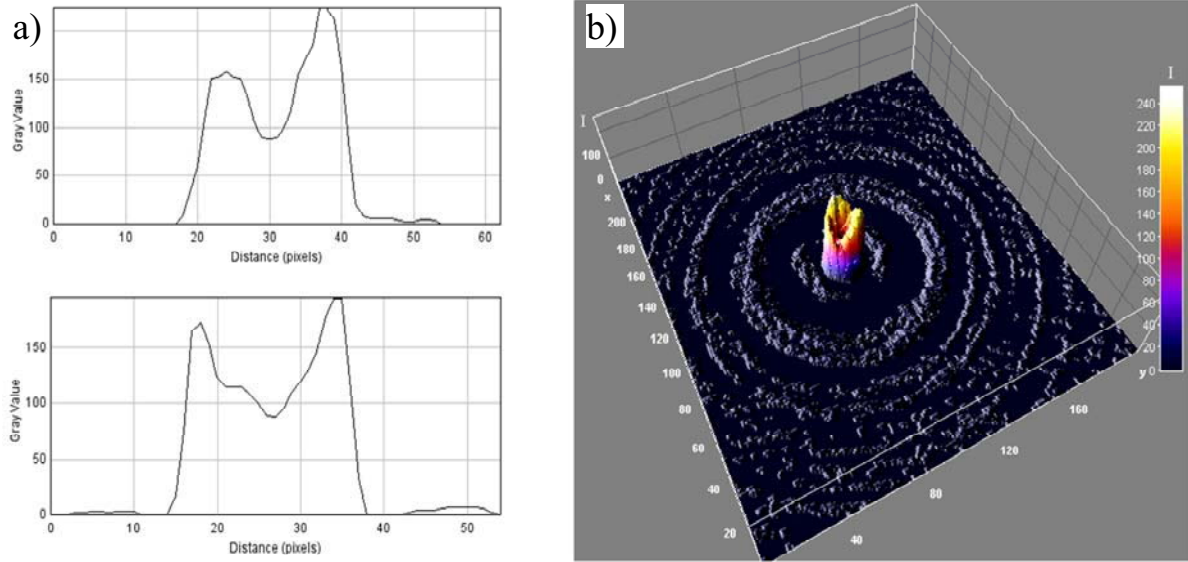


Figure 3.12: An example of intensity profiles of a droplet a) along the lines passing through the droplet image mid body in x and y -directions; b) on the 2D image

3.5.2 Basic DPIV Mathematics

Conventionally, DPIV is used for measuring the velocity field of a gas or liquid flow which is seeded with a multitude of minute particles. As a very typical example, such an analysis on a pair of single exposed images, which is divided into interrogation windows (IW) of particles when they are illuminated by a thin laser sheet, is done by the cross correlation digital particle image velocimetry technique as described in [1, 118, 119, 139]. The general mathematical background is based on the Correlation and Shifting Theorem. In this work, to measure the droplet instantaneous velocity, DPIV is applied to an image pair of two consecutive reconstructed images from the continuous record of the droplet as it moves through the measurement zone. The presence of only one droplet in each image renders this a point measurement rather than a field measurement. Thus only one IW consisting of the entire image is used. The general mathematics will simplify to the followings.

Assume the droplet as a particle and suppose that the intensity fields, with the origin of the coordinate system set at the IW center, of the two images are denoted by $I_1(x, y) = I(x - x_1, y - y_1)$ and $I_2(x, y) = I(x - (x_1 + \Delta x), y - (y_1 + \Delta y))$ at time t_1 and t_2 where (x_1, y_1) are the coordinates of the particle at t_1 ; Δx and Δy are the distances in x and y -directions that the particle has moved during time interval Δt ($t_2 - t_1$). The cross-correlation function between two fields will be:

$$S_{12}(\eta, \xi) = \int_{\Re} I_1(x, y) I_2(x + \eta, y + \xi) dx dy. \quad (3.16)$$

From the Correlation Theorem, the cross-spectrum is

$$G_{12}(f_x, f_y) = F[S_{12}(\eta, \xi)] = F[I_1(x, y)] F[I_2(x, y)]^*, \quad (3.17)$$

with F denoting Fourier transform operation; f_x and f_y being the variables in the transform domain with the origin also located at the images' center. The symbol $*$ denotes the complex conjugate of a function. The cross-correlation function S_{12} is related to G_{12} through the inverse transform. Using the Shift Theorem, equation (3.17) can be written as:

$$G_{12}(f_x, f_y) = \{F[I(x, y)] \times \exp[-j2\pi(f_x x_1 + f_y y_1)]\} \{F[I(x, y)]^* \times \exp[j2\pi(f_x (x_1 + \Delta x) + f_y (y_1 + \Delta y))]\}, \quad (3.18)$$

and then shortened down as:

$$G_{12}(f_x, f_y) = F[I(x, y)] F[I(x, y)]^* \exp[j2\pi(f_x \Delta x + f_y \Delta y)]. \quad (3.19)$$

The product $F[I(x, y)] F[I(x, y)]^*$ in equation (3.19) is the auto-spectrum of the particle image with itself. This equation clearly indicates that the contribution to the cross-spectrum function is due purely to the displacement of the particle. There is certainly no uncorrelated noise term typically present in the general case amongst different particles in two images. While this should be obvious, it is intrinsically what happens mathematically when DPIV is used as a tool for analyzing images containing only one particle which is a droplet in this work. If we define a function $S(\eta, \xi)$ as the auto-correlation function of the particle image with itself, again with the Shift Theorem the cross-correlation function finally becomes

$$S_{12}(\eta, \xi) = F^{-1}[G_{12}(f_x, f_y)] = S(\eta - \Delta x, \xi - \Delta y), \quad (3.20)$$

which shows that the peak of the auto-correlation is shifted to a position corresponding to the displacement of the particle. With a known image magnification and the time separation between the two images, the particle velocity can then be calculated. As the analysis is done for the entire image as a single IW and with the presence of only one particle, a few problems often faced in conventional flow PIV analysis are not present such as the velocity gradient effects on PIV result (e.g. in [118]). However, note that the above formulation is made for a particle with an assumption that its image intensity is unchanged except for the only change in the coordinates. For reconstructed droplet images, this is not true anymore and the cross-correlation analysis is affected by the quality of the reconstruction from MDIH. This will be discussed in the next chapter on the analysis of measurement uncertainty.

The PIV analysis applied on digital images is done in discretized form. Suppose that the rectangular images are pixel arrays of size $M \times N$ px^2 and the intensity fields of two images are respectively $I_1(i,j)$ and $I_2(i,j)$ with $0 \leq i \leq M-1$ and $0 \leq j \leq N-1$. The cross-correlation between these images is then:

$$S(\Delta x, \Delta y) = \sum_{i=0}^{M-1} \sum_{j=0}^{N-1} I_1(i, j) I_2(i - \Delta x, j - \Delta y), \quad (3.21)$$

in which $0 \leq \Delta x \leq M-1$ and $0 \leq \Delta y \leq N-1$. In this work, a function in normalized form is used which always gives values less than unity:

$$\rho(\Delta x, \Delta y) = \frac{\sum_{i=0}^{M-1} \sum_{j=0}^{N-1} I_1(i, j) I_2(i - \Delta x, j - \Delta y)}{[\sum_{i=0}^{M-1} \sum_{j=0}^{N-1} I_1^2(i, j)]^{0.5} [\sum_{i=0}^{M-1} \sum_{j=0}^{N-1} I_2^2(i, j)]^{0.5}}, \quad (3.22)$$

$0 \leq \rho(\Delta x, \Delta y) \leq 1$. The location of the peak of this function will give the displacement of the droplet. This function is calculated using the Convolution Theorem and Fourier transform as described earlier but in discrete form. Fast Fourier transform algorithm is used in the program. This function can also be computed directly but the time required for computation is substantially longer.

3.5.3 DPIV Application

Image recordings of the droplets are taken by the high speed MotionPro X3 camera which is capable of a maximum frame rate of 65 kHz. However, the higher the rate it is operated at, the narrower the ROI. A frame rate of 5 kHz was chosen as it is a good compromise between appropriate setting for PIV measurement and the viewing area. For the experimental conditions in this work, droplets range from 5 to nearly 30 px in diameter and move about 6 to nearly 30 px between consecutive realisations. The droplet holograms with initial size of $1280 \times 200 \text{ px}^2$, after going through the reconstruction process, are expanded to become $1280 \times 1280 \text{ px}^2$ which is appropriate for the application of the Fast Fourier Transform algorithm [32].

After each pair of reconstructed images in the time series is cross-correlated using the mentioned algorithm, the peak value of the cross-correlation is searched for in the image and then a two dimensional Gaussian function model is least square fitted to the local area surrounding this peak. This step helps to locate more correctly the position of the maximum of the cross-correlation function. As this peak location is sub-pixel accurate, good results of displacements between droplet images are therefore obtained. The velocity is then calculated by dividing this displacement by the time interval of 0.2 ms between frames with the magnification factor $\mathcal{M} = 3.996$ being also accounted for. Figure 3.13 shows an example of the DPIV cross-correlation analysed on two reconstructed droplet images at time t_1 and t_2 . Note that these images are cropped down from $1280 \times 1280 \text{ px}^2$ to $512 \times 200 \text{ px}^2$ to display here.

The use of DPIV in this work is not only to measure the droplet velocity but also as a means to check the repeatability of the droplet trajectory. A consequence of the use of MDIH to construct the DPIV image pairs is that as well as detecting movement in the (x,y) image plane, out of plane movement of the droplet can also be detected. This process requires locating where the focal plane of the droplet has shifted to along the z -axis. As has been shown in Figure 3.10 and will be further discussed in Chapter 4, use of in-line holography renders detection of this movement difficult due to degree of elongation of the

droplet in the z -direction for the set up used here. As such only the in-plane motion of the droplet is used to construct the droplet trajectory.

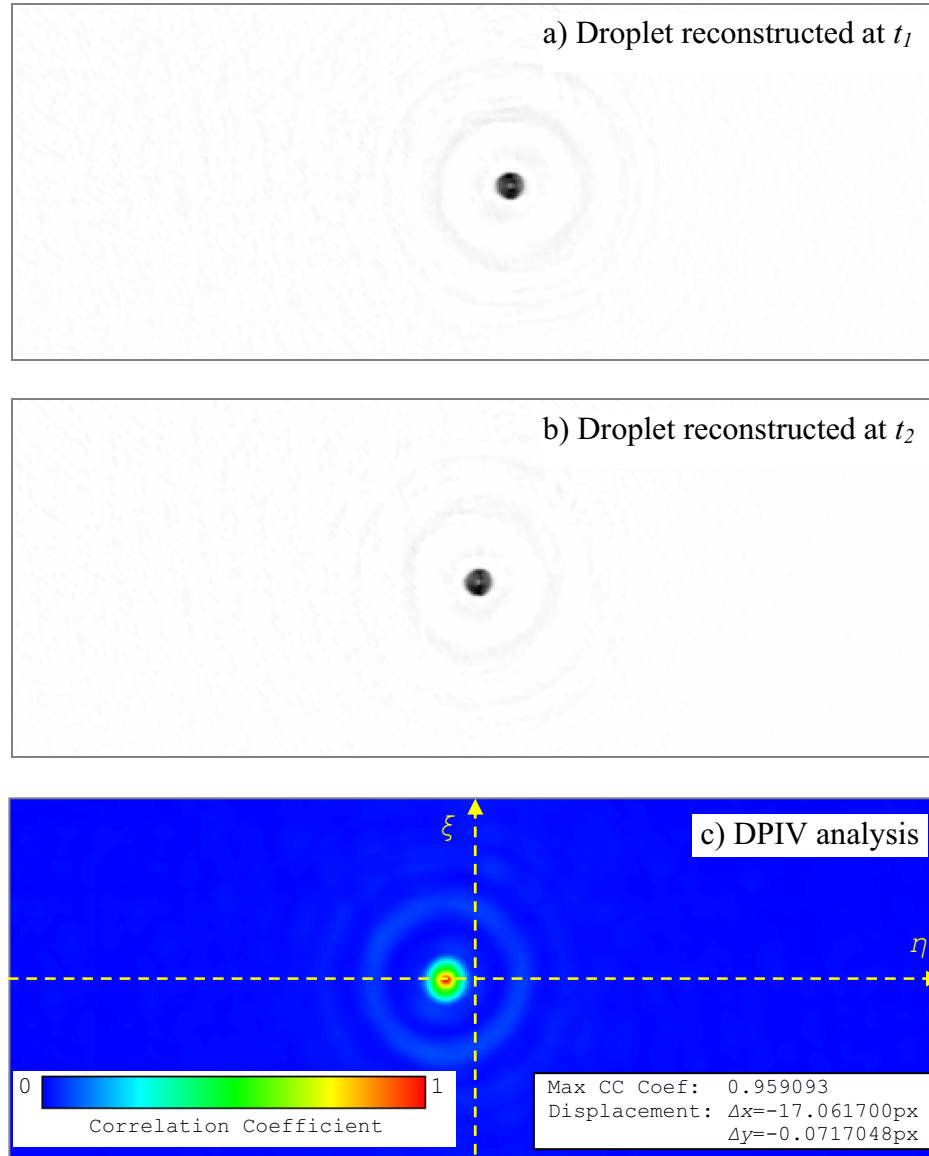


Figure 3.13: Cross-correlation between two consecutive reconstructed droplet images: a) Droplet image at t_1 ; b) Droplet image at t_2 ; and c) DPIV cross-correlation analysis

Figure 3.14 shows a series of reconstructed images of an evaporating droplet when passing through a measurement zone located near the end of the droplet trajectory. The actual number of consecutive images possible for each setting depends on the speed of the droplet for a particular frame rate. In Figure 3.14, although only 16 are shown, 64 individual

images record the droplet as it moves along the 3.8 mm length in the measurement zone x -direction. Sixty three individual velocity measurements are possible from this series of images which are recorded at a framing rate of 5 kHz. Evaporation is clearly evident in these images which show the droplet size reducing. In this figure, the droplet enters the measurement zone with diameter of 54 μm and velocity of 0.37 m/s and exits in the last frame with a diameter of 25 μm and velocity of 0.19 m/s.

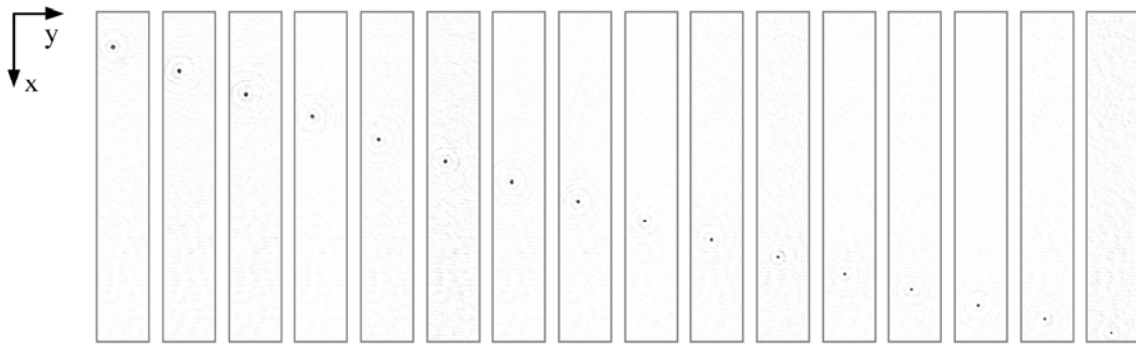


Figure 3.14: Instantaneous time series of a single droplet passing through a measurement zone near the end of its lifetime. Every 4th image is shown

Capturing the entire droplet trajectory, which might be over 30 mm in length, requires overlapping successive measurement zone velocity measurements. Zone overlap used is 0.3 mm in the x -direction resulting in a 3.5 mm displacement of each successive measurement zone. Figure 3.15 shows the result of one such measurement in which ten $3.8 \times 0.6 \text{ mm}^2$ measurement zones consisting of around 400 individual droplet measurements per zone are combined to yield the entire droplet trajectory. As mentioned in previous section, the cross-correlation depends on the reconstruction quality which has been found to cause a failure percentage of about 20% of the data points. For those failure points, a method used is to use values of a function which is least-square fitted to the neighboring data points. In Figure 3.15, two components presented are u and v which are the velocity in x and y directions, respectively. Combining these zones in the x -direction typically requires a small amount of shift around the centerline of the reactor in the y -direction to account for drift as a result of a small horizontal v -velocity component. The shift used is typically less than the width of the measurement zone over the length of the trajectory. Some evidence of this horizontal movement can also be seen in the instantaneous images of Figure 3.14.

The very good repeatability of the droplet trajectory is evident in this figure with little evidence of miss alignment from the measurement zone overlap. The horizontal v -velocity is almost zero along the trajectory the distribution of which has a mean of 0.0024 m/s and standard deviation of 0.007 m/s. With such a small velocity in the y -direction along the whole trajectory, all droplets are expected to experience the same heating load.

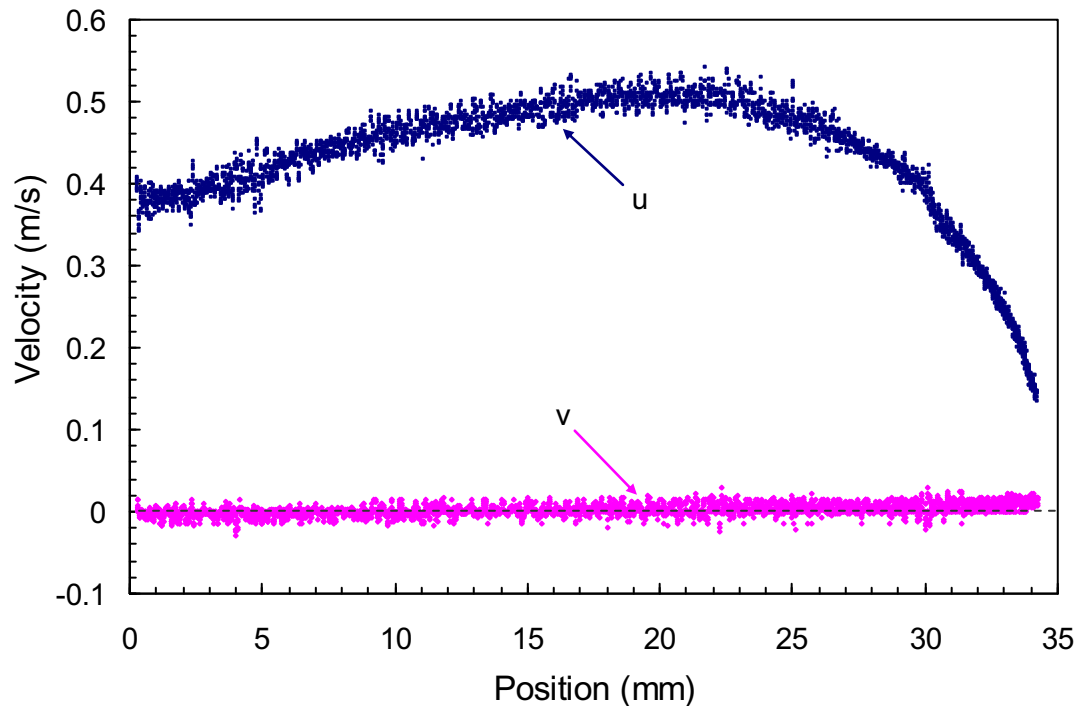


Figure 3.15: Measurement of the u and v -velocity components of a series of evaporating droplets. The measurement domain is made up of 10 overlapped measurement zones. Each point corresponds to an individual droplet measurement

Chapter 4

Uncertainty Analysis

4.1 Introduction

There are many factors that may affect the accuracy of the results. For the MDIH measurement, examples are the repeatability of the droplet generator, the effect of the difference in the refractive indices between the carrier and burner gases, the criterion used to determine the focal plane position. For DPIV analysis, the result is affected by the quality of the MDIH reconstruction (the noise) which influences the cross-correlation, the accuracy of the timing or clock speed of the computer which controls the camera. The calculation of the evaporation rate is influenced by the scattering in the measurements. All these will be assessed and discussed in this chapter.

4.2 MDIH Measurement Uncertainty

4.2.1 Uncertainty from Droplet Generator and Random Noise

A number of tests were undertaken to check the effect of the repeatability of the droplet generator. In fact, the random noise effect is also included in this check as it is inherently present in all recordings and cannot be separated such as the thermal noise coming from the CCD sensor of the camera. These tests were done with the burner off and hence no evaporation was deemed to occur. Tests undertaken included the effect of drift, transient

operation and sensitivity to the generator input parameters including the supplied voltage, the pulse width and the oscillating frequency. From the distributions of droplet diameters (each established from nearly 1000 measurement samples) measured with N_2 as carrier gas at the speed of 0.2 m/s, the largest variation resulted in a statistical uncertainty in the droplet diameter of $\pm 4\%$ at 95% confidence for a mean droplet diameter of approximately 62 μm which is shown in Figure 4.1.

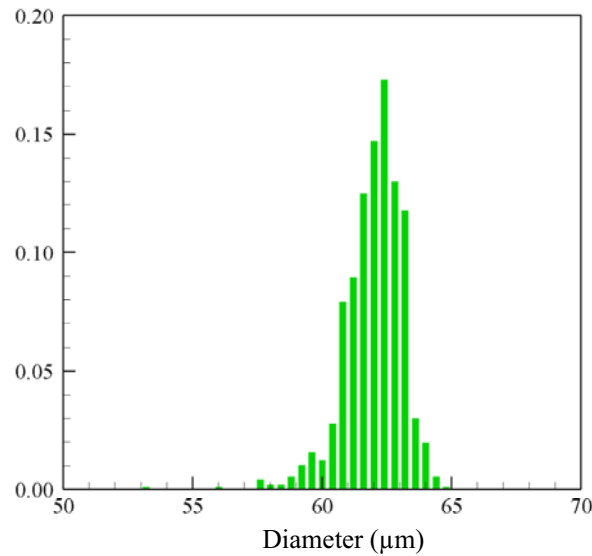


Figure 4.1: Droplet size distributions for droplets of approximately 62 μm with burner off

4.2.2 Uncertainty from Optics Imperfections

Even though the image has been improved, there are still areas where the hologram is affected by the noise from imperfections in the optics when the droplets pass through. These imperfections are to some extent dust from lenses, mirrors and reactor's walls but more severely the impurities inside these Quartz walls such as the air bubbles. This noise expands the measurement distribution which has much larger standard deviation. For most of the cases in this system the uncertainty due to this type of noise is $\pm 7\%$.

To check the sensitivity of the result on the hologram noise, a model of normally distributed (Gaussian) random numbers with zero mean but varying standard deviation is added to the hologram. This noise model is chosen because it is naturally present in many

systems. It is based on the Box-Muller transformation [10] of uniform random numbers which have an equidistribution property [77]. The uniform numbers are pseudo-randomly generated using the method of [83], the process of which is initialized with a seed derived from the system's current time in milliseconds to give a different sequence of random numbers for each run. Figure 4.2 shows an example of the effect of Gaussian noise with distribution standard deviation σ of 5, 10, 15 and 20 (σ_5 , σ_{10} , σ_{15} and σ_{20}) on 60 measurement samples. Note that σ_0 means no noise is added and that these sigma values are the grey values (the hologram is an image of 8bit giving a pixel value range of 0-255). The larger the sigma is the more fluctuation in the droplet sizes calculated. The sample standard deviation increases originally from 1.09 to 1.11, 1.49, 1.78 and 2.08 μm for σ_5 , σ_{10} , σ_{15} and σ_{20} respectively while the sample mean reduces from 61.58 to 61.52, 61.01, 60.48 and 60.17 μm . This artificial noise test indicates the noise from the existing imperfections to be a great source of error which suggests that a system with better quality reactor's walls would clearly improve the result.

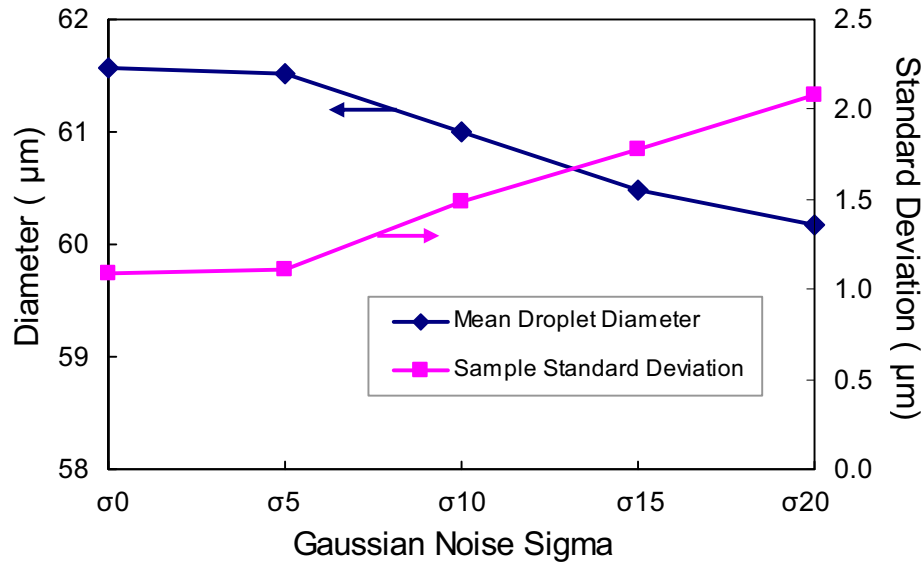


Figure 4.2: Effect of Gaussian noise with different sigma on MDIH results

4.2.3 Uncertainty from Refractive Index Difference between Gases

When the burner is in operation, the combustion gas represents a field with a refractive index which could be far different from that of the N_2 carrier gas. To study this effect,

Helium was used to simulate the low density combustion gases. Figure 4.3 shows the distributions of droplet sizes with use of N_2 as both droplet carrier and burner gases (Figure 4.3a), and use of Helium as carrier gas with N_2 as burner gas (Figure 4.3b). For these cases, the speeds of carrier gas and the burner gas are adjusted to be about 0.2 m/s and 0.05 m/s respectively. Each distribution represents more than 1000 measurement samples. The mean and standard deviation of the distributions are 62 μm and 1.43 μm for the N_2 gas combination, and 60.46 μm and 1.21 μm for the He/ N_2 combination. Although the difference of around 1.5 μm between the means of these distributions is significant at the 95% confidence level, it lies within the range of uncertainty found for the droplet generator repeatability.

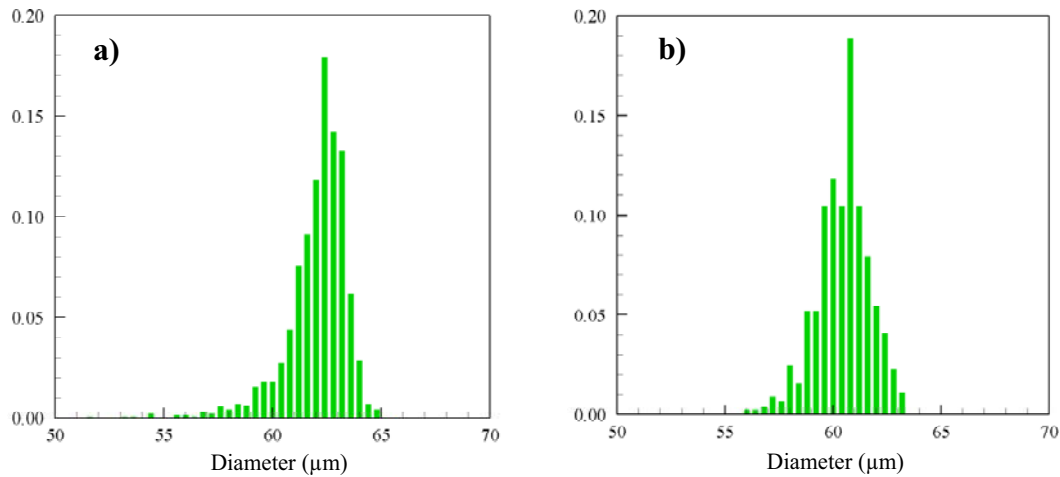


Figure 4.3: PDF distributions of droplet diameters with
a) N_2 as carrier gas and main gas and b) Helium as carrier gas and N_2 as main gas

4.2.4 Uncertainty from Criterion Used to Determine the Focal Plane

As mentioned, the criterion used to find the focal plane of the droplet is to find the axial position in the z -direction which has the largest area falling below an intensity threshold value. Figure 4.4 presents a typical variation in droplet diameter calculated from the measured area for each position which satisfies this criterion. Droplets are characterized by elongated shapes in the optical path which measure approximately 900 μm or 15 times the droplet diameter. Even though improved by use of magnified DIH, it is clear that lack in sensitivity in droplet location along the z -axis brought on by this elongation means that the z -

component of velocity cannot be accurately determined. Other optical arrangements such as that used in Sheng et al. [113, 114] give far greater sensitivity but cannot be used here in this system.

As this work focuses on determining the droplet size with acceptable uncertainty rather than determining the exact location of the focal plane, the axial resolution chosen is $50\text{ }\mu\text{m}$ in the z -direction which is a good compromise between the processing time and the droplet sizing aim. As illustrated in Figure 4.4, there are peaks in the profiles around the central part marked as the Focal Interval. The variation in the droplet size in this interval is small with the maximum RMS (root-mean-square) of $1.5\text{ }\mu\text{m}$.

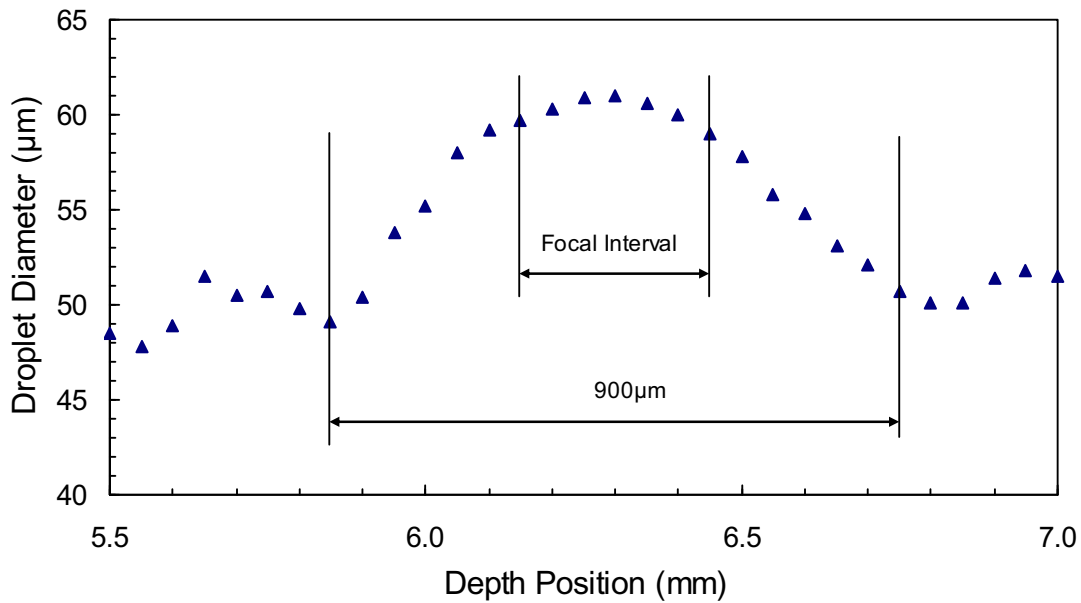


Figure 4.4: A typical variation in the z -direction of droplet diameter which falls below a set intensity threshold value

4.2.5 Uncertainty in Droplet Size Calculation

As in the literature, to study their behavior droplets are assumed to be spherical even though this would certainly contribute error to droplet size estimation. As the droplet size is calculated from the area that falls below an intensity threshold value, it is affected by this value itself. This proposes a need to study the sensitivity of droplet size on this threshold value. Figure 4.5 shows the distribution mean and standard deviation of 60 measurement

samples as functions of the threshold value. The threshold values studied span the gradient field surrounding the droplet with a minimum intensity value of 160 and maximum of 200 on the 8-bit images. It can be seen from the standard deviation curve that the effect of the noise is larger with smaller threshold. With the average threshold of choice of 180, the uncertainty at the 95% confidence level found from the distribution of errors is $\pm 3.6 \mu\text{m}$ or $\pm 5.8\%$ relatively. As mentioned earlier about the measurement limit at the lower end of around $10 \mu\text{m}$, investigation for this size indicates that the error is nearly $\pm 3.8 \mu\text{m}$ which means a relatively large uncertainty of $\pm 38\%$.

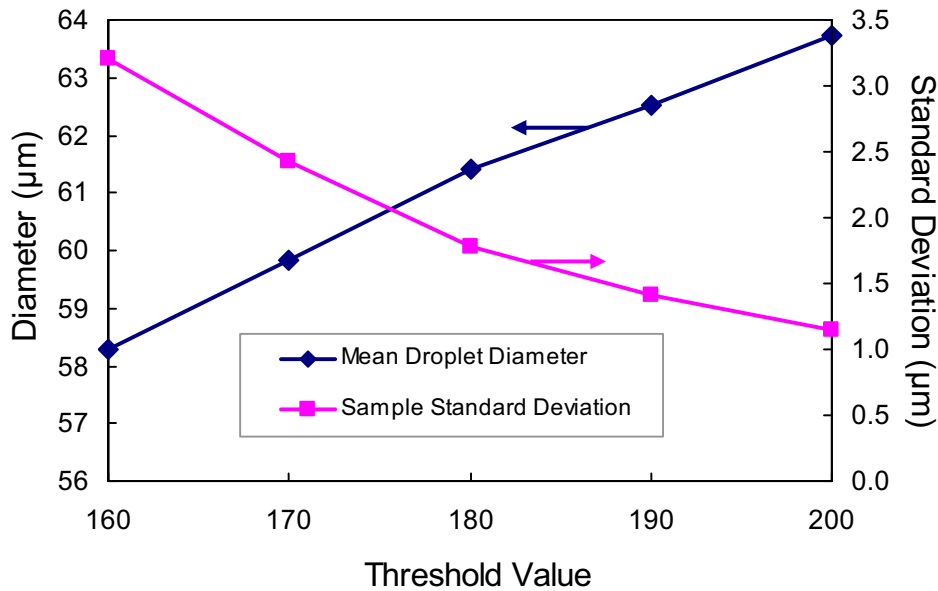


Figure 4.5: Calculated size and standard deviation as functions of individual threshold values which span the gradient field surrounding the droplet

4.2.6 Uncertainty in Reference Source

In the earlier discussion on the collimation setup, it was assumed that the reconstruction wave is a plane wave coming from a point source in infinity. The reconstruction using a plane wave exactly the same as a reference wave will re-create the object image in the same position with the same size. However, in practice the reference wave is not a plane wave but rather a wave diverging or converging from or to a point and so, the use of a plane wave for reconstruction will create an object image at different position and size. By denoting the distances from the hologram recording plane (in this setup it is the focus plane of the optics

system) of the object, reference wave point source and reconstruction wave point source as z_o , z_r and z_c , respectively, the virtual image is reconstructed at z_i with a transverse magnification M_t which can be calculated via the following relationships [19]:

$$z_i = \left(\frac{1}{z_c} + \frac{1}{z_o} - \frac{1}{z_r} \right)^{-1} \quad (4.1)$$

and

$$M_t = \left(1 + \frac{z_o}{z_c} - \frac{z_o}{z_r} \right)^{-1}. \quad (4.2)$$

To check the uncertainty coming from the reference source, the grid image is used. This check is the extension of the calibration process described in section 3.4.4. The grid image is placed at the furthest point (where the droplets could be present) of $z_o = -12$ mm from the focus plane, with a plane reconstruction wave ($z_c = -\infty$) the image is found to be located at about -12.05 mm with $M_t \approx 1.0015$ and from the above equations the reference wave is diverging from -8012 mm and the reconstructed image position is calculated to be at a very close value $z_i = 12.018$ mm. At a closest point of $z_o = -2$ mm, the error is even smaller to be 0.025% ($M_t \approx 1.00025$) and the calculated image position is -2.0004 mm.

Even though the error from this set up is negligible compared to other errors, as the grid slide is extremely thin, the elongation effect is much smaller than that of droplet measurements and the reconstructed image is much better located.

4.2.7 Uncertainty due to the Selection of M

As described in section 3.4.3, the selection of M in the digital reconstruction filter may affect the MDIH result. To study this effect, M values of 1, 2, 3, 4, 5, 6 and 7 are tested and a typical result of a diesel droplet measurement is shown in Figure 4.6 for droplet diameter roughly of 85 μm . These are again images of $200 \times 200 \text{ px}^2$. It can be seen that the filter quickly converges once $M = 3$. For $M = 1$, which is equivalent to the conventional reconstruction case, the out-of-focus twin image effect is obvious.

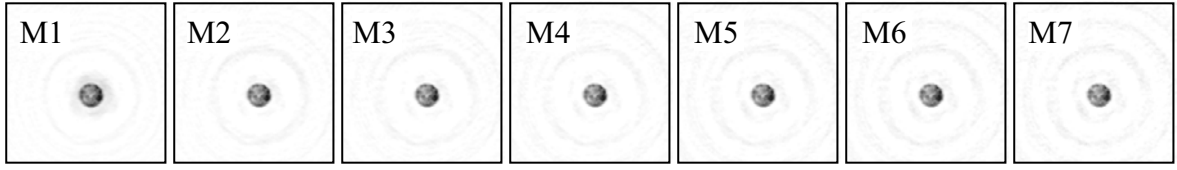


Figure 4.6: Reconstruction of 85 μm diesel droplet at different M values of the filter

Figure 4.7 presents the droplet size variation with M values for three droplet examples. The diamond symbols in this figure represent the droplet shown in Figure 4.6. For $M = 3-6$, the droplet size is almost the same with very small variations of less than $1.5 \mu\text{m}$. For $M = 7$, the sizes are seen to reduce and according to [93], for higher M values the degradation occurs to the image. As mentioned, $M = 3$ is chosen in this work as it is enough for convergence.

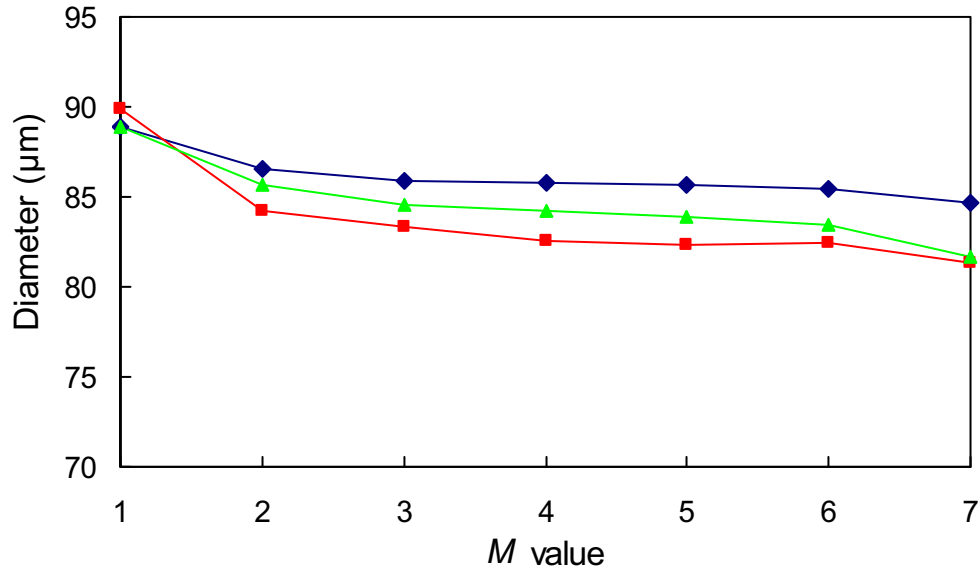


Figure 4.7: Variation of droplet diameter with respect to M . Different symbols represent different droplets.

4.3 DPIV Measurement Uncertainty

4.3.1 Uncertainty from Displacement and Camera Timing

As the instantaneous velocity is calculated from the displacement and time interval between two cross-correlated images, the accuracy of DPIV results depends on how accurately the

DPIV algorithm locates the position of the maximum cross-correlation coefficient and the timing accuracy of the camera. Since only the u component is used for the residence time calculation, the assessment of uncertainty in u is important. Uncertainty can be calculated as [126]:

$$B_u = \frac{\partial u}{\partial x} B_x + \frac{\partial u}{\partial t} B_t = \frac{1}{\Delta t} B_x - \frac{\Delta x}{\Delta t^2} B_t \quad (4.3)$$

in which, Δx and Δt are respectively the calculated distance and time interval between two images while B_x and B_t are respectively the uncertainty in displacement and time interval. Since the clock speed of the camera is 90 MHz, the timing uncertainty, B_t , is 0.9 μ s. With time interval Δt of 0.2 ms and the theoretical sub-pixel accuracy of DPIV of about 1/20th of a pixel, the uncertainty in the velocity result B_u can be seen as a function of Δx . Theoretically, the maximum uncertainty reaches approximately 0.75×10^{-3} m/s when Δx approaches zero which, however, is not the case even at the end of the trajectory where droplets tend towards a minimum velocity, Figure 3.15.

4.3.2 Uncertainty from MDIH Reconstruction Position

DPIV results may also be affected by the reconstructed position of the droplet in the depth direction along the z -axis. Variation in this direction corresponds to correlating images with different droplet cross-sectional area as shown in Figure 4.4. To analyse this effect, pairs of reconstructed images of a droplet at different depth positions were cross-correlated and the error was found to be negligible of 0.3%.

4.3.3 Uncertainty from Image Noise

The PIV result is also affected by the quality of the reconstruction as mentioned in section 3.5.2 and this is termed a noise effect. To investigate this, the droplet reconstructed images are added with Gaussian random noise as has been applied in section 4.2.2. Figure 4.8 shows the effect of different sigma values of the noise distribution on the cross-correlation

coefficient and the displacement in the x -direction. While the displacement is not varying much of less than $0.5 \mu\text{m}$ (relative error of less than 1%) within sigma values tested, the cross-correlation coefficient is very sensitive to the noise and reduced from 0.96 at $\sigma 0$ to 0.12 at $\sigma 20$. From this test, it can be seen that the quality of the reconstruction image is a very important factor in DPIV analysis, the cross-correlation would fail if more noise is added which explains the failure of about 20% of the data points as mentioned in section 3.5.3. For pairs of images that the cross-correlation works, the errors in velocity results are expected to be not significant.

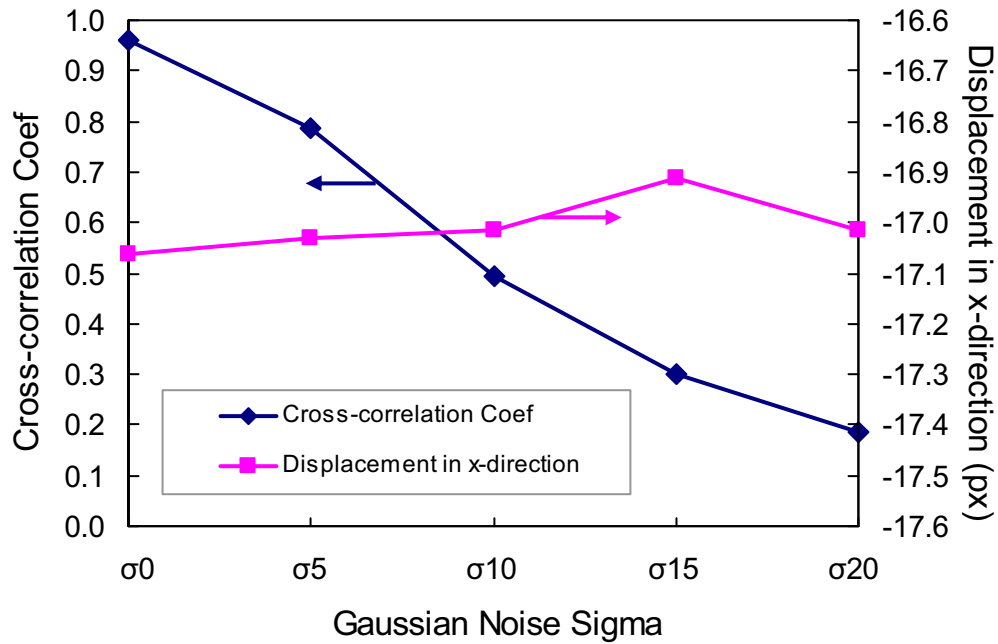


Figure 4.8: Effect of Gaussian noise with different sigma on cross-correlation results

4.4 Uncertainty in Calculating the Evaporation Rate

As there are two types of measurement used in this work including average and instantaneous measurements, the uncertainty in evaporation rate calculation is different for each type. The estimation of the error is based directly on the plots showing the variation of squared diameter against residence time and in the following sub-sections such typical estimations will be presented.

4.4.1 Uncertainty in Average Measurement

For a time interval $\Delta t = (t_2 - t_1)$, the average evaporation rate is calculated from the ratio $\Delta D^2 / \Delta t = (D_1^2 - D_2^2) / (t_2 - t_1)$. By treating D_1 and D_2 as separate variables the uncertainty in K_v can be estimated as

$$U_{K_v}^2 = \frac{1}{\Delta t^2} P_{\Delta D^2}^2 = \frac{1}{\Delta t^2} (P_{D_1^2}^2 + P_{D_2^2}^2) \quad (4.4)$$

in which the uncertainty in residence time is deemed negligible as reflected in the negligible uncertainty in DPIV results. $P_{D_1^2}$ and $P_{D_2^2}$ are uncertainty in D_1^2 and D_2^2 . For multiple tests, the above equation can be finalized as [123] (at 95% confidence level)

$$U_{K_v} = \frac{2}{\Delta t} \sqrt{\frac{RMS_{D_1^2}^2 + RMS_{D_2^2}^2}{N_t}} \quad (4.5)$$

with $RMS_{D_1^2}$ and $RMS_{D_2^2}$ being root-mean-squares of D_1^2 and D_2^2 and N_t the number of repeated tests. It is clear from this derivation that the longer the time interval used for estimating the evaporation rate, the lower the uncertainty is. Figure 4.9 shows an example of the variation of squared diameter against the residence time during steady evaporation of dodecane for ten droplets ($N_t = 10$). For this period, $RMS_{D_1^2}$ and $RMS_{D_2^2}$ are 0.00017 and 0.000056 mm² respectively with Δt being 0.0205 s. U_{K_v} is 0.0055 mm²/s or about 2.5% of the average K_v of 0.218 mm²/s found from least square linear fit (see figure).

Another type of average rate calculation used for more detailed analysis is the division of the whole evaporation process (including unsteady evaporation) into consecutive data blocks (each block is equivalent to a measurement zone) and as shown in Figure 4.10 for 5 zones of dodecane droplets, the relative error is estimated to be 21.8% as the largest for the early stage and 4% as the smallest for the final stage.

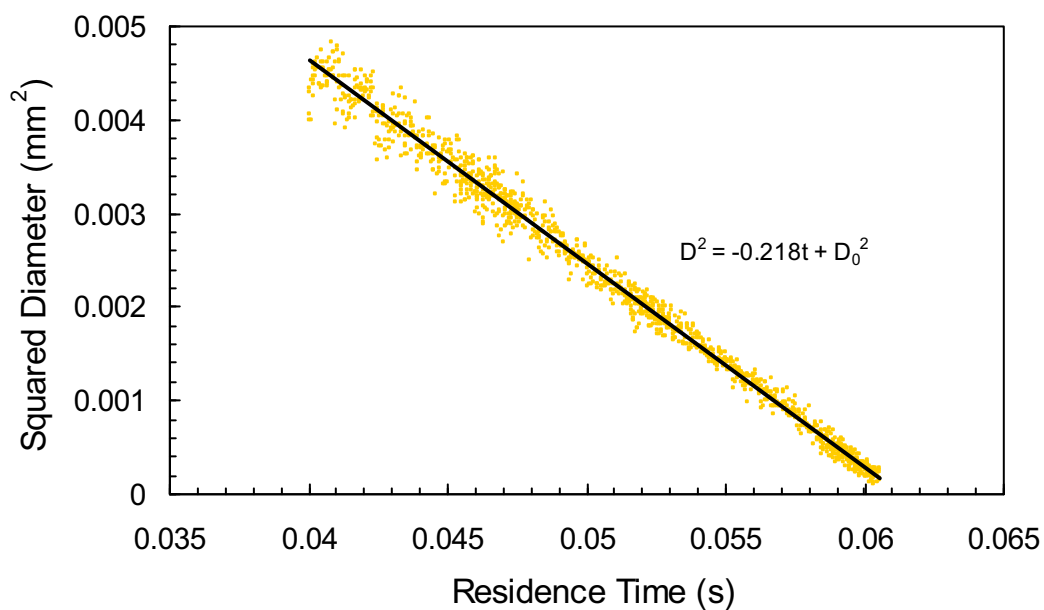


Figure 4.9: Example of average evaporation rate found for the steady evaporation period of dodecane droplet

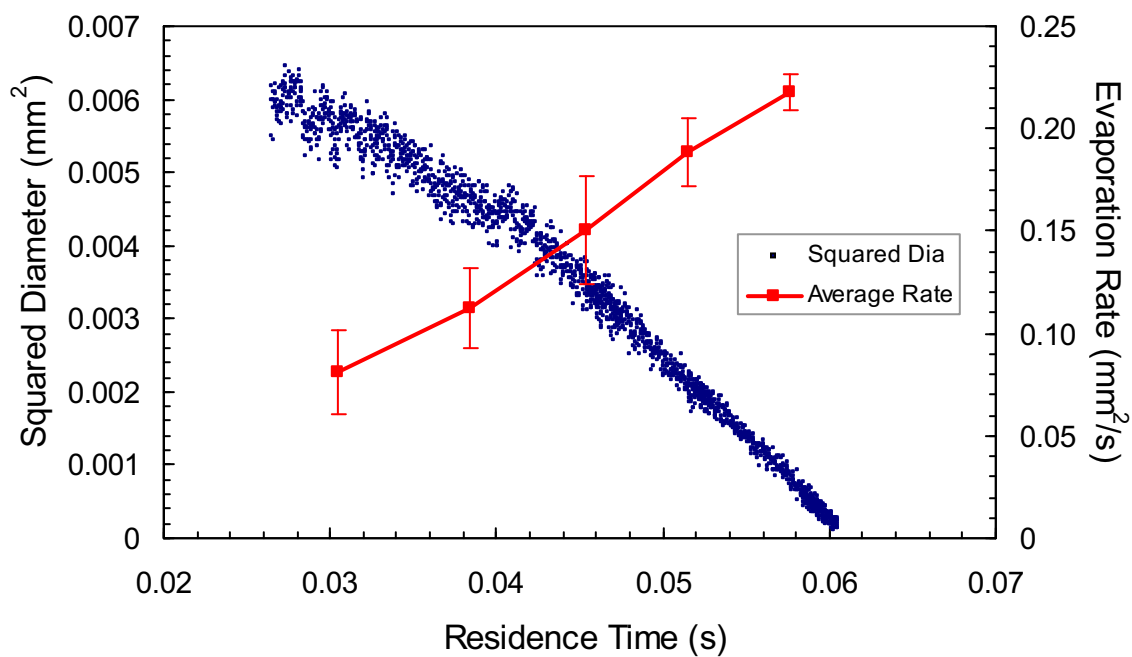


Figure 4.10: Average evaporation rates of 5 consecutive data blocks with error bars. Each block is equivalent to a measurement zone

4.4.2 Uncertainty in Instantaneous Measurement

For instantaneous set up which enables more detailed investigation of the effect of initial diameter on the droplet evaporation (shown later in Chapter 5), the rate K_v is measured for a particular zone (the viewing area of the camera at a certain position) and the time interval is about as short as one of the above blocks. Following the same calculation, the maximum relative error is estimated to be about 22% of the “instantaneous” rate of the zone at the injector tube exit. Even though this is a large uncertainty as found for previously mentioned data blocks in the early stage of evaporation, the repeatability of these K_v results has been consistently found.

Chapter 5

Experimental Results

5.1 Introduction

Velocity measurement plays a vital role in this work. It is used not only for residence time calculation but also as the input for the droplet evaporation model which is the topic of the next chapter. Based on a typical DPIV result, this chapter discusses the overall dynamics of the droplets. Thereafter, measurement results on the evaporation of small droplets of dodecane, decane and nonane will be detailed followed by that of automotive light diesel as a multi-component fuel for comparison. This chapter will start with some description of the experimental conditions and fuels.

5.2 Experimental Conditions and Fuels

As mentioned, the aim to study droplets with sizes less than 90 μm has led to selection of the oscillating piezo-electric nozzle. A nozzle with a diameter of 80 μm is used for this work. Smaller nozzles are also available, however different tests performed for all these nozzles on fuels of investigation as well as other widely used alkanes indicated the problems of very high delicacy and strong sensitivity to liquid properties (similar problems have also been encountered in other work [35, 140]). While smaller nozzles are highly unstable in those

tests, the 80 μm nozzle is much better but its operable range is still limited. Nonane, decane and dodecane chosen for this work are those giving the best performance (heptane, octane, undecane and tridecane were attempted but they did not work or worked very unstably). Light diesel, which also gives stable performance, is also used in this work to compare between pure and multicomponent liquids. To have droplets with different sizes the input signal to the nozzle can be adjusted by varying the voltage, frequency and pulse width. However the liquid properties dramatically limit the possible droplet size range.

For this system, attempts have also been made to study not only evaporation but also combustion by setting the oxygen content to as high as 24% in the post combustion gas. However, droplet combustion cannot be obtained which is deemed not favored by the conditions used. It has been known that besides the dependence on the surrounding gas temperature and oxidizer content, ignition also depends on the fuel vapor concentration and kinetic effects [71, 111, 112]. Similar observations have been noted in another entrained flow reactor setup [35]. Only investigation of evaporation is therefore possible. Nevertheless, it has been suggested (e.g. [86]) that the study of droplet evaporation is more relevant than combustion. In practical spray combustion devices, droplet evaporation is the dominant process starting soon after fuel injection and atomization. Combustion occurs later to the mixture of fuel vapor from the spray and the air rather than individual combustion flames surrounding individual droplets. Furthermore, droplet combustion is actually the droplet evaporation in very hot environment as the flame, acting as the heat source, is very close to the droplet [71].

The evaporation of a droplet, as shown in the literature, depends on a number of factors including initial droplet diameter and temperature, surrounding gas temperature and pressure, droplet Reynolds number, liquid properties, array effect (droplet interaction reviewed in Chapter 2), etc. Due to the great difficulty mentioned earlier in obtaining repeatable data, only the effects of ambient temperature and initial diameter on the droplet evaporation are studied. To study the effect of ambient temperature, two heating conditions have been established as shown in Figure 3.4. An assumption used here is that each symbol (measured point) on these curves represents the average temperature of the gas surrounding

the droplet at that position even though there exist temperature gradients between each position. These temperature gradients differentiate the conditions in this work from those of a large number of studies that used a constant temperature field. Together with the variation in droplet velocity during its lifetime, the whole process is therefore supposed to be transient. For analysis of the results, knowledge of temperatures at positions between the measured points is obtained by least square fitting an 8th degree polynomial to those sampled temperatures along the reactor centerline. As mentioned previously, droplet initial diameter can be varied by altering the signal sent to the nozzle. However due to the strong sensitivity to the fuel properties, for each fuel the stable operation can only be obtained in a very narrow range of sizes and so the initial diameter effect could not be systematically studied.

Table 5.1 summarizes the experiments done in this work. Although a huge amount of effort has been spent for experimentation, with mentioned difficulties only series listed in the table have been obtained. Each series here represents roughly about 4000 individual droplet measurements. The numbers listed in the table are the means of the distributions checked prior to each series of experiment.

Table 5.1: Summary of experiments

Heating condition (see Figure 3.4)	Droplet diameter (μm)			
	Dodecane ($\text{C}_{12}\text{H}_{26}$)	Decane ($\text{C}_{10}\text{H}_{22}$)	Nonane (C_9H_{20})	Diesel
T_H	75	74	84	85
	65	52	63.5	76
T_L	76.5	45.5	X	X

The thermophysical properties of the fuels used for this investigation are listed in Tables 5.2 and 5.3. For nonane, decane and dodecane, the data are taken from the API technical data book [127]. For diesel, it is however impossible to get a similar set of data as it is a complex fuel. Some properties take average values, for example the boiling point takes the

average value of the range given in the MSDS. The properties listed are just indicative which are treated in this work as properties of a single representative liquid for approximate calculations. While dodecane has been used in some studies to approximate standard light diesel, it can be seen here that indicative data of diesel such as the density, viscosity and boiling point are much higher than those of the three alkanes. In fact, whereas n-nonane and n-decane are amongst the heaviest hydrocarbons present in gasoline, n-decane and n-dodecane belong to the lightest group in diesel. N-dodecane is also present in kerosene.

Table 5.2: Basic properties of liquid dodecane, decane, nonane and light diesel

Fuel Type	Molecular weight (g/mol)	Density @15.55°C (mg/ml)	Boiling Point (°C)	Critical Temperature (°C)	Critical Pressure (MPa)
Diesel	167	850 ^a	265 ^m	296.25 ⁱ	2.46 ⁱ
Dodecane	170.34	751.69	216.32	384.85	1.82
Decane	142.29	733.48	174.16	344.55	2.11
Nonane	128.26	721.38	150.55	321.45	2.29

^aApproximate value

^mMiddle of the range

ⁱIndicative value

Table 5.3: Thermophysical properties of liquid dodecane, decane, nonane and light diesel

Fuel Type	Heat of Vaporisation (kJ/kg)	Surf. Tens. @ 25°C (dynes/cm)	Viscosity @ 38°C (cSt)	Thermal Conductivity (W/mK)	Heat Cap. @15.55°C (kJ/kgK)	Acentric Factor
Diesel	270	29.30 ^a	3.0 ^a	0.13831 ⁱ	1.9 ⁱ	N/A
Dodecane	260.84 ^b	24.93	1.5452	0.09093 ^b	1.212	0.5764
Decane	278.33 ^b	23.39	1.0154	0.09458 ^b	1.214	0.4923
Nonane	290.96 ^b	22.40	0.8078	0.09716 ^b	1.212	0.4435

^aApproximate value

ⁱIndicative value

^bAt normal boiling point

5.3 Droplet Dynamics Overview

When a pulse of signal is sent to the piezo-electric nozzle, the vibration generates a pressure wave and the droplet is ejected at the speed of 2 m/s [133]. The droplet then follows the carrier gas through the injector tube to enter the reactor. For both temperature settings, the carrier gas is supplied at the speed of 0.12 m/s and as such the droplet is expected to slow down. When moving in the reactor the droplet experiences more complicated condition of flow mixing between carrier and burner gases. For high and low settings respectively, the burner gas speeds are set to be 0.25 m/s and 0.175 m/s and from Figure 3.4, it can be seen that the mixing regions occupy up to around 25 mm of the trajectory for both settings. The gas speeds mentioned are indicative values calculated based on the gas flow rates and the cross sectional areas of the injection tube and the burner plate (not measured values), and that thermal expansion has already been accounted for in burner gas calculations.

A typical result of PIV measurement of a diesel droplet for the T_H condition was shown much earlier in Figure 3.15 (Chapter 3). For the T_L condition and all other fuels the variations in velocity (u-component) have similar trends. Analysis of this representative figure will therefore suffice for depicting the overall droplet dynamics in the vessel. At different positions along the centre line, the gas speeds are different due to the mixing effect between two gases and the thermal expansion. Several observations can be made of the data in this figure. Acting on the droplet is a combination of weight, inertial, buoyancy and drag forces. As they enter the reactor, the droplets undergo acceleration from the initial lower speed with a continual rise in velocity to a peak. This can be a result of the effects of gas mixing and further expansion of the cooler carrier gas of higher density when receiving heat from the burner gas. After this acceleration period the temperature is high but evaporation of the droplet reduces both size and weight so the velocity falls. For the conditions used, droplet Reynolds number is generally small (shown in the next chapter) and although gas speeds are not measured, the relative velocity (slip) between the droplet and the gas is expected to reduce past the peak velocity. For these setups, the Reynolds numbers of the gas

using the reactor's width as the characteristic dimension fall in between 200-250. More discussions on droplet dynamics will appear in later analysis of the data.

5.4 Evaporation Rates of Fuels

5.4.1 Measurement of the Average Evaporation Rate

In these measurements, the exit of the injector tube is placed level with the exit plane of the burner. The amount of overlapping zones needed for the measurement of each series depends on the temperature setting, experimental fuel and initial droplet size. As the size limit chosen for the lower end is 10 μm , the trajectory of the droplets is traced until the droplets are roughly as small as this size. An example shown previously in Chapter 3 for 85 μm diesel droplets in the high temperature setting requires 10 zones with around 4000 individual droplet measurements. Since the data in the proximity beneath the burner plate is badly affected by the flame (very noisy) all the results shown later will start from 3 mm downward from the injector tube exit.

As the first illustration of the temperature effect on the evaporation, measurement of dodecane droplets for two temperature settings are shown in Figure 5.1 with diameter variation against x -position along the centre line. In this figure, the droplet initial diameters are 75 and 76.5 μm for high and low temperature settings respectively. For convenience, the temperature profiles of the surrounding gas and the boiling point of dodecane are also shown. Although there is a slight difference between the initial sizes for the two settings (roughly 5% relative difference in volume), these two series can still be directly compared with each other.

In both series the droplets are seen to undergo a preheating stage during which expansion occurs to some degree. The obvious preheating region spans until nearly 11 mm and 14 mm for the T_H and T_L respectively which are close to where the gas temperatures exceed the boiling point of this fuel. After this region, droplets begin to reduce in size and for the T_H the evaporation happens quicker with size reduced to about 10 μm at approximately 25 mm

while for the T_L this occurs at nearly 30 mm. In this data, there is no clear sign separating the preheating and evaporation stages. This can be due to the fact that the evaporation has started during the preheating phase and size variation in this region is thus a result of the combined effect of droplet thermal expansion and evaporation, heating effect is stronger than the initial slow evaporation. With this possibility, evaporation will however be deemed to start when the droplet size starts to reduce.

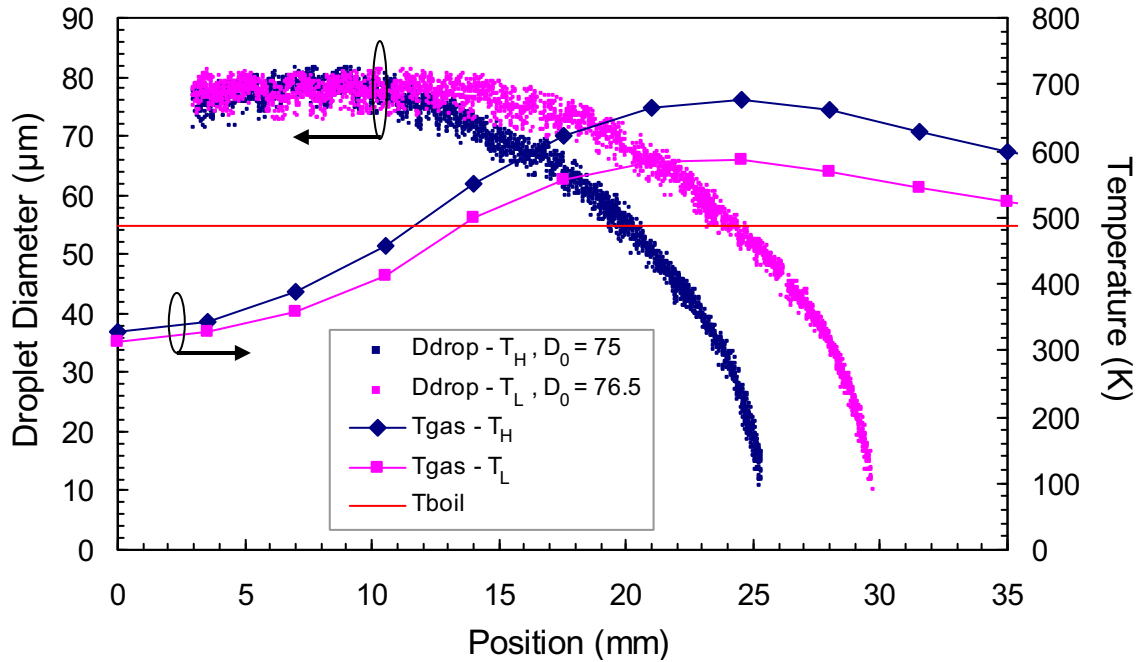


Figure 5.1: Dodecane droplet diameter variation against centre line position for two temperature settings. Initial diameters are about 75 μm and 76.5 μm for T_H and T_L , respectively. Two temperature profiles and dodecane boiling point are also shown.

As described in section 3.5.1 for residence time estimation, the velocity profiles are least squared fitted with an 8th order polynomial. Figure 5.2 shows such fits to two velocity data sets and the estimated residence times. The standard errors of these fits are typically around 0.011 m/s and correlation coefficients $R^2 \approx 0.95$. The velocity profiles of these two data sets are seen to be almost the same during the acceleration of the droplets; for region close to the entrance (preheating region with similar droplet sizes), this can be reasoned by the smaller effect of gas mixing. The continued similarity in velocity can probably be explained by the fact that given the higher burner gas speed and the stronger thermal expansion for the T_H , the

droplet size gets smaller due to faster evaporation and the droplet velocity is therefore not higher than that for the T_L . This dependence of droplet velocity on its size is in accordance with the momentum conservation law which will be mentioned in the next chapter. Once past the peak, due to the much smaller droplet size for the T_H the droplet slows down more quickly for this case. As the droplet evaporation rate depends on the temperature and the conditions surrounding the droplet, given the same trajectory the droplet size history therefore depends on its speed. In complex environments, such mutual influences imply that droplet's momentum plays an important role in its evaporation behavior. For these two series, the residence time of the T_L is 73.5 ms compared with 60.5 ms of the T_H .

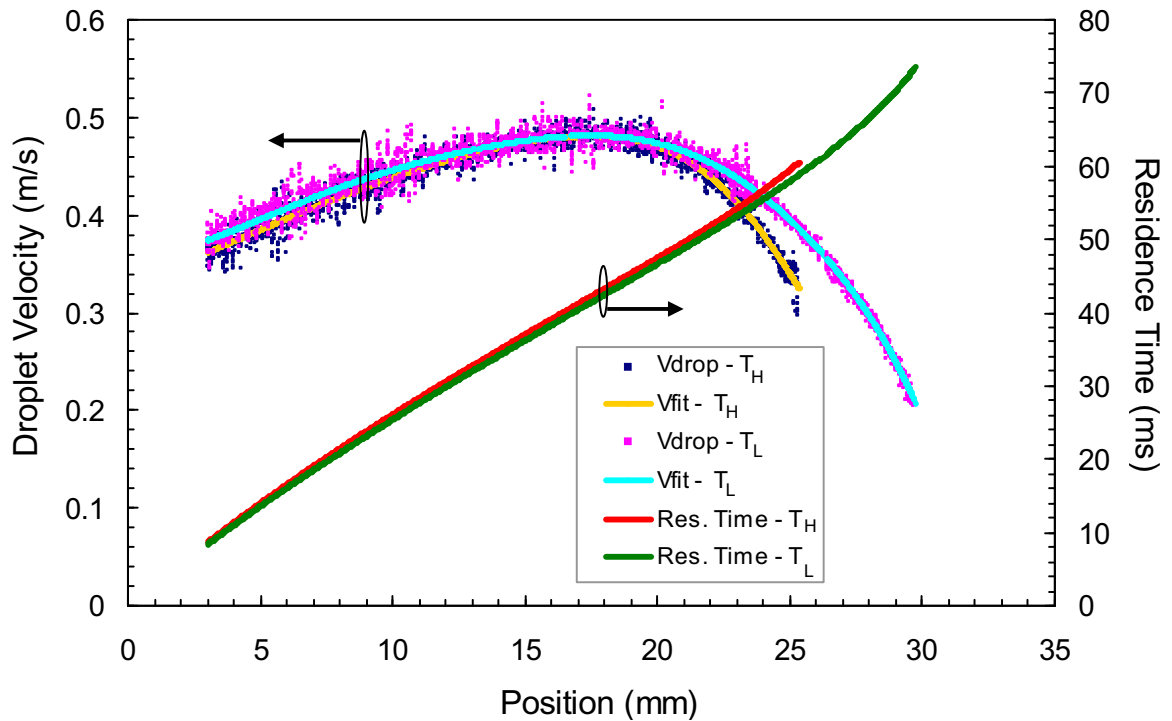


Figure 5.2: Functional fits to velocity profiles and residence time calculation for dodecane droplets for high and low temperature settings

Figure 5.3 expresses the variation of droplet diameter and squared diameter against the residence time. The plots of squared-diameter change against residence time (scale shown to the right with the unit converted to mm^2) help to better indicate when the evaporation starts. In this figure, SE_L and SE_H stand for start of evaporation for low and high temperature settings accordingly. For the T_H , the evaporation starts earlier at about 26.5 ms compared

with 31 ms for the T_L and these are even before the points the gas temperatures exceed the boiling temperature.

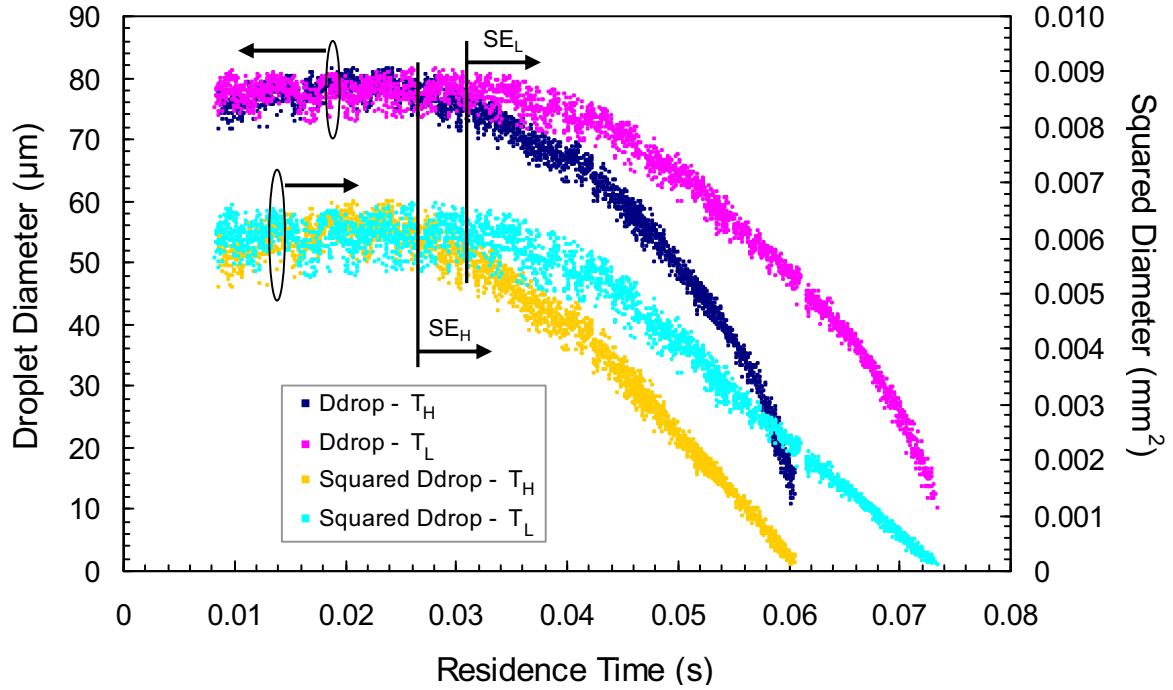


Figure 5.3: Dodecane droplet diameter and squared diameter against residence time for both temperature settings

In a majority of the studies of a single droplet undergoing evaporation in constant temperature environments, the initial preheating period is soon followed by the evaporation process during which the squared diameter of the droplet scales linearly with the residence time. It can be seen in Figure 5.3 that after the initial period of obvious preheating effect, the later period from SE_H to about 39 ms for the T_H and from SE_L to about 43 ms for the T_L is nonlinear indicating the evidence of unsteadiness [71]. It is necessary at this point to clarify some effects which may contribute to this behavior. These effects come from both the gas side and liquid side. On the gas side, possible factors include the changes in composition due to the mixing between the carrier gas and combustion gas, the variation in the gas properties, and most likely the gas temperature which clearly shows a continual increase for this period. On the liquid side, there are two competing effects including the expansion of the droplet as mentioned earlier and the evaporation. The expansion is a consequence of the increase in

droplet temperature or the preheating which lowers the liquid density. This effect is supposed to last until the droplet attains a uniform and constant temperature.

According to Hubbard et al [48], except for the preheating effect other effects of unsteadiness are negligible for an evaporation process in an infinite stagnant environment. In present work, even though the conditions are different, the unsteadiness observed is perhaps also due mostly to the preheating effect which prolongs under these low and increasing heating loads. During this period, the droplet still absorbs heat leaving only a fraction for evaporation; this evaporation effect is however supposed to become stronger whereas the expansion effect is supposed to become weaker. If the gas temperature was constant here, the unsteady period would have been much shorter. After this period, the relationship appears linear until the end; the droplet would have attained a uniform and near steady (near constant) temperature. The heat transferred to the droplet in the final period should be mainly for vaporizing it. This behavior is also an indication of the limited effect of convection on the gas side in this period which will be illucidated in the next chapter.

As the evaporation rate coefficient is defined as the negative of the gradient of D^2-t curve, $K_v = -d(D^2)/dt$ [36], a linear line fit for the D^2-t data for a certain evaporation period would yield the average rate for that period. To check if the process becomes steady and to find the start point of steadiness, a rolling rate approach is used by rolling linear line fits to D^2-t data with the pivot point of rolling being the end point, starting from about a measurement zone away from this point until the SE point. Results of such operations for two temperature settings are shown in Figure 5.4 in which the unit of this rate is mm^2/s . The process is found to become steady at about 40 ms and 42 ms for the T_H and T_L conditions as after this point the rate is almost constant which is about 0.218 and 0.172 mm^2/s for two settings, respectively. Note that this approach is done only to find the start point of steadiness and steady rate if this period exists under these conditions. Figure 5.4 also includes the line fit for the whole evaporation process as an illustration which yields a higher average rate K_v of 0.179 mm^2/s for the T_H compared to a rate of 0.152 mm^2/s for the T_L . There is still evidence of K_v variation over the steady period which is however very small and, if ignoring the measurement uncertainty, is due to variations on the gas side.

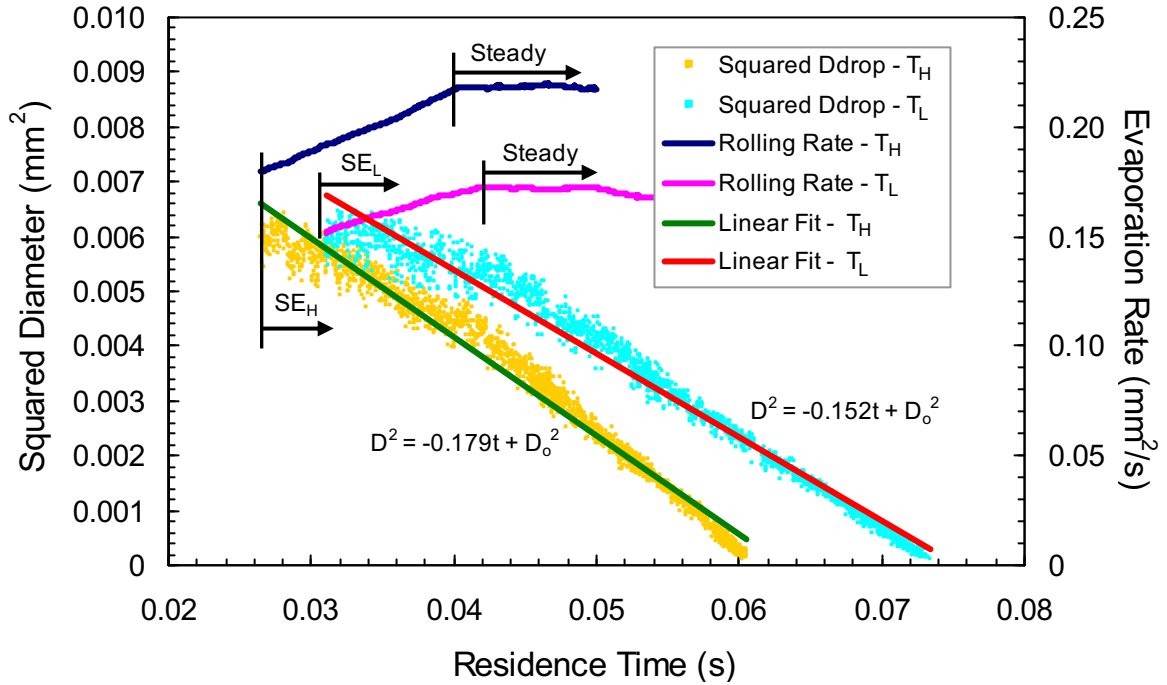


Figure 5.4: Linear fits for dodecane evaporation data for two temperature settings for the whole evaporation process. Average and rolling evaporation rates are also shown for two settings which are found by rolling linear line fits with pivot point being the end point starting from about a measurement zone away from this point until the SE point

Certainly it is difficult to separate the effects of different parameters, more understanding of the process can be obtained by plotting the average rate in smaller intervals against the gas temperature. Figure 5.5 shows the averaged rates of consecutive measurement blocks (see section 4.4.1 for these blocks) for two temperature settings. It can be inferred from this figure that the gas temperature is not the only factor that influences the droplet behavior. In the initial period of evaporation of the two temperature settings, at the same gas temperature T_H shows a higher evaporation rate which is further evidence of the consequence of the preheating effect. Another possibility here is the difference in droplet Reynolds number which depends on droplet diameter and velocity relative to the surrounding gas. Given slight differences in droplet diameters and their absolute velocities for two temperature settings (compared at the same gas temperature, e.g. at 480 K, diameters are about 76 and 78 μm and velocities about 0.45 and 0.47 m/s for T_H and T_L) the relative velocities, though not known, are expected to be similar.

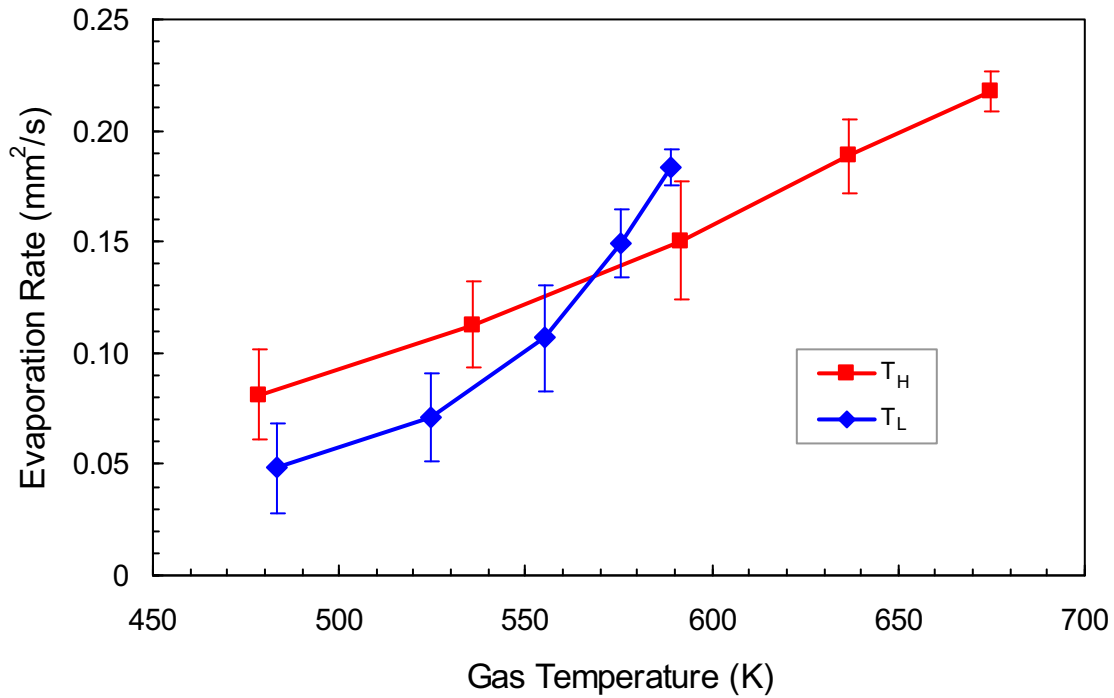


Figure 5.5: Average rates of dodecane of consecutive data blocks for both temperature settings

While the earlier part can be largely affected by the preheating effect, the later part of the process further away from the preheating phase is supposed less influenced by this effect. The differences in diameters and velocities however become larger for this later part. For example at nearly 590 K (the maximum temperature of the T_L) the diameters are nearly 68 and 59 μm while velocities are 0.48 and 0.43 m/s for T_H and T_L . T_H should therefore be in favor of a higher evaporation rate at this stage as larger droplets with higher velocity (from the momentum law the relative velocity should also be higher) would evaporate more quickly due to stronger interaction between droplet and the external flow [45, 53]. However, Figure 5.5 indicates that the evaporation rate for T_L becomes higher than for T_H which shows little or no effect of Reynolds number under this condition but rather the stronger influence of other factors. These factors includes possibly the effect of the gas properties which affect the heat and mass transfers on the droplet surface and most likely the droplet temperature as at this stage while the process for T_L is steady state, that for T_H is still slightly influenced by the unsteady phase even though the droplet temperatures should be more

stable and reach closer to the maximum values. This verifies the fact that the preheating effect can even dominate the whole vaporisation process in some situations [71]. The overall effect of gas temperature is seen in both temperature settings to increase K_v .

In the same manner with dodecane, Figure 5.6 shows the variation of decane droplet diameter against x -position for T_H and T_L . For these data sets, the initial diameters are 74 and 45.5 μm for T_H and T_L respectively with velocity and temperature profiles being also included. For the T_H , the SE of the 74 μm decane droplet starts at about 9.4 mm (22 ms) compared with 10.2 mm (26.5 ms) of the 75 μm dodecane droplet shown earlier. This is as expected due to the lower boiling point of decane given almost the same initial sizes. Although direct comparison between these two data sets for decane is not possible as was done earlier for dodecane, observations can still be made. While the SE of the larger droplet for T_H occurs at gas temperature of about 435 K, the SE of the smaller droplet for T_L occurs much earlier at about 377 K (8.5 mm or 20 ms). This is because less sensible heat is required for the smaller droplet (lower thermal inertia) and more heat portion is therefore left for evaporation. Another reason for the above observation is that the larger droplet has stronger expansion effect than the smaller droplet as it has a volume about 4.3 times larger.

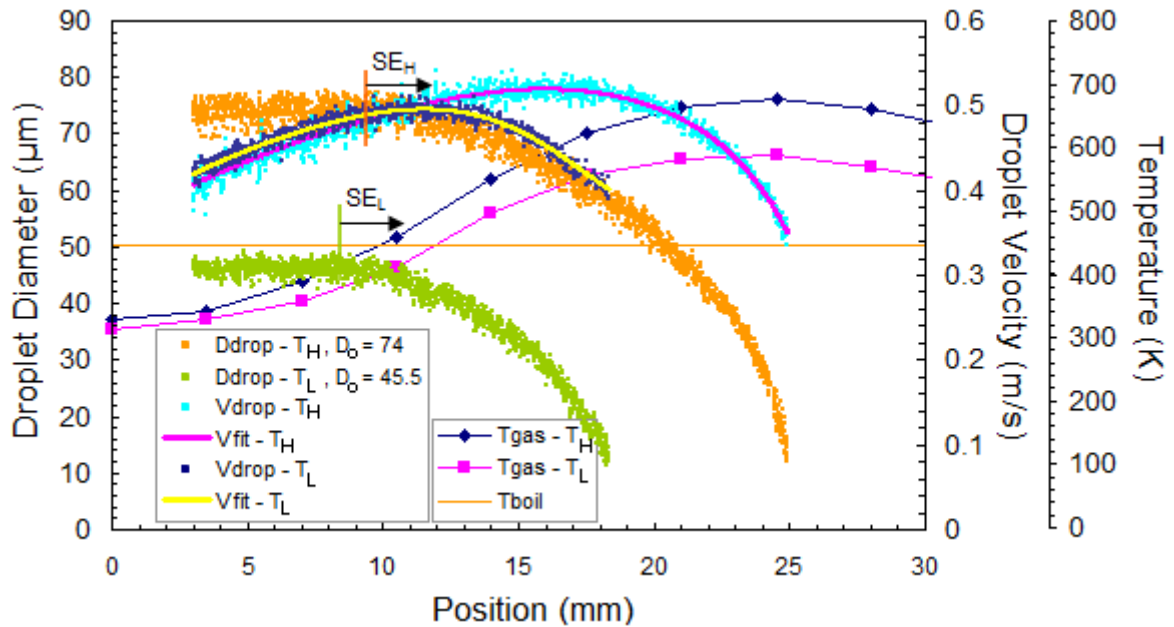


Figure 5.6: Diameter and velocity of decane droplets against position. Initial diameters are 74 μm and 45.5 μm for T_H and T_L , respectively. Gas temperature profiles are also included

From the velocity profiles, larger droplet is seen to have a slightly lower speed after the injector tube exit as it experiences larger drag while flowing through this tube. However, under the influence of the gas flow mixing and thermal expansion initially in the reactor, larger droplet gains more momentum and accelerates to a higher peak velocity than smaller droplet even though this process takes longer. For both cases, droplets start to slow down once passed the mixing zone as their size gets smaller. Though slightly different between two cases, for current settings the velocity should play a very limited role on the droplet behavior as discussed earlier.

To find the steady evaporation rate and steady start point for these decane droplets, a rolling fit approach is applied with the results shown in Figure 5.7. It has to be mentioned here that the operation is done starting from a measurement zone away from the end point as more localized measurement is deemed inappropriate as explained later in section 5.4.2. While a steady period is found for the larger droplet for the T_H , this period does not exist for the smaller droplet for the T_L as the droplet completely evaporates before it can reach a steady point (this should be specific to the temperature condition used). Larger decane droplets reach a steady state at about 40 ms and the steady evaporation rate is $0.222 \text{ mm}^2/\text{s}$ compared with $0.218 \text{ mm}^2/\text{s}$ of dodecane reported earlier at the same temperature setting. Again, the average rates for the whole evaporation process of the larger and smaller droplets are, in turn, 0.172 and $0.1 \text{ mm}^2/\text{s}$.

Even though no data is obtained for the larger decane droplet for T_L to make a more detailed comparison, the behavior of the smaller droplet can be more understood by plotting its evaporation rates averaged in consecutive data blocks against the gas temperature and comparing to that of the larger droplet as done in Figure 5.8. Although the smaller droplet completes its life at a lower evaporation rate and lower temperature, at the same gas temperature it has a slightly higher rate than the larger droplet. Again this is understood to be due to higher thermal acceleration of the smaller droplet which should attain higher and more uniformed temperatures and there being more energy available for evaporation as mentioned. However, this difference would not be present if they are both evaporating steadily at the same gas temperature.

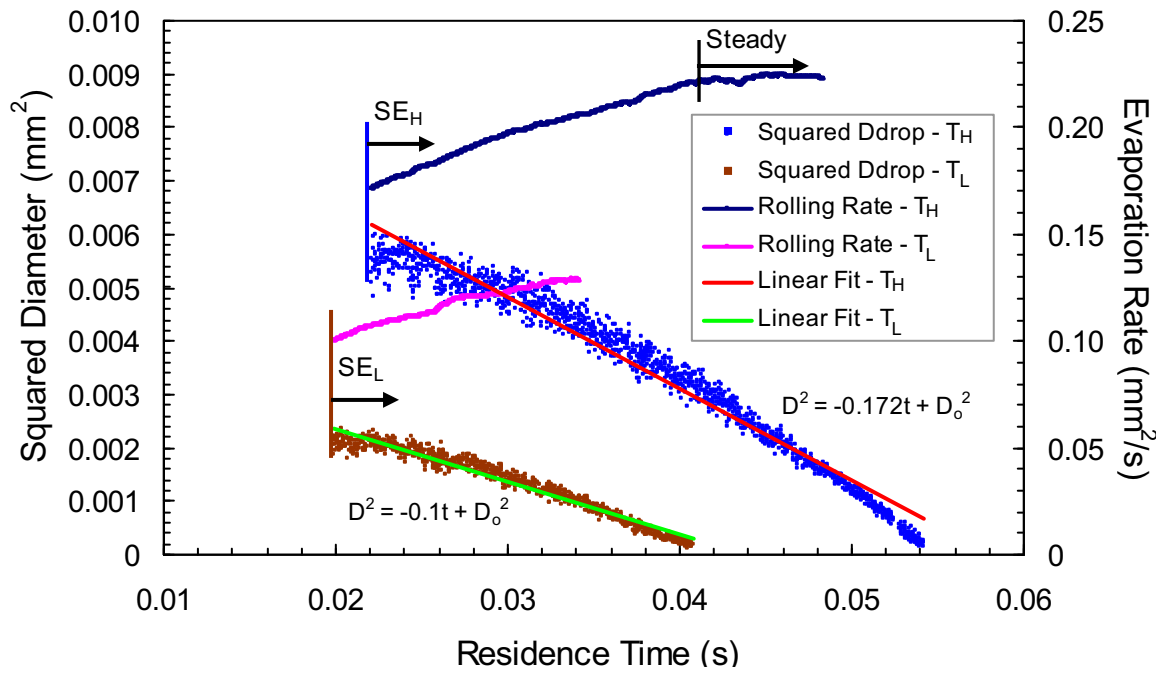


Figure 5.7: Linear fits for decane data for two temperature settings for the whole evaporation process. Average and rolling evaporation rates are also shown which are found by rolling linear line fits with pivot point being the end point starting from a measurement zone away until the SE

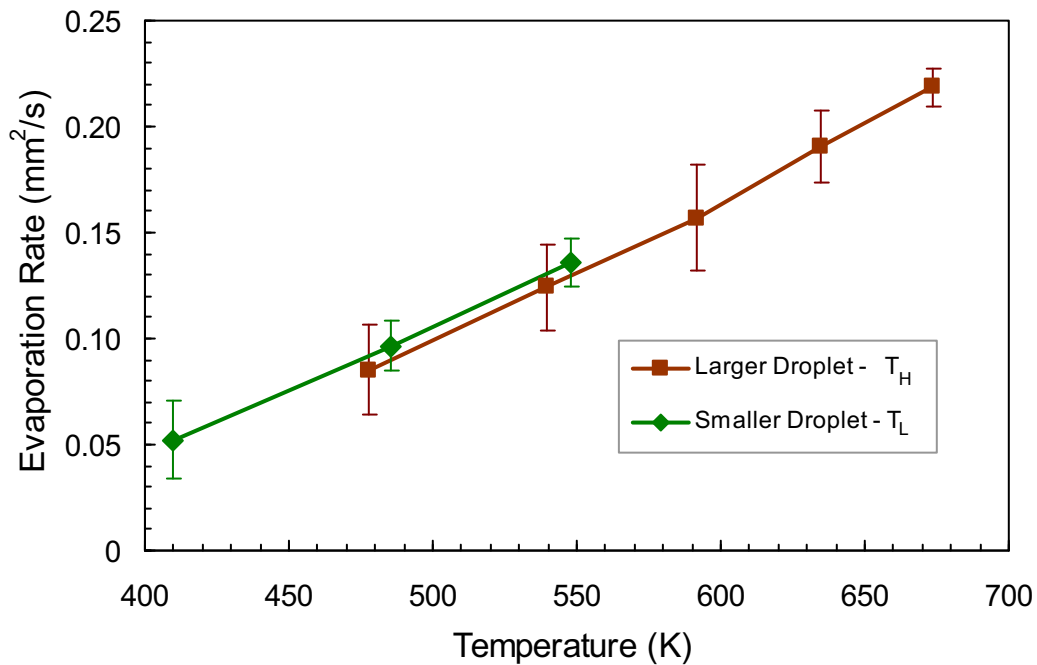


Figure 5.8: Average evaporation rates of decane droplets in consecutive data blocks for two temperature settings

As mentioned, diesel as a standard and multicomponent fuel is also used to study the behavior of droplets of these sizes. For comparison, decane and dodecane droplets for T_H shown earlier are compared with diesel droplet at the same temperature setting in Figure 5.9 in which their sizes are almost the same (diesel 76 μm , dodecane 75 μm and decane 74 μm). The boiling points of these fuels together with gas temperature are also indicated for better analysis. Marks and arrows with the same color as the data points indicate the SE of each fuel. The SEs of diesel, decane and dodecane occur at 9.8, 9.4 and 10.2 mm respectively.

Except for slightly stronger expansion for dodecane than decane, the histories of these two fuels are seen to be close to each other which suggest rather similar evaporation rates for the whole duration (the relative difference in volumes is only about 4%). The observed stronger expansion due to initial preheating for dodecane than decane is to some extent similar to that found in Kristyadi et al [60] although it is not possible to make a direct comparison regarding the timing and level of expansion due to a number of conditional differences such as Kristyadi's much higher initial velocities at 6 m/s, spatially constant temperatures of nearly 650 K and bigger droplet sizes of 99-135 μm . Furthermore these authors used an inter-distance of 6 times the diameter while it is at least 30 times in this work; the shorter distance is known to mitigate the preheating effect [105]. Stronger expansion of dodecane is also supported by the combustion data in [31] for heavy paraffin in which the heating period is also found to be longer for higher molecular weight fuels.

Although having a much higher indicated boiling point than dodecane, diesel starts to evaporate early at about 27.6 ms (while dodecane occurs at 26.5 ms) which is when the gas temperature is still very well below its indicated boiling point. The expansion of the diesel droplet is seen to be even less than dodecane (again the relative difference of about 4% by volume is very small). These are not unexpected because the diesel used consists of components with boiling points ranging from 433-644 K and this early evaporation, which lessens the expansion, should be due to those components at the lower temperature end. However it takes longer at 67.9 ms for diesel to evaporate to a diameter of 10 μm compared to about 60.6 ms of dodecane.

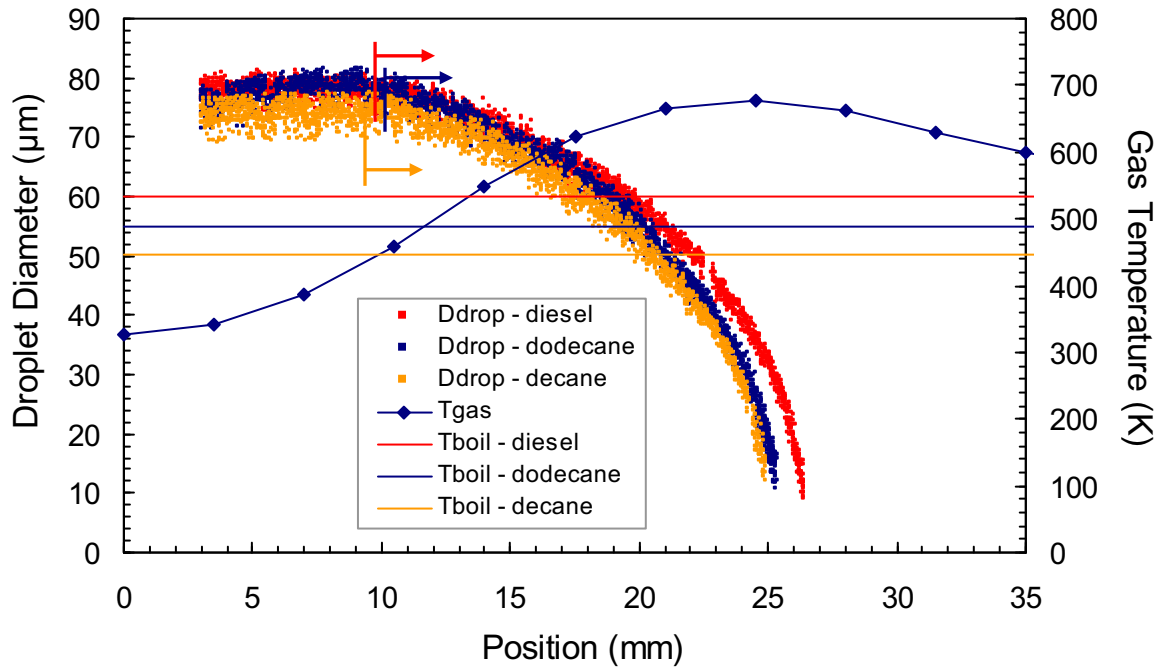


Figure 5.9: Comparison of diesel droplets of 76 μm , dodecane droplets of 75 μm and decane droplets of 74 μm at high temperature setting. Gas temperature and boiling points of these fuels are also shown

For more detailed analysis of the diesel data, Figure 5.10 expresses the squared diameter against the residence time for the whole evaporation period. The slower evaporation of diesel is represented by a linear fit which yields an average K_v of 0.155 mm^2/s compared with a higher K_v of 0.179 mm^2/s of dodecane or 0.172 mm^2/s of decane. By rolling linear fits as done for dodecane and decane, diesel is also found to start unsteadily as expected and noticeably it reaches a near steady period at about 50 ms with a rate of 0.192 mm^2/s even though there is still some variation over this late period. At this stage, it appears to show no sign of multicomponent effect but rather a behavior close to the diffusion-limited extreme [40, 74] which is represented by a constant evaporation rate. This is evidence of the very low Reynolds number which plays almost no effect on the droplet internal behavior.

The opposite extreme is the infinite mixing mode which exhibits for a multicomponent fuel a preferential vaporisation behavior causing the evaporation rate to reduce during the droplet lifetime [149] as the lighter fractions (continually transported outwards) evaporate earlier leaving the heavier to evaporate later and slower; such behavior can be found in for

example Elkotb et al [30] at higher Reynolds numbers. However for this condition, internal mixing (if existing) should have very little effect on the evaporation of this complex mix of a large number of hydrocarbons [2]. The data obtained is therefore reasonable given the conditions used and there is likely no shear driven internal circulation. Initially, however, the droplet could have expressed a preferential vaporisation behavior for a short period as the initial heating rate was slow and the components were adjusted to attain a near constant concentration profile for the rest of its lifetime, a phenomenon found in for e.g. [55, 74].

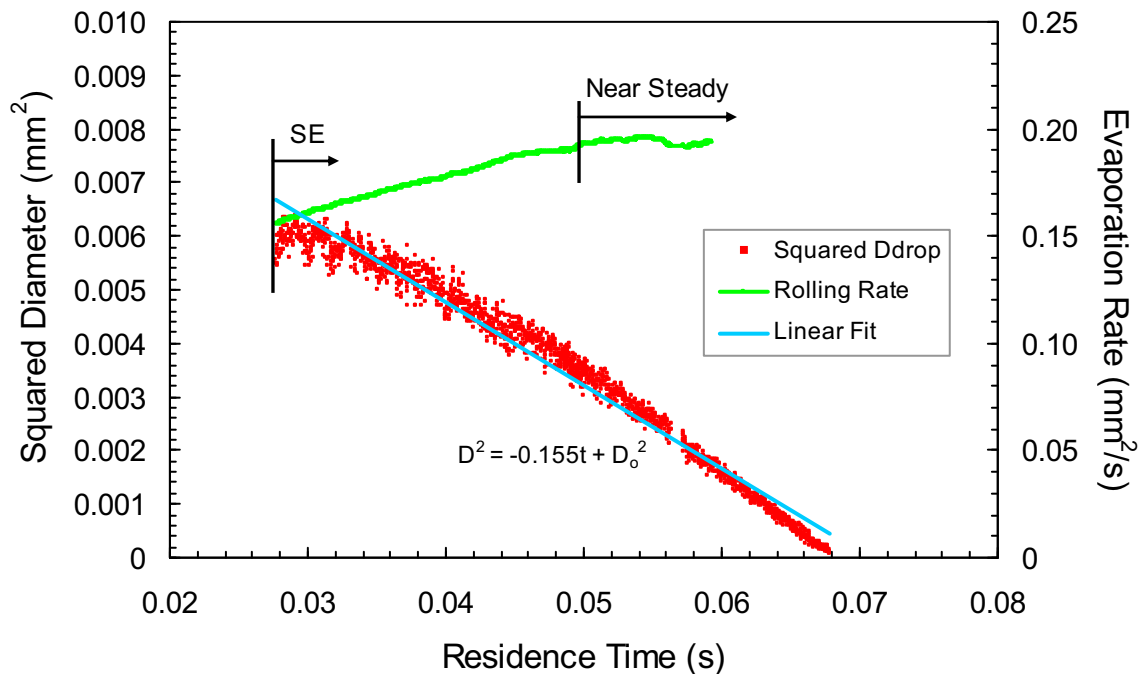


Figure 5.10: Average and rolling evaporation rates of 76 μm diesel droplets for T_H

The near steady value of K_v found above for diesel is similar to the calculations by Hallett in [40] and experimental data of Kobayashi [56] cited therein for diesel of similar density ($\approx 830 \text{ kg/m}^3$) and droplet size of about $1200 \mu\text{m}$ using the suspended droplet technique with a similar temperature range. Elkotb et al [30] has shown diesel evaporation rates to be similar to those of kerosene which is a lighter distillate fraction and this K_v value obtained here compares favorably with the kerosene value of Khan et al [53] for $900 \mu\text{m}$ droplets undergoing evaporation at a similar peak temperature. Also according to these authors, at normal ambient pressure the variation in the evaporation rate with initial diameters in the

range of 770-1700 μm is very little and, as seen here, this finding is likely to extend to sizes in the current work which means droplet initial diameter can play no significant role in low Reynolds number conditions. However for higher Reynolds number (either high relative velocity or high ambient pressure), initial diameter can be very important as the interaction between the droplet and the external flow is more considerable, particularly for larger droplets as will be shown in the next chapter.

Again, the role of ambient temperature can be verified by plotting the evaporation rates averaged in consecutive data blocks against this temperature for the whole evaporation duration for three fuels, Figure 5.11. Given the large uncertainty, the rate of decane is seen to be consistently, though very slightly, higher than dodecane for all temperatures except for the final stage with similar rates. Similar to dodecane and decane, the rate of diesel also increases with gas temperature but is always lower than that of these fuels for the whole temperature range. While some authors (e.g. [59]) treated dodecane as light diesel in their investigations, in this work the difference obtained between two fuels is not small but also not large given the indicated uncertainty in estimating these rates.

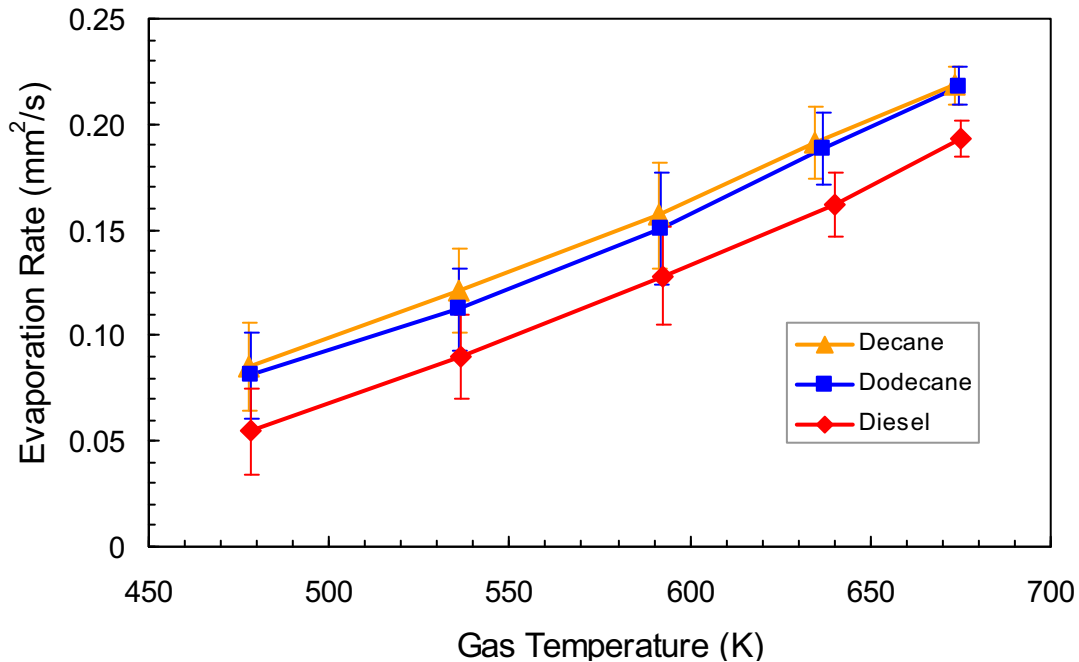


Figure 5.11: Average evaporation rates of diesel, dodecane and decane in 5 consecutive data blocks for T_H

Figure 5.12 compares the history of smaller dodecane droplets of 65 μm and that of nonane droplets of 63.5 μm for T_H . The boiling points of these fuels and gas temperature are also indicated. Whereas this small dodecane droplet also shows expansion with SE starting at about 10 mm (22 ms), nonane with the lowest boiling point of 424 K is seen to evaporate right at the beginning at 3 mm (8 ms) or even earlier when the gas temperature is still very low (about 340 K). There is no expansion for nonane which recalls the similar observation by Kristyadi et al [60] for heptane, though in different conditions mentioned earlier, as these volatile substances have very low molecular weights.

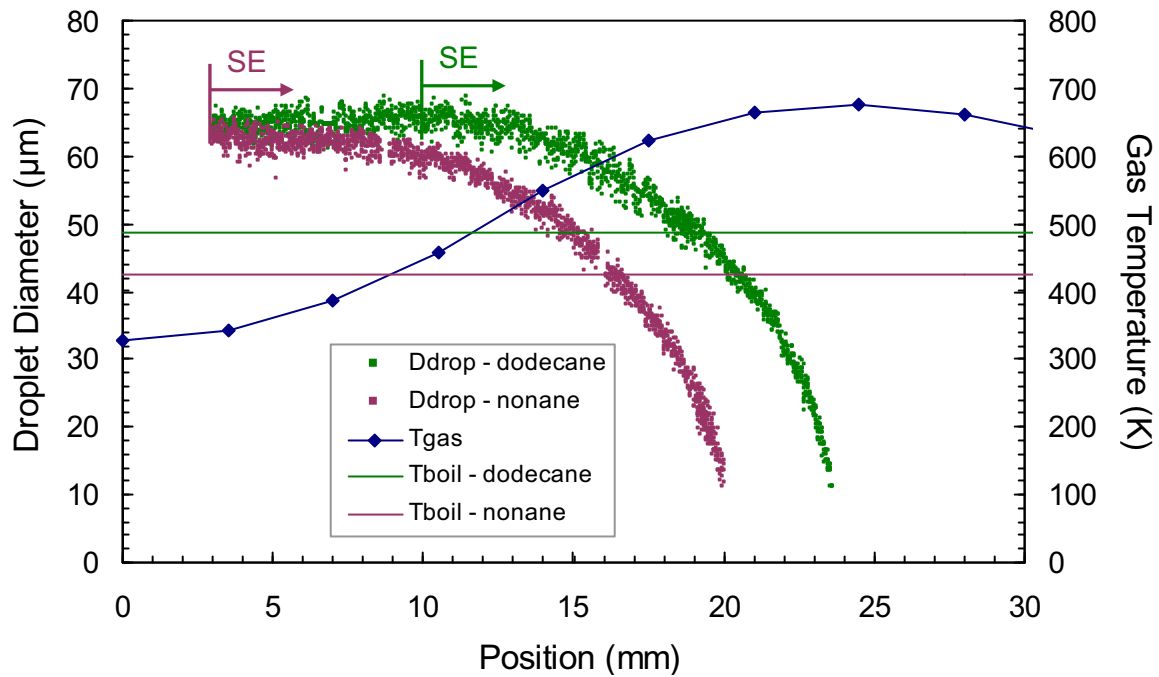


Figure 5.12: Dodecane and nonane droplet diameters, initial values of 65 and 63.5 μm , against position for T_H . Gas temperature and boiling points are also shown

Variation of squared diameter of these droplets against the residence time is shown in Figure 5.13 which also appears to be characterized by a linear relationship in the late period. However the rolling rate approach indicates that their rates have not reached a steady period (this is reasonable considering the gas temperature shown) but are close to those steady rates of dodecane and decane droplets reported earlier. In particular this dodecane droplet reaches $K_v = 0.222 \text{ mm}^2/\text{s}$ while it is $0.215 \text{ mm}^2/\text{s}$ for nonane droplet. The ends of these series are at 23.6 mm (50 ms) and 20 mm (46 ms) for dodecane and nonane respectively.

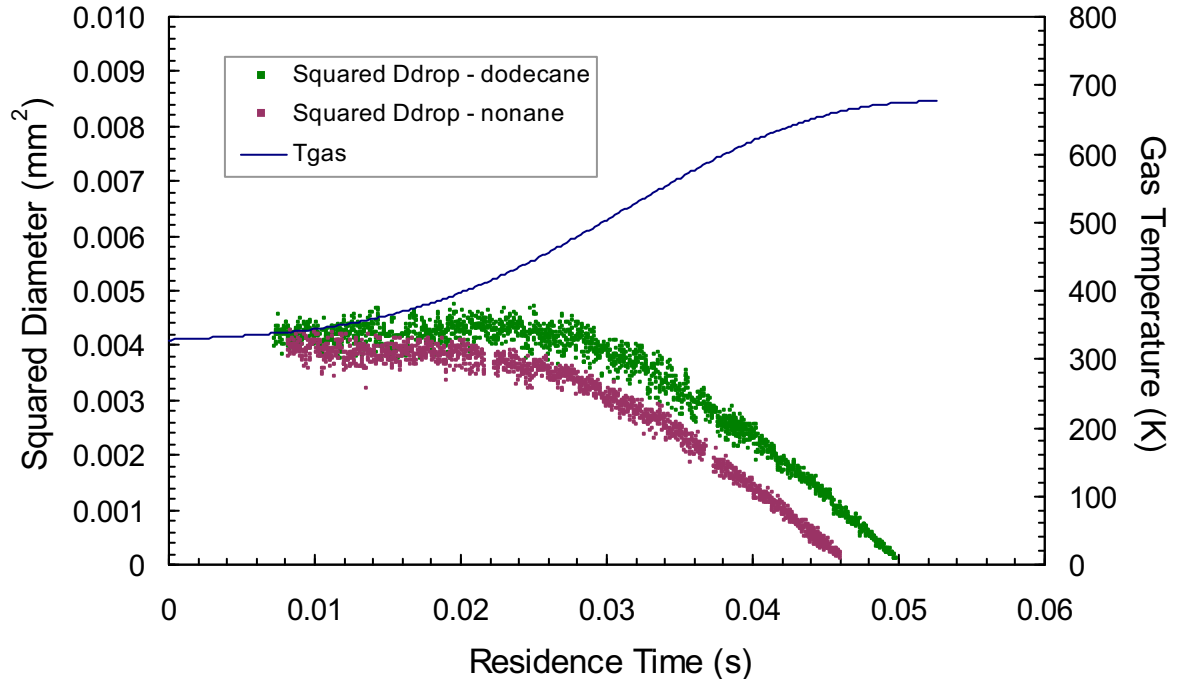


Figure 5.13: Square diameter against residence time for dodecane and nonane droplets in Figure 5.12. Gas temperature is also shown.

Similar comparison for bigger diesel droplet of 85 μm and that of nonane droplet of 84 μm for T_H is shown in Figure 5.14. From the assessment of the nonane D^2 - t curves (see Figure A.1 in Appendix A) its SE is seen to start early at 5.8 mm (15 ms), even earlier than smaller droplets of dodecane and decane reported earlier. As measured, for this size the SE of diesel occurs late at 14.7 mm (34 ms), much later than the nonane droplet and the 76 μm diesel droplet. Expansion of diesel droplets observed in this work was also seen in the data of much larger diesel droplets of Faeth and Lazar [31]. This diesel droplet evaporates to the measureable limit of 10 μm at 34.2 mm (82 ms) while it is much shorter at 26.3 mm (60 ms) for the nonane droplet. As a consequence of the early SE of nonane, its overall average rate is 0.155 mm^2/s while for diesel this is around 0.164 mm^2/s .

By applying a rolling fit approach, this diesel droplet is found to reach a near steady evaporation at 32 mm (68 ms) with the evaporation rate being also about 0.19 mm^2/s similar to the steady rate of the smaller diesel droplet (see Figure A.2 in Appendix A). This late

occurrence of the near steady period indicates the prolonged preheating for most of its lifetime and the droplet temperature only becomes uniform at a near steady value here. The similar steady K_v found for these sizes supports the argument that diameter does not affect the steady rate but the preheating period. Further comment on this particular diesel series will be given in section 6.6.5. In Figure 5.14, nonane droplet reaches steadiness at nearly 40 ms which is almost similar to that of the 74 μm decane droplet with a roughly similar K_v of about $0.22 \text{ mm}^2/\text{s}$. From the analysis of the average rates of each data block, nonane consistently has higher rates than dodecane and decane at low temperatures but once approaching a steady period for the present condition (gas temperature $> 600 \text{ K}$), their rates are nearly the same which is favored by the combustion data of Aldred and Williams for a larger range of n-Alkanes [7] and agrees with observations of Law [69] for similar temperature.

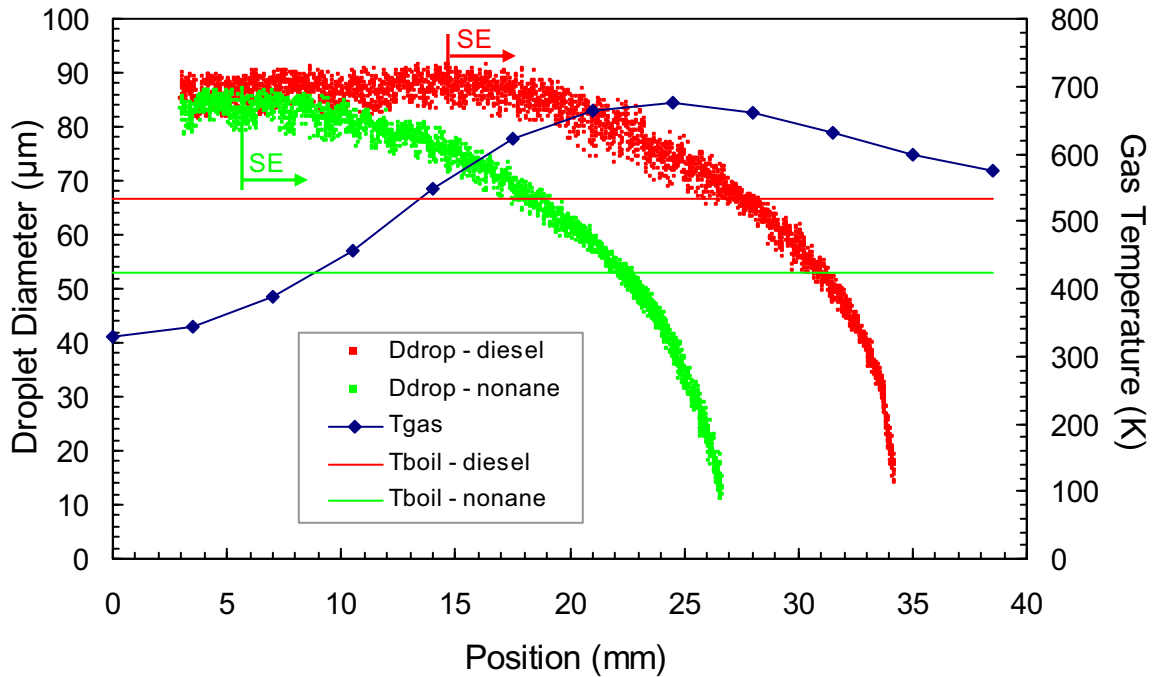


Figure 5.14: Diesel and nonane droplet diameters, initial values of 85 and 84 μm , against the position for T_H . Gas temperature and boiling points are also shown.

For summary, Table 5.4 lists the average and near steady evaporation rates found from the rolling rate approach for fuels investigated. For series that the near steady period was not found, the ending rolling rate is used. Measurement uncertainty of these rates is also shown.

Table 5.4: Summary of fuels' evaporation rates

Heating condition	Fuel	Droplet initial diameter (μm)	Average rate (mm^2/s)	Near steady rate (mm^2/s)
T_H (Peak temperature: 676 K)	Dodecane	75	0.179 ± 0.005	0.218 ± 0.009
		65	0.157 ± 0.005	$0.222^e \pm 0.009$
	Decane	74	0.172 ± 0.005	0.222 ± 0.009
		52	0.115 ± 0.005	$0.160^e \pm 0.008$
	Nonane	84	0.155 ± 0.005	0.220 ± 0.009
		63.5	0.100 ± 0.005	$0.215^e \pm 0.009$
	Diesel	85	0.164 ± 0.005	0.190 ± 0.008
		76	0.155 ± 0.005	0.192 ± 0.008
T_L (Peak temperature: 587 K)	Dodecane	76.5	0.152 ± 0.005	0.172 ± 0.008
	Decane	45.5	0.100 ± 0.005	$0.130^e \pm 0.01$

^e: ending rolling rate

5.4.2 Instantaneous measurement of the evaporation rate

To investigate more thoroughly the effects of temperature and droplet size, the instantaneous evaporation rates of diesel droplets with different sizes and temperatures were examined in different conditions. Figure 5.15a shows a separate set up used for this type of measurement while in Figure 5.15b the temperature profile is shown. In this set of measurements, the injector tube exit was positioned 10 mm lower than the burner plane and although the carrier gas enters the injection tube at room temperature, conduction of heat from the reactor gases along the tube preheats the carrier gas prior to exit from the tube. For the conditions used this preheating gives rise to an exit temperature of 430 K (much higher than that of the average setup of 325 K but still below the boiling point of the lightest component of diesel).

The droplet will undergo some preheating in this tube before entering the vessel. Mixing of the carrier gas with the burner gases yields a more steady increase in temperature up to a maximum of 650 K. For this condition, the droplet experiences higher and steadier temperatures in the vessel. The preheating effect is therefore expected to be much less with droplet temperature being more uniform enabling the evaporation to proceed steadily with the gas temperature.

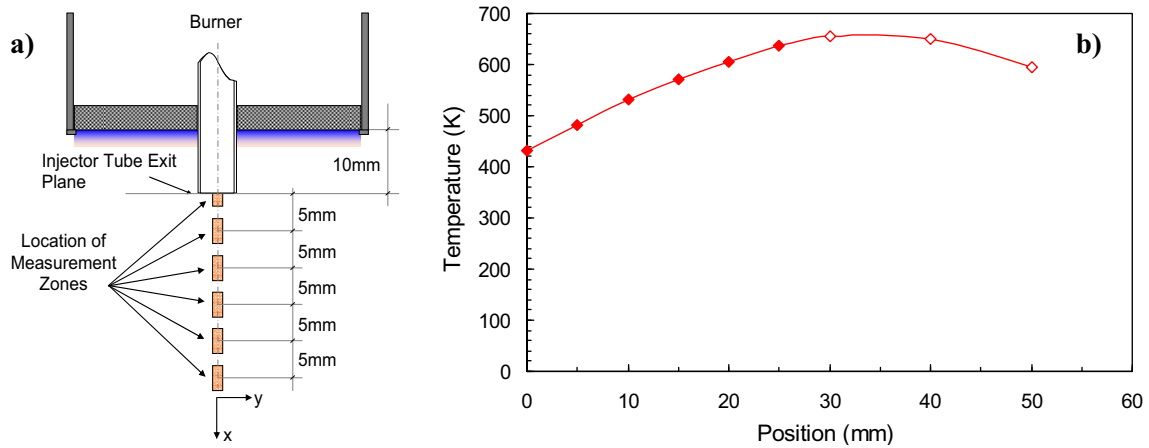


Figure 5.15: Instantaneous measurement setup: a) measurement zones; b) temperature profile along the reactor centerline measured at positions relative to the injector tube exit plane. The red diamond symbols correspond to the centre of each measurement zone

It needs to be clarified here that, though being named “instantaneous”, this type of measurement is used to estimate the average rate of each zone as shown in Figure 5.15a. Each zone represents a separate series of measurements, although undertaken at identical reactor conditions. Figure 5.16, which shows the variation of droplet squared diameter against the residence time, presents the measurements at two locations of $x = 10$ mm (5.16a) and $x = 20$ mm (5.16b) and for different initial diameters D_o . In each graph, the open and filled symbols are for each diameters D_o . For each D_o , three separate droplet trajectories are expressed by triangles, squares and diamonds. Here, droplet residence time is relative to the measurement zone by referencing this time to the first appearance of the droplet in the zone.

Despite the variation amongst the individual droplets for each condition, K_v for each condition appears to be independent of residence time and as such is represented by an

average K_v determined from a linear fit to the data. The equation corresponding to each droplet is also shown in Figure 5.16. The effect of different reactor temperatures on K_v is also evident. At $x = 10$ mm where the average zone temperature is 530 K, the average values of K_v for the droplets with $D_o = 64$ μm and $D_o = 50$ μm are 0.07 and 0.088 mm^2/s respectively, while at $x = 20$ mm and $T = 600$ K, $K_v = 0.161$ and 0.162 mm^2/s respectively for droplets with $D_o = 58$ μm and $D_o = 46$ μm . Although some difference is noted for the 10 mm location, this is apparently due to the slight effect of preheating at positions close to the entrance as also found for locations $x = 0$ mm and $x = 5$ mm (the results for all the measurement locations are shown in Figures A.3 - A.8 in Appendix A). Initial diameter plays almost no effect on K_v which is again in agreement with the kerosene data of Khan et al [53] and the finding from previous section.

It is noticed that with their size range (Khan et al [53]) and at high temperature of 1073 K the dependence on droplet diameter was found to increase (evaporation rates nearly doubling with diameter). At higher pressures (up to 1 MPa) the dependence is even greater. This is because at higher temperature, the natural buoyancy due to droplet evaporation is higher and at higher pressures the buoyancy is much stronger [72, 89]. The effect of initial diameter, as mentioned, is manifested in the interaction with external gas flow which depends also on the droplet relative velocity and shape (the droplet can even be distorted by the effect of drags) [30]. In view of the above, the negligible effect of initial size seen here can be due to small differences between sizes available for study and weak interaction with the ambient gas due to low relative velocity, low ambient temperature and low pressure used.

Attempts have also been made to investigate the truly instantaneous evaporation rate the variation of which is presented in Figure 5.17 as an example by the probability distribution of these rates in the above measurement zones: at $x = 10$ mm for 64 μm droplets in Figure 5.17a and at $x = 20$ mm for 46 μm droplets in Figure 5.17b. It is seen that the variation for $x = 20$ mm is less than for $x = 10$ mm which is similar to the uncertainty analysis shown in Figure 4.10. Though the means of these distributions are close to the average rates found in respective zones in Figure 5.16, the large distribution standard deviation (0.79 mm^2/s at $x=10$ mm and 0.49 mm^2/s at $x=20$ mm) renders this rate being not proper for more localized

analysis which also explains the reason for the rolling rate operation to start from a measurement zone away from the pivot point (the end point of the series).

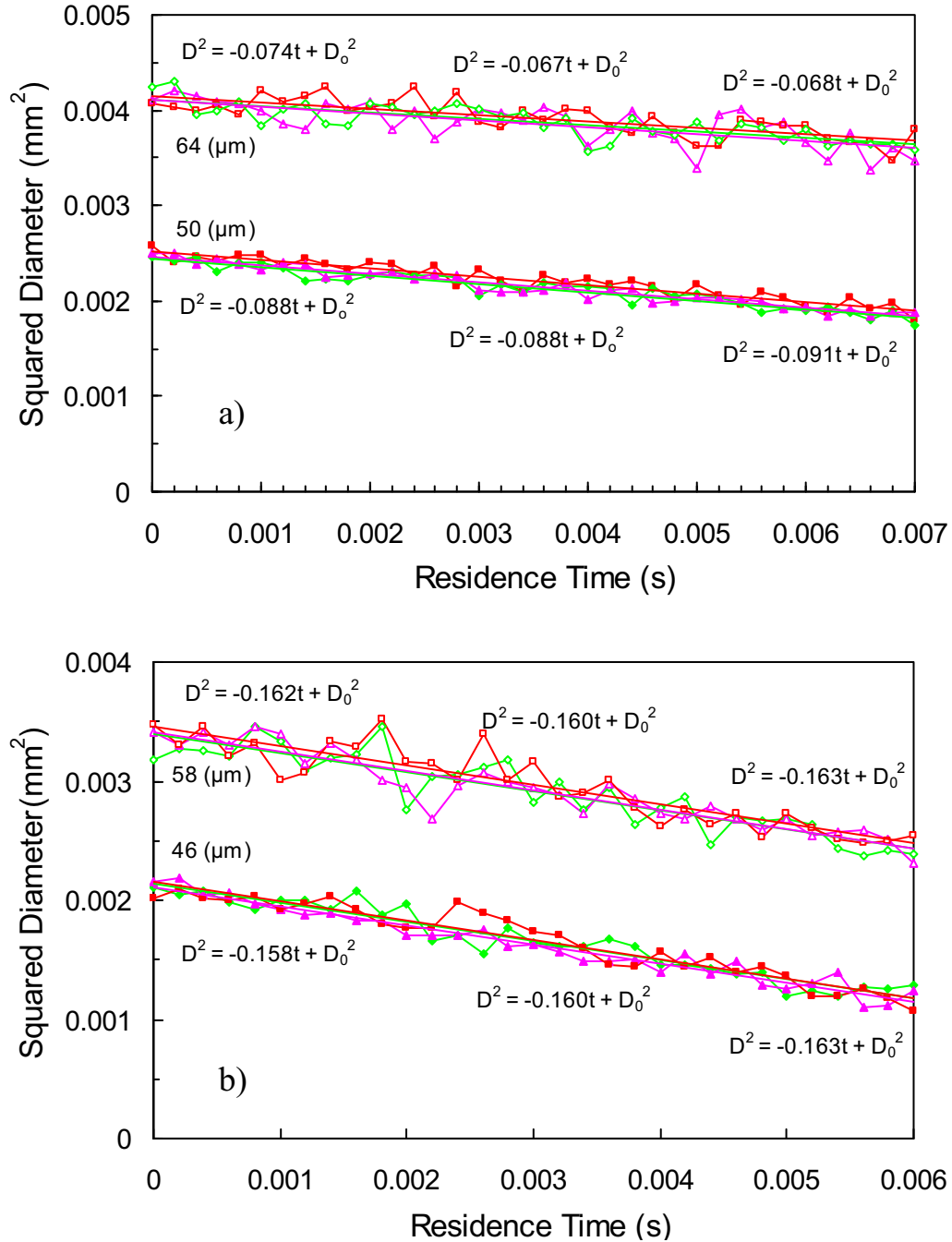


Figure 5.16: Droplet size histories at two different measurement locations and for different initial droplet diameters: a) $x = 10$ mm ($T = 530$ K), $D_o = 64$ μm and 50 μm ; b) $x = 20$ mm ($T = 600$ K), $D_o = 58$ μm and 46 μm . Equations shown are lines of best fit for three individual measurements each of which has a separate symbol.

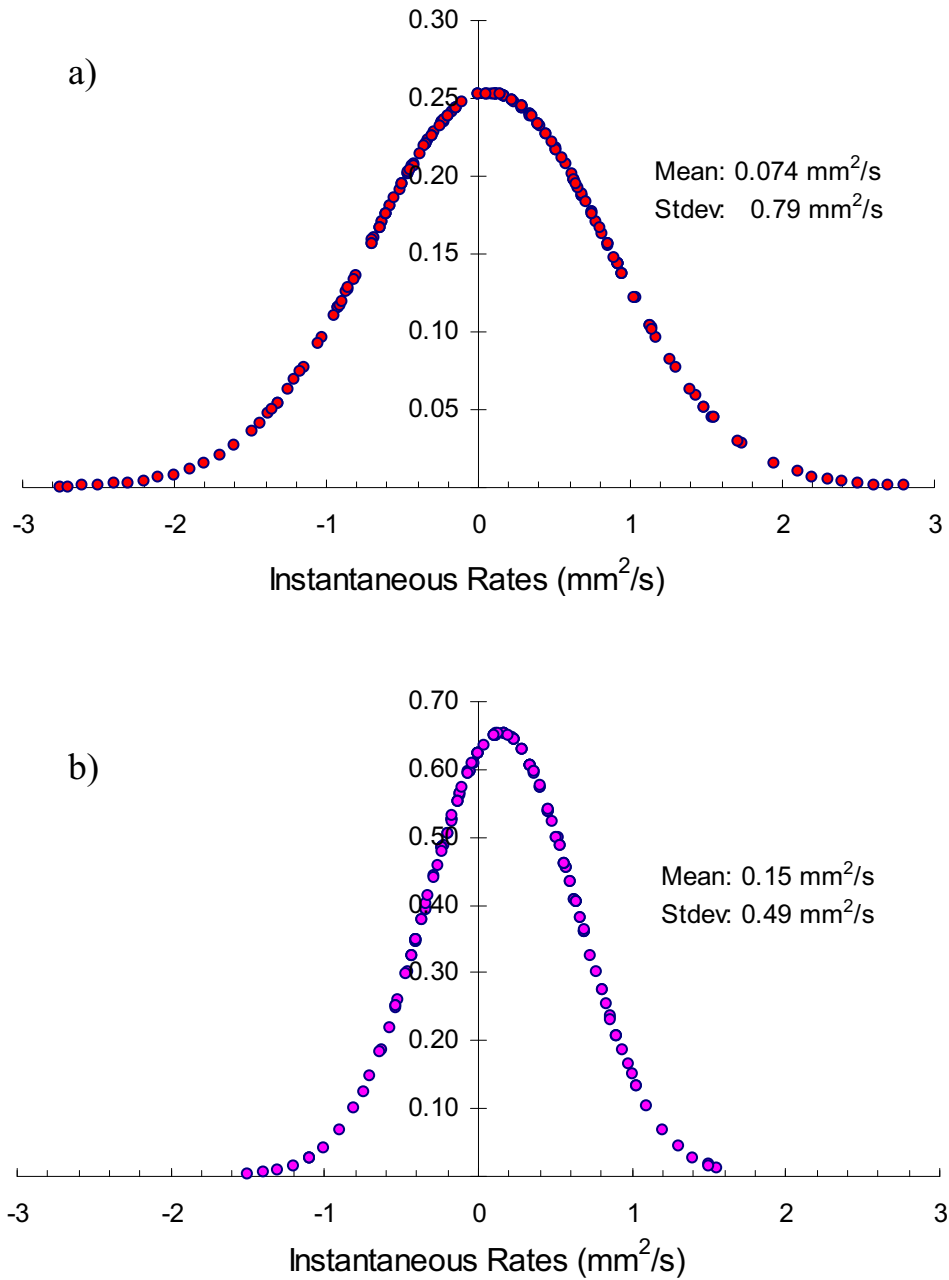


Figure 5.17: Normal probability distribution of instantaneous rate a) in the measurement zone at $x = 10$ mm and b) in the measurement zone at $x = 20$ mm

Although already evident from the data in Figure 5.16, the effect of temperature on K_v in this type of measurement is shown in Figure 5.18 for all the locations of Figure 5.15. For these conditions it is also evident that evaporation rates depend strongly on temperature with size and compositional changes playing almost no roles. The rate in this type of

measurement is initially higher than that in the average measurement at the same gas temperature which demonstrates the effect of preheat prior to the vessel entrance.

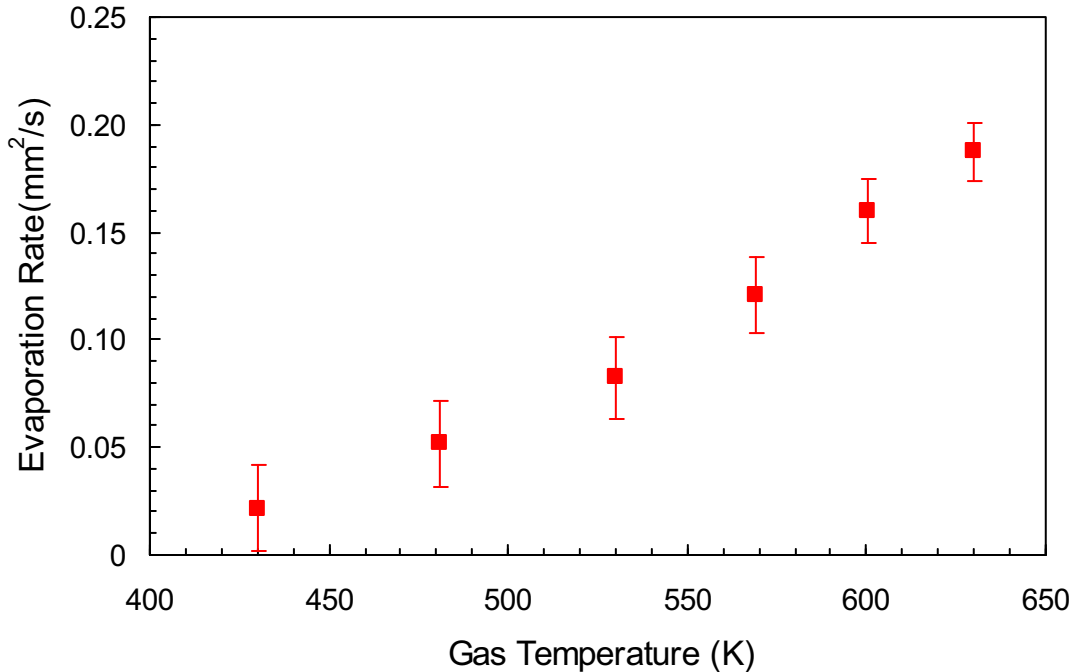


Figure 5.18: “Instantaneous” K_v of diesel droplets plotted against the gas temperature for six measurement locations in Figure 5.15

5.5 Summary of main findings

From the current experimental investigation of the behavior of dodecane, decane, nonane and diesel droplets it was found that while the gas temperature has very strong influence on the evaporation rate, the droplet size influences the preheating stage. The smaller the droplet is, the faster the initial preheating is. However for the low convections used, the droplet size has almost no effect on the steady evaporation rate. While nonane does not show any sign of expansion, this effect was seen to be stronger for dodecane than decane. Diesel shows similar level of expansion to decane as it evaporates early due to light components in this fuel. Amongst alkanes, while the lighter fuel evaporates faster at low temperatures, the rates of these fuels become similar around the peak gas temperature used. Diesel shows the lowest evaporation rate at all gas temperatures and very little sign of multicomponent effect.

Chapter 6

Droplet Evaporation Modeling

6.1 Introduction

As reviewed earlier, there have been a considerable number of theoretical investigations ranging from simple to complex, and specific to situation a model is formulated. In this work, the aim is to formulate a simple and fast droplet model and to assess its capability and efficiency. Though aiming for simplicity, the accuracy depends on the assumptions used which need to be properly justified. With this model, some parameters which cannot be obtained from laboratory measurements can be determined qualitatively thus enabling more analysis of the evaporation process of these droplets in the present situation. To enable a more detailed investigation of the liquid phase, extra effort is applied taking into account some important effects such as the spatial variation of droplet internal temperature. Further knowledge of droplet behavior can be obtained by extending the application of the models to other conditions. As diesel presents a behavior rather similar to those of single alkanes, attempt to simulate this fuel using the simple model has also been made. This chapter will start with the justification of those assumptions which is then followed by the mathematical developments of the simple model. It is then applied to fuels used in this work and compared with experimental data. Discussion of the effects of initial diameter, gas temperature and chemistry on the process will be given.

6.2 Model Formulation

6.2.1 Justification of Assumptions

For pure evaporation, the problem is much simpler than the combustion case. The present formulation is similar to that in [59] but with some differences. A noticeable difference that can be seen in this setup compared with many other studies is the variation of surrounding gas temperature along the droplet trajectory rather than being constant. The typical behavior of an initial transient period followed by a steady state period may or may not be attained.

One of the very first matters usually faced when dealing with a particular droplet evaporation process is the decision to treat it as 1D or 2D problem. 2D problems are usually considered when detailed droplet transport is necessary which is often coupled with considerable gas convection. It has even been stated elsewhere that detailed internal transport, while essential for multicomponent fuels, is not important in describing the preheating and the evaporation of a single liquid droplet. Furthermore with droplet Reynolds number lower than unity, the need for a 2D model reduces even further [99, 100]. For these reasons the model developed here is 1D.

On the gas side, the problem is treated based on assumptions of quasi steady evaporation in an unbounded stagnant environment. The quasi steady gas phase assumption is based on the fact that the heat and mass transfer in this phase is much faster than the diffusion process within the droplet and so the droplet surface state is regarded as being frozen during the gas phase transport time [68, 69]. To account for the convection in this system, even though small here, film theory is used like many other studies (e.g. [4, 59]). A factor that needs to be considered in monodisperse systems such as the one used here is the effect of droplet interaction [35]. Examples of the calculation made by Sangiovanni and Labowsky [105] have shown that inter-distances as close as around 15 times the diameter should make the process different from an isolated case. In this work, as the droplet inter-distances are more than 30 times the diameter, this effect is negligible.

On the liquid side, an infinite conductivity model will first be used for this work. This can be justified based on the low ambient temperature conditions used [5]. This assumption is furthermore supported by the fact that the use of a conduction limit model and the more detailed vortex model yielded close results for droplet lifetime to the infinite conductivity model, examples of this can be found in the work of [5] for hexane, decane and hexadecane. The use of this model will eliminate the need to solve the differential equations in the liquid phase, making the calculations simpler and faster. In this system, the heat transferred to the droplet will be mainly thermal conduction from the hot surrounding gas while thermal radiation is deemed negligible as wall temperatures (the radiant heat source) measured a maximum of 600 K during experiments at the highest temperature setting [3]. Although the droplet absorbs heat from the surrounding gas, this amount of heat is negligible compared to the whole environment and so the gas temperature is treated as being not affected.

In hot environments, the droplet evaporation problem could easily be solved by assuming that the droplet is at its boiling point and no preheat is needed [131]. However in reality and particularly in this system when considering such temperature conditions the droplet temperature, starting from cold, is an unknown and is expected to be always below the boiling point of the investigated liquid during the whole process. Preheating is essentially the first step to bring the droplet up to a state where strong evaporation can happen. As the rates of preheating and conforming to the gas flow have been shown to strongly affect the droplet behavior [76], the inclusion of this effect as evidenced in the experimental data is very important. The problem must therefore be solved by analyzing the phase change process on the droplet surface. With the assumption that the gas phase heat and mass transfers are the rate limiting processes (the phase transition is much faster), the fuel vapor at the droplet surface is saturated and thus the relationship between the vapor pressure and droplet temperature can be expressed by the Clausius-Clapeyron equation. The droplet temperature calculated in this model is supposed to be not affected by the assumptions used on the gas phase but rather on the liquid phase [109].

Perhaps, the most significant assumptions that will be used for this model are the approximation of the surrounding gases by the air with its thermophysical properties being

spatially constant but varying with time and the unique binary diffusivity represented by one for the pair of air - fuel vapor. The assumption of using air properties for calculation is based on an analysis of the exhaust gas at the exit of the reactor which has shown that the average molecular weight (MW) is nearly 27 and on the deduction that during the process the ambient compositional change is not significant (at the beginning the droplet is surrounded by N_2 and later by a gradual mix between the post burner gases and this gas, given the MW of N_2 to be also close to that of the air). Assumption of using a unique binary diffusivity is based on the fact that the species can be classified into two distinctive groups of molecular weights [68], one is the vapor of the Alkanes with very high MW of 128-170 compared to the other being the rest of the gases with typical variation of MW between 18-46 which is approximated by the air. These assumptions have been used very often in the literature as they offer a much simpler formulation without greatly compromising simulation accuracy.

Given the above assumption of gas properties, in solving the energy equation in the gas phase the Lewis number, which is the ratio of thermal diffusivity and mass diffusivity, is also assumed to be spatially constant but temporally varying. These assumptions, as has been reviewed earlier, can cause erroneous flame size calculation in combustion case. However for pure evaporation, with a proper choice of the reference scheme at which these properties are calculated, the model is supposed to be acceptable [48].

To model diesel, one approach is to use the continuous thermodynamic theory as has been done in [125]. For fuel with a single distribution function (typical of standard light diesel, see [125]) a well mixed liquid phase model can also be used as advised by Abdel-Qader and Hallett [2] who pointed out that it gives close prediction to that of an effective diffusivity model which accounts for internal circulation. For simplicity purpose, this fuel can be treated as a representative single fuel with typical properties such as that presented in [107, 109]. The modeling of diesel using this simple approach is left to later section 6.6.5.

6.2.2 Mathematical Development

The formulation is based on the conservation of mass and energy in the gas and liquid phases and the process occurring at the droplet-gas interface. The inputs to the problem are

the initial droplet diameter, the droplet absolute velocity along its trajectory and the gas temperature. For problems involving convection, the first important parameter that needs to be found is the droplet Reynolds number which is dependant on the droplet relative velocity. To solve for these, the force balance is applied (drag/momentum law can also be used [117]) on the droplet via the equation

$$m_d \frac{du}{dt} = m_d g - F_D - F_B, \quad (6.1)$$

in which m_d is the droplet mass while F_D and F_B are drag force and buoyancy, respectively. Representing them in terms of droplet diameter and relative velocity u_{rel} and rearranging,

$$u_{rel}^2 = \frac{4D}{3\rho_g C_D} \left[(\rho_l - \rho_g)g - \rho_l \frac{du}{dt} \right] \quad (6.2)$$

in which ρ_g and ρ_l are, in turns, the densities of gas (air) and liquid (droplet). C_D is the drag coefficient which takes the widely used correlation for Reynolds numbers (Re) < 1000 ,

$$C_D = \frac{24}{Re} (1 + 0.166 Re^{2/3}) \quad (6.3)$$

with $Re = Du_{rel} / \nu_g$ in which ν_g is the kinematic viscosity of the air. It is necessary to mention here that the relative velocity can also be calculated by estimating the gas velocity based on the gas flow settings and the temperatures measured along the droplet trajectory. However, this will introduce another source of uncertainty and is therefore not used.

Using the overall mass conservation in the gas phase, fuel vapor species conservation and droplet mass conservation with the gas phase boundary shifted to the new film position to account for convection [131], we have the relation

$$\dot{m}_d = -\pi D \rho_g D_{fg} Sh \ln(1 + B_Y) \quad (6.4)$$

or

$$\frac{dD}{dt} = -\frac{2\rho_g D_{fg}}{\rho_l D} Sh \ln(1 + B_Y) \quad (6.5)$$

in which \dot{m}_d is the mass evaporation rate and D_{fg} is the binary mass diffusivity of fuel vapor-air pair calculated via the equation derived by Chapman and Enskog (presented in [98])

$$D_{fg} = \frac{0.0266T_{ref}^{3/2}}{P \left(\frac{2MW_f MW_g}{MW_f + MW_g} \right)^{1/2} \sigma_{fg}^2 \Omega_D} \quad (6.6)$$

with σ_{fg} and Ω_D being respectively the characteristic length and dimensionless collision integral calculated from collision diameters σ_f and σ_g and characteristic Lennard-Jones energy ε_f and ε_g of the fuel vapor and the air [98]. Expressions for σ_{fg} and Ω_D are

$$\sigma_{fg} = 0.5(\sigma_f + \sigma_g) \quad \text{and} \quad \Omega_D = \frac{1.06036}{T_*^{0.15610}} + \frac{0.193}{\exp(0.47635T_*)} + \frac{1.03587}{\exp(1.52996T_*)} + \frac{1.76474}{\exp(3.89411T_*)}$$

with $T_* = T_{ref} k_B / (\varepsilon_f \varepsilon_g)^{0.5}$ being the dimensionless temperature, k_B the Boltzmann constant.

In equations (6.4) and (6.5), B_Y is the mass transfer number which is defined as

$$B_Y = \frac{Y_s - Y_\infty}{1 - Y_s} \quad (6.7)$$

with Y_s and Y_∞ being the vapor mass concentration on the droplet surface and in the far field ($Y_\infty \approx 0$ for this system), Y_s is calculated via

$$Y_s = \frac{MW_f p_v}{MW_f p_v + MW_g (p - p_v)} \quad (6.8)$$

with p_v being the saturated vapor pressure which is related to the droplet temperature through the Clausius-Clapeyron equation describing equilibrium vaporisation.

By further using the gas phase energy conservation and shifted boundary position, the heat flux across the interface can be expressed as

$$q = \frac{k_g (T_g - T_l)}{D} Nu \frac{\ln(1 + B_Y)}{B_Y}. \quad (6.9)$$

in which k_g is the gas thermal conductivity, T_l is the droplet temperature. The last equation needed for this model is the energy balance between the liquid and gas phases

$$Q = \pi D^2 q = m_d C_{pl} \frac{dT_l}{dt} + \dot{m}_d H \quad (6.10)$$

in which C_{pl} and H are the specific heat capacity and heat of vaporisation of the liquid fuel. This equation means that the heat transferred to the droplet is used for heating it up and vaporizing it.

In the above equations, Sh and Nu are the Sherwood and Nusselt numbers to be calculated from the Reynolds number via the most widely used correlation

$$\begin{aligned} Sh &= 2 + 0.6 \text{Re}^{1/2} Sc^{1/3} \\ Nu &= 2 + 0.6 \text{Re}^{1/2} \text{Pr}^{1/3} \end{aligned} \quad (6.11)$$

in which Sc is the Schmidt number $Sc = \nu_g / D_{fg}$ and Pr is the Prandtl number $Pr = \nu_g \rho_g C_{pg} / k_g$ with C_{pg} being the specific heat capacity of the gas.

As has been widely suggested, the 1/3 rule reference scheme is used in this work for estimating the thermodynamics properties of air (i.e. to calculation at temperature $T_{ref} = (T_g + 2T_s)/3$). The thermophysical properties of fuels as functions of the droplet temperature are calculated as instructed in [127]. These calculations are shown in Appendix B.

6.3 Application to Investigated Alkanes

The aim of this section is to examine how the simple model predicts the droplet behavior of the investigated alkanes and to give further analyses of the evaporation process, especially in relation to the effects of droplet initial diameter, gas temperature and fuel chemistry. For the model, to calculate the binary diffusivity, the collision diameters and Lennard-Jones energies of fuels and air are needed. While the collision diameters are in Ångström, the Lennard-Jones energies are often quoted in ϵ_f/k_B in Kelvin. For these fuels, two sets of σ_f and ϵ_f/k_B from Hirschfelder et al [46] and Paredes et al [96] are under controversy. The more recent set from Paredes et al [96] which is shown in Table 6.1 was found to give more realistic results [109] and is therefore chosen for this work. For air, σ_g and ϵ_g/k_B are taken from [124] to be respectively 3.711 Å and 78.6 K.

Table 6.1: Collision diameters and Lennard-Jones energies of fuel vapor taken from [96]

Fuels	$\sigma_f(\text{\AA})$	ε_f/k_B (K)
Nonane	6.5694	460.0856
Decane	6.5627	456.7366
Dodecane	6.5972	454.6768

Due to the differences in diameters, velocity profiles and thus different heating conditions, the ability to have a systematic presentation is somehow limited. Direct comparisons when possible will be shown on the same plots leaving the others to discussions on separate plots. As the very first comparisons, Figure 6.1 presents model predictions for dodecane which are paired with experimental data from Figure 5.1 for diameter variation against x -position. As a reminder, for a particular series of data, the measured droplet absolute velocity and gas temperature profiles are the inputs for the model.

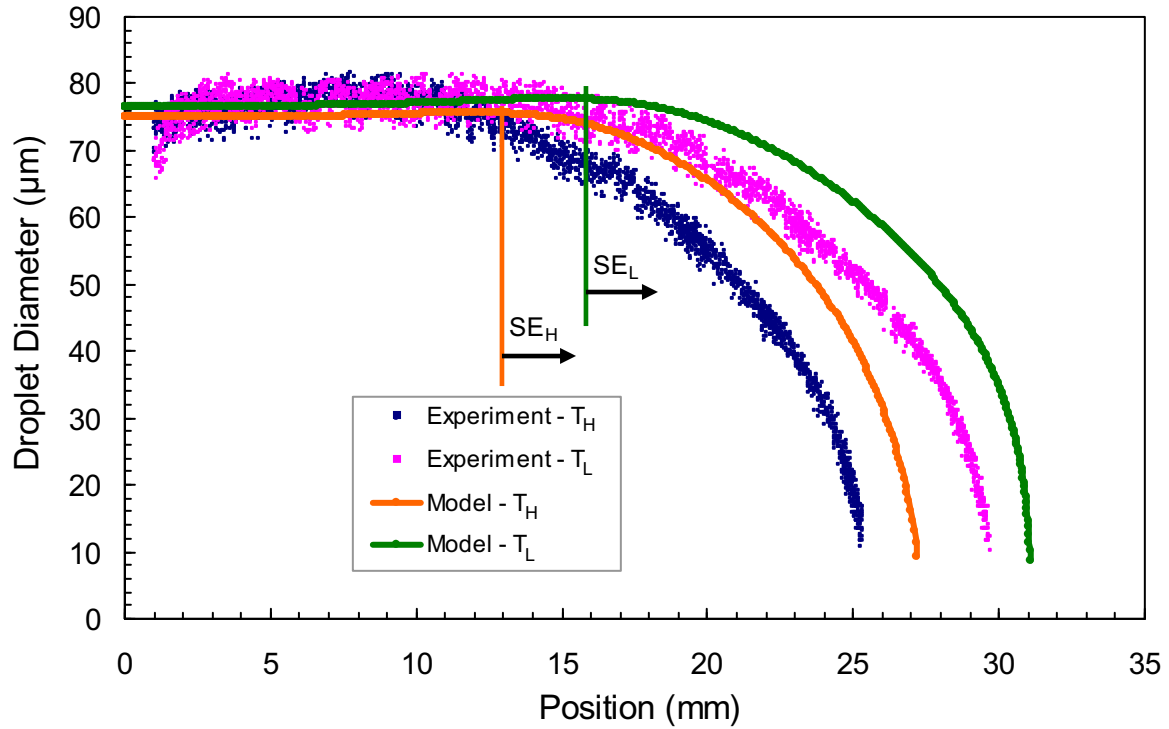


Figure 6.1: Comparison between model predictions and dodecane experimental data in Figure 5.1 for both temperature settings. Shown are variations of diameter against position

In this figure, comparisons are made for both temperature settings. At first examination, the model predicts $\approx 10\%$ longer evaporation time than the measured. The predictions also show a later start of evaporation while droplet expansion due to initial warming is also seen from the model results. However, the predicted expansion is slightly less than measured which can be a consequence of neglecting a small amount of radiation heat transfer likely present in the proximity of the burner flame during the very early stage. This difference is larger for T_H which is reasonable as the flame luminosity is stronger than for T_L . However, experimental data in this region is still affected by the noise from the flame. Given some differences, the model is expected to give further understanding of the process.

Figure 6.2 shows the calculated droplet Reynolds number as well as its absolute and relative velocities. Once entering the reactor, while the absolute velocity increases to a peak, the droplet relative velocity varies slightly just around 0.08 m/s. In the final period, this relative velocity falls to zero as expected. For the whole lifetime, droplet Reynolds number is very low starting from around 0.3 and falling down to zero at the end. During the evaporation period, this number varies in a very narrow range from about 0.16 to near zero and as such plays almost no role as argued in previous chapter.

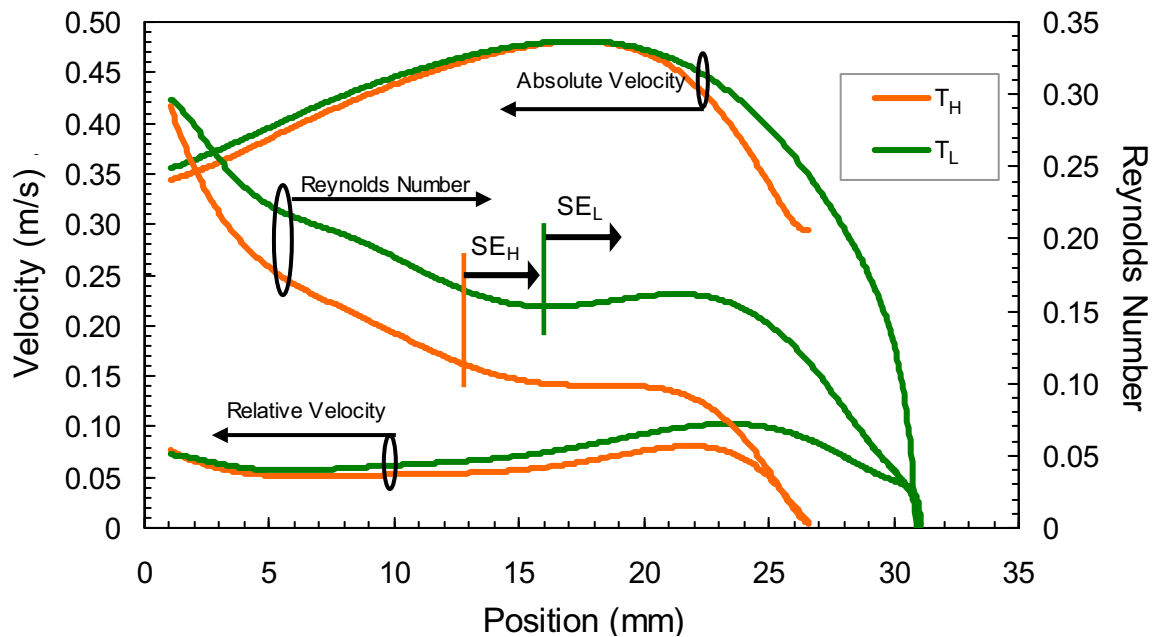


Figure 6.2: Measured absolute velocity, predicted relative velocity and Reynolds number of dodecane droplets against position in both temperature settings

To analyse the evaporation process, model predictions are shown in Figure 6.3 in which squared diameter are expressed against the droplet residence time. Dodecane boiling point and temperature profiles for two gas settings are also included in this figure. SE_L occurs at 38.6 ms while SE_H occurs at 33 ms both after the gas temperatures exceed the droplet boiling point. The predicted average evaporation rates found by linear fits to the whole evaporation periods, though not shown here, are 0.179 and 0.147 mm^2/s for high and low temperature settings respectively which are almost the same with measurements (0.179 and 0.152 mm^2/s). Given almost similar initial diameters for these two series, this confirms the role of gas temperature in increasing this average rate of the whole evaporation process.

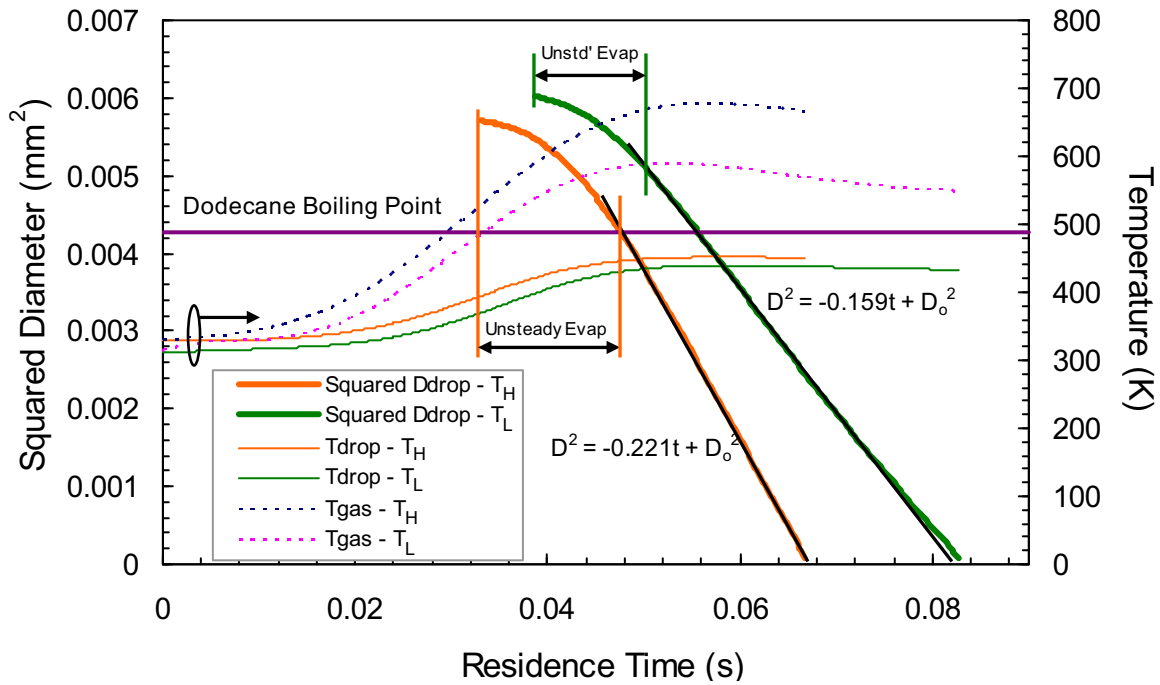


Figure 6.3: Comparison of predictions for dodecane droplets at two temperature settings. Shown are droplet squared diameters, droplet temperatures, gas temperature profiles and dodecane boiling point.

As one of the most desired quantities, variation of the predicted droplet temperatures is also included in Figure 6.3. As expected, the plots indicate that the droplet temperature depends on the gas temperature, it starts low at ambient temperature and increases with the gas temperature until reaching the peak values and maintains this state until the end of its lifetime (though for T_L , this temperature decreases lightly as the gas temperature is reduced

during this late period). These peak values are higher for T_H as expected but are seen to be well below the dodecane boiling point (452 K for T_H and 440 K for T_L compared to the boiling point of 488 K). These low steady droplet temperatures are reasonable as even in hot combustion process, this temperature can still be around 10-20 K below the boiling point [130].

The evaporation experiences an initial unsteady period which is marked “Unsteady Evap” in Figure 6.3. This behavior, as evidenced in experimental results, is seen to correlate with droplet temperature which continually rises before reaching peak values. This unsteady period is longer for T_H than T_L due to the fact that the gas temperature for T_H reaches its peak later and that more energy is needed for the droplet temperature to reach a higher peak. After this period, the evaporation proceeds nearly steadily and line fits to this period for both temperature settings yield near steady rates of 0.221 and 0.159 mm^2/s , very close to the measured rates of 0.218 and 0.172 mm^2/s . To enable a deeper investigation of the evaporation process, Figure 6.4 shows the variation of evaporation rate and droplet temperature against the gas temperature for two settings.

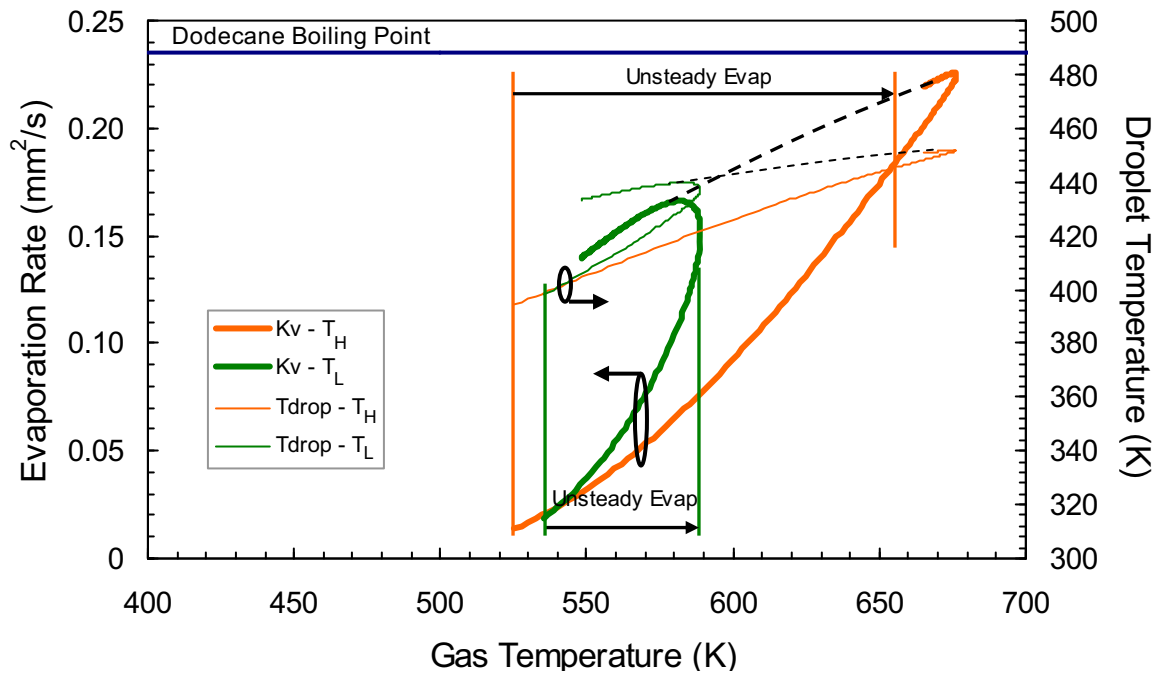


Figure 6.4: Evaporation rate and temperature of dodecane droplets against gas temperature for two temperature settings

A couple of observations can be made about this figure. The droplet temperature tightly follows the gas temperature and when comparing between the two series the difference in droplet temperature (at the same gas temperature) is apparent. Between the two temperature settings, the evaporation rate is also obviously different. The unsteady period (as marked) is seen to occupy a portion with large variations in evaporation rate and droplet temperature. In Figure 6.3, even though the final evaporation process looks almost linear (approximated by a steady rate), it is seen in Figure 6.4 that there is actually no such separation between unsteady and steady regions but rather a continuous increase in the evaporation rate with the gas temperature. However in later period, the variation is very small with the droplet temperature being very near its peak value. These can be understood as the equilibrium values if the gas temperature is kept constant at its peak.

For both series, after the gas temperature reaches its peak, the evaporation continues at higher rate on the later side of the peak (at the same gas temperature) though decreasing with the decrease in this temperature. This again correlates with the droplet temperature. On the later side though gas temperature is reduced, the droplet temperature is still higher due to thermal inertia (especially because this model treats the droplet as a lumped-parameter model with spatially constant temperature [131]) which causes a higher evaporation rate as the mass transfer number B_Y depends on the vapor concentration Y_s on the surface which is sensitive to the liquid phase temperature. This correlation also explains the observed difference in evaporation rates between the two temperature settings mentioned earlier. Further analysis indicates that the dash curves extending the later side of the evaporation rate curve and droplet temperature curve of the T_H series meet the respective curves of the T_L series and these would mean true steady state curves of dodecane with gas temperature.

Figure 6.5 shows the variation of evaporation rates against the droplet diameter for both temperature settings. The gas temperature profiles are also included. The unsteady evaporation period now shrinks to a smaller region in this plot leaving a larger space of near steady evaporation for analysis. It is clear that the evaporation rate follows the gas temperature. The aim is however more to focus on the late period where the gas temperatures show much less variation (this ability is limited if shown as Figure 6.4). For T_H

the evaporation rate is almost constant with gas temperature while droplet size changes considerably. This confirms that droplet diameter has no effect for these conditions. From both series, it is clear that the evaporation rate curve always has the same trends with the gas temperature curve and for T_L the rate decreases clearly with the decrease in gas temperature at the end. A similar plot for experimental data cannot be obtained due to the large uncertainty for this type of localized analysis as discussed much earlier. In summarising the effect of gas temperature for these two series, it can be seen that this temperature improves all types of evaporation rate, i.e. the average, the near steady and the instantaneous rates.

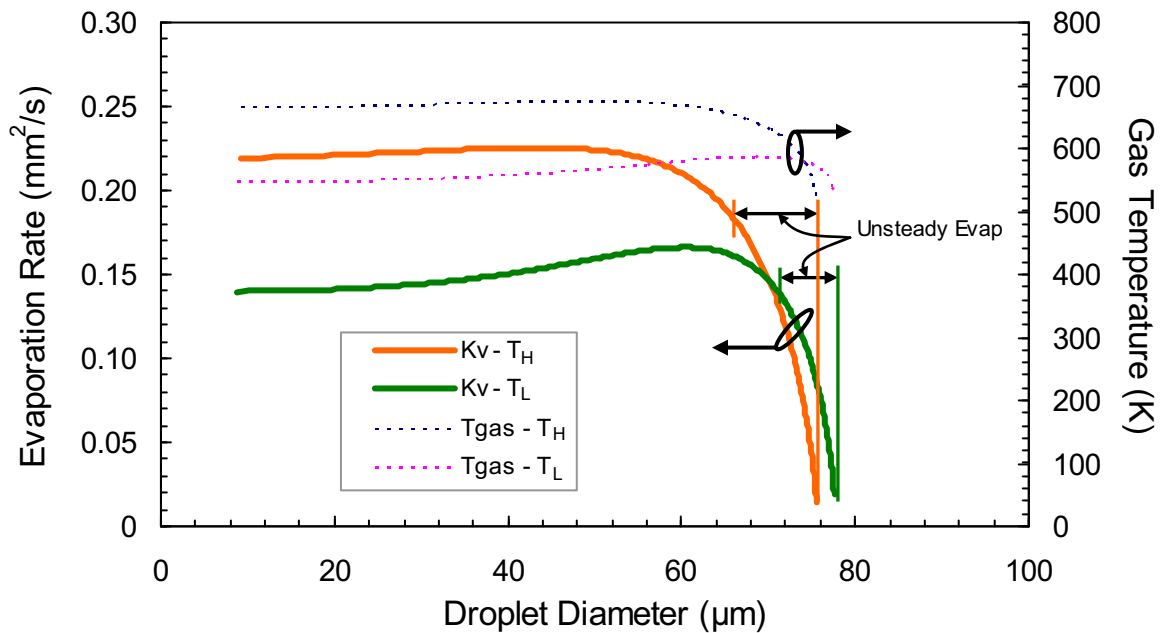


Figure 6.5: Predicted evaporation rates of dodecane droplets versus the droplet diameter for two temperature settings. Gas temperature profiles are also included.

Figure 6.6 compares the model prediction with experimental data for decane droplets in Figure 5.6. For these series, it can be seen again that the model predicts slightly longer the evaporation time (4-7% longer). For both cases, the predictions of preheating show less or even no effect of expansion and the predicted SEs therefore start earlier. For the later part, while the prediction for T_H has the form resembling the data that for T_L appears slightly different from the data. Though not shown here, the prediction for the 45.5 μm decane droplet also indicates that there is no steady period and that the average rate found for the whole evaporation process is 0.091 compared to the measured 0.1 mm^2/s .

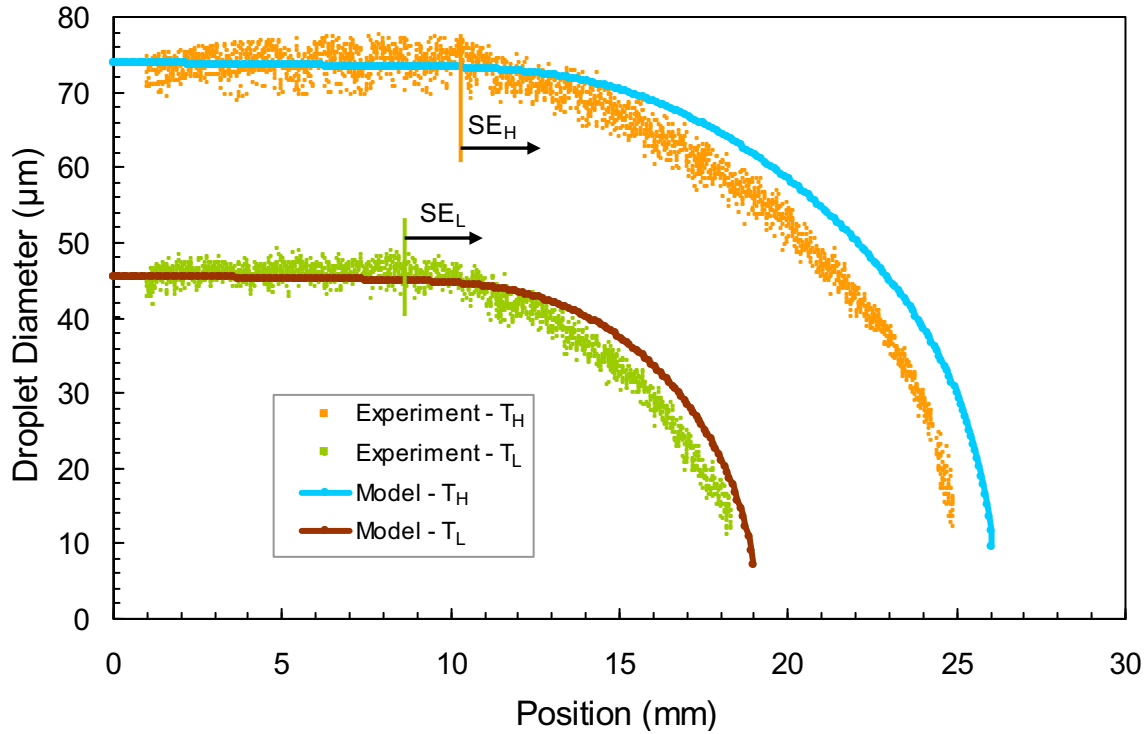


Figure 6.6: Comparison of model predictions with experimental data of decane in Figure 5.6 for two temperature settings. Shown are variations of diameter against position.

Figure 6.7 shows the variation of the predicted evaporation rate and temperature of decane droplets in Figure 6.6 against the gas temperature. The unsteady evaporation period is also marked for each series and, as seen, this occupies the whole lifetime of the $45.5\ \mu\text{m}$ droplet while more predicted details for the $74\ \mu\text{m}$ droplet will be described in the next paragraph. In agreement with Figure 5.8, this figure indicates that at the same gas temperature the smaller droplet has a higher rate than the bigger droplet (certainly during the unsteady period) which is now clearly to be due to its higher temperature. This is reasonable as has been discussed earlier due to the lower thermal inertia. To get an idea, for these liquids with a typical thermal diffusivity of around $0.1\ \text{mm}^2/\text{s}$ [98], the heat diffusion time (assuming no convection) within the droplet would be around $4\ \text{ms}$ for a $40\ \mu\text{m}$ size while it is around $16\ \text{ms}$ for an $80\ \mu\text{m}$ size. Low thermal inertia also means that more energy per unit volume is left per unit time for evaporating the smaller droplet. Again, a small difference in the droplet temperatures would make the rates become significantly different. Although the life of the smaller droplet ends earlier, it is expected that both droplets would reach the same

temperature for the same gas temperature if this smaller droplet were to last longer as at the end of its lifetime their temperatures become closer together. This also means that they would reach the same evaporation rate. Together with the previous discussion for dodecane droplets, it can now be understood that while the droplet initial diameter plays no role on the steady evaporation rate, it has a direct consequence on the rate during the preheating phase.

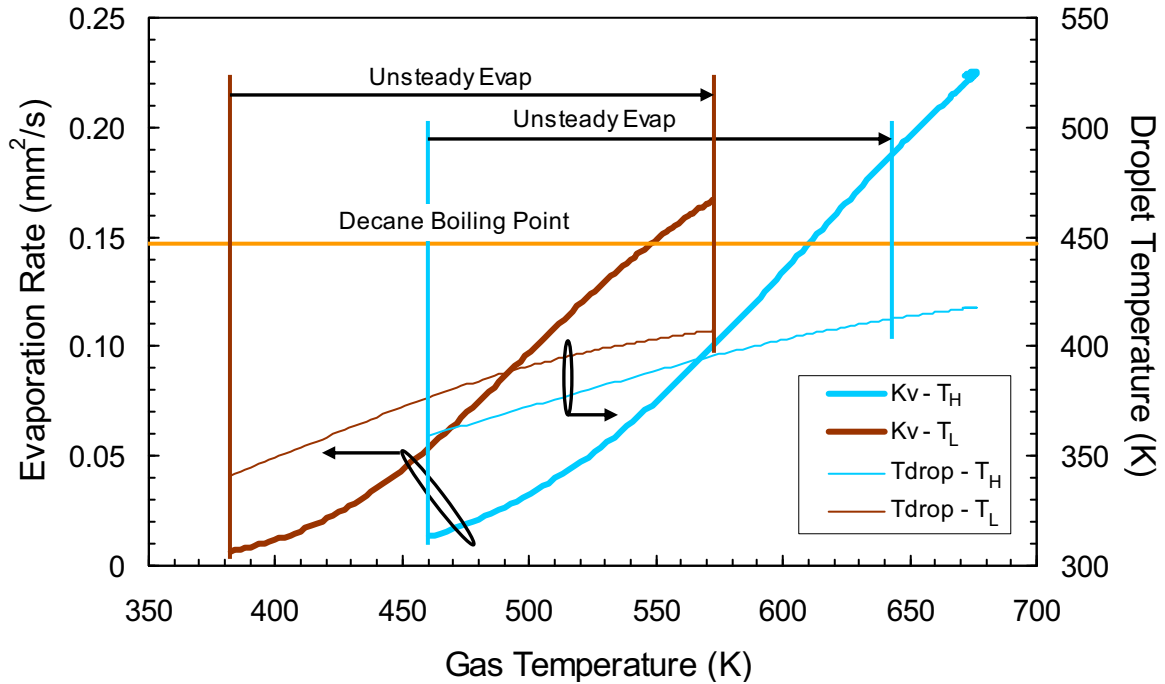


Figure 6.7: Evaporation rate and temperature of decane droplets against gas temperature for 74 μm droplet in high temperature setting and 45.5 μm droplet in low temperature setting

To gain more understanding and to investigate the effect of fuel chemistry, the 74 μm decane droplet is compared with 75 μm dodecane droplet in Figure 6.8 in which, variations of squared diameters against the residence time during the evaporation process for T_H are shown. In this figure the predicted droplet temperatures are also plotted together with fuels' boiling points. As expected, the decane droplet starts to evaporate earlier. Similar to dodecane, its evaporation starts unsteadily and this is confirmed here to correlate with its temperature. During this period decane temperature rises close to the peak which is around 418 K compared with 452 K of dodecane. Given the boiling points of decane and dodecane are 447 K and 488 K, the droplet temperatures are 29 K and 36 K below the boiling points respectively. Again after the unsteady period, the later process manifests a near steady

behavior due to very little variations in the ambient and droplet temperatures. Line fits to this late period indicate similar evaporation rate of $0.221 \text{ mm}^2/\text{s}$ for decane and dodecane given very little difference in the condition due to the difference in initial diameters (4% by volume) of the two fuels. This similarity is supported by the experimental evidence in the previous chapter (the respective measured values are 0.222 and $0.218 \text{ mm}^2/\text{s}$) and favored by the mentioned combustion data in [7] for a range from octane to hexadecane in which the size investigated is $1100 \text{ }\mu\text{m}$ with combustion rates being much higher of about $0.86 \text{ mm}^2/\text{s}$. This somehow implies the same effect for the present droplet sizes as that much larger size.

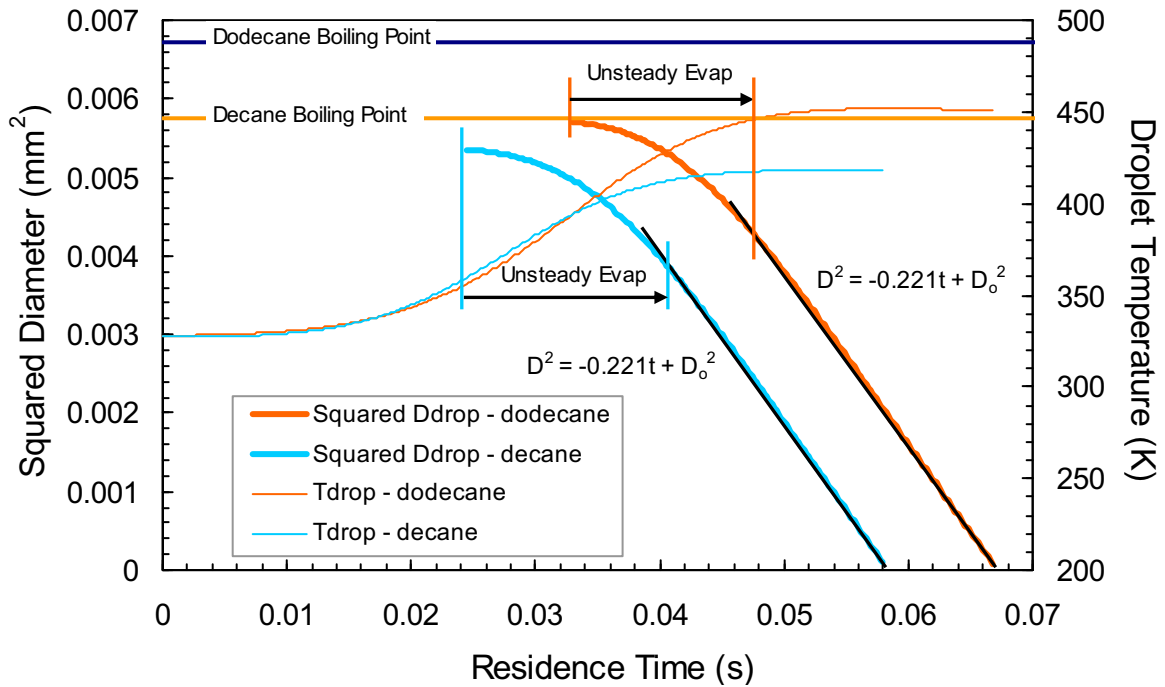


Figure 6.8: Model prediction for dodecane and decane for T_H . Shown are the variations of squared diameters against residence time. Boiling points and droplet temperatures are also included

To see more detailed the effect of gas temperature and fuel chemistry, the evaporation rates and droplet temperatures of the two series in Figure 6.8 are plotted against the gas temperature in Figure 6.9. Again, during the early portion of unsteadiness the droplet temperature and evaporation rate increase considerably with the gas temperature. The late period with little increase of these parameters was treated in Figure 6.8 as the near steady behavior. For all gas temperatures the decane droplet evaporates quicker than dodecane,

especially at low gas temperatures, which is supported by the experimental data (slightly different though). Attention to the period after the unsteady phase helps to explain why when the gas temperature is closer to the peak, the rates of decane and dodecane are almost the same as represented by the similar near steady rates found. While the role of gas temperature is obvious, initial diameter is also found to play no effect on the steady rate of decane droplet when plotting the rate against the diameter (though not shown here).

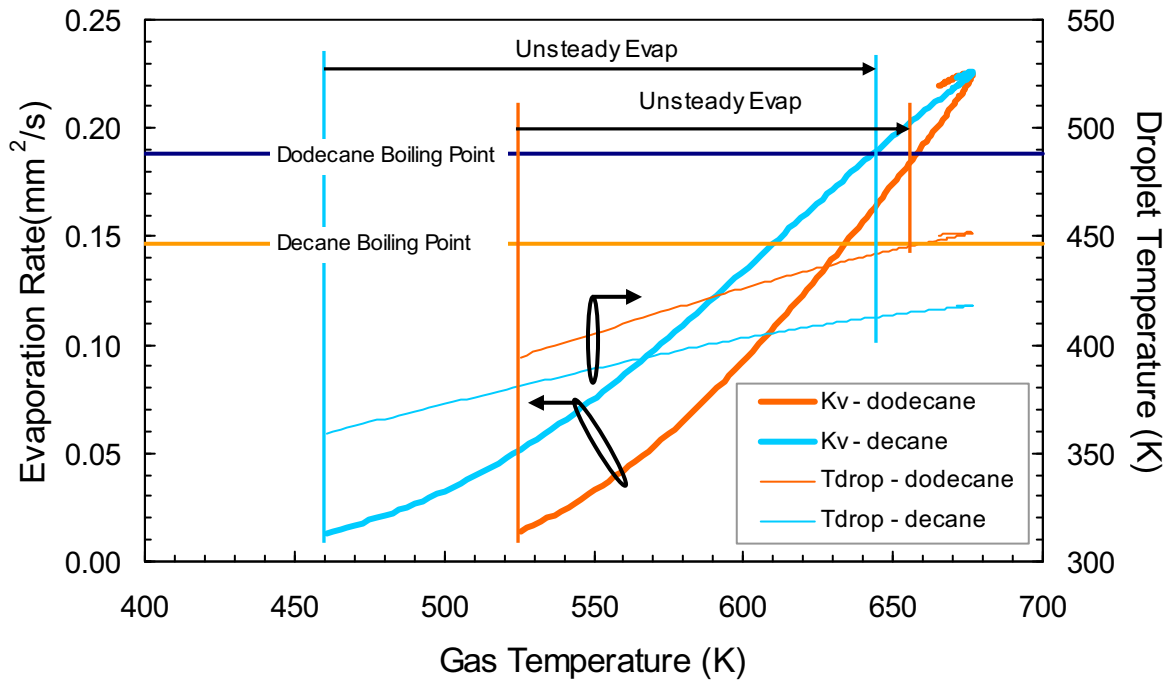


Figure 6.9: Evaporation rate and droplet temperature variations against gas temperature for dodecane and decane droplets in Figure 6.8 (at the high temperature setting)

Figure 6.10 presents the predictions for the 65 μm dodecane droplet and 63.5 μm nonane droplet shown in Figure 5.12 for T_H . For both series the model predicts about 5-7% longer the droplet evaporation time. It is necessary to mention here that these differences come not only from the model side but also from experimental side. As seen, while the predicted SE for dodecane occurs at about 11 mm (slightly later than the measured), nonane is predicted to show evaporation right from the beginning with no expansion. For these droplets, the modeled D^2 - t curves, shown in Figure A.9 in Appendix A, also show a near steady period starting from around 20 mm (42.2 ms) for dodecane and 16.8 mm (38.8 ms) for nonane after the initial unsteady behavior. The near steady rates of dodecane and nonane are respectively

0.222 and 0.205 mm²/s which are almost the same as the ending rolling rates of 0.222 and 0.215 mm²/s reported earlier for these series. Little variation in this period is certainly due to little variation in the gas temperature. At this stage the actual droplet temperature, which will be investigated later in more detail, is expected to be uniform. The current assumption of uniform droplet temperature of this model quickly provides an idea of how the droplet temperature affects the process in present conditions.

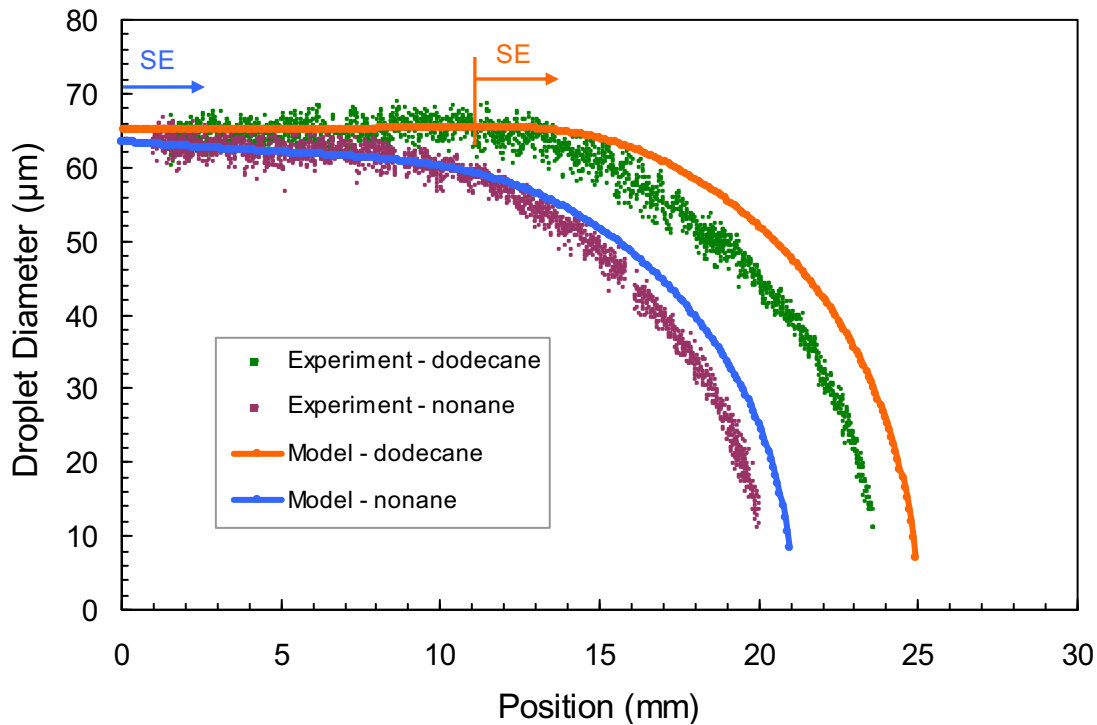


Figure 6.10: Comparison of model predictions with experimental data for the 65 μm dodecane droplet and 63.5 μm nonane droplet in Figure 5.12 for the high temperature setting. Shown are variations of diameter against position.

To get a closer look and to study the chemistry effect, Figure 6.11 illustrates the variation of predicted droplet temperature and evaporation rate against the gas temperature for two series in Figure 6.10. While this dodecane droplet also attains the maximum temperature of 452 K similar to the bigger droplet (36 K below its boiling point), the nonane droplet reaches 398 K as the maximum which is 26 K below its boiling point of 424 K. Similar to the comparison between dodecane and decane, nonane is seen here to evaporate much faster than dodecane (and decane) at low temperature but the difference in their rates becomes

smaller with the increase in gas temperature and very small once this temperature passes 650 K for which the droplet temperature is also near stable. This is in agreement with the similarity found for their measured rates once they approach a near steady state.

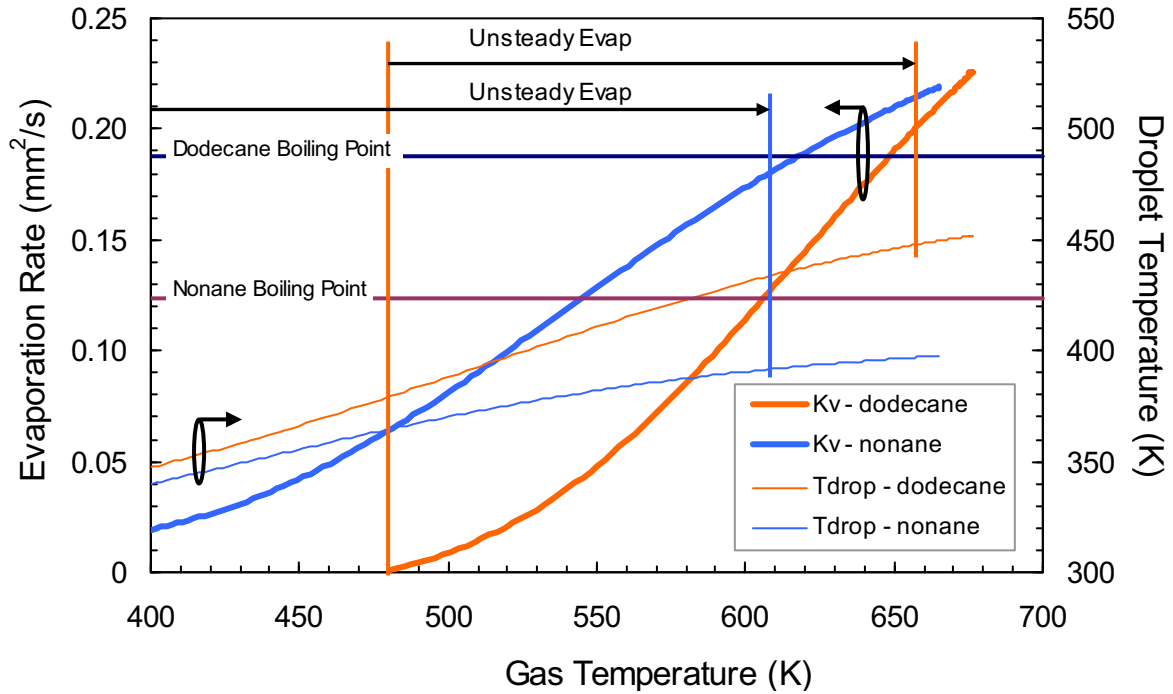


Figure 6.11: Predicted evaporation rate and droplet temperature variations against gas temperature for dodecane and nonane droplets in Figure 6.10

Figure 6.12 is another example showing how the model predicts for the 52 μm decane droplet and 84 μm nonane droplet for T_H for which the evaporation time is just less than 6% longer than measured. Given its simplicity, the prediction obtained is not poor. Overall, it gives some lag for the SE point and slightly longer evaporation time. Other than that, it predicts good evaporation rate, especially the near steady rate. In this model the droplet temperature is assumed to be uniform which is however likely untrue as even in extremely high Reynolds number environment, this mode can never be attained [65]. Furthermore, this model does not provide an assessment of the effect of the convection from the gas side on the droplet internal heat transport. The Stefan flow effect is another factor that is known to slow down the evaporation which also needs to be examined. Extension of this model is therefore needed. Though aiming at including more effects, the simplicity is still the goal of this extension the mathematical development of which will be shown in the next section.

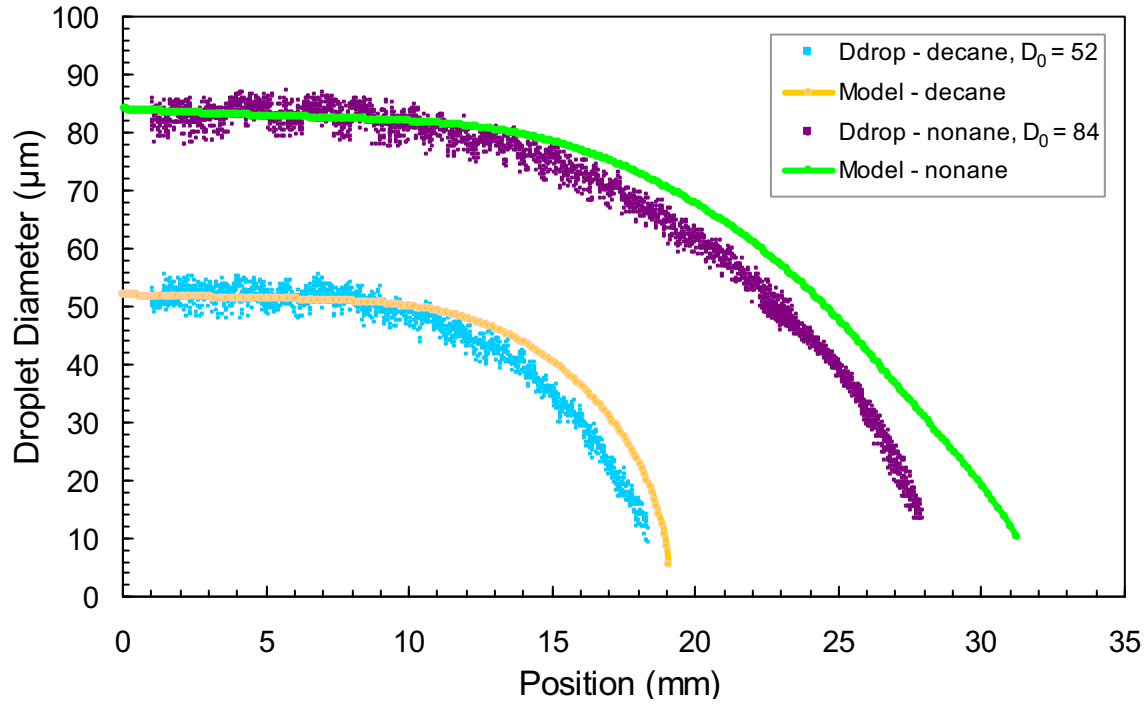


Figure 6.12: Comparison of model predictions with experimental data of 52 μm decane droplet and 84 μm nonane droplet for the high temperature setting. Shown are variations of diameter against position.

6.4 Extension to Effective Conductivity Model

As mentioned, to explore the droplet internal temperature distribution and to assess the slip effect on the liquid phase in current experimental conditions, development of the simple model to an effective conductivity model is necessary. This can be done with and without accounting for the Stefan flow effect. This section first introduces the extension to account for this effect and then develops the effective conductivity model.

6.4.1 Integration of Stefan Flow Effect on the Gas Side

The effect of Stefan flow can be defined as the resistance of the heat and mass transfer between the surrounding gas and the droplet surface and thus can be treated as the thickening of the resistance films on the gas side [110]. To account for this, correction factors $F_Y = \delta_M/\delta_{M0}$ and $F_H = \delta_T/\delta_{T0}$ are introduced with (δ_M, δ_T) and $(\delta_{M0}, \delta_{T0})$ being the

thicknesses of the (mass, thermal) diffusion films with and without the Stefan flow effect. The Sherwood and Nusselt numbers are now expressed in a modified form

$$Sh^* = 2 + (Sh - 2) / F_Y \quad (6.12)$$

$$Nu^* = 2 + (Nu - 2) / F_H.$$

The equations (6.4), (6.5) and (6.9) now becomes

$$\dot{m}_d = -\pi D \rho_g D_{fg} Sh^* \ln(1 + B_Y), \quad (6.13)$$

$$\frac{dD}{dt} = -\frac{2\rho_g D_{fg}}{\rho_l D} Sh^* \ln(1 + B_Y) \quad (6.14)$$

and

$$q = \frac{k_g (T_g - T_s)}{D} Nu^* \frac{\ln(1 + B_Y)}{B_Y}. \quad (6.15)$$

Note that T_l in equation (6.9) is now replaced with the droplet surface temperature T_s in equation (6.15).

The correction factors F_Y and F_H are functions of the mass and heat transfer numbers B_Y and B_H [4]

$$F_Y = (1 + B_Y)^{0.7} \frac{\ln(1 + B_Y)}{B_Y} \quad (6.16)$$

$$F_H = (1 + B_H)^{0.7} \frac{\ln(1 + B_H)}{B_H}.$$

While B_Y is calculated from equation (6.7) (Y_s is found from T_s which is known from the previous time step), B_H is another quantity which also needs to be calculated. It is noticed that the mass evaporation rate can also be expressed via

$$\dot{m}_d = -\pi D \frac{k_g}{C_{pg}} Nu^* \ln(1 + B_H) \quad (6.17)$$

and by equating equation (6.17) with equation (6.13), the following relationship is found

$$B_H + 1 = (1 + B_Y)^{\frac{1}{Le} \frac{Sh^*}{Nu^*}}. \quad (6.18)$$

To calculate B_H , an iterative procedure is applied by firstly assigning B_H a value of B_Y and then F_H is found from equation (6.16). Once Nu^* and Sh^* are found from equation (6.12), they will be substituted into equation (6.18) to find a new B_H . The procedure keeps circulating until $|B_{H2}-B_{H1}| < 0.001$ which is the accuracy chosen for this work (for this condition, a maximum of 3 loops are needed for convergence).

Once B_H is found, the heat flux q across the interface is calculated from equation (6.15). The rate of heat flow transferred into the droplet for sensible heating is now calculated as

$$Q_l = \pi D^2 q - \dot{m}_d H. \quad (6.19)$$

This equation is equivalent to equation (6.10) which expresses the energy balance at the droplet surface. However equation (6.10) does not apply here as the droplet temperature is now non-uniform and Q_l is therefore used as the input for the liquid phase model shown in the following section.

6.4.2 Liquid Phase Model

Under convective environments, the liquid phase should be treated as a vortex model. However for simplicity an effective conductivity model proposed by [4] is applied. Considering the low droplet Reynolds number used here, this choice is further justified as the circulation is deemed very weak (or even does not exist) in which case a treatment close to a conduction limit model is mostly suitable. As the main aim is to investigate the temperature distribution within the droplet, an assumption used here is to treat the liquid phase properties as being constant. Variable properties treatment is possible such as done in [55], however the computational effort is very large. In addition, for low temperatures and low convections used here, the simplified approach is suitable as long as a proper selection of the reference temperature for calculating the liquid properties is made [55] as this temperature is a very important factor.

Since this is a problem of a moving boundary, the governing equation for energy is best expressed in a non-dimensional form

$$\bar{r}_s^2 \frac{\partial \bar{T}}{\partial \tau} - 0.5 \frac{d\bar{r}_s^2}{d\tau} \eta \frac{\partial \bar{T}}{\partial \eta} = \frac{\chi}{\eta^2} \frac{\partial}{\partial \eta} \left(\eta^2 \frac{\partial \bar{T}}{\partial \eta} \right) \quad (6.20)$$

in which $\bar{r}_s = r_s / r_o$ is the droplet non-dimensional radius, $\tau = \alpha_l t / r_o^2$ non-dimensional time, $\eta = r / r_s$ non-dimensional radial coordinate, $\bar{T} = (T - T_o) / T_o$ non-dimensional temperature and $\chi = k_{eff} / k_l$ a factor representing the enhanced thermal conductivity coefficient inside the droplet due to improved heat transport under convection. r_o and T_o are the initial droplet radius and temperature. r and r_s are the radial coordinate in the droplet and its radius - the moving boundary. α_l and k_l are the liquid thermal diffusivity and conductivity.

Equation (6.20) is subjected to the following initial and boundary conditions:

$$\left\{ \begin{array}{ll} \bar{T}|_{\tau=0} = \bar{T}(\eta) = 0 & \text{droplet temperature is initially uniform at } T_o, \\ \frac{\partial \bar{T}}{\partial \eta}|_{\eta=0} = 0 & \text{symmetry requirement and} \\ \frac{\partial \bar{T}}{\partial \eta}|_{\eta=1} = \frac{Q_l}{4\pi r_s \chi k_l T_o} & \text{heat transferred across the droplet surface for preheating.} \end{array} \right. \quad (6.21)$$

The correction factor χ is approximated as the following expression [4]

$$\chi = 1.86 + 0.86 \tanh[2.245 \log_{10}(Pe_l / 30)] \quad (6.22)$$

in which Pe_l is the liquid Peclet number which is defined as the ratio of the surface regression rate and the diffusion coefficient. Pe_l is calculated as the product

$$Pe_l = Re_l Pr_l \quad (6.23)$$

with Re_l and Pr_l being the liquid Reynolds and Prandtl numbers. The liquid phase Reynolds number is defined as

$$Re_l = \frac{u_s D \rho_l}{\mu_l} \quad (6.24)$$

in which u_s is the maximum velocity at the droplet surface and μ_l is the liquid dynamic viscosity. The velocity u_s is found from the force balance at the droplet surface [117]

$$u_s = \frac{1}{6\pi} \frac{\mu_g}{\mu_l} C_F \text{Re} u_{rel}. \quad (6.25)$$

In equation (6.25), C_F is the skin friction coefficient which, as mentioned in [4], can be found from the correlation accounting for the Stefan flow effect and for $B_Y < 20$ found here in this work

$$C_F = \frac{12.69}{\text{Re}^{2/3} (1 + B_Y)^{0.75}}. \quad (6.26)$$

Though the above correlation for C_F is recommended for $10 \leq \text{Re} \leq 100$, it is still used here as an approximation as no better data is present.

As the accuracy of the extended model (especially of the evaporation rate or droplet lifetime) is strongly dependant on the reference temperature used for estimating the liquid properties (except for the liquid viscosity which is calculated at the droplet surface temperature), it needs to be carefully chosen. Abramzon and Sirignano [4] suggested an arithmetic mean $0.5(T_o + T_{boil})$. Kneer et al [55] recommended to use a modified form $\zeta(T_o + T_{boil})$ with ζ being chosen from 0.55 - 0.6. However their recommendations are appropriate for high temperature environments. For present condition, a mean value of $0.5(T_o + T_{dmax})$ is used with T_{dmax} being the equilibrium or maximum droplet temperature found from the earlier Lump model.

With Q_l found from the gas side calculation being used as one of the inputs for equation (6.20), it is solved using the Crank–Nicolson discretization scheme. For current conditions with low to moderate gas temperatures a choice of 100 grid points for the spatial coordinate and a time step of 0.1 ms is made to ensure convergence. Note that this time step is only suitable for the present conditions. For higher gas temperatures, a finer step will be expected and simulation time will be longer. With this choice, the model runs for about 16 s compared to about 8 s of the Lump model on a 2.4 GHz clock speed CPU for a typical 75 μm droplet.

6.5 Comparison of Extended Models and Data

As an illustration, Figures 6.13, 6.14 and 6.15 compare the numerical results of three models (i.e. the earlier Lump model, the ‘effective conductivity without Stefan flow’ and the ‘effective conductivity with Stefan flow’ models) with experimental data of dodecane droplets of 75 and 76.5 μm for both temperature settings (Figure 6.13), decane droplets of 74 and 45.5 μm both settings (Figure 6.14) and nonane droplets of 84 and 63 μm high temperature setting (Figure 6.15). At first examination, all three models predict longer evaporation time, with the effective conductivity models giving lifetime closer to the data. Though simple, the Lump model predicts better the local behavior (similar curve form) whereas the effective conductivity models predict earlier evaporation and an initially faster evaporation rate. This difference is a result of treating the liquid properties as constants (fixed density) and therefore neglecting the effect of expansion of effective conductivity models. The difference is large at the middle of the droplet’s lifetime, around the preheating zone and the initial period of evaporation. It is clear from these plots that the improvements made to the model still cannot bring the predictions closer to the measurement as desired and, if putting aside the model defects, this points to the possible existence of the uncertainty in adjusting the measurement zones.

The Stefan flow effect starts with the evaporation and becomes stronger with time (gas temperature) as represented by the larger deviation between two effective conductivity models. This effect is however very small and agrees with these situations of slow evaporation and low convection. In conditions of high temperature and strong convection, it is expected to be significant. For all cases, the difference is smaller for small droplets with short lifetimes due to lower temperature reached by the droplet which implies weaker effects of Stefan flow and density variability. Given some deviation from those measured, the simplified effective conductivity model is supposed mainly to provide more realistic droplet temperature. It is necessary however to assess the droplet internal state during its lifetime in advance by investigating the liquid Reynolds and Peclet numbers. While Reynolds number represents the fluid motion, Peclet number represents the effect of this motion on the heat

transfer within the droplet. This is an advantage of this model although it does not provide such details which can only be obtained from the vortex model.

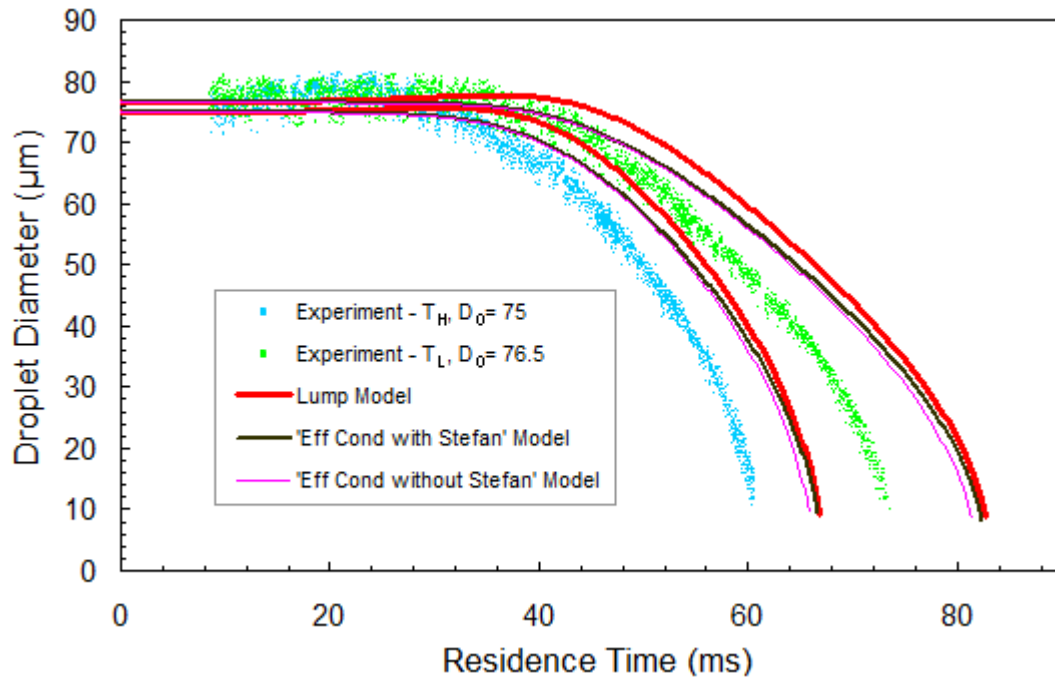


Figure 6.13: Comparison of results of three models (D vs t) with experimental data of 75 μm and 76.5 μm dodecane droplets in high and low temperature settings respectively

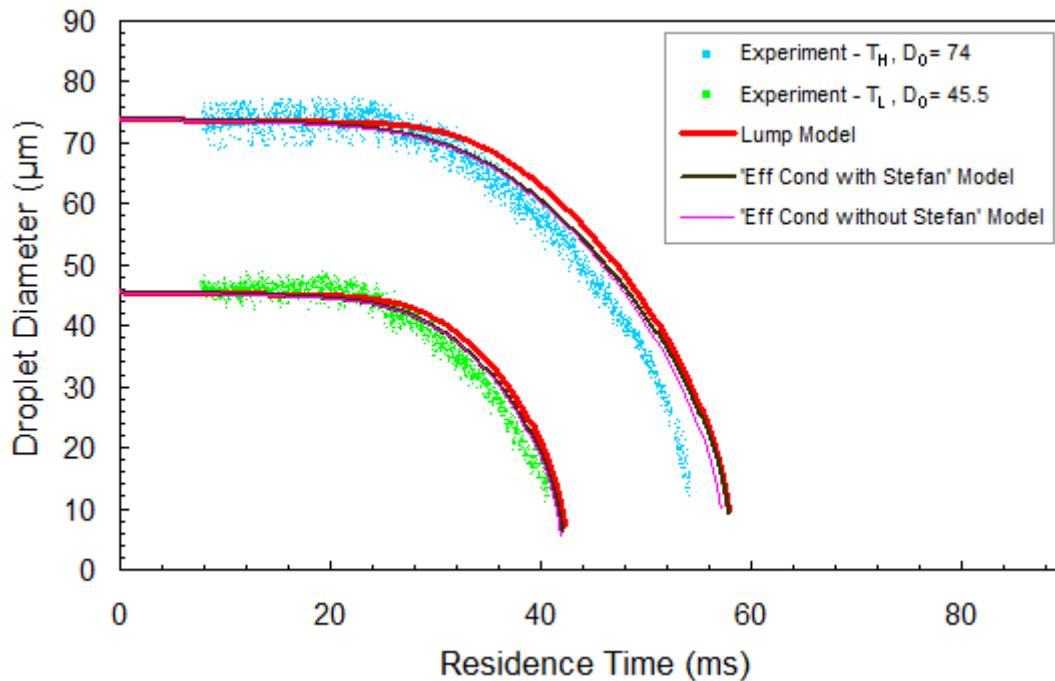


Figure 6.14: Comparison of results of three models (D vs t) with experimental data of 74 μm and 45.5 μm decane droplets in high and low temperature settings respectively

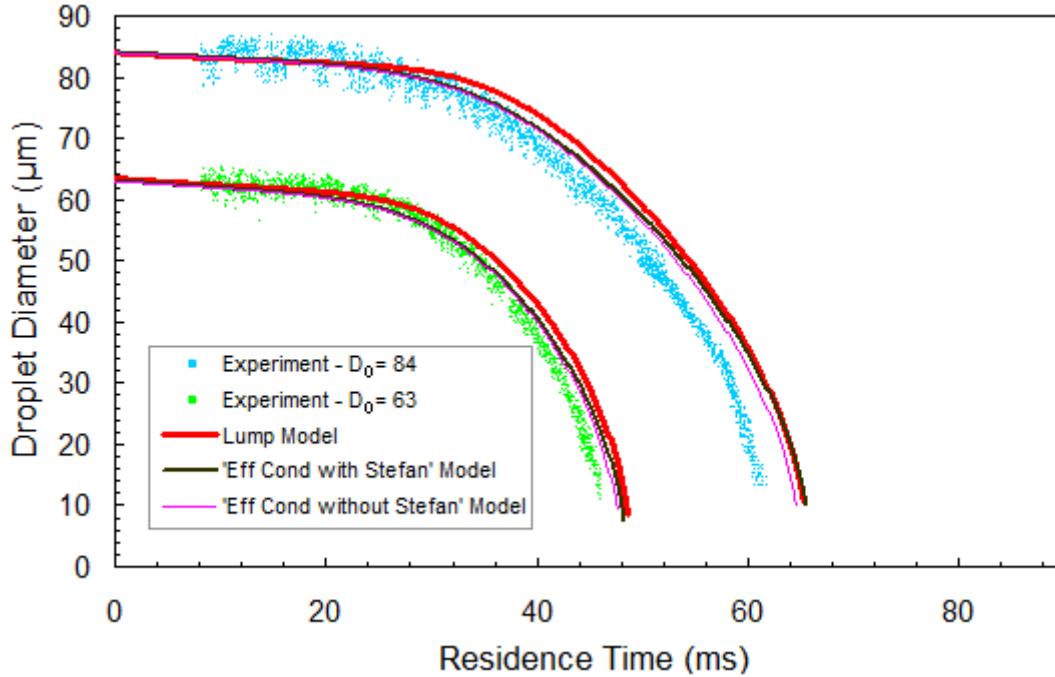


Figure 6.15: Comparison of results of three models (D vs t) with experimental data of 84 μm and 63 μm nonane droplets both in the high temperature setting

Figure 6.16 shows the variation of liquid Reynolds number and Peclet number of the 75 μm dodecane droplet as an example. Liquid Prandtl number is also indicated which reflects the change in the droplet dynamic viscosity which in turn depends on the droplet temperature. As seen in this figure, the Reynolds number is too low - much less than unity - which implies that the liquid phase is in the “viscous” regime for the whole of its lifetime. Even with much higher Prandtl number than the gas phase, due to this low Reynolds number the Peclet number is also very small and the internal heat transport can be taken as mostly through conduction [4]. The convection on the gas side is supposed to slightly improve the evaporation rate but not strong enough to cause any significant effect on the droplet internal fluid motion. For a droplet of larger diameter, these numbers will be higher due to the higher droplet Reynolds number (see equations 6.23-6.26) and the effect of external convection on the droplet internal heat and mass transport should therefore be stronger; this will be investigated later in this chapter. With such the above findings, the temperature distribution found from the model for this droplet is reckoned to realistically describe the liquid phase thermal state.

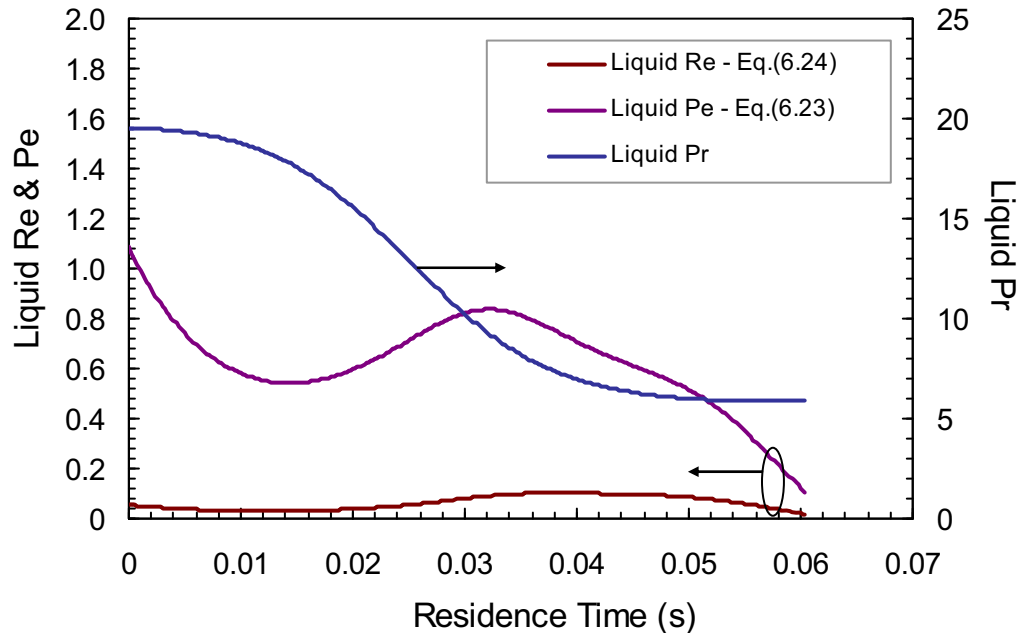


Figure 6.16: Liquid Prandtl, Reynolds and Peclet numbers of the 75 μm dodecane droplet evaporating at the high temperature setting

Simulation of the dodecane droplet evaporation is again shown in Figure 6.17 with the focus shifted now to the interpretation of the process in terms of the more detailed droplet temperatures. It is apparent here that during the preheating and the initial period of evaporation the center and the surface of the droplet have different temperatures and for this particular case, the maximum difference is 16.7 K. Though appears not large, it has been discussed that the behavior is sensitive to the droplet surface temperature (through the mass transfer number B_Y and the Clausius-Clapeyron equation which nonlinearly relates the droplet surface temperature to the vapor mass fraction Y_s at the interface). The initial, strongly unsteady evaporation is seen to correlate with the difference between two temperatures which implies the initially large amount of heat required for sensible heating. Once the droplet temperature becomes almost uniform at around 47.6 ms, the near steady period starts. Though not shown here, the droplet temperature found from the Lump model (Figure 6.3) is slightly lower than this surface temperature during the initial preheating period with the maximum difference of only 3.7 K occurring at around 31 ms; for the near steady period all temperatures are virtually the same. This explains the efficiency of the simple Lump model. During the initial period, as the temperature is low the slightly lower

predicted lump temperature than the more realistic surface temperature can lead to small incorrectness in the evaporation rate. For the near steady phase, the predicted rate of the Lump model is supposed to be closer to reality while that of the effective conductivity model is lower due to its treatment of constant liquid density (cf. equation 6.14).

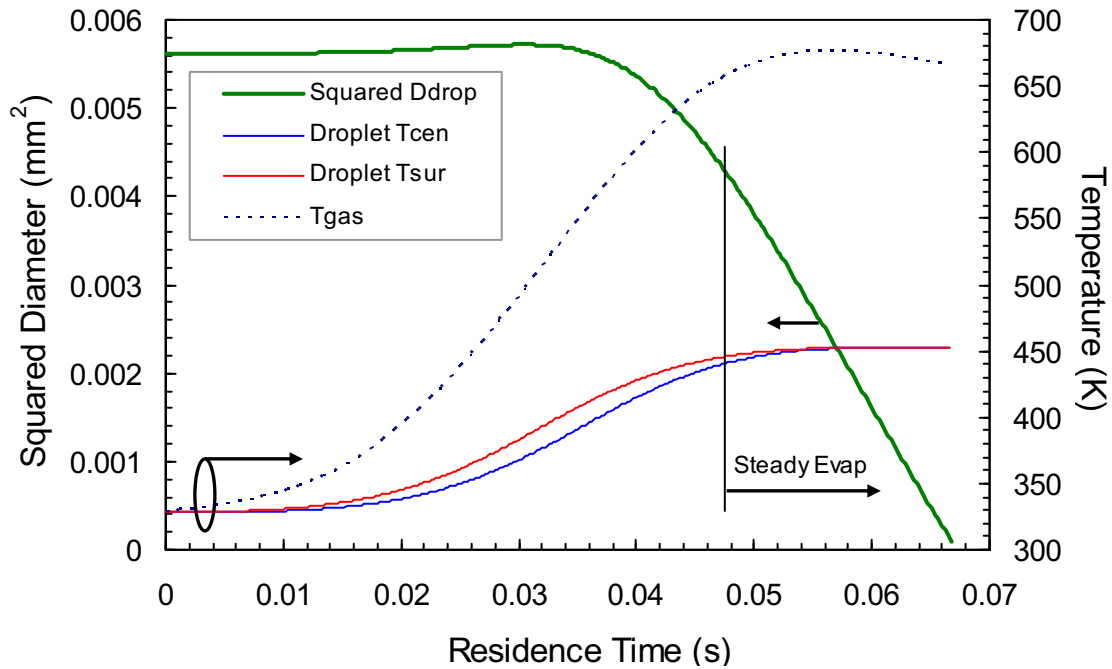


Figure 6.17: Droplet center and surface temperatures simulated by the effective conductivity model for the 75 μm dodecane droplet evaporating at the high temperature setting. Shown are also the gas temperature and droplet squared diameter.

To further understand the transport processes on the gas side in these conditions, Figure 6.18 shows the variation of the gas phase Lewis number (Le) and the mass and heat transfer numbers (B_Y and B_H , equations 6.7 & 6.18) during the lifetime of the 75 μm dodecane droplet as a typical example. With the assumptions used (see section 6.2.1) the Lewis number found here only provides a qualitative assessment. As seen, this number varies between 3.5 and 4.2, much higher than unity, a value widely used in many studies. This is also reflected in the difference between B_Y and B_H shown, see equation (6.18). In those investigations where Le assumes unity, $Sh = Nu$ as $Pr = Sc$, B_H (formulated for pure vaporisation with no sensible heating) equals B_Y when a steady state is reached. This is also a simple method used in [15] to find the steady state droplet temperature for a number of

hydrocarbons. Clearly the assumption of unity Le , if used here, will lead to error and, as seen, B_Y is always higher than B_H during the final steady phase. This renders the process to be dominated by mass diffusion for current conditions. Given B_H being defined as the ratio of the enthalpy available in the gas phase to the heat required for vaporizing the droplet, in combustors with high temperature and high pressure where the process is dominated by the heat transfer, the reverse is expected with $B_H > B_Y$.

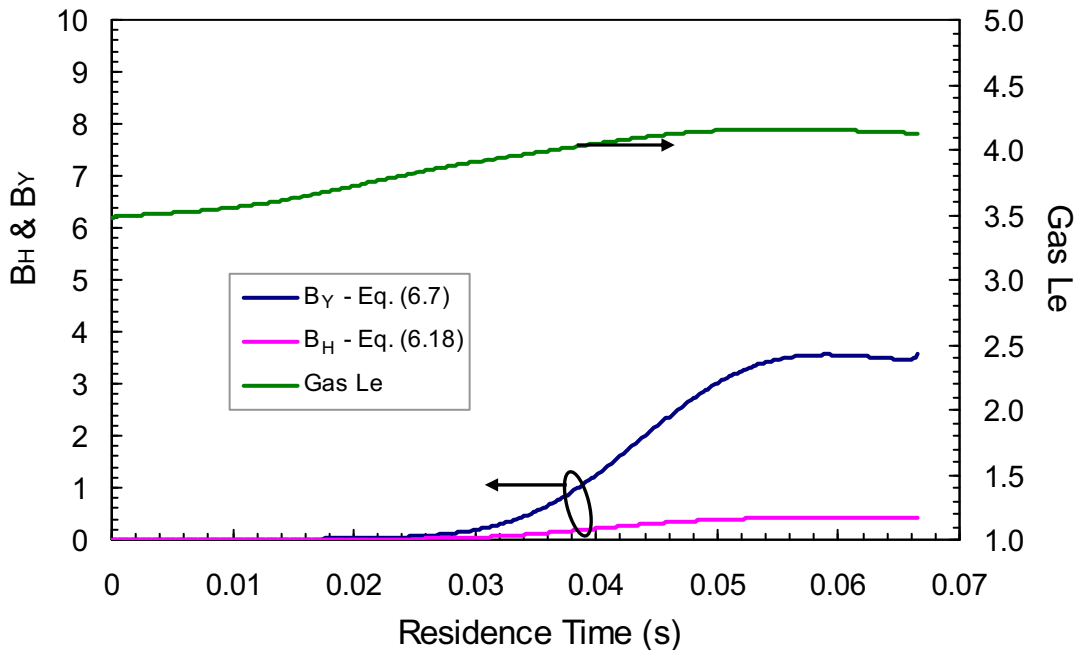


Figure 6.18: Gas Lewis and mass and heat transfer numbers for the 75 μm dodecane droplet evaporating at the high temperature setting

Application of the extended model to the smallest droplet in this work, the 45.5 μm decane droplet, reveals that the difference between the center and surface temperatures is small with a maximum of 5.5 K. This is indicative of the effect of droplet size on the evolution of its internal temperature distribution. For current investigation, the study of this effect, gas temperature effect and chemistry effect is however limited due to the difficulty in experimentation. To investigate these effects and the droplet behavior in a wider range of conditions, the next section is devoted to the evaporation simulation for different droplet sizes and gas temperatures. Furthermore the effect of droplet Reynolds number can also be investigated by simulating for different droplet initial velocities. Though giving some

difference from the present data, assessment of the suitability of the simple Lump model for conditions closely representing that in realistic devices will be performed, especially when the droplet size becomes just tens of microns. The simulation of diesel will also be explored.

6.6 Predicted Behavior in a Variety of Conditions

6.6.1 Effect of Gas Temperature

To investigate the effect of gas temperature on the droplet behaviour, four conditions of 500, 1000, 1500 and 2000 K have been used and the environment is assumed to be quiescent air. A droplet of initial size of 100 μm at 300 K is suddenly exposed to such environments and dodecane, as a widely investigated fuel, is chosen for this investigation. Included in this investigation is the comparison between two models: the effective conductivity with Stefan flow model here after referred to as Eff Cond model for short (though χ in equation 6.20 is set to 1 for the case of no slip effect, it still however accounts for the effect of droplet regression on the liquid phase transport through the term $d\bar{r}_s^2/d\tau$) and the simple Lump model. This comparison enables further analysis of the process. Figures 6.19, 6.20, 6.21 and 6.22, in turn, show the predictions of two models on the variations of diameter, evaporation rate and droplet temperatures at 500, 1000, 1500 and 2000 K. As the droplet lifetime at 500 K is much longer than that at the other three temperatures, Figure 6.19 has a separate time scale of 0-0.18 s while in Figures 6.20, 6.21 and 6.22 the time scale is 0-0.06 s.

A number of observations can be made from these figures. For all cases and for both models the evaporation rate curves reflect the droplet temperature curves. They both increase monotonically initially before attaining a steady state together. This is understood to be the initial unsteady period of preheating which is followed by the period of constant evaporation rate (D^2 -law behavior) until the end as expected. It is clear that the steady rate increases with gas temperature as does the equilibrium droplet temperature which is however always below the boiling point (for 500, 1000, 1500 and 2000 K the steady state droplet temperature predicted by both models is about 422.3, 471.2, 480.3 and 483.7 K

respectively compared with 488 K as boiling point). The droplet expansion is seen (from the Lump model) to be stronger for higher temperature. From both models, the preheating process is found to be faster for higher temperature as observed in the steeper droplet temperature curves; however the preheating time relative to the droplet lifetime is longer.

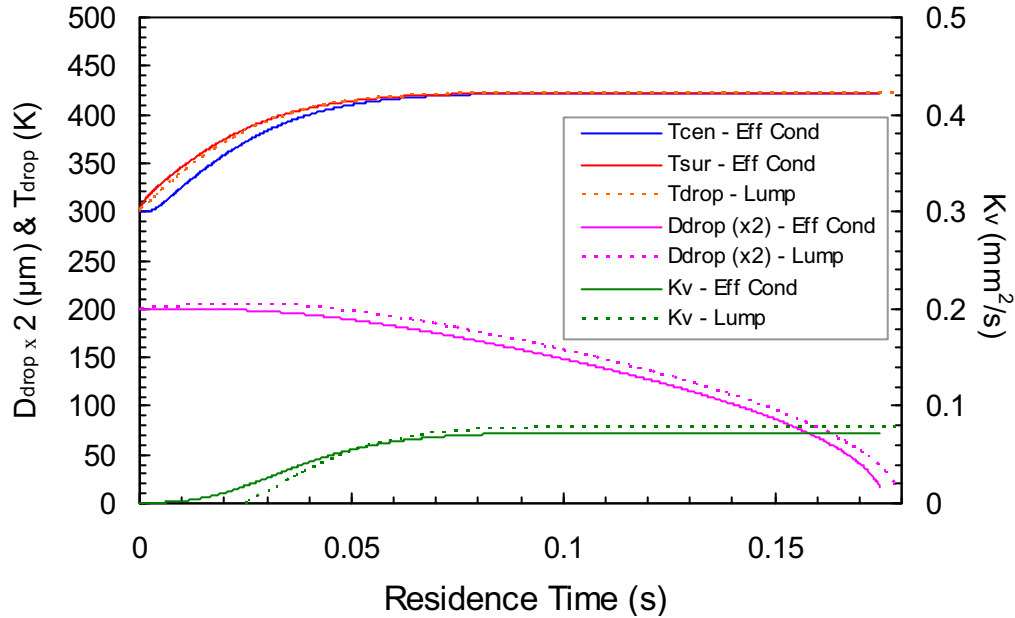


Figure 6.19: Predicted variations of droplet diameters (x2), temperatures and evaporation rates by the Eff Cond and the Lump model for 100 μm dodecane droplet at 500 K

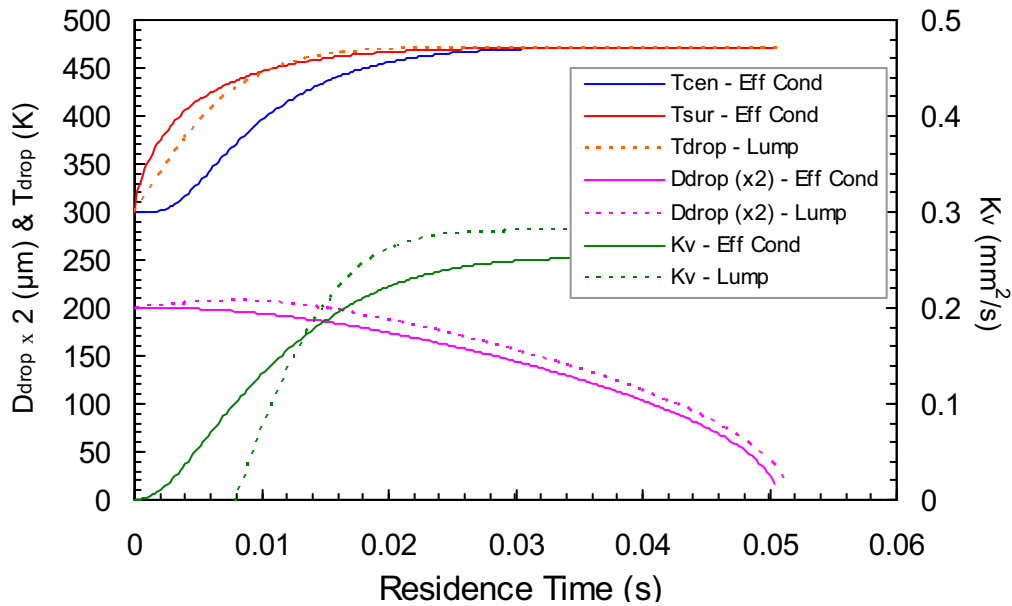


Figure 6.20: Predicted variations of droplet diameters (x2), temperatures and evaporation rates by the Eff Cond and the Lump model for 100 μm dodecane droplet at 1000 K

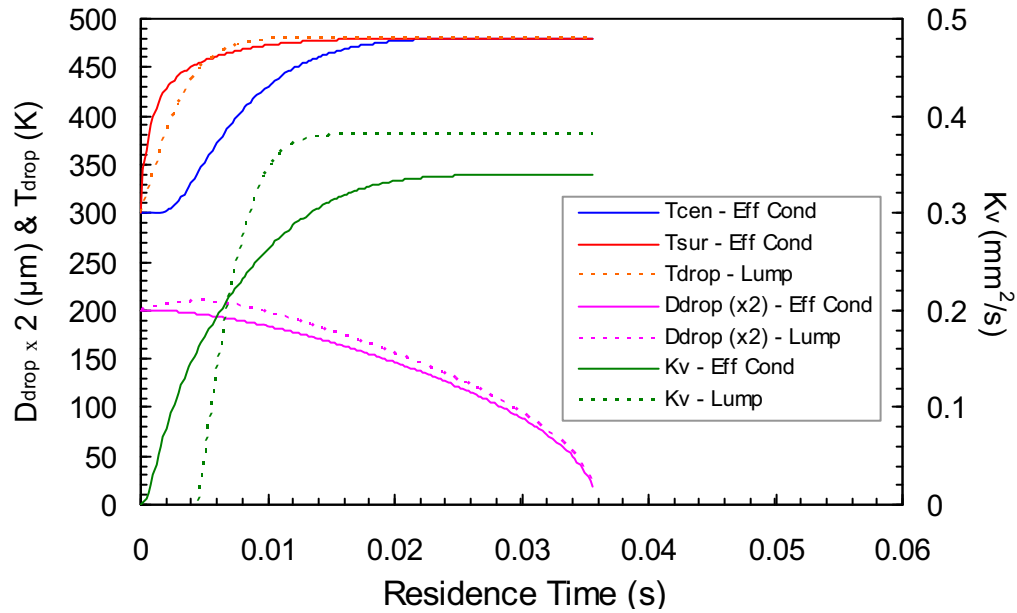


Figure 6.21: Predicted variations of droplet diameters (x2), temperatures and evaporation rates by the Eff Cond and the Lump model for 100 μm dodecane droplet at 1500 K

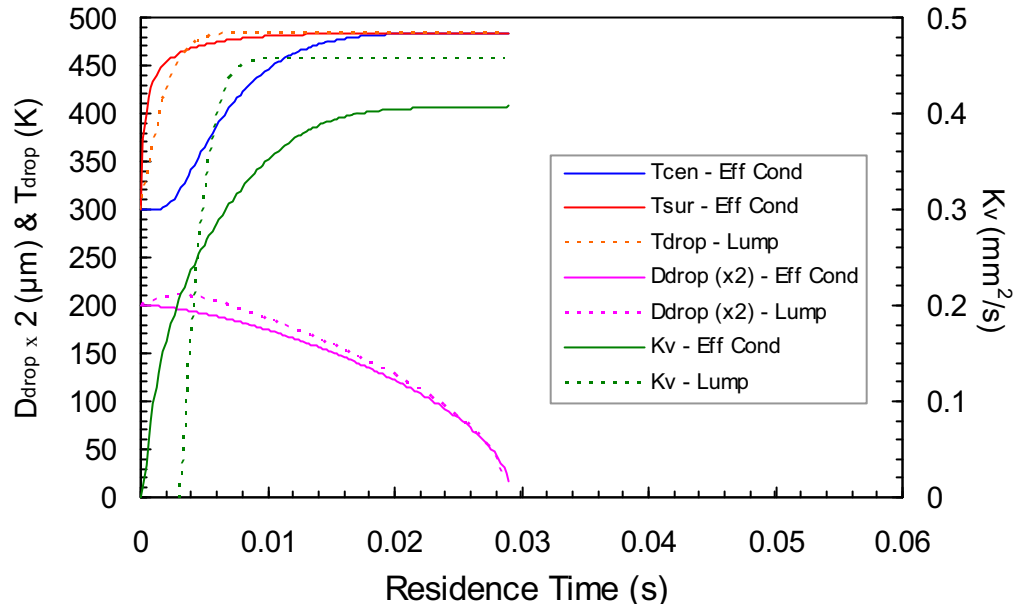


Figure 6.22: Predicted variations of droplet diameters (x2), temperatures and evaporation rates by the Eff Cond and the Lump model for 100 μm dodecane droplet at 2000 K

Between two models, the lifetimes predicted are different and this difference is larger for the lower temperature. This is understandable because for very long process the difference between two models is largely accumulated. For the evaporation rate predictions, the

difference between two models is larger for higher temperature which is certainly due to the larger variation in density in a wider range of temperatures. It would be ideal if in high temperature and high convection conditions such as those in real combustors, the Lump model can be used to simulate the behaviour of small droplets and this will be investigated later. In quiescent environments with $Re = 0$, the effect of Stefan flow is negligible (the mathematical integration of this effect also does not apply) and the equilibrium droplet temperatures found from two models are similar. For conditions used in this work with very small Stefan flow effect the simple Lump model therefore still presents its efficiency. In highly convective conditions this effect, as shown in the following section, is significant and its inclusion for the Lump model is necessary.

For all cases, the Lump model predicts an earlier start of the steady period which is directly related to the predicted droplet temperature which gets stabilized faster. This is a consequence of assuming the conduction of heat in the droplet to be infinitely fast of this model while for the Eff Cond model, the behavior (treatment) is close to the extreme of conduction limit. The latter therefore renders a higher surface temperature as reflected in the initially higher evaporation rate. The faster rate of the Eff Cond model further leads to a larger amount of heat spent for vaporisation and a smaller amount transferred into the droplet interior for heating up (see equations 6.13, 6.15 and 6.19, whereas the term $\ln(1+B_Y)$ increases with B_Y , the term $\ln(1+B_Y)/B_Y$ decreases). With a larger amount of sensible heat received for the Lump model, the droplet reaches an equilibrium state faster, for example at 2000 K this occurs at 9.4 ms with the droplet being 94 μm while for the Eff Cond model this starts later at 21.6 ms at a smaller size of 57 μm . The Eff Cond model is supposed to describe the initial process more realistically except for the expansion phenomenon which can only be obtained with variable density treatment.

During the period of adjusting to an equilibrium state, at the very low gas temperature (500 K condition) both the surface and center temperatures found from the Eff Cond model are close to the Lump temperature. This is reasonable since under very low heating rate, the process resembles the situation of infinite rate of liquid heat transport. At higher gas temperatures, the difference between the center and surface temperatures becomes larger and

their profiles are further distinct from the Lump profile. To better illustrate the internal evolution of the droplet radial temperature distribution, Figures 6.23a, b, c and d, in turn, show the development of this distribution with time for the 500, 1000, 1500 and 2000 K conditions. Due to the lifetime difference (nearly 175 ms at 500 K compared to less than 50 ms at three other temperatures) and for the clarity purpose, a time scale of 0-60 ms is used.

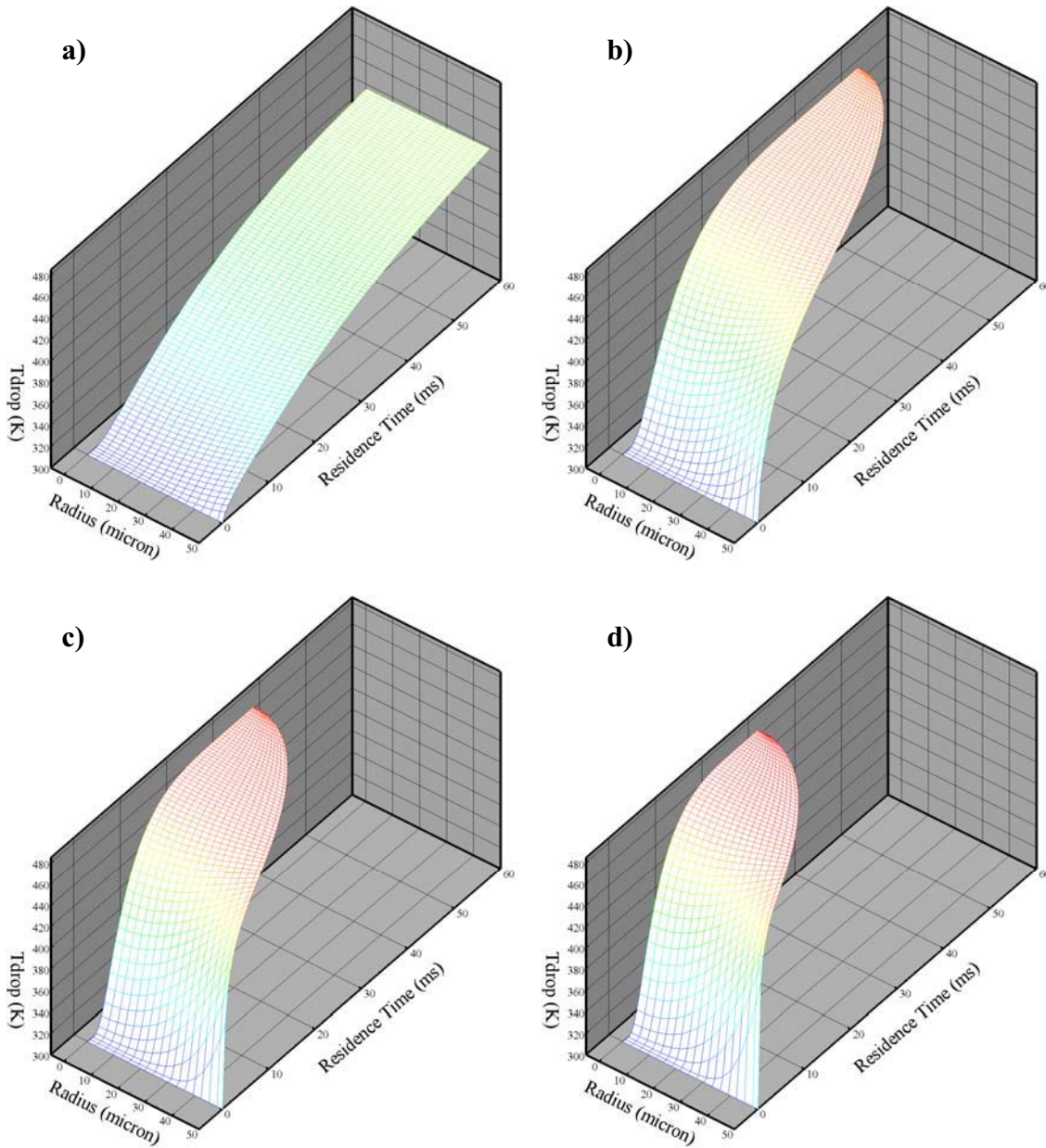


Figure 6.23: Gas temperature effect on the temperature distribution of a 100 μm dodecane droplet evaporating in still air at a) 500 K, b) 1000 K, c) 1500 K and d) 2000 K

It can be clearly seen from Figure 6.23a that the profiles along the radial co-ordinate slightly curve up near the droplet surface initially but then adjust to become leveled for most of its lifetime even though this figure does not show a full droplet history. This also indicates that the Lump model best represents the process in low temperature condition as was seen efficient for the experimental data in this work. At higher temperatures, the initial profiles apparently become steeper near the surface to reflect more pronounced the conduction limit of the liquid. As mentioned, while the Eff Cond model provides a more realistic liquid phase temperature distribution during the unsteady phase, the evaporation rate predicted by the Lump model for the equilibrium (steady) phase is more accurate as it uses the correct liquid density. To summarise the gas temperature effect on the droplet behavior in quiescent environments, Figure 6.24 shows the variation of the preheating time, which is defined as the time taken for the droplet temperatures predicted by the Eff Cond model to become uniform and steady, the droplet lifetime and steady evaporation rate found from the Lump model. The gas temperature is clearly seen to increase the evaporation rate and to reduce the preheating time and lifetime. Variation of these parameters is drastic between 500 and 1000 K. The preheating time and lifetime are much longer at 500 K.

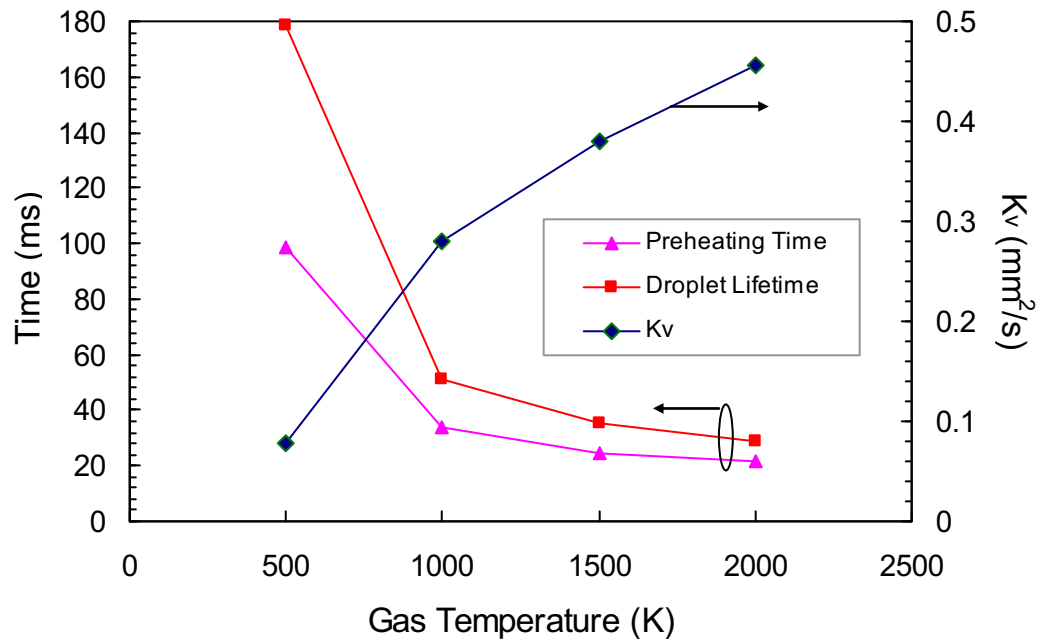


Figure 6.24: Gas temperature effect on the preheating time, droplet lifetime and evaporation rate of a 100 μm dodecane droplet evaporating in still air

6.6.2 Effect of Droplet Initial Velocity

In combustors using a spray nozzle, putting aside the liquid properties and the nozzle characteristics (e.g. hole size and shape), the exit velocity of a fuel jet depends on the injection pressure and combustion chamber pressure. An increase in injection pressure leads to an increase in the jet velocity. Once encountering the chamber gas, the atomization occurs and the jet breaks down into a multitude of small droplets with much lower velocities. The higher the chamber pressure is the lower the velocity of a droplet is. With stricter requirements regarding the combustion efficiency and emission, the system is generally designed to have very high injection pressures which can be above 2000 bar. Given this fact and the chamber pressure variation in a lesser extent (usually below 100 bar) the spray tip velocity can be of the order of few hundreds m/s [58]. It has however been made aware that the droplet of a certain size has a limit in its Reynolds number as it will be shredded into smaller sizes if its velocity relative to the gas is over a size dependant limit [117].

The effect of initial velocity is manifested through the improvement on the heat and mass transfers on the gas side as well as on the internal transport within the droplet through the slip effect. An investigation of a range of velocities possibly found in combustion devices is therefore desired. In convective environments, the higher the Reynolds number is the stronger the Stefan flow effect is as the modified Sherwood and Nusselt numbers are further deviated from the originals for certain F_Y and F_H , see equations (6.12). In higher temperature environments the Stefan flow effect is also more significant due to the increase of F_Y and F_H (always higher than unity) with B_Y and B_H , and this sensitivity is even stronger at higher Reynolds number. This is understandable when reviewing the definitions of F_Y and F_H as the ratios of the gas modeled boundary thicknesses with and without the Stefan flow which become very sensitive to δ_M and δ_T when δ_{M0} and δ_{T0} are small (for large Re). This effect is therefore important and is included in the Lump model for this investigation.

Again, a 100 μm dodecane droplet is used which assumes an initial temperature of 300 K and is injected into still air of 1500 K at 10, 30, 60 and 90 m/s. To illustrate the Stefan flow

effect, Figure 6.25 compares the predictions of the Lump model with and without it on the changes in droplet size and evaporation rate for the case of an initial velocity of 90 m/s. Variation of the droplet velocity is also indicated in this figure. Figure 6.26 presents the changes in Sherwood and Nusselt numbers, and droplet temperature for these two situations.

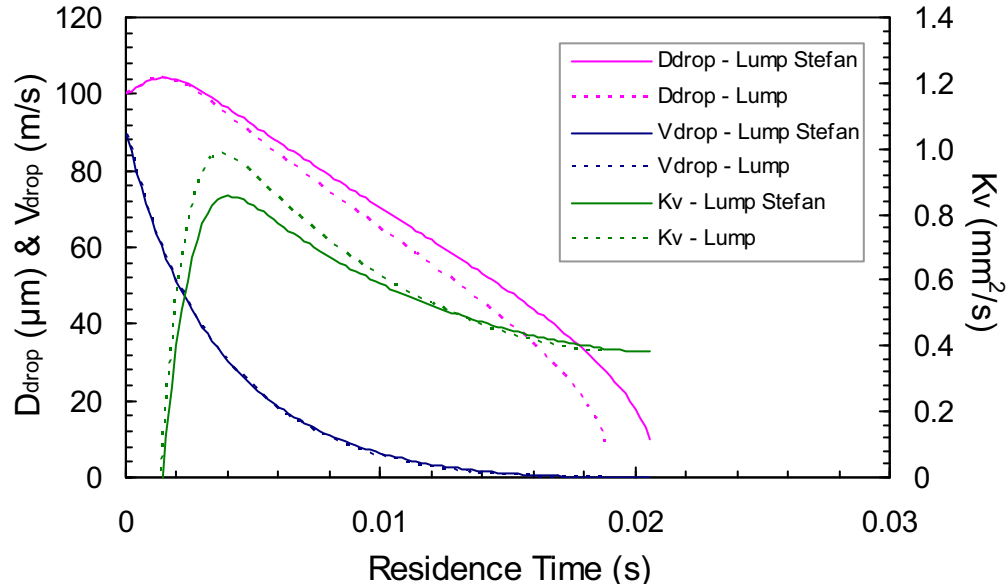


Figure 6.25: Stefan flow effect on the lifetime and evaporation rate of a 100 μm dodecane droplet with $V_o = 90$ m/s undergoing evaporation in still air at 1500 K. Shown is also the droplet velocity.

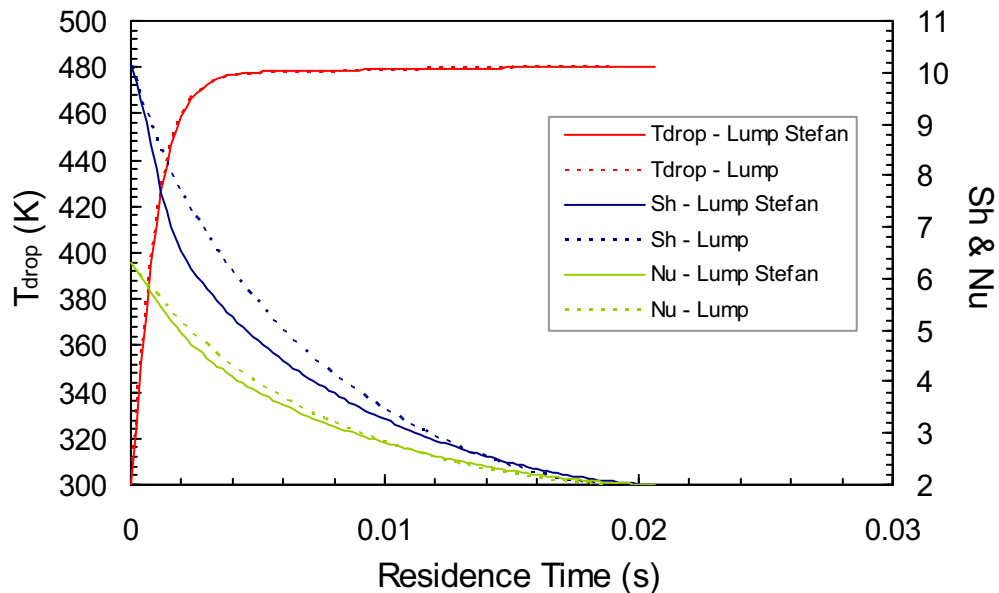


Figure 6.26: Stefan flow effect on the Sherwood, Nusselt numbers and the temperature of a 100 μm dodecane droplet with $V_o = 90$ m/s undergoing evaporation in still air at 1500 K

The Stefan flow effect is seen in this situation to be responsible for around 10% longer in the droplet lifetime which is reflected in the lower evaporation rate for more than half of its lifetime. For the final period, the slower rate of prediction without accounting for the Stefan flow effect is due to the lower Reynolds number; this is a result of lower velocity and smaller droplet size due to the faster evaporation in the earlier part. These can actually be observed in the comparison between the Sherwood number and its modification in Figure 6.26 which is the final representation of the Stefan flow effect. The Nusselt number and its modification also vary in a similar manner with the Sherwood numbers as expected and they all fall down to 2 at the end which is their value in a quiescent environment ($Re = 0$). Due to the varying effect of the Reynolds number for this condition it is apparent that the evaporation rate does not attain a steady state value as in a quiescent environment but shows a gradual decrease until the end after an initial sharp increase. The droplet temperature is nevertheless seen to attain a near steady phase (insignificantly increasing with time during this period) and shows very little signs of being affected by the Stefan flow effect.

To compare between the Eff Cond model and the Lump model (both accounting for the Stefan flow effect), Figure 6.27 shows their predictions regarding the variations of droplet diameter, evaporation rate and droplet temperatures for the 90 m/s condition as a typical example of a strongly convective environment. Similar to the quiescent environment, due to the assumption of fixed density at the mean value the Eff Cond model predicts a higher rate very shortly at the beginning and then a lower rate for most of the droplet's lifetime. For this condition, the predicted rates from both models are higher than those of the quiescent case (Figure 6.21) but finally asymptote to these values at the end. Again, given such difference between their rates, it is seen here that the lifetimes estimated by both models are almost the same. The droplet temperatures are found to reach similar near steady values given also that the Lump model predicts a slightly earlier stabilized point.

Prediction of the Lump model for all droplet initial velocities is shown in Figure 6.28 in which the behavior in the quiescent environment (presented as 0 m/s) is also included for assessment. In this figure, besides the variations in diameter and evaporation rate, the droplet Reynolds number is also included and it is seen to be initially around 7, 21, 43, and 64 for

the 10, 30, 60 and 90 m/s conditions respectively. This number decreases when the droplet gets smaller and falls down to zero at the end. It is obvious here that the higher the initial velocity of the droplet is, the shorter the lifetime is; however significant improvement occurs below 10 m/s and in the higher velocity range the improvement is much less. It is also noticed from the diameter curves that the expansion effect is smaller for the higher velocity (much smaller than for the quiescent case) because the evaporation starts earlier as is also reflected in the evaporation rate curve. The higher the initial velocity is, the further away from the D^2 -law the behaviour of the droplet is (see the evaporation rate curves).

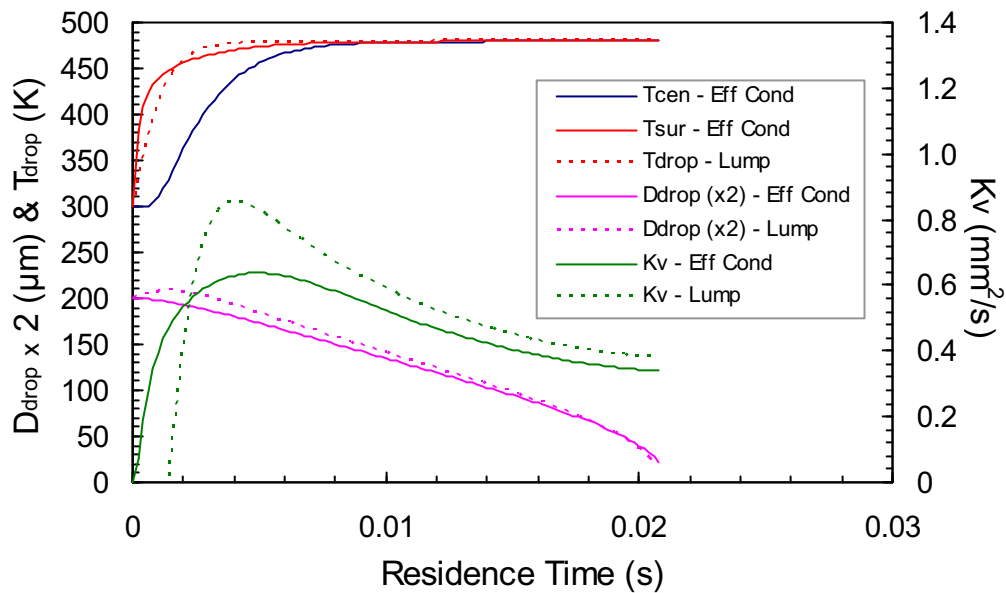


Figure 6.27: Predicted variations of droplet diameters (x2), temperatures and evaporation rates by the Eff Cond and the Lump models for a 100 μm dodecane droplet with $V_o = 90$ m/s undergoing evaporation in still air at 1500 K.

In the liquid phase, the Reynolds and Peclet numbers found from the Eff Cond model are shown in Figure 6.29 while the droplet center and surface temperatures are shown in Figure 6.30. Note in these figures that the time scale has been adjusted to 0.02 s to show clearer details. In Figure 6.29, the Reynolds and Peclet numbers have the same trend which exhibits an initial increase to a peak and then a decrease until the end. This initial behavior reflects the change in the dynamic viscosity, see equations (6.23-6.25), which varies as a function of the droplet surface temperature. The decrease after the peak is apparently due to the fall of the droplet Reynolds number. Amongst these conditions the difference is considerable. For

the 10 m/s condition, the peaks of the Reynolds and Peclet numbers are only about 120 and 1100 while for the 90 m/s condition, these are about 2300 and 21100.

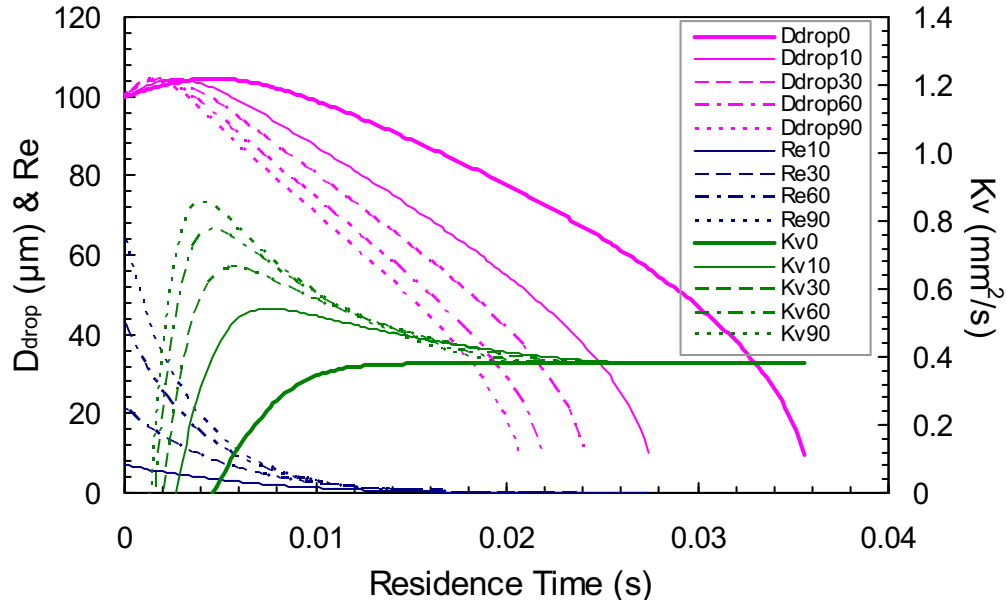


Figure 6.28: Effect of V_o on the variations of diameter and evaporation rate of a 100 μm dodecane droplet undergoing evaporation in still air at 1500 K. 0, 10, 30, 60 and 90, in turn, means $V_o = 0, 10, 30, 60$ and 90 m/s. Shown is also the droplet Reynolds number.

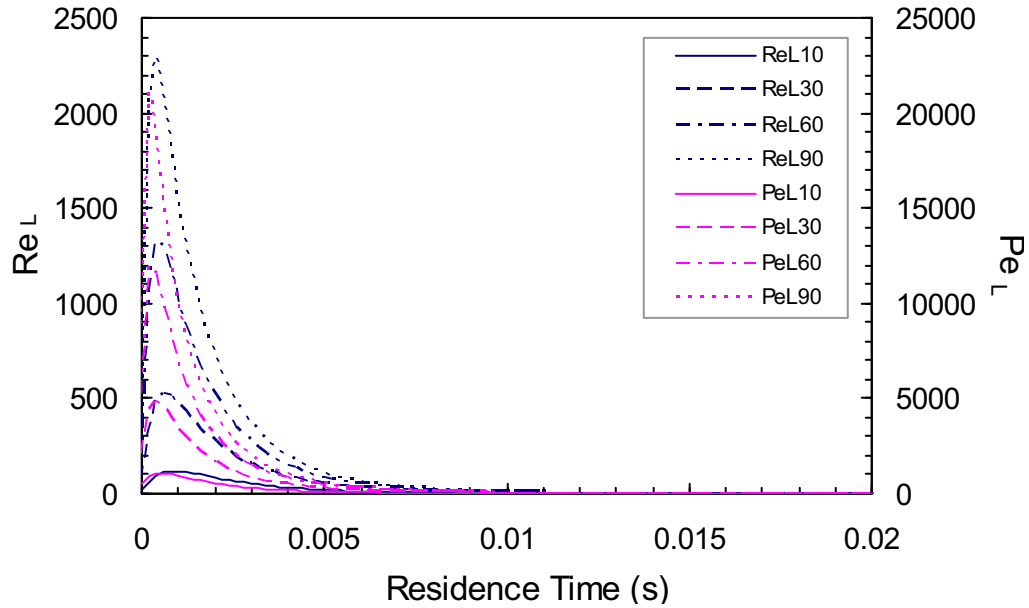


Figure 6.29: Effect of V_o on the liquid Reynolds and Peclet numbers of a 100 μm dodecane droplet undergoing evaporation in still air at 1500 K. 10, 30, 60 and 90, in turn, means $V_o = 10, 30, 60$ and 90 m/s.

In Figure 6.30, to compare between convective and quiescent conditions the droplet temperatures in Figure 6.21 are also indicated. Compared to the quiescent case, even at $V_o = 10$ m/s the improvement in the liquid phase internal heat transport has been significant and the droplet temperatures become uniform much earlier. The higher the velocity is, the earlier this uniformity occurs as expected. Amongst convective conditions, although the differences in Re_l and Pe_l are very large, the improvement seen is not significant. The early occurrence of droplet temperature uniformity at the 10 m/s condition can partly be a direct consequence of the small droplet size investigated, the effect of which will be further explored in the next section. For these conditions, the droplet attains virtually the same steady state temperatures.

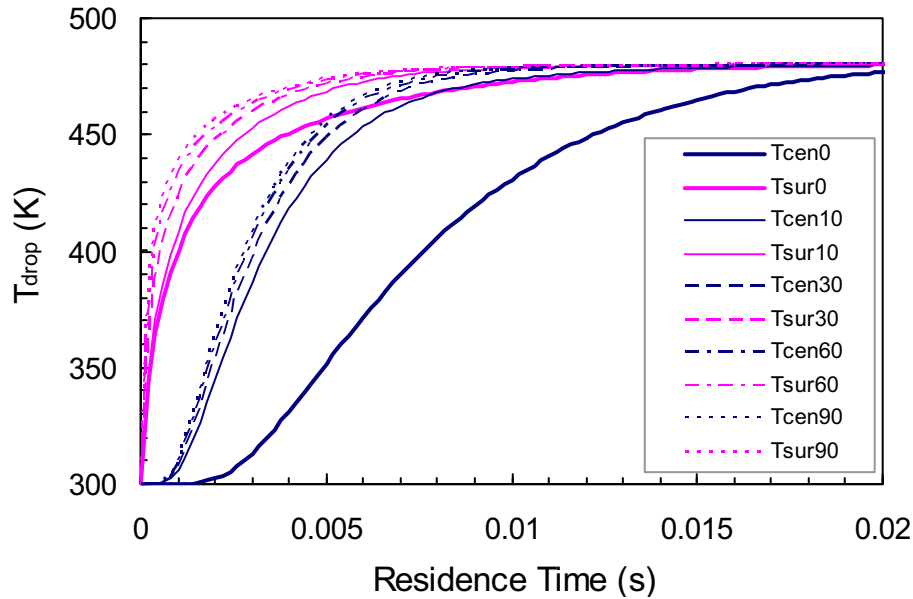


Figure 6.30: Effect of V_o on the temperatures of a 100 μm dodecane droplet undergoing evaporation in still air at 1500 K. 0, 10, 30, 60 and 90, in turn, means $V_o = 0, 10, 30, 60$ and 90 m/s.

6.6.3 Effect of Droplet Size

To investigate the effect of droplet size, a diameter of 300 μm is chosen which has been the focus of a considerable amount of research. Again, comparison between models for this size is needed and these are shown in Figures 6.31 and 6.32 for $V_o = 0$ and 90 m/s to represent the quiescent and strongly convective cases, respectively.

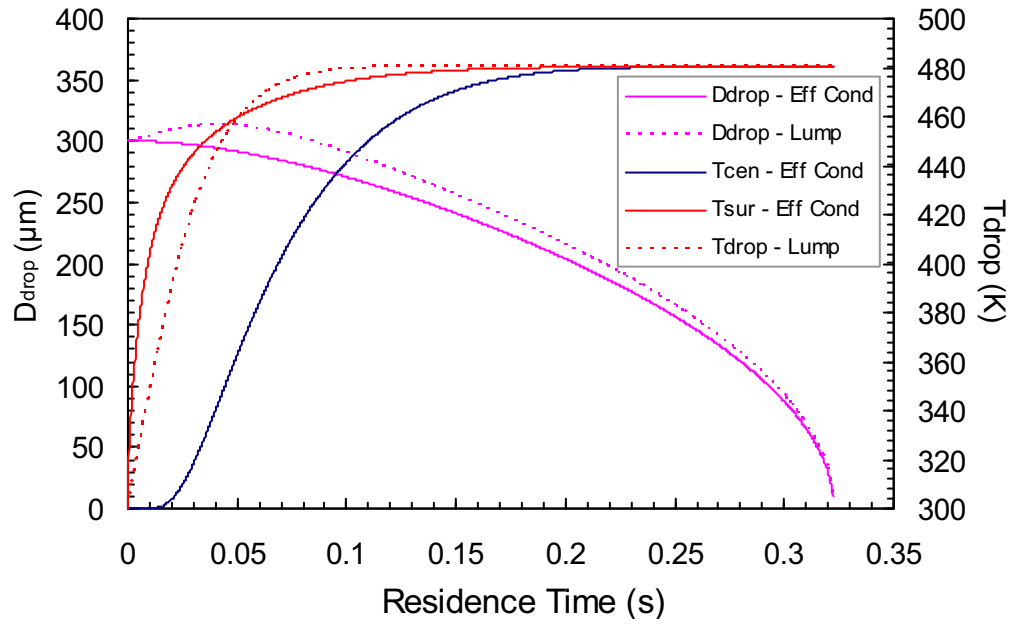


Figure 6.31: Predictions by the Eff Cond model and the Lump model for a 300 μm dodecane droplet with $V_o = 0$ m/s undergoing evaporation in still air at 1500 K

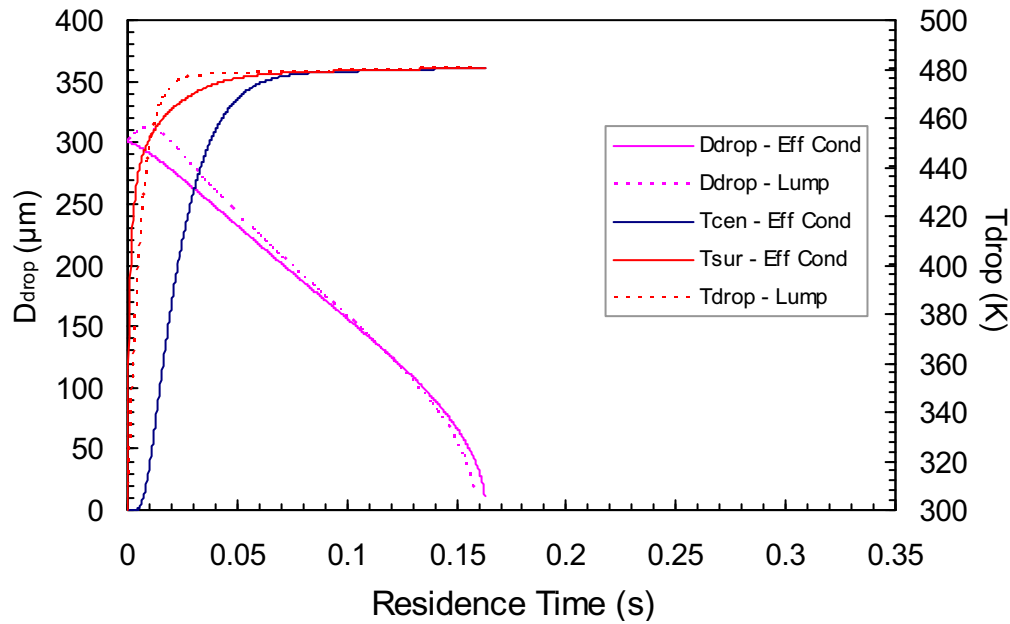


Figure 6.32: Predictions by the Eff Cond model and the Lump model for a 300 μm dodecane droplet with $V_o = 90$ m/s undergoing evaporation in still air at 1500 K

For both cases, the characteristics of predictions and differences in droplet temperatures and lifetime are similar to that of the 100 μm size (see Figures 6.21 and 6.27). Compared to the quiescent case and all other convective cases investigated, this convective case has the

largest difference between the lifetimes predicted by two models which is however only about 2.5% given the fact that for this size with a much larger volume (27 times that of the 100 μm droplet), the effect of density variation (reflected by the initial expansion) is larger. For the quiescent case, there is almost no difference as seen earlier for the 100 μm droplet. Similar to the 100 μm droplet, the equilibrium temperature predicted by two models for the 300 μm droplet after the initial unsteady period for the quiescent case is also 480 K. For the convective case, the droplet temperature still slightly increases during the later period until the end (as also found for the 100 μm droplet and will be explained later) although this increase is very slight from 478 to 480 K.

To compare between two droplet sizes, the data need to be shown in the normalized forms because the 300 μm droplet has a very long lifetime compared to the 100 μm droplet. As the very first illustration, Figure 6.33 expresses the variation of D^2 normalized by D_o^2 against time normalized by the droplet's lifetime for both diameters in the conditions of $V_o = 0, 10$ and 90 m/s. It is obvious from this figure that in quiescent condition ($V_o = 0$), the curves of both sizes lie almost on each other which characterise a linear relationship after an expansion period. Besides meaning the same steady evaporation rate for both sizes, this implies that in this condition the expansion characteristic time is qualitatively proportionate to the droplet's lifetime and hence the surface area while its strength is also proportionate to this area. In convective conditions, the relationship curves away from the linear behavior with a larger degree seen for the larger droplet. This is a consequence of the stronger interaction between the larger droplet and the surrounding gas. The higher the initial velocity is, the further away the curves are from the D^2 -law as expected. This plot also confirms that for both sizes, the convection effect in the condition of $V_o = 10$ m/s is already significant when considering the condition of $V_o = 90$ m/s, especially for the larger droplet. Another point that can be clearly observed here is the earlier start of evaporation and less effect of expansion for higher initial velocity which has been mentioned earlier.

As a reflection of the observations in Figure 6.33, Figure 6.34 reports the evaporation rate against the normalized time. Also included in this figure is the droplet Reynolds number for the conditions of $V_o = 10$ and 90 m/s. The evaporation rates in the quiescent condition for

two droplet sizes present coincident curves in this plot; this suggests again that the preheating time is also proportionate to the droplet surface area. While the same steady evaporation rate is clearly found for two sizes in this condition, under convection the rate of the bigger droplet is always higher than that of the smaller droplet. The higher evaporation rate of the bigger droplet is seen to correlate with its Reynolds number which, being the function of the droplet diameter, is significantly higher than that of the smaller droplet. From this plot, the slight increase in the droplet temperature reported earlier during the later period can be understood to relate to the Stefan flow effect and this temperature only approaches the steady value found in the quiescent condition when the evaporation rate approaches the steady rate in that condition at the end.

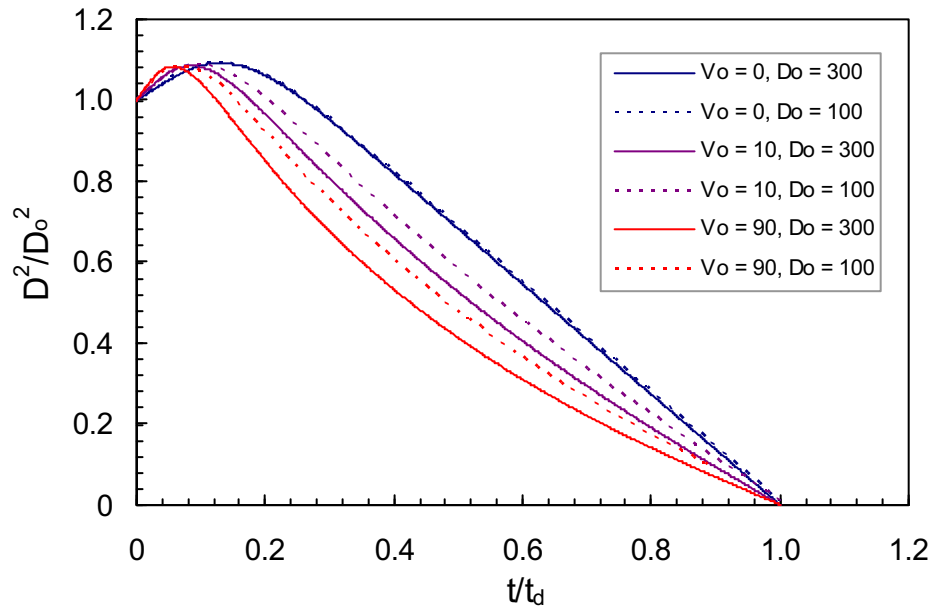


Figure 6.33: Lump prediction of normalized squared diameter against the normalized time for the 100 and 300 μm droplets with $V_o = 0, 10$ and 90 m/s evaporating in still air at 1500 K

To investigate the droplet temperature in more details, Figure 6.35 shows the variation of the center and surface temperatures against the normalised time with a scale of up to only 0.7 . For clarity purpose, only the quiescent and 90 m/s conditions are shown. Included in this figure is also the droplet Peclet number. As expected, for the quiescent condition two sizes have the same temperature profiles because in this condition the droplet internal heat transfer is characterized by a diffusional process (the effect of droplet regression rate is negligible)

the characteristic time of which is proportionate to the squared radius (surface area) and thus the droplet lifetime (given the treatment of constant liquid thermal diffusivity). For the 90 m/s condition, the difference between the surface and center temperatures is larger for the larger droplet and the external convection has a more direct consequence on the smaller droplet even though the Peclet number is much smaller than that of the larger droplet which reaches to a maximum of about 21100 compared to about 92300 of the larger droplet. The preheating time relative to the lifetime is smaller for smaller droplet. This implies an advantage for combustors using high injection velocities and small droplet sizes such as modern diesel engines because the evaporation process becomes steady faster (even though in these devices, other effects are also important such as the spray effect [71]).

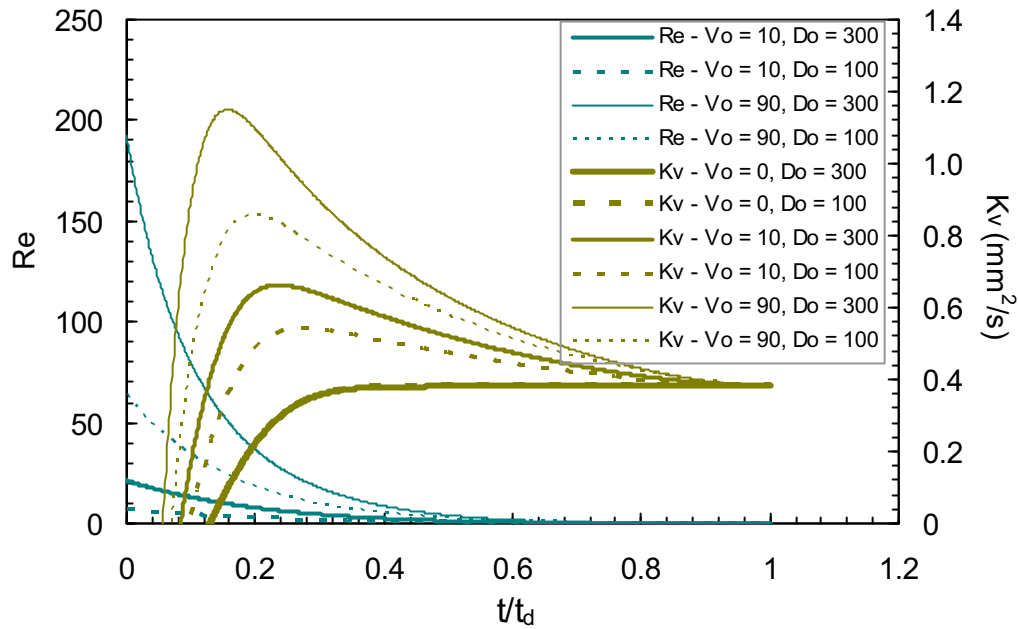


Figure 6.34: Lump predictions of evaporation rate and droplet Reynolds number for the 100 and 300 μm dodecane droplets with $V_o = 0, 10,$ and 90 m/s evaporating in still air at 1500 K

In summarising the size effect on the droplet behavior, Figure 6.36 shows the preheating time and the lifetime of two sizes for all values of V_o investigated and the ratios of these quantities of the bigger droplet to those of the smaller droplet. It is clear that the preheating time and the lifetime of the $300 \mu\text{m}$ droplet are substantially longer than those of the $100 \mu\text{m}$ for all conditions. At 10 m/s, the effect of convection on the behavior of both sizes has however been significant and for higher velocities, the process becomes less improved.

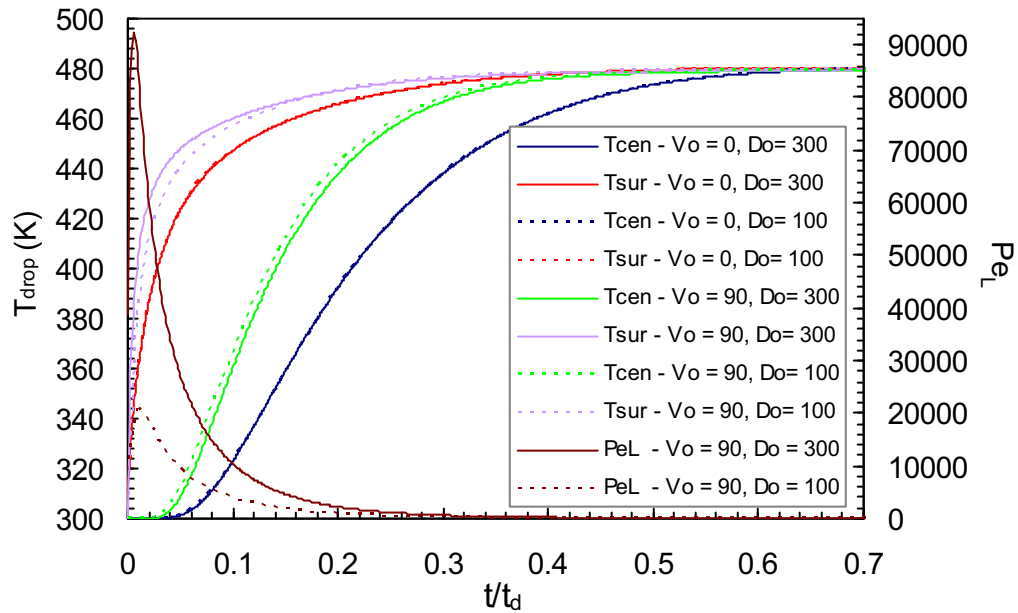


Figure 6.35: Eff Cond predictions of droplet temperatures and Peclet number for the 100 and 300 μm droplets with $V_o = 0$ and 90 m/s evaporating in still air at 1500 K

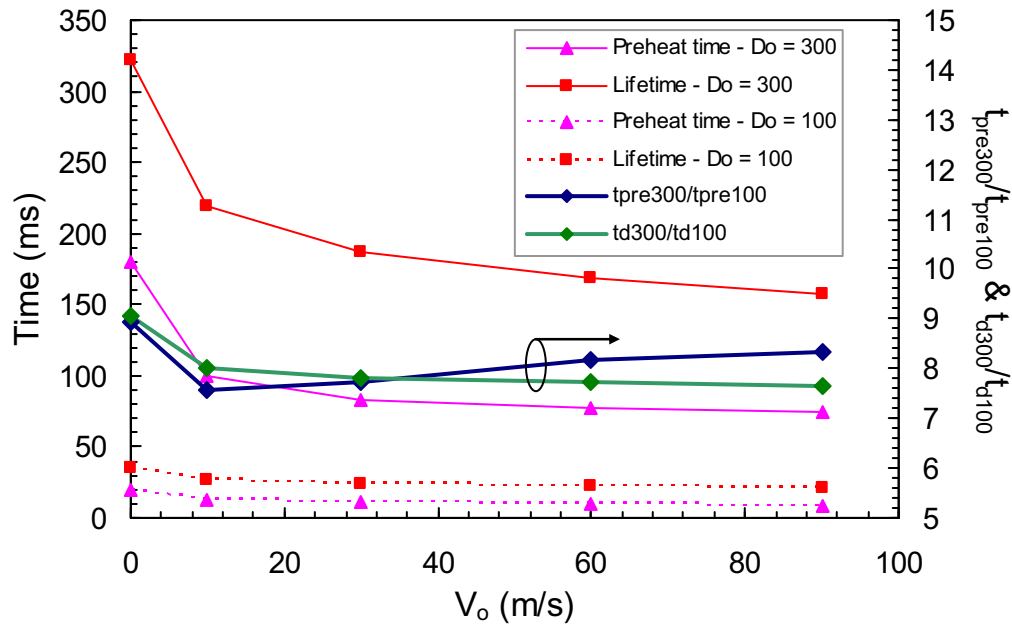


Figure 6.36: Variation of droplet preheating time and lifetime of the 100 and 300 μm droplets evaporating in still air at 1500 K against droplet initial velocity. Shown are also ratios of preheating time and lifetime of the 300 μm droplet to those of the 100 μm droplet.

In quiescent condition, both the preheating time and the lifetime of the 300 μm droplet are around 9 times those of the 100 μm droplet which is the ratio of their surface areas.

Under convection, the lifetime ratio decreases which is due to the larger convection effect on the evaporation rate of the bigger droplet. For the preheating time ratio, the decrease at 10 m/s is even more than the decrease in the lifetime ratio which implies that the heat transport in the bigger droplet is more affected than the smaller droplet in this condition. For higher velocity, this ratio then rises back to the lifetime ratio at around 30 m/s and then becomes higher at 60 and 90 m/s which is an indication that the heat transport inside the smaller droplet becomes more influenced than the larger droplet under these stronger convections.

6.6.4 Effect of Fuel Chemistry

To compare the models and to investigate the chemistry effect in more details, decane and nonane are included. Rather than showing all cases, only typical examples which are deemed necessary are shown in this section. Figures 6.37 and 6.38 compare the predictions by the Eff Cond and the Lump models of the variation of droplet diameter, evaporation rate and droplet temperatures of a 100 μm nonane droplet with $V_o = 0$ and 90 m/s evaporating in still air at 1500 K to represent the quiescent and convective environments, respectively.

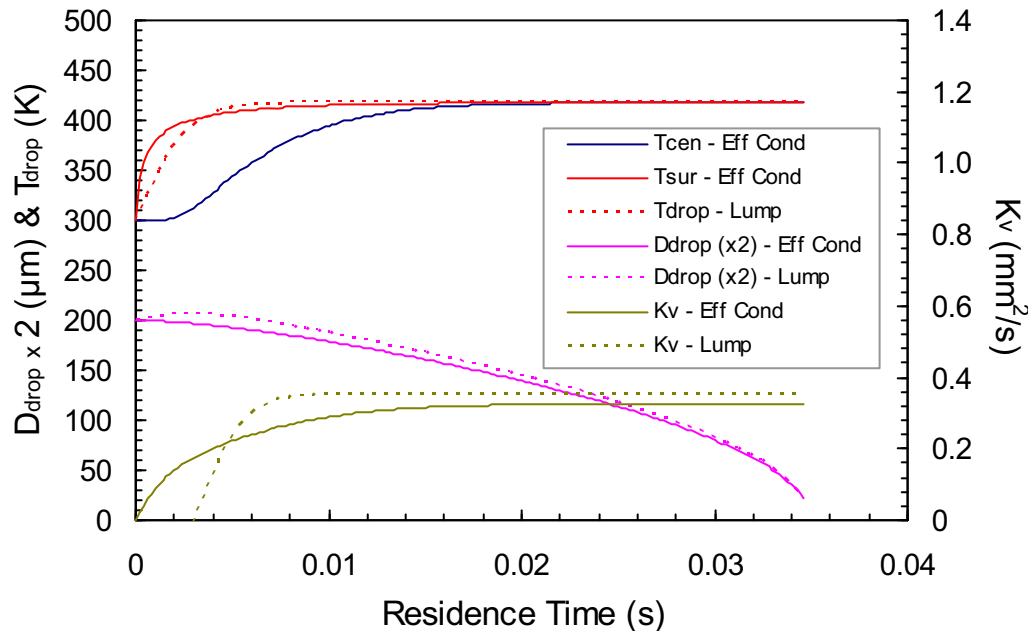


Figure 6.37: Predictions of diameter (x2), evaporation rate and temperatures of a 100 μm nonane droplet with $V_o = 0$ m/s evaporating in still air at 1500 K by the Eff Cond and the Lump models

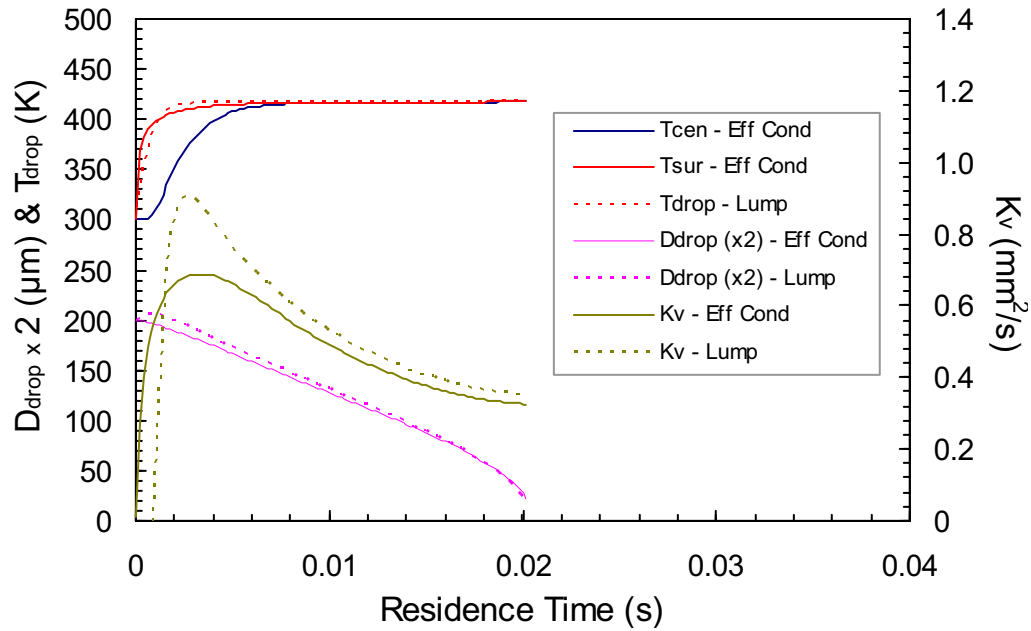


Figure 6.38: Predictions of diameter ($\times 2$), evaporation rate and temperatures of a 100 μm nonane droplet with $V_o = 90$ m/s evaporating in still air at 1500 K by the Eff Cond and the Lump models

As expected, nonane with much less effect of expansion brings the predicted rates between two models closer to each other given the same characteristics in the predicted droplet temperatures by two models. In quiescent environment, similar to dodecane droplet in Figure 6.21 there is no difference in the predicted lifetimes for nonane droplet. However at 90 m/s with a much shorter lifetime, the difference for nonane is 1% like dodecane in Figure 6.27 although this difference is negligible. This also applies to decane though not shown here. Afterall, these favor the applicability of the simple Lump model for conditions in combustors where the droplets are small and undergoing evaporation at high velocity and high gas temperature such as diesel engines.

To study the chemistry effect for these fuels, rather than investigating in convective conditions, quiescent conditions are used to provide the fundamental knowledge such as the difference in their steady state evaporation rates. In convective conditions, these rates vary in the same manner for all fuels, i.e. to be always higher and approach the quiescent steady rate at the end when the droplet velocity falls down to zero (e.g. see Figure 6.34 for dodecane).

Figures 6.39 and 6.40 compare the variations in diameter and evaporation rate for dodecane, decane and nonane at 500 K and 1500 K, respectively. At 500 K, the steady evaporation rate K_v is the highest for nonane and lowest for dodecane. This is reflected in the shortest lifetime of nonane and the longest lifetime of dodecane with a difference of about 35%. At 1500 K, it is now clear with a reverse situation that dodecane has the highest rate while nonane has the lowest rate. This can be due partly to the much higher droplet temperature for dodecane than nonane and therefore a lower density for this fuel, see equation (6.14). However it is also evident for this condition that the relative difference is very small of only 8.2% with K_v of nonane being $0.352 \text{ mm}^2/\text{s}$ and dodecane being $0.381 \text{ mm}^2/\text{s}$ while for the low temperature case, the relative difference is large of about 23.2% with K_v of nonane being $0.0961 \text{ mm}^2/\text{s}$ and dodecane being $0.078 \text{ mm}^2/\text{s}$. A very small difference of only 2.8% between their lifetimes is therefore expected for the 1500 K condition. In fact, these droplets finish their lives like having the same evaporation rate and this is favored by the mentioned observation in Aldred and Williams [7] though for higher evaporation rates in combusting conditions. In convective conditions, though not shown, the difference in the lifetime of small droplets of these fuels becomes also insignificant.

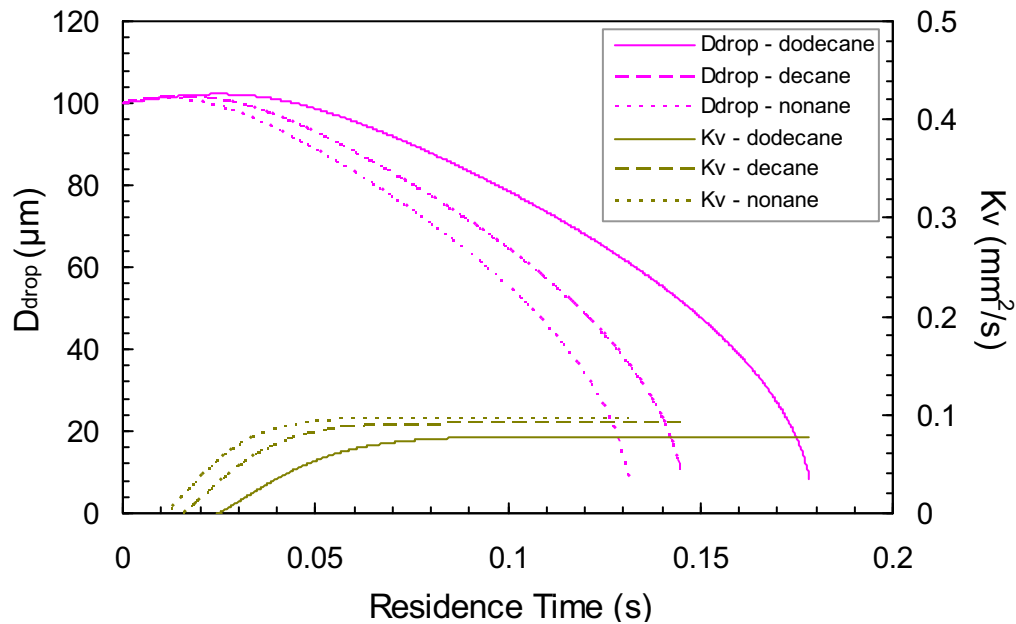


Figure 6.39: Variations of diameter and evaporation rate of the $100 \mu\text{m}$ droplets of dodecane, decane and nonane with $V_o = 0 \text{ m/s}$ evaporating in still air at 500 K

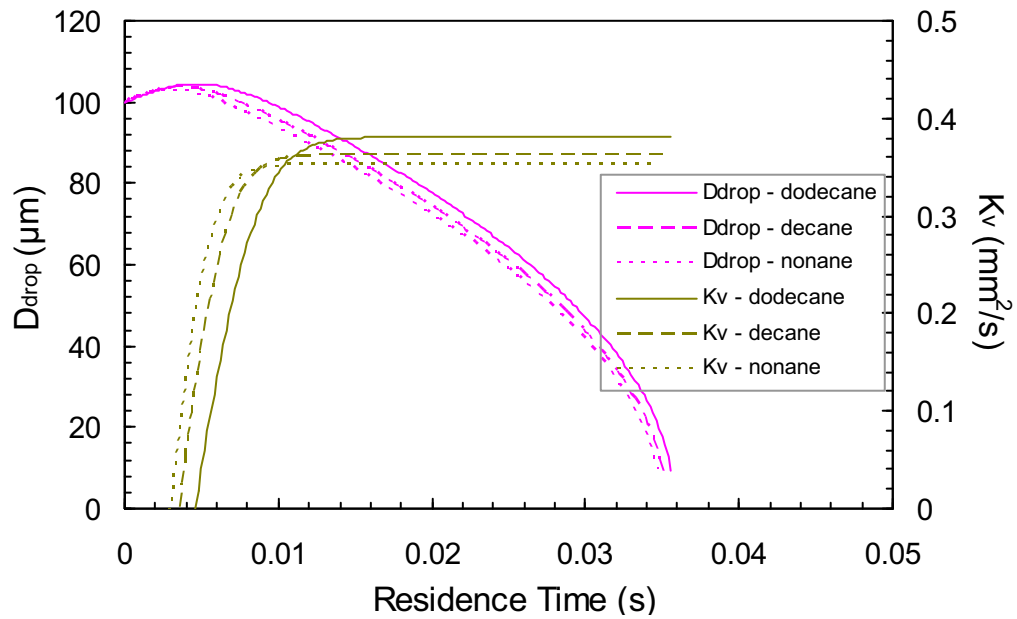


Figure 6.40: Variations of diameter and evaporation rate of the 100 μm droplets of dodecane, decane and nonane with $V_o = 0$ m/s evaporating in still air at 1500 K

To summarise the chemistry effect, Figure 6.41 illustrates the variation of steady state K_v against gas temperature. As seen, being lower at low temperature, the K_v of the heavier Alkanes become closer and then passes that of the lighter once the temperature passes 750K.

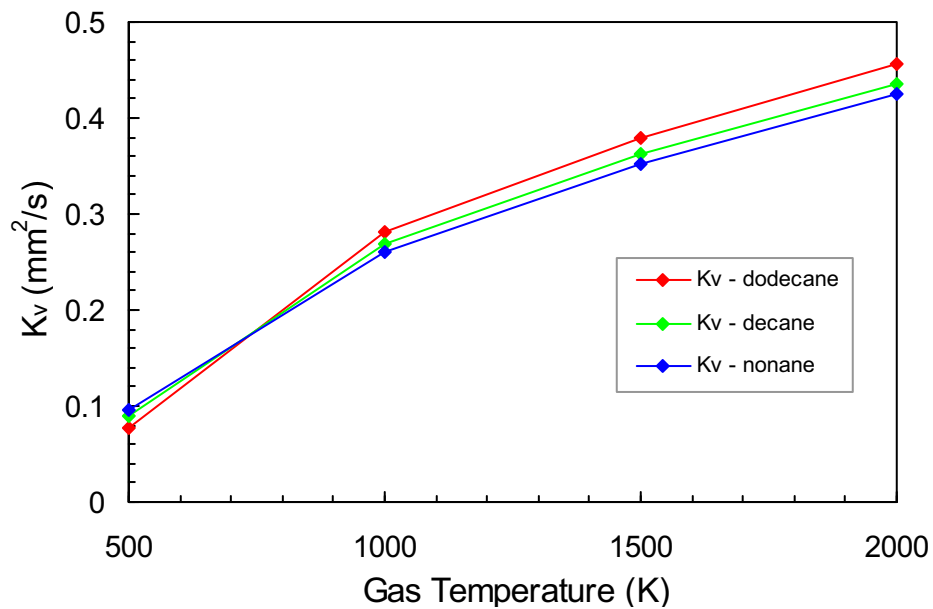


Figure 6.41: Variation of steady state K_v of the dodecane, decane and nonane droplets against gas temperature

On the liquid side, these fuels have close thermal diffusivity (e.g. at 1500K, α_L is estimated to be 0.0516, 0.0562 and 0.0593 mm²/s for dodecane, decane and nonane, respectively). Their preheating time is therefore close to each other or to be more precise it is the longest for dodecane and the shortest for nonane to reflect their α_L values even though they reach different steady state temperatures. An example of the predicted temperatures of their 100 μ m droplet is shown in Figure 6.42 for the 1500 K condition. Under convection the preheating time becomes shorter for all fuels as depicted earlier for dodecane.

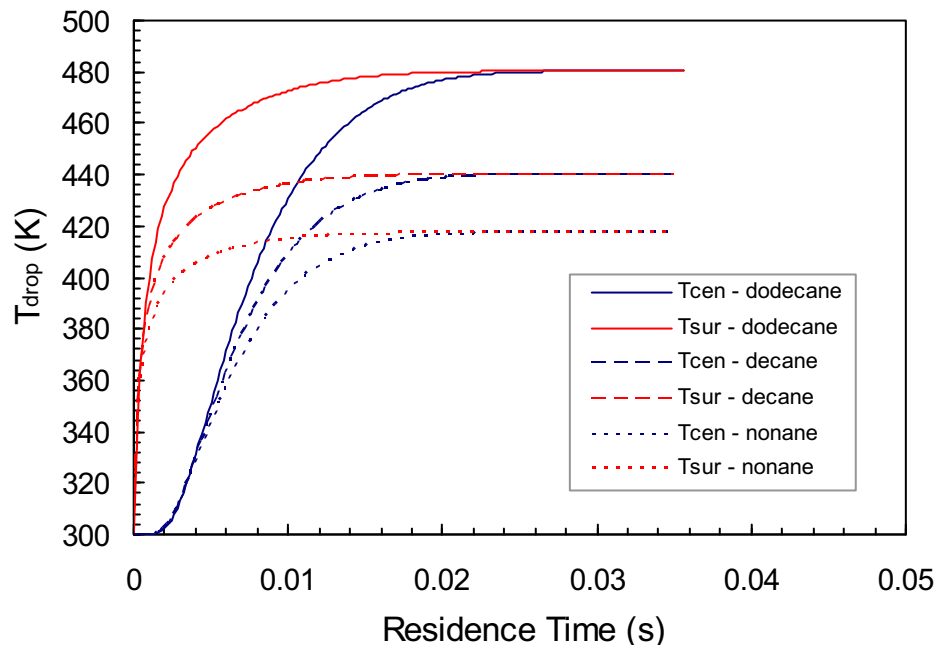


Figure 6.42: Temperature variation of the 100 μ m droplets of dodecane, decane and nonane with $V_o = 0$ m/s evaporating in still air at 1500 K

6.6.5 Multicomponent Effect

As a multicomponent fuel, diesel appears to behave rather similarly to those alkanes for the experimental conditions used in this work. The question that needs to be addressed is if this fuel can be modeled as a single fuel with a set of representative properties here. This can however be a non-trivial task because the condition used is of variable temperature while it has been shown earlier that the evaporation rate of a single alkane can be higher or lower than the adjacent alkanes depending on the gas temperature. Also the behavior of diesel, as

has been discussed earlier, depends on the convection condition which presents a behavior between the two mentioned extremes of the liquid phase so this simple approach of using a representative fuel for modeling diesel may be limited. It is perhaps easier to do this when the behavior is close to the diffusion limit extreme (as in present conditions) because on the other side of well-mixed extreme, the behavior is like the batch distillation process with droplet temperature increasing continually and evaporation rate decreasing until the end which is obviously different from those of typical single component fuels.

As apparent in Chapter 5, diesel presents a slower rate than dodecane but not far away and as such, tridecane ($C_{13}H_{28}$) properties have been used as the input for the model. The prediction results, in comparison with the experimental data, are shown in Figures 6.43 and 6.44 for diesel droplets of initial diameters of 76 and 85 μm , respectively. It is clear from Figure 6.43 for the 76 μm droplet that the model gives delay similar to those presented earlier for other fuels which also leads to about 9.6% longer the evaporation time. However, more importantly the local behavior appears rather similar to the measurement for the evaporation period and the predicted steady state evaporation rate is found to be $0.205 \text{ mm}^2/\text{s}$ compared with $0.192 \text{ mm}^2/\text{s}$ of diesel. For the 85 μm series in Figure 6.44, the difference in the lifetime is small and this unsystematic difference again suggests a high possibility of the existence of some mismatch between adjacent measurement zones in the early part of the droplet lifetime for all series. The portion of the curve in the late evaporation period presents a very slight different form from the measurement given little variation of gas temperature during this period. Like the 76 μm series, for this series while the experimental data may show an earlier start of evaporation the model predicts a much earlier start of the near steady period with predicted rate being $0.202 \text{ mm}^2/\text{s}$, slightly higher than the measured of $0.19 \text{ mm}^2/\text{s}$. Beside these, the model with use of tridecane properties cannot predict the expansion strength correctly. It can be inferred here that use of a selected alkane, while leading to correct prediction of one or more parameters, will lead to incorrect prediction of other parameters, especially for this multicomponent fuel.

The strong expansion of the 85 μm series that lasts long may signal that the droplet internal concentration starts early its adjustment (on the way to a steady profile in the final

period) to behave close to a diffusion limit mode otherwise longer preferential behavior would have suppressed this expansion due to fast evaporation of volatile components. The obvious preheating period of around 27-29 ms for these diesel droplets can be compared to 1600 ms of the 900 μm kerosene droplets of Khan et al [53] at roughly the same temperature.

Given the above similarities and differences, the prediction using tridecane properties enables a further assessment of the diesel droplet behavior. It is understood here that for standard light diesels, properties of some alkane such as dodecane, tridecane or even some more proper set of properties can be used to approximate the droplet evaporation process (especially the lifetime) in certain conditions. Especially in high temperature environments and with use of small droplets as widely found in more recent combustion devices, the application of this simple approach of using a representative set of properties is favored as the lifetime is very short and local differences would not greatly modify this extremely important quantity. However the very high convection present in most of these devices, besides shortening down the droplet lifetime and so favoring the use of this model, also shifts the behaviour of this multicomponent fuel towards the side of the well-mixed extreme which may hinder the application of this model.

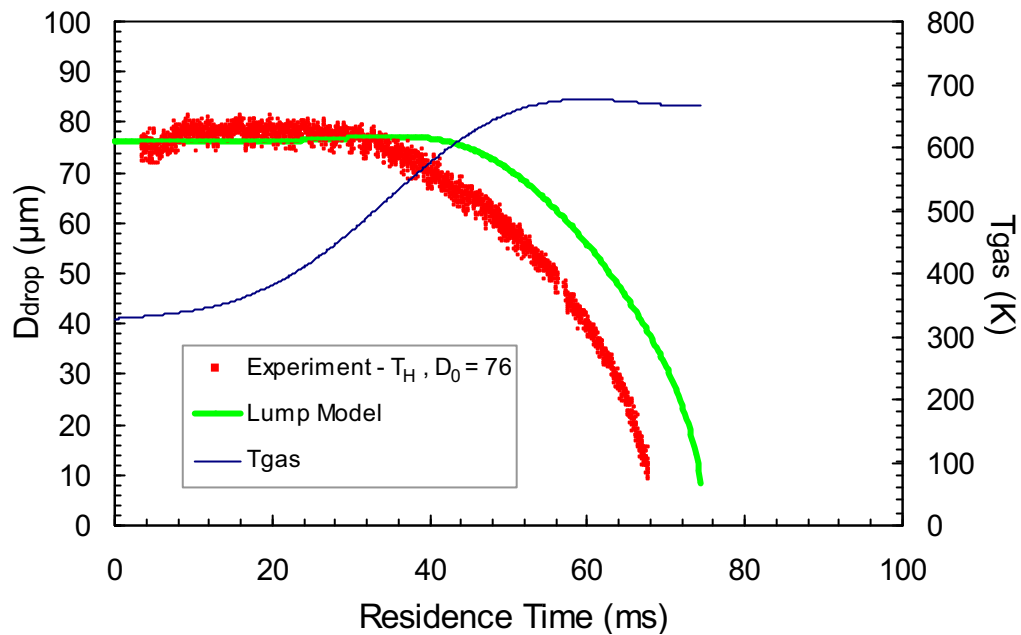


Figure 6.43: Comparison of the Lump prediction using the properties of tridecane with the experimental data of the 76 μm diesel droplet. Shown is also the gas temperature.

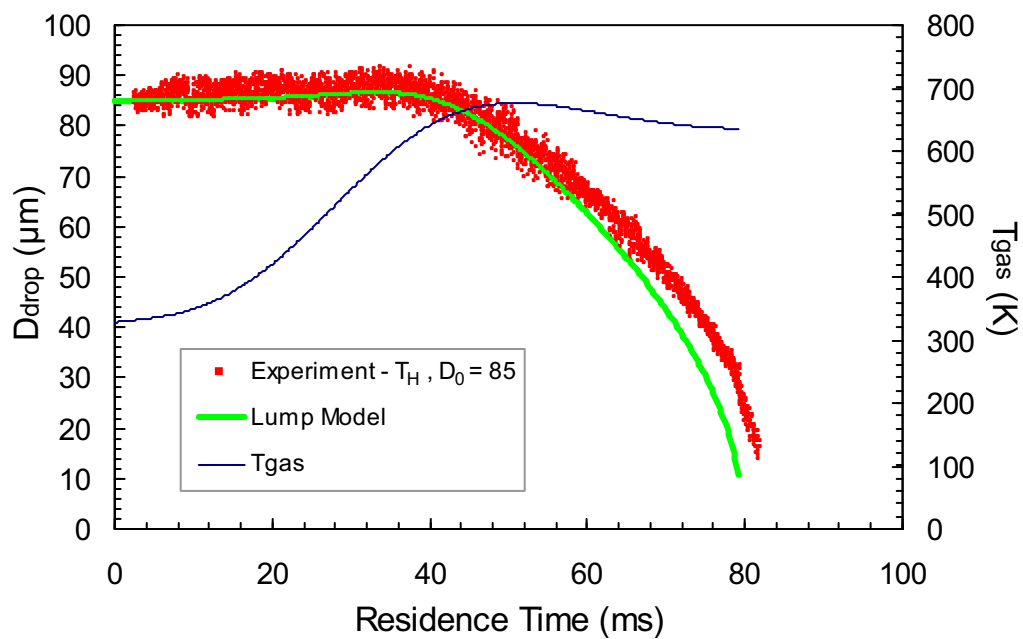


Figure 6.44: Comparison of the Lump prediction using the properties of tridecane with the experimental data of the 85 μm diesel droplet. Shown is also the gas temperature.

Chapter 7

Conclusions

In this work, an MDIH-DPIV technique has been successfully developed to measure the evaporation rates of fuel droplets whose sizes are typical of those found in the sprays produced from modern high pressure injection systems. When combined with high speed digital particle image velocimetry, magnified digital in-line holography enables the measurement of both the average and instantaneous evaporation rates of fuel droplets with sizes down to 10 μm undergoing heating loads in slightly convective flows. Smaller size is possible, but the higher magnification setting needed will narrow the measurement zone for most typically sized CCD arrays rendering the measurement difficult in such conditions where droplet position can be variable. This new technique offers a long distance of focus which makes it even more attractive for measurements in similar situations.

With the new technique developed, a full analysis of measurement uncertainty has been undertaken. Uncertainty analysis of the MDIH results indicated that while small for other sources, largest errors of about $\pm 4 \mu\text{m}$ were found resulting from the optics imperfections and $\pm 3.8 \mu\text{m}$ from the threshold value chosen for droplet size estimation. For velocity data, assessments have shown that PIV analysis depends on the quality of reconstruction. While the algorithm can fail to cross-correlate up to 20% of data points for some series, the velocity error was found negligible. This has been verified by applying a Gaussian noise model on the reconstructed images which indicated that the increase in the noise level represented by the noise distribution standard deviation σ of up to 20 (out of 255 of 8-bit image) reduces the correlation coefficient originally from around 0.96 to 0.12 while the

variation in the displacement relative error is within only 2%. The affect of reconstruction position on the PIV result was also investigated which was found to be negligible.

Given the uncertainty found for each component technique, the uncertainty in the evaporation rate was estimated based directly on the D^2 - t curve. For average measurement the error was found to be typically small of about 2.5% for the whole evaporation period, but for more local rates in 3.5 mm blocks of data as well as for instantaneous measurement of similarly sized block, the largest error was found to be around 22%.

Application of this technique to study the droplet evaporation behavior and to investigate the effect of droplet initial diameter, gas temperature and fuel chemistry on the process for nonane, decane, dodecane and light automotive diesel yielded the following results:

- ❖ For average rate measurements which cover almost the entire droplet evaporation history, at peak temperatures used of nearly 680 K all alkane fuels were found to evaporate at rather similar rates with indications of very slightly higher rates for lighter fuels. At lower temperature, this trend becomes clearer. Diesel however presents the lowest rate of all fuels under current conditions but not far from the rate of dodecane.
- ❖ For all fuels, the evaporation rate was found to be very sensitive to the gas temperature; it increases almost linearly with this temperature. With the use of two gas temperature settings the evaporation behavior was also found to be largely influenced by the preheating effect. For both settings, there exists an initial period which shows some degree of expansion for all fuels except for nonane. While diesel has a higher indicated boiling point, the expansion is slightly less than dodecane and the evaporation starts early when the temperature is still well below the indicated boiling point due to the evaporation of light components of this fuel. Decane was seen to experience a similar level of expansion as diesel.
- ❖ From both the average and instantaneous measurements it was found that in these conditions, convection has very little effect on the process. The droplet initial diameter

was found to play no noticeable role on the evaporation rate but it increases the preheating time and expansion level. This initial diameter also has very slight effect on the droplet velocity. For all cases, the droplet relative velocity falls to zero at the end when the droplet gets smaller and completes its life.

- ❖ Diesel as a multicomponent fuel initially shows preferential vaporisation behaviour but appears later to behave like a single component fuel to reach a near steady period but at a later time than dodecane. During this period the evaporation is supposed to proceed in the diffusion-limited mode. The near-steady evaporation rates of diesel are similar to those of other studies with much larger droplets in rather similar conditions which is another evidence of no effect of initial diameter on this rate.

A simple Lump model which incorporates a number of assumptions such as infinite liquid conductivity, spatially constant thermophysical properties for single liquid droplet but accounting for the preheating effect and convection by using film theory was formulated. In general, this model was found efficient to approximate the experimental data in terms of evaporation rate but not the droplet lifetime which can be due to possible delay in predicted start of evaporation and/or the experimental uncertainty in measurement zone adjustment. Expansion of diesel, dodecane and decane was also found from the model however its strength is slightly weaker than observed which was thought to be due to the neglect of the thermal radiation likely present near the flame front. The use of this model provided the following results.

- ❖ After entering the vessel, it takes a significant amount of time for the “cold” droplet to reach near steady temperatures; this reflects slow heating rates in the conditions used. The droplet temperature, which depends on the gas temperature, was found to control its evaporation rate and so explains the strong dependence of this rate on the surrounding gas temperature. The initial unsteady evaporation was seen to correlate with the droplet temperature which continually increases with the gas temperature. For the final near-steady period, the droplet temperature is well below the liquid boiling point and is almost constant given little variation of the surrounding gas temperature.

- ❖ During its lifetime, the droplet relative velocity was found to be very small of less than 0.1 m/s. The droplet Reynolds number decreases monotonically from around 0.3 near the reactor entrance to zero at the end which explains the very limited role of convection on the evaporation process in these conditions.

To investigate the Stefan flow effect and more realistic droplet temperature for current conditions, extension of the model was made which integrates an effective conductivity concept for the droplet treating its thermophysical properties including the density as fixed for simplicity. This extension also helps to explore the possibility of the Lump model to be used for simulating the droplet behaviour in extended conditions for which some further investigations on the droplet behavior have been done. The following are the main findings:

- ❖ For current conditions, the Stefan flow effect was found very small. The strongly unsteady period was seen to correlate with the difference between the droplet surface and center temperatures. For all cases the maximum difference is however not large, for example it is about 16.7 K for 75 μm droplet and even much smaller of 5.5 K for 45.5 μm droplet. The liquid phase internal transport was found to be mostly by pure thermal conduction and therefore such the above temperature difference was understood to be an advantage gained for small droplet size. This explains the efficiency of the infinite conductivity concept used in the Lump model for present conditions. The droplet temperature was found to be almost uniform before it reaches the near steady period.
- ❖ If putting aside the experimental uncertainty in adjusting the measurement zones which was likely present, the lifetime predicted by the effective conductivity model without accounting for the Stefan flow effect is the closest to the data while the Lump model gives better local prediction as it accounts for liquid density variation. The smaller the droplet is the closer the predictions of these models and the data are to each other. This poses the question of whether the Lump model can be applicable to other conditions.
- ❖ From the extended simulations of the dodecane droplet of 100 μm undergoing evaporation in still air at constant temperatures of 500, 1000, 1500 and 2000 K, it was

found that while small for 500 K, the difference between the droplet surface and center temperatures at high gas temperature during the initial unsteady period is significant (e.g. at 2000 K this difference is about 150 K). The droplet temperature is always lower than the boiling point (e.g. nearly 5 K below the boiling point at 2000 K). At higher temperature the preheating time is shorter but relative to the lifetime it is longer. Also at higher temperature the lifetime of the Lump model is closer to that of the Eff Cond model despite the fact that its predicted rate during the initial unsteady period can be largely incorrect. For all temperatures, the steady droplet temperatures predicted by two models are the same. The increase in evaporation rate and decrease in preheating time and lifetime with gas temperature were found large between 500-1000 K.

- ❖ From the extended simulations of the dodecane droplet of 100 μm with different initial velocities of 10, 30, 60 and 90 m/s undergoing evaporation in still air at 1500 K, the Stefan flow effect, which slows down the evaporation, was found to be stronger for higher velocity and was thus accounted for in the Lump model. The velocity was found to increase the evaporation rate which asymptotes to the rate in the quiescent case at the end when the droplet velocity falls to zero. The predicted lifetime of the Lump model was found to be almost the same with that of the Eff Cond model at all investigated velocities bearing in mind that the 90 m/s condition is supposed to be close to that in many real combustors. Also at higher velocities, the expansion was seen to be weaker and the preheating time is shorter due to the improvement in the liquid phase heat transport; predictions by both models should be closer to the real behaviour.
- ❖ The effect of diameter was studied by additionally investigating a 300 μm dodecane droplet. While the expansion is much stronger for this size, for the 90 m/s condition the difference in lifetime predicted by both models is the largest which is however only 2.5%. For this size, certainly the difference between the droplet center and surface temperatures in the initial period is much larger, but the steady temperatures found from two models are the same. In the quiescent condition, while the preheating time was found to be proportionate to the droplet surface area, the two sizes have the same steady evaporation rate which confirms no role of droplet size on this rate. Under convection,

the larger droplet has a higher evaporation rate at the same initial velocity due to greater interaction with the external gas. While the larger droplet is more influenced by external convection in the 10 m/s condition, in conditions with a velocity higher than 30 m/s the convection has a more direct consequence on the smaller droplet with its preheating time relative to its lifetime being shorter.

- ❖ From the extended simulations of the 100 μm droplets of dodecane, decane and nonane for the above ranges of temperatures and initial velocities, it was found that for lighter fuels the two models tend to give closer predictions, not only the lifetime but also the evaporation rate due to less effect of expansion and less variation in the liquid density (less variation in droplet temperature). At high velocity and high temperature the difference between predictions becomes small for all fuels and this again supports the usability of the Lump model in depicting those small single component droplets evaporating in high temperature, strong convection conditions. Investigation in the quiescent condition revealed that at low gas temperature, the evaporation rate of the heavier fuel is slightly slower but then becomes higher than that of the lighter fuel once this temperature exceeds 750 K; however, the relative difference becomes very small.
- ❖ To explore the possibility of using a set of properties for simulating the diesel in the experimental condition used, that of tridecane have been used as the input for the Lump model. This is based on the fact that the evaporation behavior looks rather similar to that of a single fuel. While this set of properties was seen not able to predict the expansion and possibly also the droplet lifetime, the local behaviour is well predicted for one set of data and closely predicted for other set of data. It was inferred that for a light diesel fuel, some alkane such as dodecane or tridecane could be used to approximate some important process parameters (e.g. lifetime or evaporation rate) in certain conditions. For small diesel droplets evaporating at high temperature, this simple approach may be efficient, however under the very strong convection, this is uncertain as diesel would evaporate preferentially in turn of the component molecular weight.

Bibliography

1. Abdel-Khalik, S. I., Tamaru, T. and El-Wakil, M. M., A Chromatographic and Interferometric Study of the Diffusion Flame around a Simulated Fuel Drop. *15th Symposium (International) on Combustion*, the Combustion Institute, Pittsburgh, PA, 1975. p. 389-399.
2. Abdel-Qader, Z. and Hallett, W. L. H., The Role of Liquid Mixing in Evaporation of Complex Multicomponent Mixtures: Modelling Using Continuous Thermodynamics. *Chemical Engineering Science*, 2005. 60: p. 1629-1640.
3. Abramzon, B. and Sazhin, S., Droplet Vaporisation Model in the Presence of Thermal Radiation. *Heat and Mass Transfer*, 2005. 48: p. 1868-1873.
4. Abramzon, B. and Sirignano, W. A., Droplet Vaporisation Model for Spray Combustion Calculations. *International Journal of Heat and Mass Transfer*, 1989. 32: p. 1605-1618.
5. Aggarwal, S. K., Tong, A. Y. and Sirignano, W. A., A Comparison of Vaporisation Models in Spray Calculations. *AIAA Journal*, 1984. 22: p. 1448-1457.
6. Agoston, G. A., Wood, B. J. and Wise, H., Influence of Pressure on the Combustion of Liquid Spheres. *Jet Propulsion*, 1958. 28: p. 181-188.
7. Aldred, J. W. and Williams, A., The Burning Rates of Drops of n-Alkanes. *Combustion and Flame*, 1966. 10: p. 396-398.
8. Bird, R. B., Stewart, W. E. and Lightfoot, E. M., Interphase Transport in Nonisothermal Mixtures. In: *Transport Phenomena*, John Wiley & Sons, NY, 2nd Ed, 2002. p. 671-725.

9. Birouk, M. and Gökalp, I., Current Status of Droplet Evaporation in Turbulent Flows. *Progress in Energy and Combustion Science*, 2006. 32: p. 408–423.
10. Box, G. E. P. and Muller, M. E., A Note on the Generation of Random Normal Deviates. *The Annals of Mathematical Statistics*, 1958. 29: p. 610–611.
11. Buchhave, P., Particle Image Velocimetry - Status and Trends. *Experimental Thermal and Fluid Science*, 1992. 5: p. 586-604.
12. Burger, M., Schmehl, R., Prommersberger, K., Schäfer, O., Koch, R. and Wittig, S., Droplet Evaporation Modeling by the Distillation Curve Model: Accounting for Kerosene Fuel and Elevated Pressures. *Heat and Mass Transfer*, 2003. 46: p. 4403–4412.
13. Castanet, G. and Lemoine, F., Heat Transfer within Combusting Droplets. *Proceedings of the Combustion Institute*, 2007. 31: p. 2141-2148.
14. Cheng, S. and Chandra, S., A Pneumatic Droplet-on-demand Generator. *Experiments in Fluids*, 2003. 34: p. 755-762.
15. Chin, J. S. and Lefebvre, A. H., Steady-state Evaporation Characteristics of Hydrocarbon Fuel Drops. *AIAA Journal*, 1983. 21: 1437-1443.
16. Choi, Y. S. and Lee, S. J., Three-dimensional Volumetric Measurement of Red Blood Cell Motion Using Digital Holographic Microscopy. *Applied Optics*, 2009. 48: p. 2983-2990.
17. Choo, Y. J. and Kang, B. S., The Characteristics of the Particle Position along an Optical Axis in Particle Holography. *Measurement Science and Technology*, 2006. 17: p. 761–770.
18. Chou, G. F. and Prausnitz, J. M., Adiabatic Flash Calculations for Continuous or Semicontinuous Mixtures Using an Equation of State. *Fluid Phase Equilibria*, 1986. 30: p. 75-82.

19. Collier, R. J., Burckhardt, C. B. and Lin, L. H., Optical Holography, Academic Press, New York, 1971.
20. Cotterman, R. L., Bender, R. and Prausnitz, J. M., Phase Equilibria for Mixtures Containing Very Many Components. Development and Application of Continuous Thermodynamics for Chemical Process Design. *Industrial and Engineering Chemistry*, 1985. 24: p. 194-203.
21. Cotterman, R. L. and Prausnitz, J. M., Application of Continuous Thermodynamics to Natural-gas Mixtures. *Rev. Inst. Francais Pet*, 1990. 45: p. 633-643.
22. D'Alessio, J., Lazzaro, M., Massoli, P. and Moccia, V., Thermo-optical Investigation of Burning Biomass Pyrolysis Oil Droplets. *27th Symposium (International) on Combustion*, 1998. 2: p. 1915-1922.
23. Daïf, A., Bouaziz, M., Chesneau, X. and Ali Chérif, A., Comparison of Multicomponent Fuel Droplet Vaporisation Experiments in Forced Convection with the Sirignano Model. *Experimental Thermal and Fluid Science*, 1999. 18: p. 282-290.
24. Dombrovsky, L. A. and Sazhin, S. S., A Simplified Non-isothermal Model for Droplet Heating and Evaporation. *International Communications in Heat and Mass Transfer*, 2003. 30: p. 787-796.
25. Dombrovsky, L. A. and Sazhin, S. S., Absorption of Thermal Radiation in a Semi-Transparent Spherical Droplet: a Simplified Model. *Heat and Fluid Flow*, 2003. 24: p. 919-927.
26. Dombrovsky, L. A., Sazhin, S. S., Sazhina, E. M., Feng, G., Heikal, M. R., Bardsley, M. E. A. and Mikhalevsky, S. V., Heating and Evaporation of Semi-Transparent Diesel Fuel Droplets in the Presence of Thermal Radiation. *Fuel*, 2001. 80: p. 1535-1544.
27. Dushin, V. R., Kulchitskiy, A. V., Nerchenko, V. A., Nikitin, V. F., Osadchaya, E. S., Phylippov, Yu. G. and Smirnov, N. N., Mathematical Simulation for Non-equilibrium Droplet Evaporation. *Acta Astronautica*, 2008. 63: p. 1360-1371.

28. Dwyer, H. A., Calculations of Droplet Dynamics in High Temperature Environments. *Progress in Energy and Combustion Science*, 1989. 15: p. 131-158.
29. El Wakil, M. M., Priem, R. J., Brikowski, H. J., Myers, P. S. and Uyehara, O. A., Experimental and Calculated Temperature and Mass Histories of Vaporizing Fuel Drops. National Advisory Committee for Aeronaut, Technical Note 3490, 1956.
30. Elkotb, M. M., Aly, S. L. and Elsalrawy, H. A., Evaporation Characteristics of Fuel and Multifuel Droplets. *Combustion and Flame*, 1991. 85: p. 300-308.
31. Faeth, G. M. and Lazar, R. S., Fuel Droplet Burning Rates in a Combustion Gas Environment. *AIAA Journal*, 1971. 9: p. 2165-2171.
32. Frigo, M. and Johnson, S. G., FFTW User's Manual for Version 2.1.5, Massachusetts Institute of Technology, 16-March-2003.
33. Frohn, A. and Roth, N., Droplet Systems. In: *Dynamics of Droplets*, Springer-Verlag, Berlin, 2000. p. 85-102.
34. Gabor, D., A New Microscope Principle. *Nature*, 1948. 161: p. 777-778.
35. Garcia-Perez, M., Lappas, P., Hughes, P., Dell, L., Chaala, A., Kretschmer, D. and Roy, C., Evaporation and Combustion Characteristics of Bio-oils Obtained by Vacuum Pyrolysis of Wood Industry Residues. *IFRF Combustion Journal*, 2006. Article Number 200601, ISSN 1562-479X.
36. Godsave, G. A. E., Studies of the Combustion of Drops in a Fuel Spray. *4th Symposium (International) on Combustion*, 1953. p. 818-830.
37. Goodman, J. W., Foundations of Scalar Diffraction Theory. In: *Introduction to Fourier Optics*, McGraw-Hill, International ed., NY, 1996. p. 32-62.
38. Goodman, J. W., Holography. In: *Introduction to Fourier Optics*, McGraw-Hill, International ed., NY, 1996. p. 295-392.

39. Grabowski, W., Measurement of the Size and Position of Aerosol Droplets Using Holography. *Optics and Laser Technology*, 1983. 15: p. 199-205.
40. Hallett, W. L. H., A Simple Model for the Vaporisation of Droplets with Large Numbers of Components. *Combustion and Flame*, 2000. 121: p. 334-344.
41. Hallett, W. L. H. and Beauchamp-Kiss, S., Evaporation of Single Droplets of Ethanol–Fuel Oil Mixtures. *Fuel*, 2010. 89: p. 2496-2504.
42. Hallett, W. L. H. and Clark, N. A., A Model for the Evaporation of Biomass Pyrolysis Oil Droplets. *Fuel*, 2006. 85: p. 532-544.
43. Hanson, S. P., Beer, J. M. and Sarofim, A. F., Non-Equilibrium Effects in the Vaporisation of Multicomponent Fuel Droplets. *19th Symposium (International) on Combustion*, the Combustion Institute, 1982. p. 1029-1036.
44. Hara, H. and Kumagai, S., Experimental Investigation of Free Droplet Combustion under Microgravity. *23rd Symposium (International) on Combustion*, the Combustion Institute, 1991. p. 1605-1610.
45. Hara, H. and Kumagai, S., The Effect of Initial Diameter on Free Droplet Combustion with Spherical Flame. *25th Symposium (International) on Combustion*, the Combustion Institute, 1994. p. 423-430.
46. Hirschfelder, J. O., Curtiss, C. F. and Bird, R. B. *Molecular Theory of Gases and Liquids*. 4th Ed., Wiley, NY, 1967.
47. Honnery, D. R., Surface Growth in Sooting Laminar Diffusion Flames. *PhD Thesis*, Department of Mechanical Engineering, the University of Sydney Oct, 1991.
48. Hubbard, G. L., Denny, V. E. and Mills, A. F., Droplet Evaporation: Effects of Transients and Variable Properties. *International Journal of Heat and Mass Transfer*, 1975. 18: p. 1003-1008.

49. Jackson, G. S., Avedisian, C. T. and Yang, J. C., Observations of Soot during Droplet Combustion at Low Gravity: Heptane and Heptane/Monochloroalkane Mixtures. *International Journal of Heat and Mass Transfer*, 1992. 35: p. 2017-2033.
50. Jeng, S. M., Chen, L. D. and Faeth, G. M., An Investigation of Axisymmetric Buoyant Turbulent Diffusion Flames, NBS-GCR-82-367, 1981.
51. Jia, H. and Gogos, G., High Pressure Droplet Vaporisation; Effects of Liquid Gas Solubility. *International Journal of Heat and Mass Transfer*, 1993. 36: p. 4419-4431.
52. Katz, D. L. and Brown, G. G., Vapor Pressure and Vaporisation of Petroleum Fractions. *Industrial and Engineering Chemistry*, 1933. 25: p. 1373-1384.
53. Khan, Q. S., Baek, S. W. and Lee, S. Y., Effect of Droplet Initial Diameter on Droplet Vaporisation Regimes for Kerosene Fuel Droplet. *45th AIAA Aerospace Sciences Meeting and Exhibit*, Reno, Nevada AIAA 2007-1181, 2007.
54. Kim, H. and Sung, N., The Effect of Ambient Pressure on the Evaporation of a Single Droplet and a Spray. *Combustion and Flame*, 2003. 135: p. 261-270.
55. Kneer, R., Schneider, M., Noll, B. and Wittig, S., Diffusion Controlled Evaporation of a Multicomponent Droplet: Theoretical Studies on the Importance of Variable Liquid Properties. *International Journal of Heat and Mass Transfer*, 1993. 36: p. 2403-2415.
56. Kobayashi, K., Technical Reports, Tohoku University, 18:209, 1954.
57. König, G., Anders, K. and Frohn, A., A New Light-Scattering Technique to Measure the Diameter of Periodically Generated Moving Droplets. *Journal of Aerosol Science*, 1986. 17: p. 157-167.
58. Kostas, J., Honnery, D. and Soria, J., Time Resolved Measurements of the Initial Stages of Fuel Spray Penetration. *Fuel*, 2009. 88: p. 2225-2237.

59. Kouremenos, D. A., Rakopoulos, C. D. and Yfantis, E. A., A Fortran Program for Calculating the Evaporation Rates in Diesel Engine Fuel Sprays. *Advances in Engineering Software*, 1992. 15: p. 67-71.
60. Kristyadi, T., Deprédurand, V., Castanet, G., Lemoine, F., Sazhin, S. S., Elwardany, A., Sazhina, E. M. and Heikal, M. R., Monodisperse Monocomponent Fuel Droplet Heating and Evaporation. *Fuel*, 2010. 89: p. 3995-4001.
61. Kryukov, A. P., Levashov, V. Yu. and Sazhin, S. S., Evaporation of Diesel Fuel Droplets: Kinetics versus Hydrodynamic Models. *International Journal of Heat and Mass Transfer*, 2004. 47: p. 2541-2549.
62. Kumagai, S., Sakai, T. and Okajima, S., Combustion of Free Fuel Droplets in a Freely Falling Chamber. *13th Symposium (International) on Combustion*, the Combustion Institute, Pittsburgh, PA, 1971. p. 778-785.
63. Lage, P. L. C. and Rangel, R. H., Total Thermal Radiation Absorption by a Single Spherical Droplet. *Thermophysics and Heat Transfer*, 1993. 7: p. 101-109.
64. Landis, R. B. and Mills, A. F., Effects of Internal Diffusional Resistance on the Vaporisation of Binary Droplets. *5th International Heat Transfer Conference*, Tokyo, Japan, 1974. Paper B7-9.
65. Lara-Urbaneja, P. and Sirignano, W. A., Theory of Transient Multicomponent Droplet Vaporisation in a Convective Field. *18th Symposium (International) on Combustion*, the Combustion Institute, Pittsburgh, PA, 1981. p. 1365-1374.
66. Lasheras, J. C., Fernandez-Pello, A. C. and Dryer, F. L., Initial Observations on the Free Droplet Combustion Characteristics of Water-in-oil Emulsions. *Combustion Science and Technology*, 1979. 21: p. 1-14.

67. Lasheras, J. C., Fernandez-Pello, A. C. and Dryer, F. L., Experimental Observations on the Disruptive Combustion of Free Droplets of Multicomponent Fuels. *Combustion Science and Technology*, 1980. 22: p. 195-209.
68. Law, C. K., Quasi-steady Droplet Vaporisation Theory with Property Variations. *Physics of Fluids*, 1975. 18: p. 1426-1432.
69. Law, C. K., Multicomponent Droplet Combustion with Rapid Internal Mixing. *Combustion and Flame*, 1976. 26: p. 219-233.
70. Law, C. K., Internal Boiling and Superheating in Vaporizing Multicomponent Droplets. *American Institute of Chemical Engineers Journal*, 1978. 24: p. 626-632.
71. Law, C. K., Recent Advances in Droplet Vaporisation and Combustion. *Progress in Energy and Combustion Science*, 1982. 8: p. 171-201.
72. Law, C. K., Chung, S. H. and Srinivasan, N., Gas-Phase Quasi-Steadiness and Fuel Vapor Accumulation Effects in Droplet Burning. *Combustion and Flame*, 1980. 38: p. 173-198.
73. Law, C. K. and Law, H. K., Theory of Quasi-steady One-dimensional Diffusional Combustion with Variable Properties Including Distinct Binary Diffusion Coefficients. *Combustion and Flame*, 1977. 29: p. 269-275.
74. Law, C. K. and Law, H. K., A d^2 -Law for Multicomponent Droplet Vaporisation and Combustion. *AIAA Journal*, 1982. 20: p. 522-527.
75. Law, C. K., Lee, C. H. and Srinivasan, N., Combustion Characteristics of Water-in-oil Emulsion Droplets. *Combustion and Flame*, 1980. 37: p. 125-143.
76. Law, C. K., Prakash, S. and Sirignano, W. A., Theory of Convective, Transient, Multicomponent Droplet Vaporisation. *16th Symposium (International) on Combustion*, the Combustion Institute, Pittsburgh, PA, 1977. p. 605-617.

77. Leon-Garcia, A., Probability and Random Processes for Electrical Engineering, Addison-Wesley Publishing Company, 2nd Ed., ISBN 0-201-50037-X, 1994.
78. Lerner, S. L., Homan, H. S. and Sirignano, W. A., Multicomponent Droplet Vaporisation at High Reynolds Numbers: Sizes, Composition, and Trajectory Histories. 23rd A.I.Ch.E. Annual Meeting, New York, 1980.
79. Manrique, J. A. and Borman, G. L., Calculations of Steady State Droplet Vaporisation at High Ambient Pressures. *International Journal of Heat and Mass Transfer*, 1969. 12: p. 1081-1095.
80. Maqua, C., Castanet, G., Doué, N., Lavergne, G. and Lemoine, F., Temperature Measurements of Binary Droplets Using Three Color Laser-induced Fluorescence. *Experiments in Fluids*, 2006. 40: p. 786–797.
81. Maqua, C., Castanet, G. and Lemoine, F., Bicomponent Droplets Evaporation: Temperature Measurements and Modelling. *Fuel*, 2008. 87: p. 2932–2942.
82. Massoli, P., Beretta, F., D'Alessio, A. and Lazzaro, M., Temperature and Size of Single Transparent Droplets by Light Scattering in the Forward and Rainbow Regions. *Applied Optics*, 1993. 32: p. 3295-3301.
83. Matsumoto, M. and Nishimura, T., Mersenne Twister: A 623-Dimensionally Equidistributed Uniform Pseudo-Random Number Generator. *ACM Transactions on Modeling and Computer Simulation*, 1998. 8: p. 3-30.
84. Mattingly, J. D., Heiser, W. H. and Pratt, D. T., Aircraft Engine Design, 2nd Ed., AIAA Education Series, 2002.
85. Mawid, M. and Aggarwal, S. K., Analysis of Transient Combustion of a Multicomponent Liquid Fuel Droplet. *Combustion and Flame*, 1991. 84: p. 197-209.

86. McCreath, C. G. and Chigier, N. A., Liquid Spray Burning in the Wake of a Stabilizer Disc. *14th Symposium (International) on Combustion*, the Combustion Institute, Pittsburgh, PA, 1973. p. 1355-1363.
87. Megaridis, C. M. and Sirignano, W. A., Numerical Modeling of a Vaporizing Multicomponent Droplet. *23rd Symposium (International) on Combustion*, the Combustion Institute, 1990. p. 1413-1421.
88. Mikami, M., Yagi, T. and Kojima, N., Occurrence Probability of Microexplosion in Droplet Combustion of Miscible Binary Fuels. *27th Symposium (International) on Combustion*, the Combustion Institute, 1998. 27: p. 1933-1941.
89. Miyasaka, K. and Law, C. K., Combustion of Strongly-interacting Linear Droplet Arrays. *18th Symposium (International) on Combustion*, 1981. 18: p. 283-292.
90. Newbold, F. R. and Amundson, N. R., A Model for Evaporation of a Multicomponent Droplet. *A.I.Ch.E. Journal*, 1973. 19: p. 22-30.
91. Niioka, T. and Sato, J., Combustion and Microexplosion Behavior of Miscible Fuel Droplets under High Pressure. *21st Symposium (International) on Combustion*, 1988. 21: p. 625-631.
92. Okajima, S. and Kumagai, S., Further Investigations of Combustion of Free Droplets in a Freely Falling Chamber Including Moving Droplets. *15th Symposium (International) on Combustion*, the Combustion Institute, Pittsburgh, PA, 1975. p. 401-407.
93. Onural, L. and Scott, P. D., Digital Decoding of in-line Holograms. *Optical Engineering*, 1987. 26: p. 1124-1132.
94. Palero, V., Lobera, J. and Arroyo, M. P., Digital Image Plane Holography (DIPH) for Two-Phase Flow Diagnostics in Multiple Planes. *Experiments in Fluids*, 2005. 39: p. 397-406.

95. Palero, V., Arroyo, M. P. and Soria, J., Digital Holography for Micro-Droplet Diagnostics. *Experiments in Fluids*, 2007. 43: p. 185-195.
96. Paredes, M. L. L., Nobrega, R. and Tavares, F. W., A Completely Analytical Equation of State for Mixture of Square-well Chain Fluid of Variable Well Width. In: XIX Inter American Congress of Chemical Engineering, Agios de Sao Pedro, Brazil; 24–27 September 2000. Paper no. 396.
97. Pflaum, W. and Mollenhauer, K., Wärmeübergang in der Verbrennungskraftmaschine. Springer, Wien, NY, 1977.
98. Poling, B. E., Prausnitz, J. M. and O'Connell, J. P., Diffusion Coefficients. In: *The Properties of Gases and Liquids*, 5th Ed., McGraw-Hill, NY, 2000. p. 625-679.
99. Prakash, S. and Sirignano, W. A., Liquid Fuel Droplet Heating with Internal Circulation. *International Journal of Heat and Mass Transfer*, 1978. 21: p. 885-895.
100. Prakash, S. and Sirignano, W. A., Theory of Convective Droplet Vaporisation with Unsteady Heat Transfer in the Circulating Liquid Phase. *International Journal of Heat and Mass Transfer*, 1980. 23: p. 253-268.
101. Randolph, A. L., Makino, A. and Law, C. K., Liquid-Phase Diffusional Resistance in Multicomponent Droplet Gasification. *21st Symposium (International) on Combustion*, the Combustion Institute, 1986. p. 601-608.
102. Renksizbulut, M., Bussmann, M. and Li, X., A Droplet Vaporisation Model for Spray Calculations. *Particle & Particle Systems Characterization*, 1992. 9: p. 59-65.
103. Renksizbulut, M. and Haywood, R. J., Transient Droplet Evaporation with Variable Properties and Internal Circulation at Intermediate Reynolds Numbers. *International Journal of Multiphase Flow*, 1988. 14: p. 189-202.
104. Rubel, G. O., On the Evaporation Rates of Multicomponent Oil Droplets. *Journal of Colloid and Interface Science*, 1981. 81: p. 188-195.

105. Sangiovanni, J. J. and Labowsky, M., Burning Times of Linear Fuel Droplet Arrays: A Comparison of Experiment and Theory. *Combustion and Flame*, 1982. 47: p 15-30.
106. Sasaki, O., Abe, T. and Shimizu, T., Simultaneous Measurement of Falling Velocity and Size of Large Droplets. *Applied Optics*, 1980. 19: p. 1151–1153.
107. Sazhin, S. S., Abdelghaffar, W. A., Sazhina, E. M. and Heikal, M. R., Models for Droplet Transient Heating: Effects on Droplet Evaporation, Ignition, and Break-up. *International Journal of Thermal Sciences*, 2005. 44: p. 610-622.
108. Sazhin, S. S., Abdelghaffar, W. A., Sazhina, E. M., Mikhalovsky, S. V., Meikle, S. T. and Bai, C., Radiative Heating of Semi Transparent Diesel Fuel Droplets. *Heat Transfer*, 2004. 126: p. 105-109.
109. Sazhin, S. S., Kristyadi, T., Abdelghaffar, W. A. and Heikal, M. R., Models for Fuel Droplet Heating and Evaporation: Comparative Analysis. *Fuel*, 2006. 85: p. 1613–1630.
110. Schlichting, H. and Gersten, K., Boundary-Layer Theory, 8th Revised and Enlarged Ed., Springer-Verlag, NY, 2000.
111. Shaddix, C. R. and Hardesty, D. R., *Combustion Properties of Biomass Flash Pyrolysis Oils: Final Project Report*, Sandia Report, SAND99-8238, April 1999.
112. Shaygan, N. and Prakash, S., Droplet Ignition and Combustion Including Liquid Phase Heating. *Combustion and Flame*, 1995. 102: p. 1-10.
113. Sheng, J., Malkiel, E. and Katz, J., Single Beam Two-views Holographic Particle Image Velocimetry. *Applied Optics*, 2003. 45: p. 235-250.
114. Sheng, J., Malkiel, E. and Katz, J., Digital Holographic Microscope for Measuring Three-dimensional Particle Distributions and Motions. *Applied Optics*, 2006. 45: p. 3893-3901.

115. Shusser, M., Ytrehus, T. and Weihs, D., Kinetic Theory Analysis of Explosive Boiling of A Liquid Droplet. *Fluid Dynamics Research*, 2000. 27: p. 353-365.
116. Sirignano, W. A., Fuel Droplet Vaporisation and Spray Combustion Theory. *Progress in Energy and Combustion Science*, 1983. 9: p. 291-322.
117. Sirignano, W. A., Convective Droplet Vaporisation, Heating, and Acceleration. In: *Fluid Dynamics and Transport of Droplets and Sprays*, 2nd Ed., Cambridge University Press, NY, 2010. p. 30-89.
118. Soria, J., An Investigation of the Near Wake of a Circular Cylinder Using a Video-Based Digital Cross-Correlation Particle Image Velocimetry Technique. *Experimental Thermal and Fluid Science*, 1996. 12: p. 221-233.
119. Soria, J., Carter, J. and Kostas, J., High Resolution Multigrid Cross-Correlation Digital PIV Measurements of a Turbulent Starting Jet Using Half Frame Image Shift Recording. *Optics and Laser Technology*, 1999. 31: p. 3–12.
120. Spalding, D. B., The Combustion of Liquid Fuels. 4th *Symposium (International) on Combustion*, Williams and Wilkins, Baltimore, Md, 1953. p. 847-864.
121. Sparrow, E. M. and Gregg, J. L., Variable Fluid-property Problem in Free Convection. *Transactions of the ASME*, 1958. 80: p. 879–886.
122. Stengele, J., Prommersberger, K., Willmann, M. and Wittig, S., Experimental and Theoretical Study of One- and Two-Component Droplet Vaporisation in a High Pressure Environment. *International Journal of Heat and Mass Transfer*, 1999. 42: p. 2683-2694.
123. Stern, F., Muste, M., Beninati, M. L. and Eichinger, W. E., *Summary of Experimental Uncertainty Assessment Methodology with Example*, IIHR Technical Report No. 406, University of Iowa, Iowa City, IA, 1999.

124. Svehla, R. A., *Estimated Viscosities and Thermal Conductivities of Gases at High Temperatures*, NASA Technical Report, R-132, 1962.
125. Tamim, J. and Hallett, W. L. H., A Continuous Thermodynamics Model for Multicomponent Droplet Vaporisation. *Chemical Engineering Science*, 1995. 50: p. 2933-2942.
126. Taylor, J., *An Introduction to Error Analysis: the Study of Uncertainties in Physical Measurements*, University Science Books, 2nd Ed., ISBN 0-935702-75-X, 1997.
127. Technical Data Book - Petroleum Refining. American Petroleum Institute, 6th Ed., 1997.
128. Toker, G. R. and Stricker, J., Holographic Study of Suspended Vaporizing Volatile Liquid Droplets in Still Air. *International Journal of Heat and Mass Transfer*, 1996. 39: p. 3475-3482.
129. Tong, A. Y. and Sirignano, W. A., Multicomponent Droplet Vaporisation in a High Temperature Gas. *Combustion and Flame*, 1986. 66: p. 221-235.
130. Turns, S. R., Combustion and Thermochemistry. In: *An Introduction to Combustion: Concepts and Applications*, McGraw-Hill, NY, 1996. p. 9-82.
131. Turns, S. R., Droplet Evaporation and Burning. In: *An Introduction to Combustion: Concepts and Applications*, McGraw-Hill, NY, 1996. p. 362-422.
132. Ueki, H., Ishida, M. and Sakaguchi, D., Investigation of Droplet Disintegration in Diesel Spray Core by Advanced Laser 2-Focus Velocimeter. *SAE International*, 2005. doi: 10.4271/2005-01-1238.
133. Ulmke, H., Wriedt, T. and Bauckhage, K., Piezoelectric Droplet Generator for the Calibration of Particle-Sizing Instruments. *Chemical Engineering and Technology*, 2001. 24: p. 265-268.

134. Umhauer, H., Particle Size Distribution Analysis by Scattered Light Measurements Using an Optically Defined Measuring Volume. *Journal of Aerosol Science*, 1983. 14: p. 765-770.
135. van Beeck, J. P. A. J. and Riethmuller, M. L., Rainbow Phenomena Applied to the Measurement of Droplet Size and Velocity and to the Detection of Nonsphericity. *Applied Optics*, 1996. 35: p. 2259–2266.
136. Walker, J. D., Rainbow from Single Drops of Water and Other Liquids. *American Journal of Physics*, 1976. 44: p. 421–433.
137. Wang, C. H. and Law, C. K., Microexplosion of Fuel Droplets under High Pressure. *Combustion and Flame*, 1985. 59: p. 53–62.
138. Wang, C. H., Liu, X. Q. and Law, C. K., Combustion and Microexplosion of Freely Falling Multicomponent Droplets. *Combustion and Flame*, 1984. 56: p. 175-197.
139. Willert, C. E. and Gharib, M., Digital Particle Image Velocimetry. *Experiments in Fluids*, 1991. 10: p. 181-193.
140. Wilms, D. I. J., Evaporation of Multicomponent Droplets. *PhD dissertation*, Institut für Thermodynamik der Luft- und Raumfahrt, Stuttgart University Oct, 2005.
141. Wood, B. J., Wise, H. and Inami, S. H., Heterogeneous Combustion of Multicomponent Fuels. *Combustion and Flame*, 1960. 4: p. 235-242.
142. Wornat, M. J., Porter, B. G. and Yang, N. Y. C., Single Droplet Combustion of Biomass Pyrolysis Oils. *Energy Fuels*, 1994. 8: p. 1131-1142.
143. Wu, J. S., Liu, Y. J. and Sheen, H. J., Effects of Ambient Turbulence and Fuel Properties on the Evaporation Rate of Single Droplets. *International Journal of Heat and Mass Transfer*, 2001. 44: p. 4593-4603.

144. Yang, Y. and Kang, B., Measurements of the Characteristics of Spray Droplets using in-line Digital Particle Holography. *Journal of Mechanical Science and Technology*, 2009. 23: p. 1670-1679.
145. Yao, G., A Film-Theory-Based Model for a Multicomponent Droplet Evaporation at Both Low- and High-Pressure Environments. *Heat Transfer*, 2006. 128: p. 290-294.
146. Zeng, Y. and Lee, C. F., Modeling Droplet Breakup Processes under Micro-explosion Conditions. *Proceedings of the Combustion Institute*, 2007. 31: p. 2185-2193.
147. Zhang, H. and Law, C. K., Effects of Temporally Varying Liquid-Phase Mass Diffusivity in Multicomponent Droplet Gasification. *Combustion and Flame*, 2008. 153: p. 593-602.
148. Zhao, Y. and Qiu, H. H., Measurements of Multicomponent Microdroplet Evaporation by Using Novel Optical Techniques. In: 12th Symposium on Application of Laser Techniques to Fluid Mechanics, Lisbon, 2004.
149. Zhu, G.-S. and Reitz, R. D., A Model for High-Pressure Vaporisation of Droplets of Complex Liquid Mixtures Using Continuous Thermodynamics. *Heat and Mass Transfer*, 2002. 45: p. 495-507.
150. Zhu, G. S. and Aggarwal, S. K., Fuel Droplet Evaporation in a Supercritical Environment. *Transactions of the ASME*, 2002. 124: p. 762-770.
151. Zhu, G., Reitz, R. D. and Aggarwal, S. K., Gas-phase Unsteadiness and Its Influence on Droplet Vaporisation in Sub- and Super-Critical Environments. *Heat and Mass Transfer*, 2001. 44: p. 3081-3093.

Appendix A

Experimental Data and Model Predictions

Experimental data and model predictions that have not been indicated in the thesis are shown in this section.

A.1 Average Measurement Data

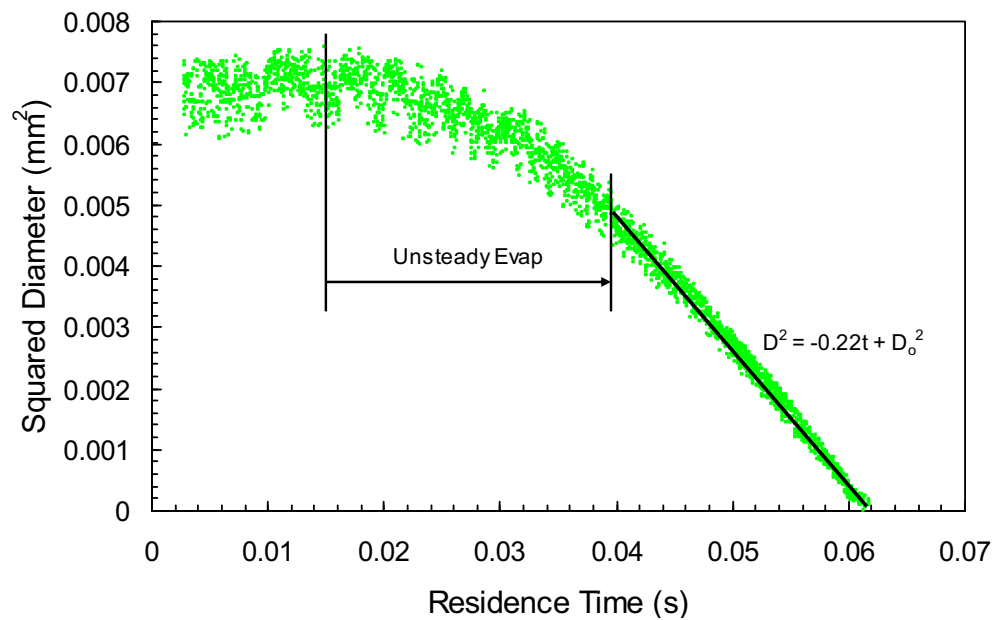


Figure A.1: Variation of squared diameter against residence time of the 84 μm nonane droplet evaporating at high temperature setting

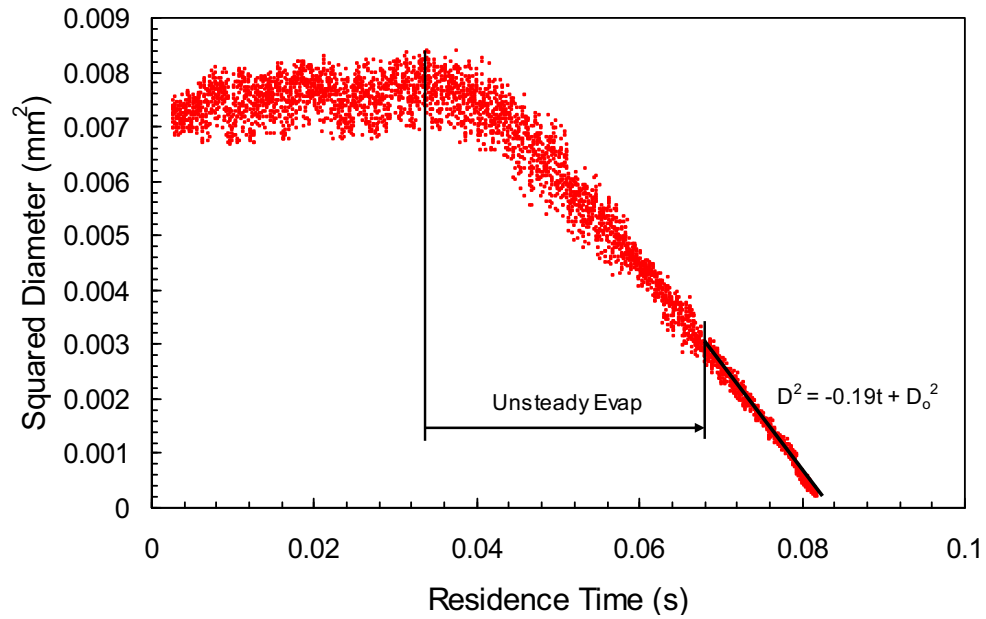


Figure A.2: Variation of squared diameter against residence time of the 85 μm diesel droplet evaporating at high temperature setting

A.2 Instantaneous Measurement Data

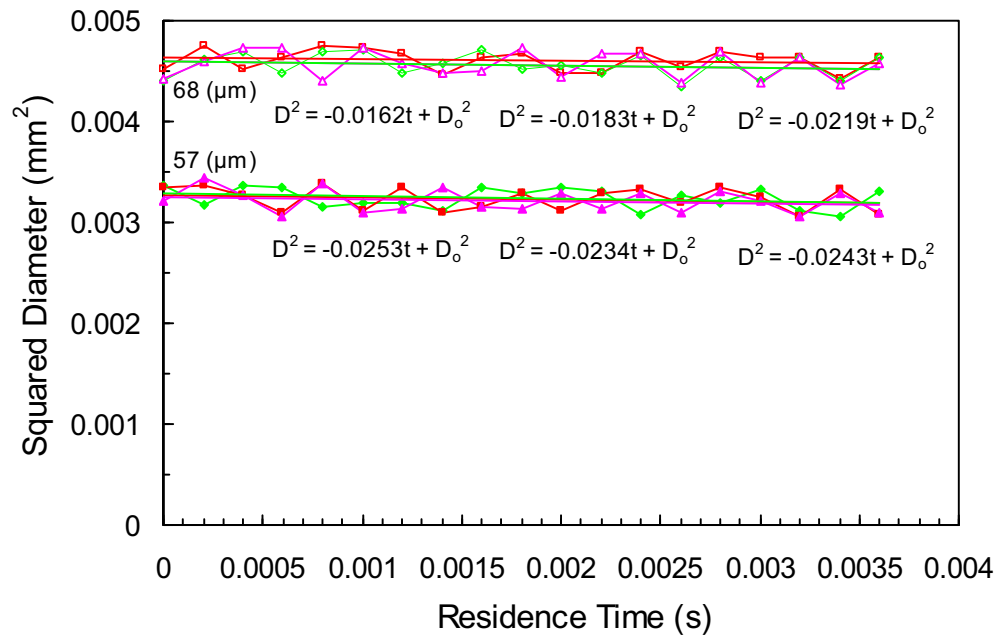


Figure A.3: Droplet size histories at measurement location $x = 0$ mm ($T = 430$ K) for initial diameters $D_0 = 68$ μm and 57 μm . Equations shown are lines of best fit for three individual measurements each of which has a separate symbol.

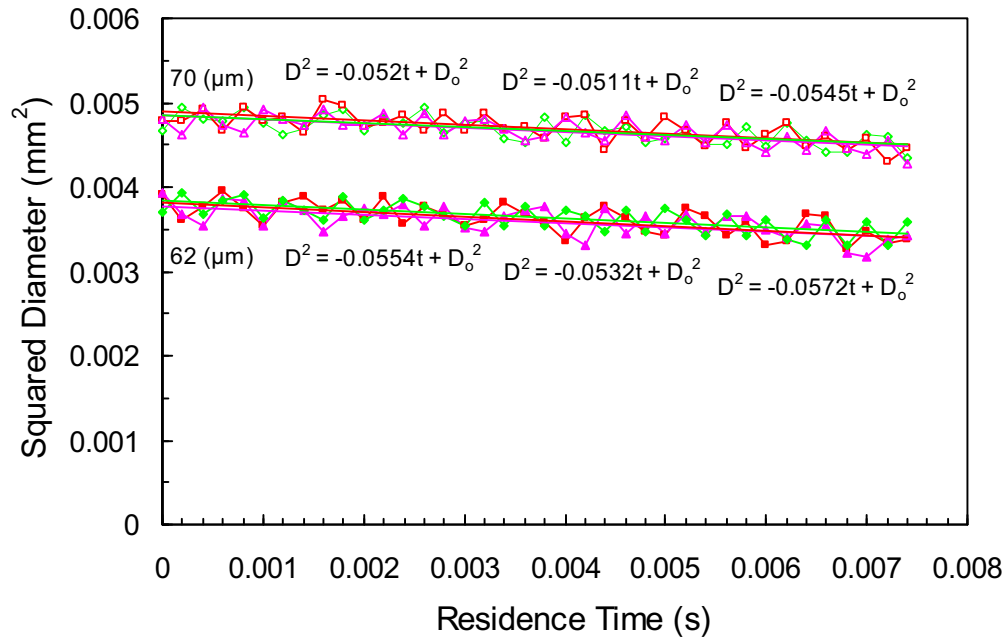


Figure A.4: Droplet size histories at measurement location $x = 5$ mm ($T = 480$ K) for initial diameters $D_0 = 70 \mu\text{m}$ and $62 \mu\text{m}$. Equations shown are lines of best fit for three individual measurements each of which has a separate symbol.

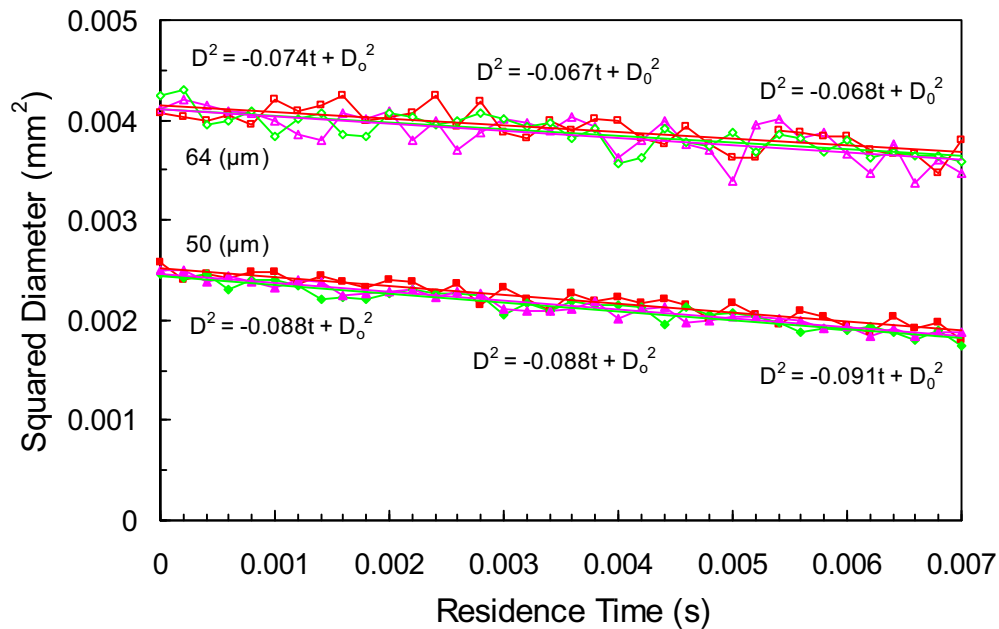


Figure A.5: Droplet size histories at measurement location $x = 10$ mm ($T = 530$ K) for initial diameters $D_0 = 64 \mu\text{m}$ and $50 \mu\text{m}$. Equations shown are lines of best fit for three individual measurements each of which has a separate symbol.

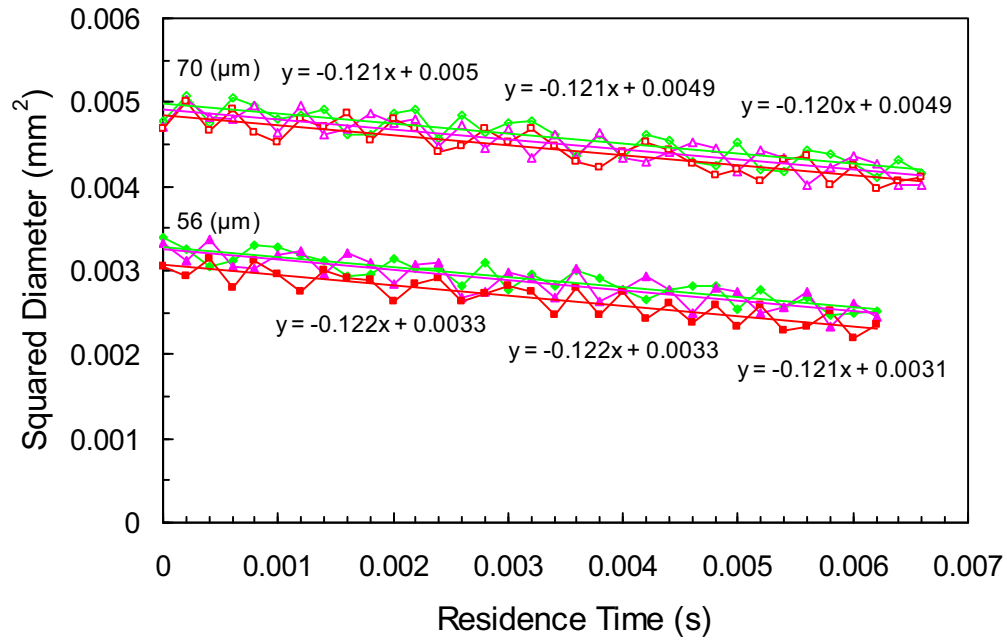


Figure A.6: Droplet size histories at measurement location $x = 15$ mm ($T = 570$ K) for initial diameters $D_0 = 70$ μm and 56 μm . Equations shown are lines of best fit for three individual measurements each of which has a separate symbol.

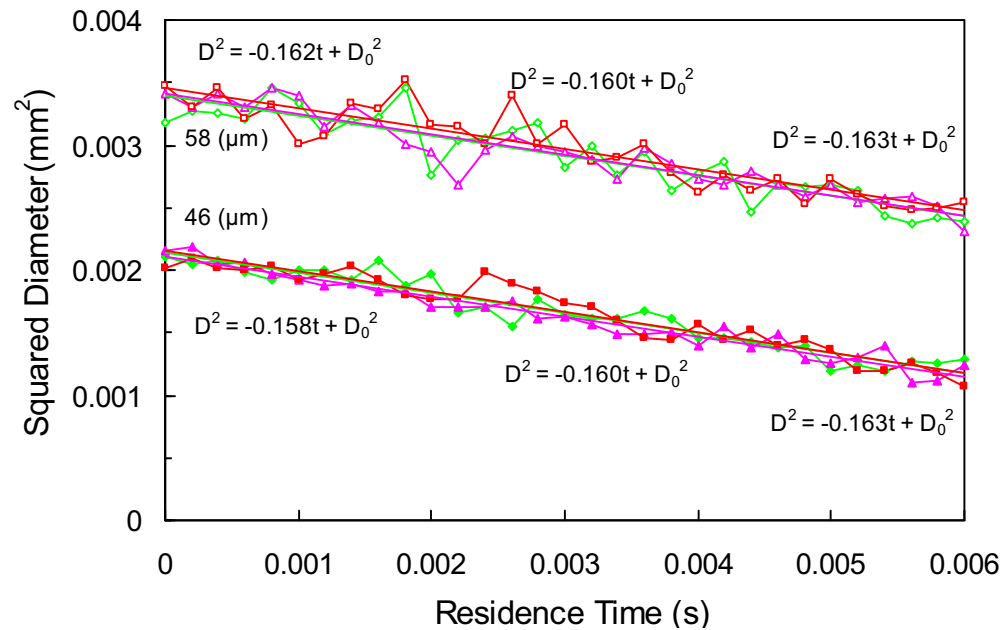


Figure A.7: Droplet size histories at measurement location $x = 20$ mm ($T = 600$ K) for initial diameters $D_0 = 58$ μm and 46 μm . Equations shown are lines of best fit for three individual measurements each of which has a separate symbol.

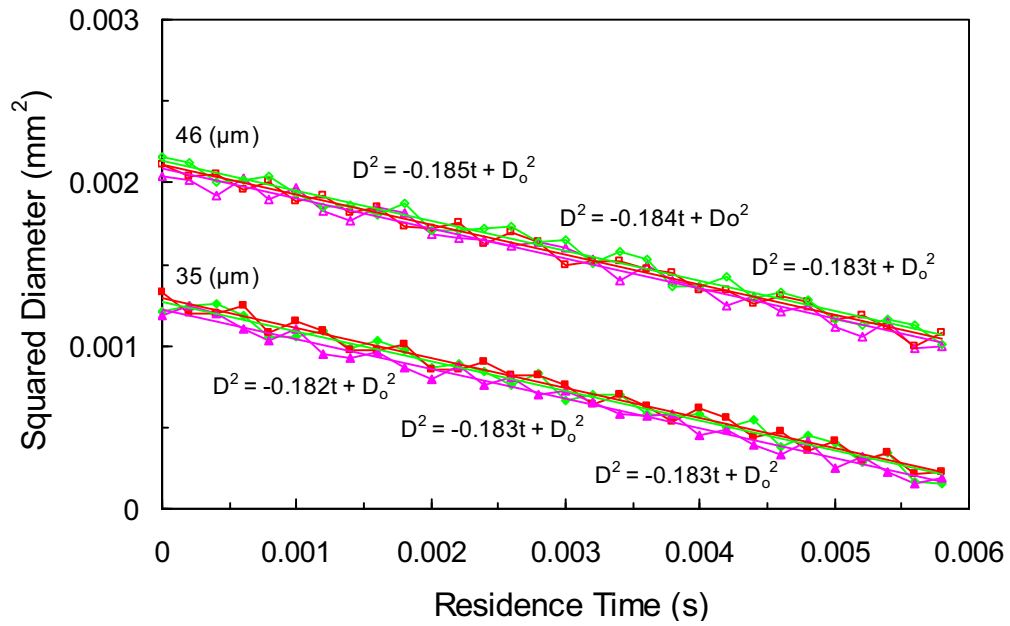


Figure A.8: Droplet size histories at measurement location $x = 25$ mm ($T = 630$ K) for initial diameters $D_o = 46$ μm and 35 μm . Equations shown are lines of best fit.

A.3 Model Predictions

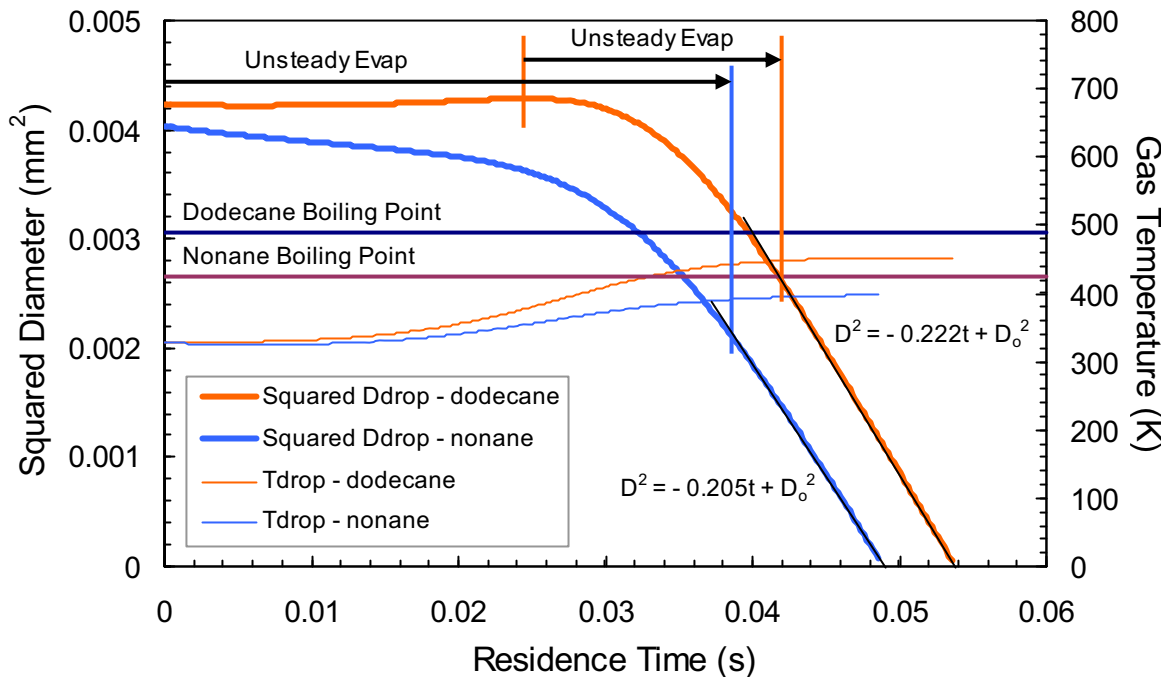


Figure A.9: Model predictions for the 65 μm dodecane droplet and 63.5 μm nonane droplet for T_H . Shown are the variations of squared diameters against residence time. Boiling points and droplet temperatures are also indicated.

Appendix B

Thermophysical Properties Calculations

The properties of the liquid fuels have been calculated following the instruction in API Technical Data Book [127] while that of air are taken from empirical correlations [97].

B.1 Latent heat of vaporisation of fuels

As the reduced temperature T_r (the ratio of T/T_{cr} – Rankine/Rankine) in this system is always higher than 0.4, the latent heat of vaporisation H of fuels is found by functional fit on graphs 7C1.8 and 7C1.13. A polynomial of order 6th is used for this fit:

$$H = lh_6 T^6 + lh_5 T^5 + lh_4 T^4 + lh_3 T^3 + lh_2 T^2 + lh_1 T + lh_0 \quad (B.1)$$

in which T is in Fahrenheit, H is in Btu/lb. The coefficients found from the fit for current fuels are listed in Table B.1. The relative error of the heat of vaporisation is around 3%.

Table B.1: Coefficients for calculating the heat of vaporisation of fuels

Fuel	lh_0	lh_1	lh_2	lh_3	lh_4	lh_5	lh_6
Dodecane	160.247	-0.11432	2.598E-04	-1.526E-06	3.605E-09	-4.108E-12	1.604E-15
Decane	161.113	-0.09084	-2.000E-04	1.375E-06	-5.751E-09	1.053E-11	-7.420E-15
Nonane	162.099	-0.10092	-4.270E-05	-4.834E-08	-6.278E-10	2.343E-12	-2.856E-15

B.2 Fuel vapor pressure on droplet surface

Vapor pressure on the droplet surface can be calculated as follows:

$$\ln p_r^{(0)} = 5.92714 - 6.09648/T_r - 1.28862 \ln T_r + 0.169347 T_r^6 \quad (\text{B.2})$$

$$\ln p_r^{(1)} = 15.2518 - 15.6875/T_r - 13.4721 \ln T_r + 0.435770 T_r^6 \quad (\text{B.3})$$

$$\ln p_r = \ln p_r^{(0)} + \omega \ln p_r^{(1)} \quad (\text{B.4})$$

in which p_r is the reduced pressure being the ratio of p_v/p_{cr} (psia/psia) and ω is the acentric factor: $\omega_{\text{dodecane}} = 0.5764$, $\omega_{\text{decane}} = 0.4923$, $\omega_{\text{nonane}} = 0.4435$. The elative error is about 3.5%.

B.3 Liquid fuel density

The liquid density is calculated based on functional fit of the graph 6A2.22 to find the density correlation factor C :

$$C = -0.6185 T_r^3 + 0.6335 T_r^2 - 0.8234 T_r + 1.3998. \quad (\text{B.5})$$

then the density can be calculated via

$$\rho = \rho_{ref} C / C_{ref} \quad (\text{B.6})$$

with ρ_{ref} and C_{ref} being the density and correlation factor at the reference condition of 60 F and 1 atm as listed in Table B.2. The error for the present conditions is only 1%.

Table B.2: Reference correlation factor and density of fuels

Fuels	Correlation factor C_{ref}	Density ρ_{ref} (kg/m ³)
Dodecane	1.077	751.69
Decane	1.077	733.48
Nonane	1.077	721.38

B.4 Liquid fuel specific heat capacity

The specific heat capacity of fuel is calculated as

$$C_{pl} = A + BT_{rb} + CT_{rb}^2 + DT_{rb}^3 + n_c[AA + BBT_{rb} + CCT_{rb}^2 + DD T_{rb}^3] \quad (B.7)$$

with n_c being the carbon number of the fuel and T_{rb} being the ratio of T/T_b (Rankine/Rankine). C_{pl} is in Btu/lb.R. The followings are constants for n-Alkanes:

$A = 0.84167$	$AA = -0.003826$
$B = -1.47040$	$BB = -0.000747$
$C = 1.67165$	$CC = 0.041126$
$D = -0.59198$	$DD = -0.013950$

The error is about 2% on average but maximum error can be as high as 20% [127].

B.5 Liquid thermal conductivity

From the freezing point to boiling point the thermal conductivity k_l of these fuels can be calculated by linear interpolation between the data at these two extremes (see Table B.3):

$$k_l = ((k_{lB} - k_{lF})T + k_{lF}T_B - k_{lB}T_F)/(T_B - T_F)$$

in which T is in Fahrenheit and k_{lB} and k_{lF} are conductivities at boiling point and freezing point, respectively. The average error of k_l is less than 5%.

Table B.3: Thermal conductivity at the boiling and freezing points of fuels

Fuels	T_B (F)	k_{lB} (w/m.k)	T_F (F)	k_{lF} (w/m.k)
Dodecane	421.38	0.09093	14.75	0.14353
Decane	345.48	0.09456	-21.35	0.14557
Nonane	303.48	0.09716	-64.28	0.15116

B.6 Liquid dynamic viscosity

To estimate the dynamic viscosity, the following correlation at low pressure has been used which is limited to the temperature range from freezing point to boiling point of each fuel:

$$\mu_l = \exp(A + BT^{-1} + C\ln T + DT^E)$$

in which μ_l is in kg/m.s, T is in Rankine and A, B, C, D and E are coefficients for each fuel as listed in Table B.4. The average error of this method is less than 5%.

Table B.4: Correlation coefficients for estimating viscosity of fuels

Fuels	A	B	C	D	E
Dodecane	-21.386	3497.4	1.3200	0	0
Decane	-16.911	2761.2	0.7511	0	0
Nonane	-22.005	2984.4	1.4540	0	0

B.7 Properties of air

The specific heat capacity, thermal conductivity and dynamic viscosity of air are simple functions of temperature [97]:

$$k_g = 3.17 \times 10^{-4} T^{0.772}$$

$$\mu_g = 0.612 \times 10^{-6} T^{0.609}$$

$$C_{pg} = 573 T^{0.097}$$

in which T is in Kelvin, k_g in J/s.m.k, μ_g in kg/m.s and C_{pg} in J/kg.K.